Observation and Characterisation of Magnetisation Ripple using Lorentz Transmission Electron Microscopy

Alison Anne Cowan MSci, PGCert

Materials and Condensed Matter Physics Group
School of Physics and Astronomy
University of Glasgow

Submitted in fulfilment of the requirements for the Degree of

Doctor of Philosophy

January 2021

Abstract

Lorentz transmission electron microscopy (LTEM) has proved itself to be an invaluable technique when investigating in-situ micromagnetic behaviour of magnetic thin films. The nano-scale visualisation of the magnetic structure allows for not only the mapping of hysteresis behaviour, but quantitative characterisation of the materials micromagnetic properties. In this thesis, much of the previous work of experimental magnetisation ripple characterisation is reviewed. A newly developed methodology for characterisation of large sets of Fresnel images displaying magnetisation ripple properties is presented which is utilised throughout the rest of the body of work.

$Ni_{45}Fe_{55}$ has long been a high moment alternative for the more commonly used permalloy composition of $Ni_{80}Fe_{20}$ in hard disk (HDD) read-write head design. In this work a conventional TEM, and LTEM study was undertaken to investigate the effect of ultra-thin $Ni_{79}Fe_{21}$ seed layers on the physical and magnetic properties of $Ni_{45}Fe_{55}$. The dramatic effect of seed layer addition resulted in grain size and texture reduction, an increase in uniaxial anisotropy and a reduction in magnetisation ripple properties. This suggests that the film is a good candidate for controlling properties of $Ni_{45}Fe_{55}$ thin films, whilst maintaining a high magnetic moment density.

Micromagnetic modelling of magnetisation ripple using MuMax^3 software has been presented using two different methods. Both models produced visually representative simulated Fresnel images, with work specifically focusing on magnetisation reversal processes and the quantitative analysis of magnetisation ripple properties. Models produced insights into the effect of parameters such as grain size, inter-granular exchange and magnetocrystalline anisotropy directionality.

Lastly, we can quantitatively assess the physical and magnetic variations between permalloy magnetostrictive samples with varying signs, without the need for external straining, to represent normal operating conditions in HDD devices. Analysis revealed near identical physical properties, with a subtle variation in bulk and magnetic ripple properties. However, it is not possible to determine if these variations are exclusively due to differences in magnetostrictive properties or if it is more likely due to compositional variations.

Declaration

This thesis is a record of research carried out by Alison Anne Cowan, at the Materials and Condensed Matter Physics group, School of Physics and Astronomy at The University of Glasgow from 2016 - 2020. With the exception of chapters 1 and 2, which contain introductory material, all work in this thesis was carried out by myself, unless otherwise explicitly stated. The contents of this thesis are original and have not been submitted in whole or part for consideration for any other degree or qualification in this, or any other university.

Alison Cowan MSci, PGCert
January 2021

Some of the work reported in this thesis is a part of the following publications:

1. **Characterisation of magnetisation ripple using Lorentz microscopy: Effect of ultra thin $\mathbf{Ni_{79}Fe_{21}}$ seed layers on magnetic properties of $\mathbf{Ni_{45}Fe_{55}}$.** Alison Cowan, Kevin McNeill, Muhammad Bilal Janjua, Stephen McVitie, *in review.*

Acknowledgements

There are many people who without, this thesis would not have been possible. I would like to thank them for their help, support and friendship throughout my PhD.

Firstly, I would like to thank my supervisor Professor Stephen McVitie for his guidance, support and 'banter' over the years. I would like to thank the CDT PIADS, specifically Professor Robert Bowman for giving me the opportunity and Dr. Caryn Hughes for all her advice and encouragement. I am also very grateful to my collaborators at Seagate Technology for their help with sample fabrication and industry insights; without them this work would not be possible. A special thanks goes to the technical staff, both Dr. Sam McFadzean and Colin How for keeping the electron microscopes going and coming to the rescue when things inevitably went wrong.

I would like to thank all MCMP group members, past and present for making my time in Glasgow a memorable one. A special mention must be given to Gavin Macauley. I can not thank you enough for your friendship and support, we've had too many funny moments in 402 to count. Also thank you for keeping me fed with fresh pasta and custard tarts. To my main woman in physics, Kayla Fallon, you are an amazing scientist and more importantly an amazing friend. A shout-out must be given to the Friday night crew, you know who you are. The PhD experience would not have been the same without you all.

To my wonderful family, I love you all. Thank you for always being so supportive.

Lastly, and most importantly, I must thank Liam Wright who started this journey with me on Day 1. Thank you for your love, patience and support (and for proof reading all my important emails).

Contents

List of Figures

List of Tables

1

Properties of Thin Ferromagnetic Films

Contents

1.1 Thesis Overview

This body of work details in-depth research into the characterisation of ferromagnetic thin films. A common denominator in all materials studied in this work, is that they exhibit a phenomenon known as 'magnetisation ripple' which can be visualised using Lorentz microscopy. This thesis will present development of an updated methodology for characterising magnetisation ripple properties, so that it can be utilised for the reliable characterisation of large amounts of both experimental and simulated Fresnel data sets of permalloy thin films.

The outline of this thesis is given below:

Chapter 1 outlines the relevant background physics of magnetism, given as an introduction to results presented later in the thesis. Within this chapter, both basic principles of magnetism and an introduction to micromagnetic modelling will be discussed.

Chapter 2 provides a description of the experimental methods that are employed in the studies of this thesis. This includes sample fabrication and electron microscopy, with specific interest in Lorentz magnetic imaging.

Chapter 3 provides a detailed description of a newly developed methodology for characterisation of magnetisation ripple properties from experimental Lorentz TEM images. It includes a discussion into previous characterisation methods, outlining how these can be improved upon for characterisation of large data sets. Properties such as ripple wavelength and dispersion are vital for better understanding of micromagnetic behaviour. This methodology will be used for all remaining results chapters within this thesis.

Chapter 4 presents a quantitative study into the control of both structural and magnetic properties through the addition of ultra-thin $Ni_{79}Fe_{21}$ seed layers, on a higher moment composition of $Ni_{45}Fe_{55}$, for hard disk drive read-write head design. TEM imaging showed a reduction in average grain size diameter, and film texture with increasing seed layer thickness. Lorentz microscopy showed

that the seedlayer acted to suppress magnetic ripple properties and improved uniaxial hysteresis behaviour. It is proposed that seed layers are a viable option of property manipulation.

Chapter 5 involves development of micromagnetic models using MuMax^3 software, to simulate the phenomenon of magnetisation ripple. Two models are investigated, the former being a simplistic model producing a directionality variation about a fixed axis, and the latter being more physically accurate by allowing for independent anisotropy contribution control. Both models were successful in producing visually representative simulated Fresnel images exhibiting magnetisation ripple. Additionally, both models allow for control of parameters, such as grain size and anisotropy, with the aim to produce trends that replicate experimental results presented in Chapter 4.

Chapter 6 details a study of permalloy thin films exhibiting magnetostrictive properties. The physical and micromagnetic variation of samples with different magnetostrictive samples was studied, without the need for external straining. Conventional TEM showed little variation between samples in terms of physical structure, however bulk magnetic measurements highlighted a variation in behaviour. Characterisation of magnetisation ripple also confirmed a change in micromagnetic behaviour. This is followed by a discussion detailing if the differences in properties can be exclusively attributed to magnetostrictive effects.

The final chapter, **Chapter 7**, summarises the results of this thesis and assesses possible future research avenues.

1.2 Introduction to Ferromagnetic Materials

Magnetic properties of materials originate from the individual magnetic moments, which are produced by the spin (**S**) and orbital (**L**) momenta of their electrons (Figure 1.1). This produces an associated magnetic dipole moment $\boldsymbol{\mu}$, which is the sum of these contributions.

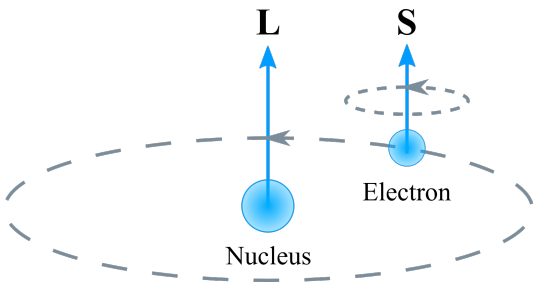

Figure 1.1: The magnetic moment in an atom is contributed by the magnetic moments of orbital motion **L** and and the spin motion of the electron **S**.

A magnetic moment can be thought of in terms of a current loop. The circulating current I encloses a surface A, giving rise to a magnetic moment $\boldsymbol{\mu}$.

$$\mu = IA = \frac{q}{t}\pi r^2 = \frac{qv}{2\pi rm}m\pi r^2 \tag{1.1}$$

where I = q/t, charge q, $t = 2\pi r/v$ which is the time of one rotation, v is the velocity of the particle and m is the mass.

The angular momentum is L = mrv so therefore the magnetic moment can be related to the angular momentum by:

$$\boldsymbol{\mu} = \frac{q}{2m}\mathbf{L} = \gamma\mathbf{L} \tag{1.2}$$

The transition metal elements, such as Ni, Fe, Co have an unfilled *3d* shell. This means certain systems can lower their energy by creating an imbalance in the number of up and down spins, thereby becoming magnetic. The Stoner theory describes a condition for magnetism at zero temperature where metals with large density of states at the Fermi level or having a large value of exchange interaction tend to be ferromagnetic. This includes d-band metals who have large density of states. s-band, or p-band metals have smaller density of states so are not ferromagnetic. Types of magnetic materials will be discussed in the following paragraphs.

A materials bulk magnetisation **M** can then be described as the integrated magnetic moment $\boldsymbol{\mu}$ per unit volume V.

$$\mathbf{M} = \frac{\int d\boldsymbol{\mu}}{V} \tag{1.3}$$

It should be noted that the overall moment is almost entirely formed by the spin angular momentum. Here, the electrons are able to interact with the electric field of the neighbouring ions and the orbital moment is quenched.

Materials can be characterised in terms of their magnetic moment alignment and behaviour in presence of a magnetic field. In diamagnetic materials, the electrons are paired with opposite and equal spins, giving a total spin in each orbital that is equal to zero. Examples of which include Copper (Cu) and Gold (Au). However, some materials have unpaired electrons. The magnetic moments of these electrons are disordered and cancel in the absence of an applied field, meaning the net magnetisation **M** of the material is zero. These materials are referred to as paramagnetic. (Figure 1.2(a)).

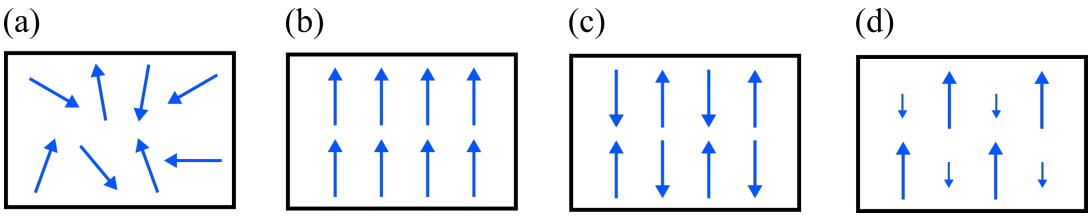

Figure 1.2: The magnetic ordering in (a) paramagnetic, (b) ferromagnetic, (c) antiferromagnetic and (d) ferrimagnetic materials.

Paramagnetic materials do not retain any magnetisation in the absence of an externally applied magnetic field because thermal motion randomises the spin orientations. They experience an ordering effect under the application of an applied field whereby the net magnetisation that is proportional to the field. This response can be described as the magnetic susceptibility χ which is the ratio of the magnetisation **M** to the magnetic field **H**:

$$\chi = \frac{\mathbf{M}}{\mathbf{H}} \tag{1.4}$$

Typical values for χ in a paramagnetic material are in the order of 10^{-5} and are dimensionless.

Materials that exhibit spontaneous magnetisation in the absence of an applied field are referred to as ferromagnetic. The spontaneous alignment of magnetic moments in a ferromagnetic was explained by Heisenberg through a quantum mechanical exchange interaction [1], the Hamiltonian of which is given by

$$H_{ex} = -2J_{ij}(\mathbf{S_i} \cdot \mathbf{S_j}) \tag{1.5}$$

where H_{ex} is the exchange energy of two interacting electron spins, $\mathbf{S_i}$ and $\mathbf{S_j}$, and J_{ij} is the material dependent exchange integral and the sum is over all interacting spins. In a ferromagnetic material, J_{ij} is positive and H_{ex} is minimised by parallel spins. The exchange interaction will be discussed further in Section 1.4.1.

In ferromagnetic materials, the neighbouring magnetic moments are aligned parallel to one another, below the Curie temperature T_C (Figure 1.2(b)). This phenomenon can be found in transition metal elements, such as iron (Fe), cobalt (Co) and nickel (Ni). The magnetisation, **M**, of a ferromagnetic material is dependent on both an applied magnetic field, **H**, and temperature T. Magnetic materials are often distinguished by their (temperature dependent) magnetic susceptibility, χ. The temperature dependence of magnetic susceptibility can be described by the Curie-Weiss law [2]. This law can be applied when the material is heated above their respective Curie temperature and is given by:

$$\chi = \frac{C}{T - T_C} \tag{1.6}$$

where C is the Curie constant, T is the temperature, and T_C is the Curie temperature. The Curie temperature for permalloy materials is in the range of 553 K to 872 K (280° - 600°), depending on its composition. [3] This means it has a sufficiently high T_C value to exhibit ferromagnetism at room temperature.

Figure 1.3 highlights the transition of ferromagnetic material to a paramagnetic state with increasing temperature.

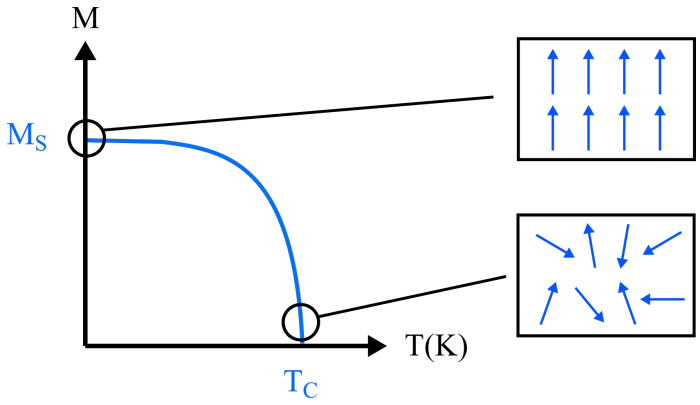

Figure 1.3: Schematic representation of the relationship between magnetisation saturation $\mathbf{M}_S$ and temperature T. In ferromagnetic materials, the magnetic dipole moments align, in a state referred to as saturation magnetisation $\mathbf{M}_S$. As the Curie temperature T_C is reached, the alignments become disrupted, causing disorder, meaning the material is now in a paramagnetic state.

In antiferromagnetic materials, the spins are arranged anti-parallel below the Néel temperature T_N (Figure 1.2(c)). At zero field, there is no overall moment. Above the Néel temperature, thermal energy destroys the alignment, causing a transition to a paramagnetic state. Figure 1.4 highlights the effect of temperature of susceptibility in para-, ferro-, and antiferromagnetic materials. It highlights how both ferro- and antiferromagnets become paramagnetic above their ordering temperatures, T_C and T_N respectively.

Ferrimagnets have oppositely aligned spins but with an unequal moment (Figure 1.2(d)). As a result, ferrimagnetic materials exhibit a net magnetic moment which is weaker than that of ferromagnetic materials. It will have a similar behaviour to that of a ferromagnetic shown in Figure 1.4(b).

By looking at the response of a material to the presence of a magnetic field, $\mathbf{H}$, we can introduce a materials magnetic flux density, $\mathbf{B}$. The magnetic induction can be related to the magnetisation $\mathbf{M}$ by,

$$\mathbf{B} = \mu_0(\mathbf{M} + \mathbf{H}) \tag{1.7}$$

where μ_0 is the permeability of free space. It can illustrate the relationship between the induced magnetic flux density **B**, measured in (T), and the externally applied magnetic field **H**, measured in (A/m) when working in SI units.

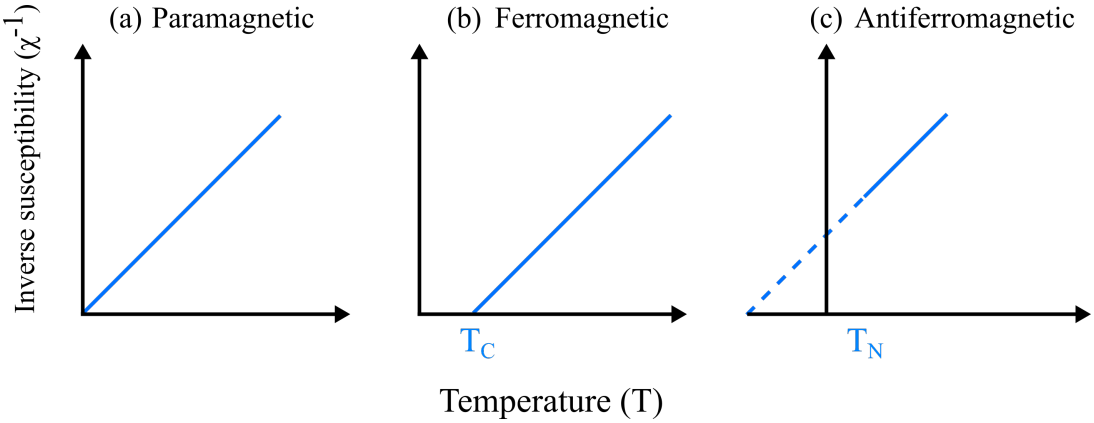

Figure 1.4: Schematic of the behaviour of the main types of magnetic materials. The temperature T dependence on the inverse susceptibility χ^{-1} of a (a) paramagnetic, (b) ferromagnetic and (c) antiferromagnetic material. For (b) and (c), the material behaviour is only being shown above the Curie and Néel temperatures respectively.

1.2.1 Magnetic Unit Systems

It is important to detail the unit systems associated with the phenomenon of magnetism. Magnetic properties can be defined in two ways; through a Gaussian / CGS (centimetre-gram-seconds) systems, or the MKS / SI (metre-kilogram-seconds) system. The Gaussian system is based on magnetostatics and the magnetic pole concept, whereas the MKS system takes an electrodynamic approach based on electric currents. For ease of understanding, a summary of the units used and their conversions are given in Table 1.1 below. For consistency of results presented in this thesis, the Gaussian unit system will be used when quoting magnetic field values, in terms of Oe (rather than A/m).

Quantity	Symbol	Gaussian Units	SI Units	Conversion
Magnetic Field	**H**	Oe	A/m	1 Oe = $1000/4\pi$ A/m
Magnetic Induction	**B**	G	T	1 G = 10^{-4} T
Magnetisation	**M**	erg.Oe^{-1}.cm^{-3}	A/m	1 erg.Oe^{-1}.cm^{-3} = 10^{3} A/m
Field Equation	-	$\mathbf{B} = \mathbf{H} + 4\pi\mathbf{M}$	$\mathbf{B} = \mu_0(\mathbf{H}+\mathbf{M})$	-

Table 1.1: Magnetic quantities with their units and conversions.

1.3 Hysteresis Loops

In a ferromagnet the individual magnetic moments of the atoms tend to be aligned parallel to each other. Ferromagnetic exchange favours parallel alignment of spins through locally aligned regions called domains. The complex behaviour of a materials magnetisation configuration in an applied field can be characterised by a hysteresis loop, whereby the hysteresis behaviour will depend on the materials history. A ferromagnetic material follows a non-linear magnetisation curve when magnetised from zero field, unlike that of a diamagnetic and paramagnetic material. A typical ferromagnetic hysteresis response is shown in Figure 1.5.

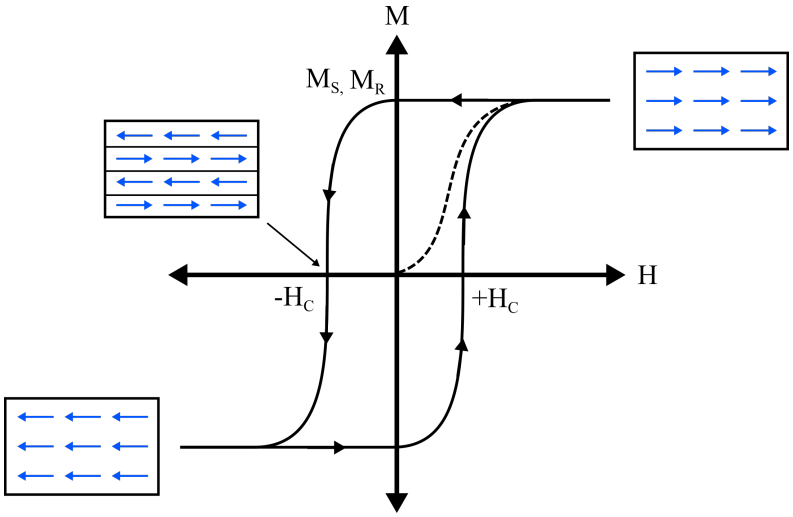

Figure 1.5: Schematic representation of a hysteresis loop of a ferromagnetic material exhibiting uniaxial anisotropy. Increasing magnetisation appears with an application of an external magnetic field **H**, where it eventually eliminates the micromagnetic structure, such as domains, until all the magnetisation lies along the direction of the field. This is known as the magnetisation saturation, M_S. Key points are marked on the loop.

The material starts from an initial demagnetised state, where the magnetisation

equals zero. As an applied magnetic field is gradually increased, the magnetisation in the sample will reach a saturation value M_S, which gives an upper limit to the magnetisation that can be achieved. This occurs as all the individual atomic moments are aligned in the same direction, parallel to the externally applied field. When the applied magnetic field drops to zero, the ferromagnetic material retains a degree of magnetisation, called the remanence M_R, which is a useful characteristic for a magnetic memory device if the value is large. The applied field is reversed to drive the magnetisation back to zero, as indicated in Figure 1.5. The value of **H** for which **M** is zero, is called the coercive field H_C. A further increase in **H**, in the negative direction, causes the magnetisation direction to reverse and a reach a negative saturation, where the moments completely align, but in the opposite direction. The **M-H** graph, like that shown in Figure 1.5, is produced by a sweeping positive and negative field between plus and minus saturation and is known as a standard hysteresis loop. In other words, it shows the history dependent nature of magnetisation in a ferromagnetic material. Once the material has been driven to saturation, the magnetising field can then be dropped to zero, where the remanent magnetisation will remain. This parameter provides the basis of magnetic recording where by information is written on a recording media (FePt) by locally magnetising areas of the media in opposite directions to represent 0's or 1's. The read head then operates to sense the local remanent magnetisation and recover the information.

The hysteresis provides quantitative information about the materials magnetic properties, such as H_C and M_R as described. Materials which retain their magnetism and are difficult to demagnetise are called hard magnetic materials, shown in Figure 1.6(b). Soft magnetic materials have low H_C and generally low M_r values, such as permalloy, shown in Figure 1.6(a). However these values are subject to change, for example, when there is an induced anisotropy. They have a large susceptibility, and allow for the relatively easy movement of domain walls. Properties of soft ferromagnetic permalloy samples are the focus of the work presented in this thesis.

Hysteresis behaviour forms an important part of the investigations reported in this thesis. They provide information on the bulk micromagnetic behaviour of

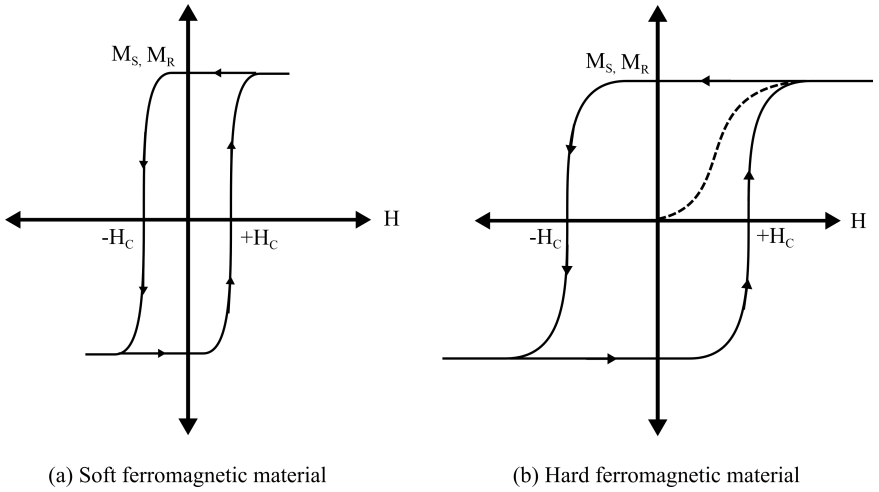

Figure 1.6: Hysteresis curve comparison of the magnetic behaviour of (a) soft ferromagnetic materials such as permalloy and (b) hard magnetic materials such as steel.

the sample. A typical hysteresis loop for the films investigated in this thesis (thin film permalloy with a defined easy axis) along both the easy and hard directions can be seen in Figure 1.7(a) and (b) respectively. This demonstrates how the magnetic response changes, depending on whether the external field is applied on the easy or hard axis of the sample.

Lorentz TEM allows for the visualisation of the dynamic micro-magnetic processes when applying an external field along both the easy and hard axis. If an external magnetic field is applied along an easy axis until saturation, as this field is gradually reduced to zero, the material still retains its magnetisation. This remains until its magnetisation is forced to switch in the opposite direction by applying a field in the opposite direction. This is called easy axis switching which is likely to consist of a domain wall nucleation which rapidly sweeps through the sample.

When an external magnetic field is applied along the hard axis, the magnetisation can change direction to align with the field in two different ways. One mechanism is coherent rotation of the magnetisation, the second is via domain formation. For the former, the magnetisation can rotate smoothly from one direction to the opposite direction (if there is some offset bias present). This occurs in films possessing

uniaxial anisotropy, and is referred to as the hard axis (Figure 1.7(b)). In larger systems it may be more energetically favourable for reversal to occur through typical domain processes. This mechanism involves nucleation of domains and domain walls, and subsequent domain wall motion.

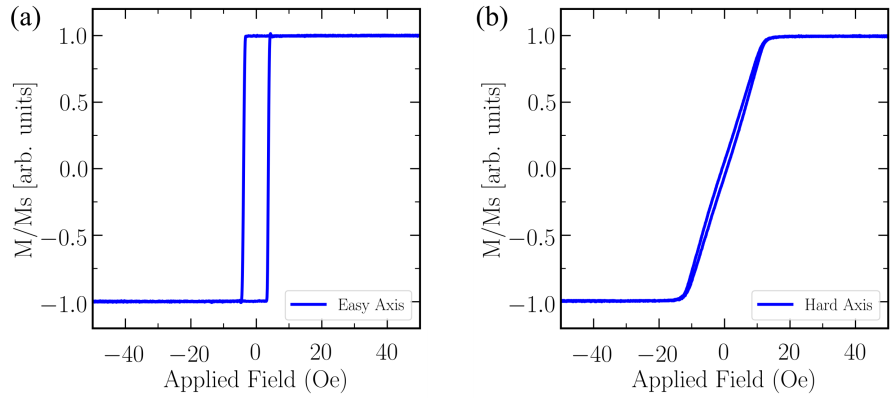

Figure 1.7: Experimental **M-H** loops for a permalloy film with induced uniaxial anisotropy, where the external field is applied along the (a) easy axis and (b) hard axis.

1.4 Magnetic Energy Terms

The net equilibrium magnetic configuration of a magnetic material can be thought of as resulting from a competition of energies. For the total energy of a ferromagnetic specimen in an externally applied field, the sum of the individual magnetic energy terms can be written as:

$$E_{total} = E_{ex} + E_k + E_d + E_z + E_\lambda \tag{1.8}$$

These terms refer to the exchange, anisotropy, magnetostatic, Zeeman and magnetostriction energies respectively. These terms dictate the micromagnetic behaviour of ferromagnetic materials, which deals with the details of magnetic structures that are observed in materials such as domain formation (Section 1.6) and magnetic hysteresis (Section 1.3). Each of these terms will be discussed

individually in the following sections, followed by how they relate to the process of domain formation.

1.4.1 Exchange Energy

The exchange energy is the energy associated with the parallel alignment of the spin system. The fundamental origin of this interaction is Coloumb repulsion between two particles with overlapping wavefunctions. The exchange energy is minimised by changing the orientation of the individual magnetic moments to lie parallel in a ferromagnetic material. It is important to note that this interaction decreases rapidly with increasing distance between atoms, therefore the exchange interaction between nearest neighbours is considered. The total exchange energy for the material assuming identical atoms is,

$$E_{ex} = -2JS^2 \sum_{ij} cos\varphi_{ij} \tag{1.9}$$

where S is the magnitude of the spin vector, J is the exchange integral and φ_{ij} is the angle between the spins i and j. The exchange interaction is a local, atomic scale interaction, which can be characterised by the exchange length parameter l_{ex}. The exchange length approximates the distance over which the direction of the magnetisation of the material is constant (i.e. width of an idealised domain wall) and is given by:

$$l_{ex} = \sqrt{\frac{2A}{\mu_0 M_s^2}} \tag{1.10}$$

where A is the exchange stiffness constant (J/m) and can be defined by $A = 2JS^2z/a$ for cubic cells in which z is the number of lattice sites in the unit crystal cell and a is the distance separating neighbouring atoms. The exchange stiffness constant serves as a characteristic of a ferromagnetic material instead of the exchange integral J between two spins. Unlike J it introduces a dependence on the crystal structure. M_S is the magnetisation saturation, and μ_0 is the permeability of

vacuum, which is a fundamental constant of 4π x 10^{-7} Hm^{-1}. For polycrystalline permalloy ($Ni_{80}Fe_{20}$), A = 1.3 x 10^{-11} J/m and M_S = 860 kA/m, which gives an exchange length l_{ex} = 5.3 nm. [4]

The continuum formulation of the Heisenberg exchange describes how neighbouring cells tend to prefer parallel alignment. The micromagnetic exchange field can be described by the following Laplacian:

$$\mathbf{H}_{exch} = \frac{2A}{\mu_0 M_s}\nabla^2\mathbf{M} \tag{1.11}$$

The exchange length and exchange stiffness are both important characteristics when simulating a granular structure, such as polycrystalline thin films, which form the subject of this thesis. The interaction between individual grains will produce a phenomenon called magnetisation ripple which will be discussed in greater detail in Section 1.7. Results from simulation models investigating magnetisation ripple will be shown in Chapter 5.

1.4.2 Magnetostatic Energy

Magnetostatic energy results from dipole interactions induced by surface and volume charges of a sample. The magnetic field is a dipole field, that means that every magnet must have two poles where the magnetic force strongly attracts an opposite pole of another magnet and repels a like pole (Figure 1.8(a)). The magnetostatic energy arises from the interaction between the field and the magnetisation it opposes and is given by:

$$E_d = -\frac{\mu_0}{2}\int_V \mathbf{M}\cdot\mathbf{H}_d dV \tag{1.12}$$

where μ_0 is the permeability of free space, $\mathbf{H}_d$ is the demagnetising field, and $\mathbf{M}$ is the magnetisation of the sample. Note that the factor of *1/2* accounts for double counting within the integral.

The demagnetising field at a point P at a position $\mathbf{r}$ to the origin of a coordinate O, can be calculated from the following equation:

$$H_d(R) = \frac{1}{4\pi}\int_V \frac{-\nabla \cdot \mathbf{M}}{|\mathbf{r\text{-}r'}|^2} dV + \frac{1}{4\pi}\int_S \frac{\mathbf{M}\cdot\mathbf{n}}{|\mathbf{r\text{-}r'}|^2} dS \tag{1.13}$$

where $\mathbf{r}$ is the position vector for the point in space where the field from the charge is evaluated, $\mathbf{r'}$ is the position of the differential magnetic charge. Meaning $|\mathbf{r\text{-}r'}|$ is the distance between the field point and charge. $\mathbf{n}$ is the outward pointing unit vector normal to the surface of the object. $\nabla \cdot \mathbf{M}$ is the magnetic volume charge density and $\mathbf{M}\cdot\mathbf{n}$ is the magnetic surface charge density. The magnetostatic energy of the specimen can be reduced by decreasing the amount of stray field generated at the edges or within the specimen. This can be achieved by the formation of the domain structure.

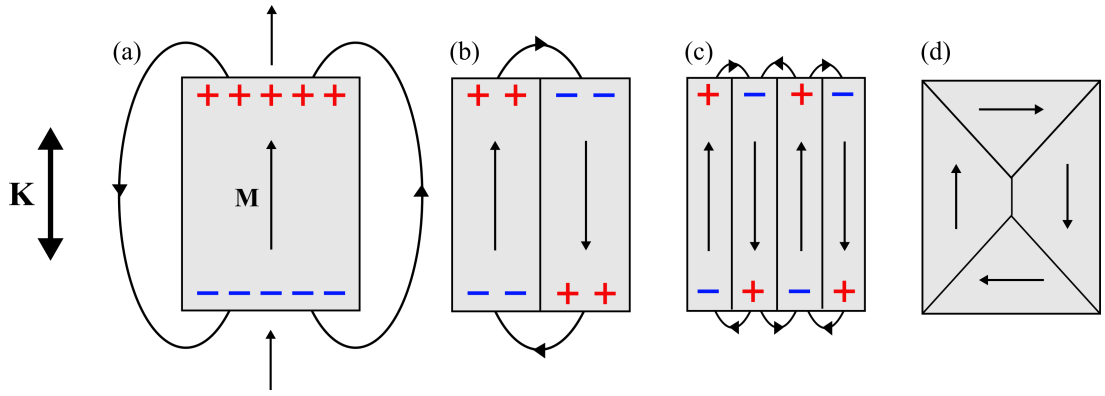

Figure 1.8: Typical domain process of reducing a demagnetisation field by splitting regions of uniform magnetisation into smaller regions with different magnetisation directions. (a) Uniform magnetisation in a rectangular ferromagnetic specimen, in which the curved lines outside the material represent the stray field and the red pluses and blue minuses represent the positive and negative charges respectively. Domain formation then occurs from (b) to (c), until (d) which demonstrates a flux closure structure in order to minimise the magnetostatic energy. The K-axis denotes the preferred directionality of magnetisation.

This effect of the magnetostatic energy is shown in Figure 1.8. Note that the K-axis refers to the anisotropy directionality which represents the preferred direction of magnetisation. A sample in which all the magnetic moments are pointing in the same direction is referred to as being in a single domain state. In this state,

the magnetostatic energy associated with the poles of the ferromagnetic is large i.e. there is a large amount of stray field energy from the contributions of $\mathbf{M} \cdot \mathbf{n}$ at the edges (Figure 1.8(a)). This is the configuration for a minimum of exchange energy as previously discussed in Section 1.4.1.

The sample can lower its total energy by being divided into several magnetic domains. Within each domain, all the magnetic moments are parallel to each other, which satisfies the minimum condition for the exchange energy. The formation of domain walls will cause a rotation of spins, thereby increasing the exchange energy. There will also be an increase in magnetostatic (1.4.2) and magnetocrystalline (1.4.4) energy. This will be discussed further in Section 1.6. The magnetostatic energy and exchange energy are in direct competition. Figure 1.8(d) shows a flux closure state, which has a minimal stray field and is the preferred state when there is little to no magnetostrictive energy and anisotropy (these energy terms will be described in the following sections).

1.4.3 Zeeman Energy

In the presence of an externally applied magnetic field, the moments within a magnetic material will attempt to align parallel to the field direction. The Zeeman energy takes into account the orientation of the magnetisation with respect to the applied field and is given by,

$$E_z = -\mu_0 \int_V \mathbf{M} \cdot \mathbf{H} dV \tag{1.14}$$

where $\mathbf{H}$ is the external magnetic field, V is the volume, and $\mathbf{M}$ is the magnetisation of the sample.

1.4.4 Magnetocrystalline Anisotropy

Magnetic anisotropy describes the dependence of the energy of a ferromagnetic body on the direction of the magnetisation. Magnetocrystalline anisotropy, E_k

energetically favours the alignment of magnetic moments along certain crystallographic directions, known as easy axis. The energetically unfavoured axis is called the hard axis. It costs energy to rotate the magnetisation direction away from the easy axis. This anisotropy energy depends on the structure of the materials lattice. The expression for the anisotropy energy can be written using α, β and γ which are the directional cosines in the crystallographic axes. For a cubic system such as Fe, the energy is given by:

$$E_k = \int_V [K_1(\alpha^2\beta^2 + \beta^2\gamma^2 + \gamma^2\alpha^2) + K_2\alpha^2\beta^2\gamma^2]dV \tag{1.15}$$

where K_1 and K_2 are the anisotropy constants for the material, and V is the volume of the material. For hexagonal or uniaxial crystals, the magnetocrystalline anisotropy energy is given by:

$$E_k = \int_V (K_1 sin^2\theta + K_2 sin^4\theta)dV \tag{1.16}$$

where θ is the angle between the magnetisation and easy axis. If we use the direction cosines, equation 1.16 becomes:

$$E_k = \int_V [K_1(1-\gamma^2) + K_2(1-\gamma^2)^2]dV \tag{1.17}$$

The material studied in this work, a permalloy magnetic alloy, is known as a soft magnetic material. This means there will be weak anisotropy resulting from the crystal structure.

The easy magnetocrystalline axis in Ni is <111> and in Fe it is <100>. For example, K_1 = -5.7 $\times$ 10^3 Jm^{-3} for *fcc* Ni. [5]

Polycrystalline materials can have no overall preferred axis as the individual crystals (or grains) are randomly orientated, unless the film is textured (which will be an important factor in the results presented in Chapters 4 and 6). Instead, the anisotropy direction varies between crystallites, resulting in 'local' easy axes.

This manifests itself in the form of magnetisation ripple, which can be visualised during Fresnel imaging.

1.4.5 Induced anisotropy

Anisotropy can be induced during or after film growth using special processing techniques. Its origin can be due to grain orientation and ordering of Ni/Fe atoms. This effect can be achieved by growing the material in a large applied field and/or annealing the sample in a large field after deposition while heated. This in turn induces a uniaxial anisotropy aligned with the field axis. This creates a well defined easy and hard axis, an example of which is shown in Figure 1.9. These plots are referred to as hysteresis loops (Section 1.3), which demonstrate a material's response to a magnetic field applied along the easy and hard axis.

Larger applied magnetic fields are required to reach the same saturation along the hard axis, compared to the easy due to the anisotropy of the film. An easy axis hysteresis loop will appear open, compared to a hard axis which will appear more closed. The uniaxial anisotropy of a thin film can be related to magnetic properties, such as the the anisotropy field H_k. This refers to the applied field needed to rotate the magnetisation to fully align with the field. The relation can be given by:

$$K_u = \frac{M_S H_k}{2} \tag{1.18}$$

where M_S is the materials magnetisation at saturation. In this work, we investigate thin films which have an overall induced uniaxial anisotropy, as well as the individual crystalline anisotropy. The anisotropy values for the induced anisotropy is significantly larger than that of the individual crystals. The effect of this, known as magnetisation ripple, will be discussed in greater detail in Section 1.7.

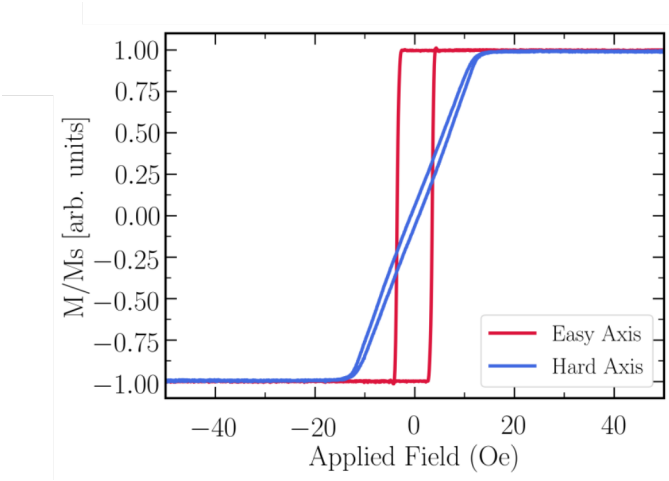

Figure 1.9: Hysteresis for 10 nm $Ni_{45}Fe_{55}$ thin film with a 0.5 nm $Ni_{79}Fe_{21}$ seed layer. Demonstrating the difference in M-H hysteresis loops when an external field is placed along the easy axis (parallel) and hard axis (perpendicular).

1.5 Magnetostriction

Magnetostriction is a physical effect present in all ferromagnetic materials. A magnetostrictive material develops mechanical deformations when subjected to an external magnetic field. The existence of magnetostriction was first discovered by James Joule in 1842 when he noted the change in length of a ferromagnetic material, in this case Nickel, with the application of an externally applied magnetic field. This effect was accordingly named after him, as the 'Joule Effect'. [6, 7] Although this is generally a small effect, the fractional change in length is in the order of 10^{-6}, it can have a substantial impact on nano-scale data storage devices, specifically in the area of shielding on the recording head. [8,9] Low magnetostriction materials are desired in the shielding of the reader head to ensure the minimisation of any stress in the presence of an externally applied magnetic field. Failure to control the induced stress on the shielding of the reader may degrade the overall performance of the recording head. This will be studied in more detail in Chapter 6.

1.5.1 Mechanism

There are two types of magnetostriction; spontaneous (**H**=0) and saturation magnetostriction (which is also referred to as 'field-induced' magnetostriction). The mechanisms of these effects are demonstrated in Figure 1.10 where the ellipsoids represent individual magnetic moments. In both cases, the magnetostriction can be simply defined as λ, which refers to the fractional change of length l, of the specimen given by:

$$\lambda = \frac{\Delta l}{l} \tag{1.19}$$

Spontaneous magnetostriction occurs when a ferromagnetic material is cooled below the Curie temperature T_C and produces a spontaneous lattice strain.

In the paramagnetic region above T_C, the atoms are in a random disordered state (Fig.1.10(a)). Reducing the temperature below T_C causes the material to become ferromagnetic (as discussed in Section 1.2), resulting in a spontaneous magnetostriction effect, λ_0 at zero field (**H**=0) or spontaneous strain, e, along a particular direction (Fig.1.10(b)).

Isotropic Spontaneous Magnetostriction

It is possible to derive a relationship between *spontaneous* magnetostriction λ_0 and *saturation* magnetostriction λ_s. To do that an isotropic material in a disordered state above T_C is considered, represented by the spherical volumes in Figure 1.11(a). As the material is cooled below T_C, spontaneous mangetostriction occurs (Figure 1.11(b)). As the material is isotropic, the magnetic domains are randomly orientated at and angle θ. The net magnetisation is consequently zero. For an isotropic material, this strain associated with the change in length, e will vary with the angle θ from the direction of spontaneous magnetisation according to:

$$e(\theta) = ecos^2\theta. \tag{1.20}$$

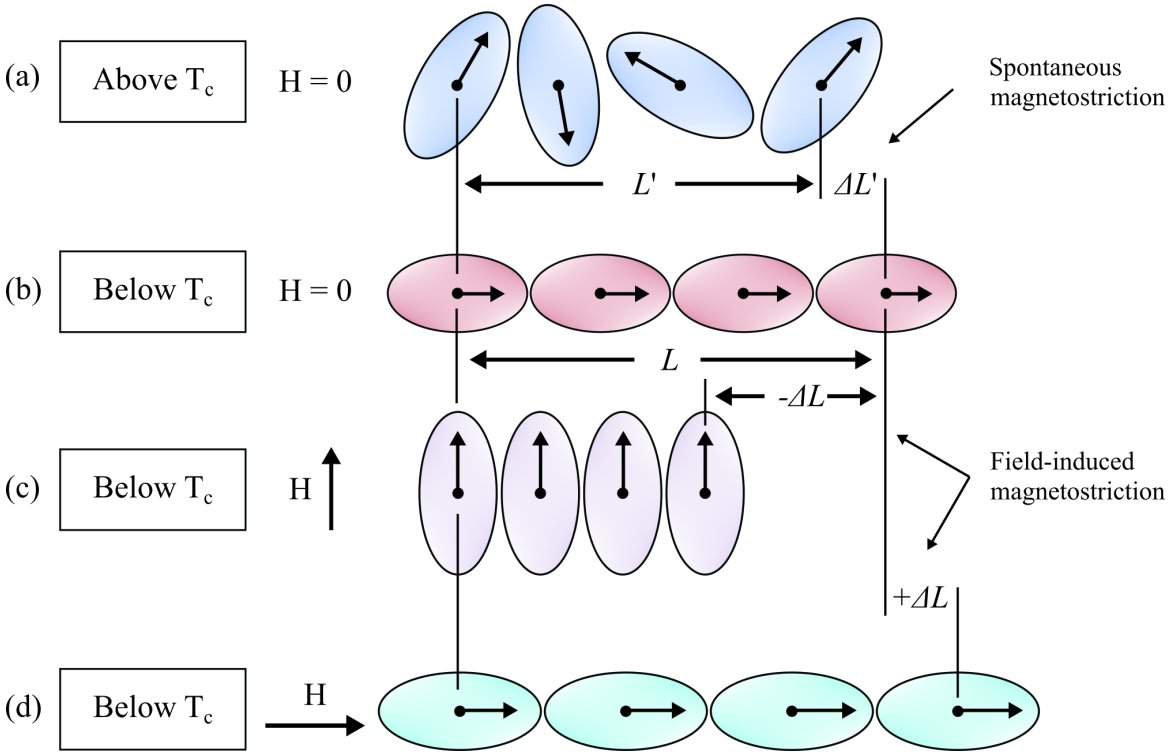

Figure 1.10: Schematic illustration of the mechanism of magnetostriction where ellipsoids represent individual magnetic moments. (a) Paramagnetic region above T_C displaying a random disordered state. (b) Spontaneous magnetostriction which occurs when a material is cooled below T_C and therefore becomes ferromagnetic. (c,d) display field-induced magnetostriction where the strain lies parallel to the applied field direction. Adapted from [10] B. D. Cullity and C. D. Graham, Introduction to magnetic materials. Hoboken, N.J.: IEEE/Wiley, 2009.

The average deformation from the effect of spontaneous magnetostriction can be obtained by integrating over all directions, assuming that the domains are randomly orientated. This gives:

$$\lambda_0 = \int_{-\pi/2}^{\pi/2} e cos^2\theta sin\theta d\theta = e \int_0^{\pi/2} -\frac{1}{3} cos^3\theta. = \frac{e}{3} \tag{1.21}$$

Saturation Magnetostriction

Saturation magnetostriction λ_s, is the magnetostriction parameter measured when a sample has been magnetically saturated. This is the point where an increase in

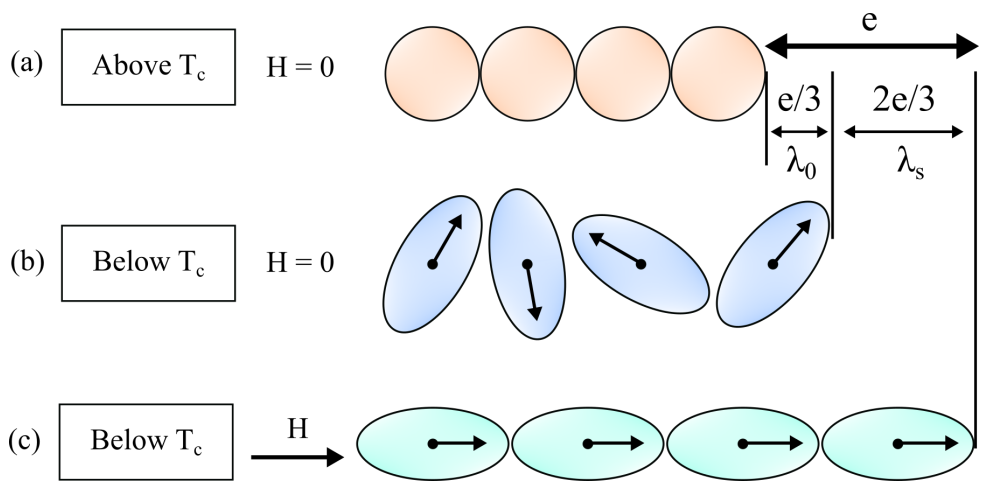

Figure 1.11: Schematic demonstrating magnetostriction in (a) a disordered paramagnetic material, (b) demagnetised ferromagnetic phase, (c) ferromagnetic material that has been magnetised to saturation

the externally applied field will not increase the final magnetostriction, as shown in Figure 1.11(c) and 1.12. It represents the strain measured in a particular direction as the sample is taken from the demagnetised state to saturation along the same direction.

In this saturated state the magnetic moments are aligned as in Figure 1.10(c,d), and so the strain will be parallel to the applied field giving:

$$\lambda_s = e - \lambda_0 = \frac{2}{3}e = 2\lambda_0. \tag{1.22}$$

If a material has a positive magnetostriction value, the sample will elongate along the direction of an externally applied magnetic field. The thickness of the sample, perpendicular to the direction of the applied field, will shrink in proportion to Poisson's ratio (ratio of compressive and expansive deformation) to ensure that the overall volume of the sample remains constant. If the magnetostriction value is negative, the opposite applies. Permalloy has a crossover from a positive to a negative magnetostriction value depending on the composition of the alloy. This crossover occurs at 80.7% Nickel. This will be discussed further in Section 1.5.4.

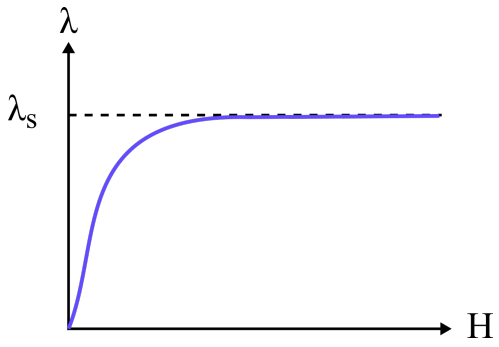

Figure 1.12: Development of magnetostriction λ of a polycrystalline material as a function of applied magnetic field **H**. Adapted from J.M.D Coey, Magnetism and Magnetic Materials. Cambridge University Press, 2009 [11].

1.5.2 Magnetostriction in Thin Films

The previous section discusses the fundamental magnetostriction mechanism which occurs in individual crystals. The materials studied in this work (Chapter 6) are thin polycrystalline materials with magnetostrictive properties. For a polycrystalline specimen, the value of the magnetostriction depends on the magnetostrictive properties of the individual crystals. Polycrystalline samples have randomly orientated grains, leading to an averaged bulk magnetostriction value. The magnetostriction can be averaged in the field direction over all possible crystal orientations. This leads to a simplified equation for a randomly orientated polycrystalline cubic material:

$$\lambda_s = \frac{2}{5}\lambda_{100} + \frac{3}{5}\lambda_{111} \tag{1.23}$$

where λ_{100} and λ_{111} refer to the saturation magnetostriction measured along the <100> and <111> direction respectively. Equation 1.23 is an established formula determined from directional microstrain measurements on 80/20 permalloy. [12] These values can be quoted as 4×10^{-6} and 5×10^{-6} respectively. [13]

1.5.3 Magnetostriction Measurement Techniques

Magnetostriction measurement techniques can be classified in one of two ways: either using direct methods referred to as the Joule Effect, or indirect methods

known as the Villari Effect. These can be differentiated by how the strain of the sample is measured.

Indirect methods measure changes in anisotropy due to stress/strain. [14-17] This method was discovered by E. Villari (1865), and was subsequently named the 'Villari Effect'. [18] The application of stress to material induces stress anisotropy. Magnetostriction can be calculated by measuring the change in the anisotropy field. The sign of the magnetostriction depends on the material or the composition. If a material contracts along the direction of the applied field when it is magnetised, it has a negative magnetostriction. In this case, the application of tensile stress will cause a decrease in the measured anisotropy field. If a material expands, it has a positive value, and the anisotropy field will be increased by tensile strain. An example of a material studied in this body of work is a $Ni_{79}Fe_{21}$ polycrystalline thin film, which has an associated magnetostriction value of λ_s = -0.2 $\times$ 10^{-6} when measured using indirect techniques. [19]

Direct methods enable the magnetostrictive strain to be measured as a function of the applied field and generally yield λ_e, which is the field dependent magnetostrictive strain. [20-22] Whereas indirect methods are suitable only for measuring the saturation magnetostriction λ_s [23].

1.5.4 Magnetostriction as a function of sample composition

Effects of magnetostriction need to be better understood in polycrystalline thin films, for development of the next generation of data storage devices. [24] As previously discussed, the magnetostrictive sign of a permalloy material depends on its composition. Therefore many experiments have taken place to investigate where the sign switching occurs, and locating when a zero-crossover value takes place. Results presented by K. Krush in 1986 [25] (shown in Figure 1.13(a)) shows how the value of saturation magnetostriction is very sensitive to the composition of the material, in this case permalloy, with a crossover from positive to negative magnetostriction occurring at 80.3% Ni.

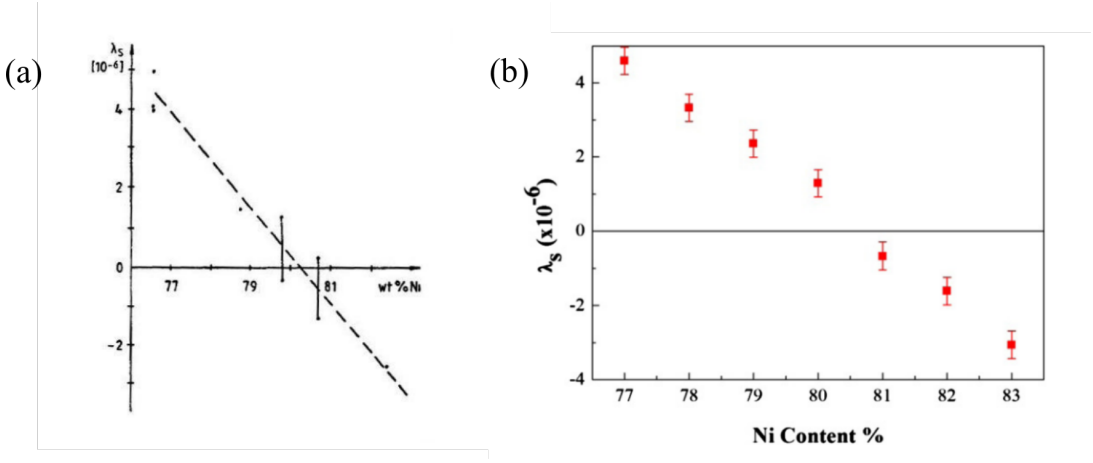

Figure 1.13: (a) Saturation magnetostiction λ_s vs sample composition for Nickel/Iron permalloy films, taken from K. Krusch (1986) [25]. (b) Measured saturation magnetostriction λ_s as a function of Ni concentration, taken from C.Hill 2013 [26]

This was reconfirmed in 2013 by using the indirect methods described in the previous section. [26] The zero magnetostriction cross over point was approximately at 80.5% Ni, as expected, and follows a linear trend. This crossover point from a positive, through zero, to a negative magnetostrictive effect will be a region of interest in work presented in Chapter 6.

1.6 Magnetic Domains and Domain Walls

As described in previous sections, magnetic domains form in ferromagnetic materials due to the competition between different energy contributions. The magnetisation of a sample does not suddenly change between domains. Instead, it will change continuously over a region called a domain wall. There are two simple 1D domain wall types often observed in films. In Bloch walls there is a rotation in plane of the domain wall. In this configuration the magnetic moments point fully out of the plane in the centre of the wall (Figure 1.14(a)). It is important to note that the magnetisation is divergence free within the film, as seen in Figure 1.15(a).

In a Néel wall there is a rotation in plane, orthogonal to that of the domain wall, and no out-of-plane component of the magnetisation occurs anywhere in the

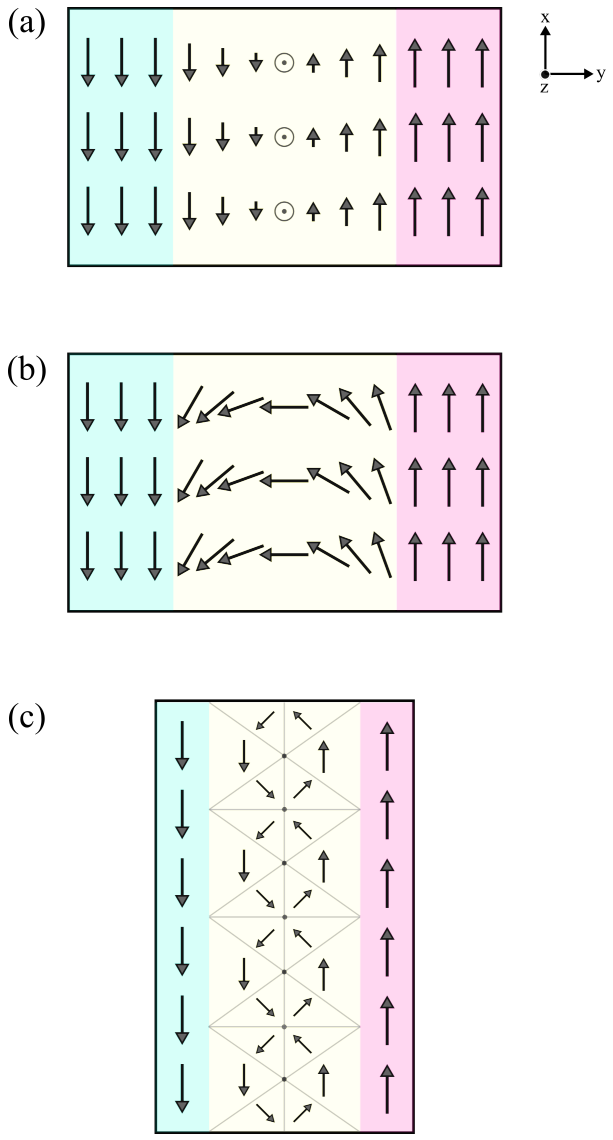

Figure 1.14: Schematic illustration of spin configurations of typical domain wall types found in ferromagnetic thin films. (a) Bloch walls, (b) Néel walls and (c) Cross-tie walls.

domain wall. This process is highlighted in Figure 1.15(b), where the magnetic charges form at the sides of the wall. Here the magnetisation is divergent within the film, leading to a magnetostatic contribution.

The existence of Bloch and Néel walls depends on the materials thickness. Bloch is divergence free and favoured for thick films. Néel is favoured for thin films, and for materials with in-plane magnetisation. Below a critical thickness (approximately 30 nm), Bloch wall formation becomes energetically costly. When the domain

wall width and film thickness become comparable, the energy associated with the surface (Bloch) and volume (Néel) will change favourability, whereby the Néel-type walls become more favourable.

It should be noted that there is a third, more complicated type of domain wall configuration called a cross-tie wall shown in Figure 1.14(c) that appear at an intermediate thickness (30-90 nm). They have a 90° wall structure separating neighbouring domains. They behave as Néel walls of opposite rotation and form vortices and antivortices due to the flux closures.

In this work presented, Néel domain walls in a 10 nm thick polycrystalline permalloy sample will be imaged using Lorentz imaging techniques described in Chapter 2.

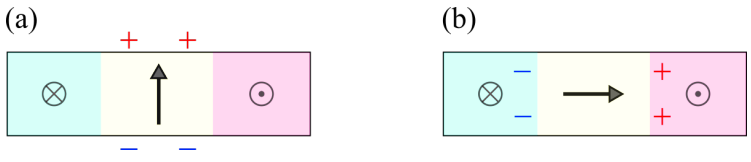

Figure 1.15: Schematic illustration of the charge distribution of typical domain wall types found in ferromagnetic thin films. (a) Bloch walls and (b) Néel walls.

1.7 Magnetisation Ripple

Fuller and Hale (1960) discovered that the magnetisation direction in a polycrystalline thin film is non-uniform on the micro-magnetic scale when visualised using Lorentz microscopy, and named the phenomenon 'Magnetisation Ripple'. [27] A polycrystalline material has a granular structure where each grain has own randomly oriented easy axis with an associated anisotropy K_g, as described in Section 1.4.4. This causes a perturbation of the domain magnetisation.

Figure 1.16 demonstrates the physical origin of the magnetisation fluctuations which results from the granular structure that is present in polycrystalline thin films. The films investigated in this body of work have an overall induced uniaxial anisotropy K_G through field and heat annealing treatments as described in Section 1.4.5. The anisotropy values for the induced uniaxial anisotropy are significantly

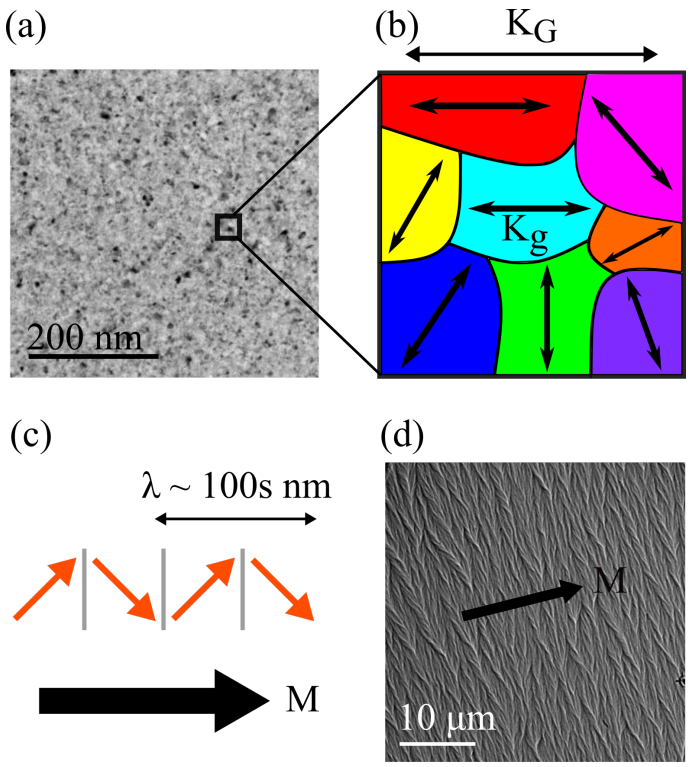

Figure 1.16: Schematic of magnetisation ripple origin. (a) $Ni_{45}Fe_{55}$ bright field TEM image, showing a granular structure, expected from a polycrystalline thin film. (b) The random direction of the granular crystalline anisotropy K_g, with an additional global uniaxial anisotropy K_G. (c) Schematic of the magnetisation fluctuations, producing low-angle domain walls, commonly referred to as magnetisation ripple, where the length scale is in the order of 100s nm. (d) Lorentz TEM image displaying strong magnetisation ripple of a $Ni_{45}Fe_{55}$ permalloy thin film. The arrow indicates the mean direction of magnetisation **M**.

larger than that of the individual grains. For example, a typical value for K_G for a permalloy material would be 500 J/m^3 (5000 erg/cc), compared to 100 J/m^3 (1000 erg/cc) for K_g, which is an inherent magnetic property originating from the granular crystalline anisotropy K_g (Section 1.4.4). The effect of this variation in anisotropy strength and direction is that it produces low-angle domain walls within the film (Figure 2.16(c)). Grain sizes of $\approx$ 10 nm will produce wave-like fluctuations with a wavelength in the order of 100s nm. Figure 1.16(d) shows a visualisation of magnetisation ripple properties by using Lorentz TEM imaging, with the mean direction of magnetisation **M** highlighted by the arrow.

There are two possible configurations which are associated with the magnetisation

ripple effect: the transverse and longitudinal components. [28] Longitudinal describes the fluctuations of the magnetisation direction are perpendicular to the mean magnetisation. Transverse refers to the parallel fluctuations. A schematic illustration of these two ripple components is shown in Figure 1.17. Fuller and Hale showed that while the exchange and random local anisotropy energies (magnetocrystalline anisotropies) for the two distributions is about the same, the magnetostatic energy is much lower for the longitudinal component, which is therefore favoured energetically.

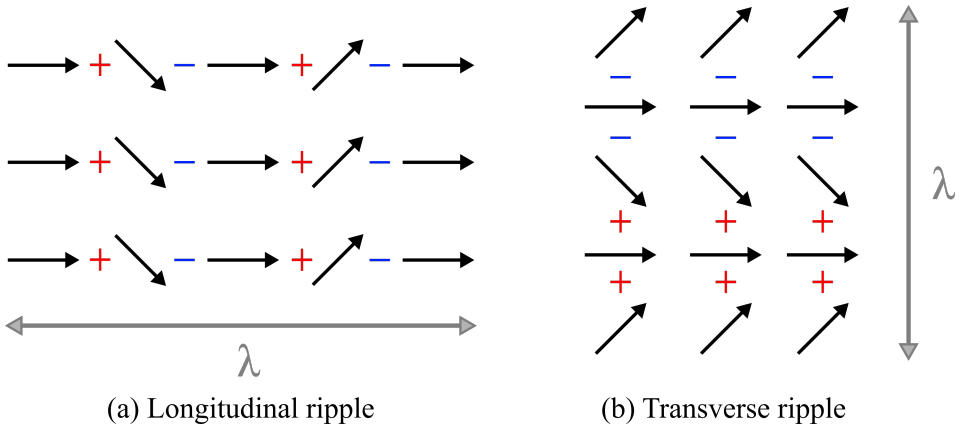

Figure 1.17: Schematic representation of (a) longitudinal and (b) transverse magnetisation ripple configurations.

A number of subsequent studies aimed to look at magnetic ripple from a theoretical perspective, that focuses directly on the dominant transverse ripple component. Theories show that the phenomenon can be explained by the randomly orientated local anisotropies of the grains in the film. It is assumed that the magnetisation is parallel to the thin film surface due to the large demagnetising field perpendicular to the film. In theory the parameter causing the ripple is a local anisotropy in each randomly-oriented crystallite, as demonstrated in Figure 1.16(b). Many highly mathematical theories of magnetisation ripple have been developed, examples include H. Hoffmann (1968) [29, 30] and K.J. Harte (1968). [28,31] In the following sections, we will only treat Hoffmann's interpretation of ripple as it is generally seen as the standard model.

Hoffmann made the basic assumption that the magnetisation will lie parallel to the thin film surface, due the the large demagnetising field perpendicular to the film. He also stated that the parameter causing the ripple is the local anisotropy present in each randomly orientated crystallite. This local anisotropy is superimposed on the overall uniaxial anisotropy which is uniform in direction.

Hoffmann stated that the direction of the magnetisation **M** exhibited an angular deviation $\phi(\mathbf{r})$. He expressed that the direction of **M** at any point $\Phi(\mathbf{r})$ as the sum of the mean magnetisation <**M**> direction ϕ_0 as given by:

$$\Phi(\mathbf{r}) = \phi_0 + \phi_{(\mathbf{r})} \tag{1.24}$$

To derive the mean ripple angle, the total energy has to be calculated, and then the derivative with respect to the angle Φ of **M** is set equal to zero. These components of the total energy are as follows:

- (a) External applied field, E_H
- (b) Uniaxial anisotropy, E_{Ku}
- (c) Exchange energy, E_{Ex}
- (d) Local anisotropy of individual grains, E_g
- (e) Magnetostatic, E_m

One further simplifying assumption is that the film possesses no overall magnetostrictive effects. If a film has an associated magnetostrictive energy, it should be added to the crystal energy. Hoffmann's approach was to minimise the total energy of the film using the variational integral:

$$\delta \int_V (E_H + E_K + E_{Ex} + E_g + E_m) dV = 0 \tag{1.25}$$

$$\delta \int_V (E_{tot}) dV = 0 \tag{1.26}$$

where V is the volume of the film.

By retaining only the initial terms in a Taylor series expansion in ϕ, Hoffmann simplified the variational problem considerably. His approximation leads to a differential equation for the magnetization fluctuation $\phi(\mathbf{r})$ which can be linearised by neglecting the longitudinal stray field (parallel to the mean direction of $\mathbf{M}$). In this so called linear ripple theory, Hoffmann derives an expression for $\phi(\mathbf{r})$ from the linearised differential equation. [29]

Magnetisation Ripple Dispersion Theory

For comparison with experimental Lorentz TEM images, it is useful to calculate, besides the magnetization fluctuation at every point, $\mathbf{r}$, the root mean square of magnetisation dispersion θ. This is defined as the root mean square of the value of $\Phi(\mathbf{r})^2$ averaged over the whole film and is referred to as ripple dispersion angle.

Magnetisation ripple dispersion relates to the variation of magnetisation orientation from the mean direction of $\mathbf{M}$, as shown in Figure 1.18. It assumes that the perturbing anisotropies are randomly oriented magnetocrystalline anisotropies. Knowing the local crystalline anisotropy in the film, allows for the dispersion to be calculated. Hoffmann predicted that an estimate of the mean value of magnetisation dispersion, θ (radians), can be given by:

$$\theta = \frac{1}{4\pi^{\frac{1}{2}}} \frac{DK}{(2d)^{\frac{1}{4}} M^{\frac{1}{2}}} \cdot \frac{1}{(AK_u(h+1))^{\frac{3}{8}}} \tag{1.27}$$

where D is the mean grain size of the polycrystalline film, d is the film thickness, K is the crystal anisotropy constant, M is the saturation magnetisation, K_u is the uniaxial anisotropy constant, and $h = H/H_k$, which is referred to as the reduced field. As shown, there are many parameters which influence the ripple dispersion variation. Some parameters can be investigated experimentally such as grain size. Theory predicts that a decrease in grain size will lead to a decrease in the magnetisation ripple dispersion. This will be investigated in greater detail in Chapter 4.

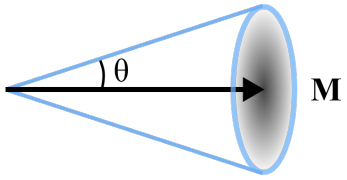

Figure 1.18: Schematic of magnetisation ripple dispersion θ: The cone, highlighted by the blue lines represents the variation in orientation of the magnetisation direction, from the mean direction of magnetisation **M**.

Magnetisation Ripple Wavelength Theory

The second characteristic proposed by Hoffmann was the magnetisation ripple wavelength (highlighted in Figure 1.17). This equation was derived by considering a region exhibiting dispersion. It does not include parameters such as crystal anisotropy as it is a long-range effect. Hoffmann used the following theoretical formula for determining the ripple wavelength along the easy and hard axis respectively:

$$\lambda_E = 2\pi \left(\frac{A}{K_U}\right)^{\frac{1}{2}} (h+1)^{-\frac{1}{2}} \tag{1.28}$$

$$\lambda_H = 2\pi \left(\frac{A}{K_U}\right)^{\frac{1}{2}} (h-1)^{-\frac{1}{2}} \tag{1.29}$$

where A is the exchange constant, $\mathrm{K}_u = \mathrm{M}_s\mathrm{H}_k/2$ is the uniaxial anisotropy constant and h is the reduced field.

Hoffmann proposed that a thin film with a larger induced anisotropy constant would have a smaller ripple wavelength, when compared to a sample with a smaller K_u value. This effect will be studied experimentally in greater detail in Chapter 4.

Equations 1.28 and 1.29 also state that the mean wavelength of the ripple decreases with increasing field strength. A detailed experimental and simulation model study into magnetisation ripple characteristics, such as ripple dispersion and wavelength as a function of field, will be discussed in all following results chapters.

1.8 Micromagnetic Simulations

Micromagnetism is the theory which describes magnetisation on the intermediate length scales above those where individual atomic spins have to be taken into account. For example, the exchange length L_{ex} is a parameter which indicates the length scale in which you would expect little variation in the directionality of magnetic moments. As L_{ex} is approximately an order of magnitude larger than the distance between individual moments, a continuum approximation can be made. In the continuum limit you remove the discrete nature of atomic spins and replace it with a smoothly varying function of position and time. This enables the application of computationally efficient numerical techniques to accurately simulate magnetic materials.

Micromagnetic simulations are a vital tool when investigating or predicting the magnetic behaviour of a specimen. In the work presented in the following results chapters, the micromagnetic simulations will be provided using the MuMax^3 software. [32] MuMax^3 is a GPU-accelerated programme that uses a model based on the Landau-Lifshitz-Gilbert (LLG) equation which represents the magnetic energy terms as effective fields to then produce dynamical behaviour.[33] MuMax^3 calculates the effective field of each cell in the simulation, and can therefore calculate the magnetisation by solving the LLG equation using finite difference methods. [34] This describes the gyroscopic precession γ of a magnetic moment due to the applied field with damping conditions α. This causes the magnetisation $\mathbf{M}$ to precess and spiral until it aligns with the effective field, which is visualised in Figure 1.19.

$$\frac{\delta \mathbf{M}}{\delta t} = -\gamma \mathbf{M} \times \mathbf{H}_{eff} - \frac{\gamma \alpha}{|\mathbf{M}|} \mathbf{M} \times (\mathbf{M} \times \mathbf{H}_{eff}) \tag{1.30}$$

$\mathbf{H}_{eff}$ is an effective field and is given by:

$$\mathbf{H}_{eff} = -\frac{1}{\mu_0} \frac{\delta E_{tot}}{\delta \mathbf{M}} \tag{1.31}$$

where E_{tot} is the total energy of the system. This will take into account the magnetostriction, anisotropy, exchange energies and the external field interactions as previously described in Section 1.4.

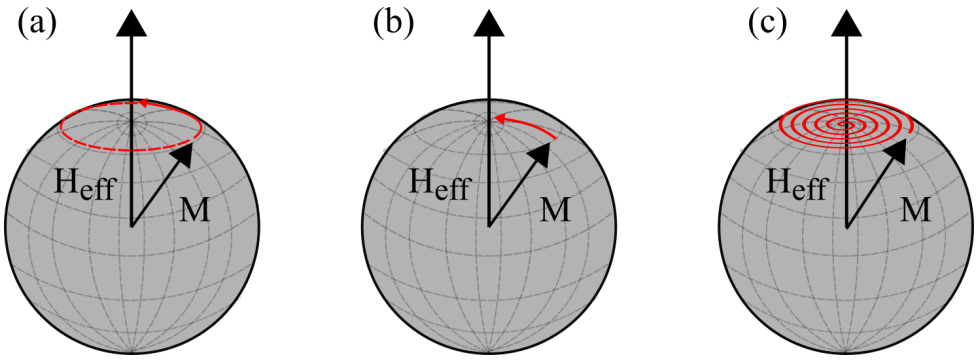

Figure 1.19: Visualization of the contributions to the magnetization dynamics as described by the LLG equation. (a) Precessional motion around the effective field $\mathbf{H}_{eff}$. (b) Dissipative motion of the magnetization toward $\mathbf{H}_{eff}$. (c) Combined precessional and dissipative motion as described by the LLG. Recreated from [34].

The most realistic micromagnetic simulation would be one that considers all the individual atomic moments in the material, such as Vampire software [35]. However this would be almost impossible to compute for the dimensions of typical magnetisation ripple (minimum of several microns). Also as magnetisation ripple has such a large length scale, atomic moment simulation would not be necessary. A way around this problem is to create areas known as cells, which have an uniform magnetisation. The cell size is an important variable when creating simulation models and is something that is investigated in Chapter 5. Cell sizes must be on the order of the exchange length of the simulated material to ensure the simulations find physical solutions. There is a trade-off between simulation time and simulation accuracy. The larger the cell size, that faster the simulation calculation time, however it will provide a less realistic simulation of the micro-magnetic characteristics. The size of the cell is normally of the order of the ferromagnetic exchange-interaction length, L_{ex} of the material in the element (e.g. $L_{ex} = \sqrt{\frac{A}{2\mu_0 M_s^2}} \approx 4$ nm for $Ni_{81}Fe_{19}$). It is important to note that if the cell size is much larger than the exchange length, the results are unrealistic. However a smaller cell size does not always make simulation more realistic i.e. there is a convergence in behaviour around the exchange length.

The finite difference (FD) method is a widely used technique for micro-magnetic simulation packages, such as MuMax^3, which is used here. [36, 37] In mathematics, finite-difference (FD) methods are numerical methods for solving differential equations by approximating them with difference equations, in which finite differences approximate the derivatives. In the case of magnetic systems, the various energy contributions have to be approximated to their FD counterparts before the effective field and LLG equations can be solved. This modelling technique requires the use of a square mesh (Figure 1.20(a)), therefore it would be difficult to successfully model any curved or irregular boundaries, like seen in finite-element (FE) simulation packages such as NMag or magnum.fe [38, 39]. However, as work presented in this includes magnetic thin films with a regular structure, the finite difference modelling approach will be favourable.

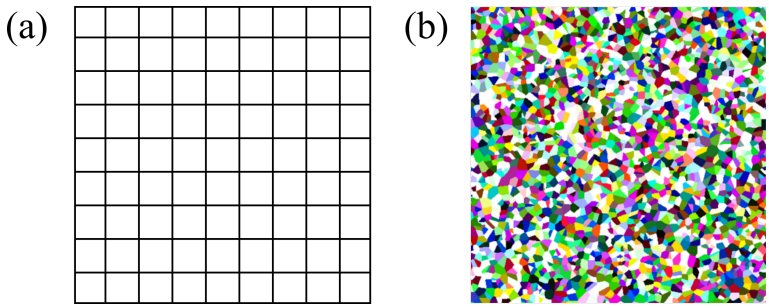

Figure 1.20: (a) Finite difference (FD) simulation set-up showing 2D cell representation. (b) Example 5 nm grains simulation for a polycrystalline permalloy structure, with the colours representing the orientation of magnetisation, which in this case is randomly distributed.

1.9 References

[1] W. Heisenberg, *Z Physik.* 49,619, (1928).

[2] P. Weiss, *J. Phys.* 6,661, (1907).

[3] P. Yu. Curie temperatures of fcc and bcc nickel and permalloy: Supercell and Green's function methods. *Physical Review B.* 77, 054431, (2008).

[4] G. Abo. Definition of Magnetic Exchange Length. *IEEE Transactions on Magnetics.* 49(8):4937 - 4939, (2013).

[5] L. McKeehan. The Crystal Structure of Iron-Nickel Alloys. *Physical Review Journals Archive.* 21,402, (1923).

[6] J. P. Joule. Elongation as a function of magnetic intensity. *Philosophical Magazine*, 30(76):225, (1847).

[7] J. P. Joule. On a new class of magnetic forces. *Sturgeons Annals of Electricity*, 8(219), (1842).

[8] E. W. Lee. Magnetostriction and magnetomechanical effects. *Reports Prog. Phys.* 18(1) 184 (1955).

[9] R. Lawrence Comstock. Introduction to Magnetism and Magnetic Recording. *Wiley.* (1999).

[10] B. D. Cullity and C. D. Graham, Introduction to magnetic materials. *IEEE/Wiley*. (2009).

[11] J.M.D Coey. Magnetism and Magnetic Materials. *Cambridge University Press*. (2009).

[12] R Grössinger. Materials with high magnetostriction. *IOP Conference Series: Materials Science and Engineering*. 60,012002, (2014).

[13] T. Ohtani. Magnetostriction of permalloy epitaxial and polycrystalline thin films. *EPJ Web of Conferences 40*, 11004, (2013)

[14] J. Kaleta and J. ÅœEbracki. Application of the Villari effect in a fatigue examination of nickel. *Fatigue and Fracture of Engineering Materials and Structures*. 19(12), 1435-1443, (1996).

[15] W.Polanschatz. Inverse magnetostrictive effect and electromagnetic non-destructive testing methods. *NDT International*. 19(4), 249-258, (1986).

[16] V S Severikov. Study of inverse magnetostrictive effect in metallic glasses $Fe_{80-x}Co_xP_{14}B_6$. *IOP Conf. Series: Journal of Physics*. 929, (2017).

[17] J. Jay and F. Le Berre. Direct and inverse measurement of thin films magnetostriction. *Journal of Magnetism and Magnetic Materials*. 322(15):2203-2214, (2010).

[18] E. Villari. Ueber die Aenderungen des magnetischen Moments, welche der Zug un das Hindurchleiten eines galvanischen Stroms in einem Stabe von Stahl oder

Eisen hervorbringen. *Annalen der Physik.* 202, 87-122, (1861) (In German).

[19] L. W. McKeehan and P. P. Cioffi. Magnetostriction in Permalloy. *Physical Review.* 28(146), (1926).

[20] V. Amelichev and P. Belyakov. Straintonic elements of the basis of magnetostriction. *International Journal of Environmental and Science Education.* 11(18):10923-10940, (2016).

[21] B. Kundys. Three terminal capacitance technique for magnetostriction and thermal expansion measurements. *Review of Scientific Instruments.* 75, 2192. (2004).

[22] R. Varghese, R. Viswan, and K. Joshi et al. Magnetostriction measurement in thin films using laser dopple vibrometry. *Journal of Magnetism and Magnetic Materials.* 363:179-187, (2014).

[23] An overview of magnetostriction, its use and methods to measure these properties. *Journal of Materials Processing Technology.* 191(1):96-101, (2007).

[24] C. Hill. Manipulation and magnetostriction of nife films for advanced reader shielding applications. *Thesis: Queen's University Belfast.* (2013).

[25] K. Krush. Sputter parameters and magnetic properties of permalloy for thin film heads. *IEEE Transactions on Magnetics.* 22:626-628, (1986).

[26] C. Hill. Whole wafter magnetostriction metrology for magnetic films and multilayers. *IOP Science, Meas. Sci. Technol.*, 24:45601, (2013).

[27] H. W. Fuller and M. E. Hale. Determination of magnetisation distribution in thin films using electron microscopy. *Journal of Applied Physics*. 31(238), (1960).

[28] K. J. Harte. Theory of Magnetization Ripple in Ferromagnetic Films. *Journal of Applied Physics*. 39, 1503, (1968).

[29] H. Hoffmann. Quantitative calculation of the magnetic ripple of uniaxial thin permalloy films. *Journal of Applied Physics*. 35(6):1790-1798, (1964).

[30] H. Hoffmann. Theory of Magnetization Ripple. *IEEE Transactions on Magnetics*. 4(1):32-38, (1968).

[31] K. D. Leaver. Magnetisation ripple in ferromagnetic thin films. *Thin Solid Films*. 2:149-172, (1968).

[32] L. Landau and E. Lifshits. On the theory of the dispersion of magnetic permeability in ferromagnetic bodies. *Academy of Sciences of Ukraine*. 169(14):14-22, (1935).

[33] M. Dvornik M. Helsen F. Garcia-Sanchez A. Vansteenkiste J.Leliaert and B. Van Waeyenberge. The design and verification of mumax3. *AIP Advances*, 4(10):107133, (2014).

[34] C. Abert. Micromagnetics and spintronics: models and numerical methods. *The European Physical Journal B*. 92:120, (2019).

[35] R. Evans. Atomistic modelling of nanogranualr magnetic materials. *University of York PhD Thesis*. (2008).

[36] D. Kumar and A. O. Adeyeye. Techniques in micromagnetic simulation and analysis. *Journal of Physics D: Applied Physics*. 50:34, (2017).

[37] J Leliaert. Fast micromagnetic simulations on GPU and recent advances made with mumax 3. *Journal of Physics D: Applied Physics*. 51:12, (2018).

[38] Hans Fangohr. Nmag micromagnetic simulation tool: software engineering lessons learned. *International Workshop on Software Engineering for Science*. 1-7, (2016).

[39] C. Abert. magnum.fe: A micromagnetic finite-element simulation code based on FEniCS. *Journal of Magnetism and Magnetic Materials* 345:29-35, (2013).

2

Instrumentation and Experimental Techniques

Contents

2.1 Introduction

In this chapter, the various experimental techniques used in this project will be outlined. In order to gain insight into the properties of magnetic materials and devices, it is important to be able to study the physical and magnetic properties of the material or device under investigation. Section 2.2 describes the substrates used in this work which make magnetic measurements and electron microscopy possible. This is followed by an outline of the deposition and annealing techniques. The B-H looper method was used in this work to produce hysteresis loops from bulk samples that could be further analysed, as described in section 2.3. Transmission electron microscopy (TEM) is the main characterisation technique used in this project, and it's set-up is detailed in Section 2.3. It is a powerful and versatile tool for acquiring high resolution experimental images that allow us to analyse the physical structure of the samples as outlined in Section 2.5. Modification of conventional TEM operations allows for the use of Lorentz imaging, which gives us the ability to acquire magnetic TEM images. It allows for direct visualisation of the micro-magnetic configuration of the material, as described in Section 2.6. The understanding of the structure and in-situ dynamics of magnetic configurations, such as magnetisation ripple and domain formation, is becoming increasingly important in various applications of magnetic materials, such as thin-film recording heads in the magnetic recording industry. [1]

2.2 Sample Preparation of Thin Magnetic Films

2.2.1 Electron Transparent Substrates

For thin film deposition, a substrate is needed. Conventionally, Si_3N_4 membranes are used in TEM imaging as they are thin enough to be electron transparent,

therefore allowing TEM imaging to be performed. The substrates were acquired from the James Watt Nanofabrication Centre and are shown in Figure 2.1. Their dimensions are 2 x 2 mm^2, with a 100 x 100 μm^2 Si_3N_4 membrane window in the centre for sample imaging. These membranes are approximately 50 nm thick and have an amorphous structure.

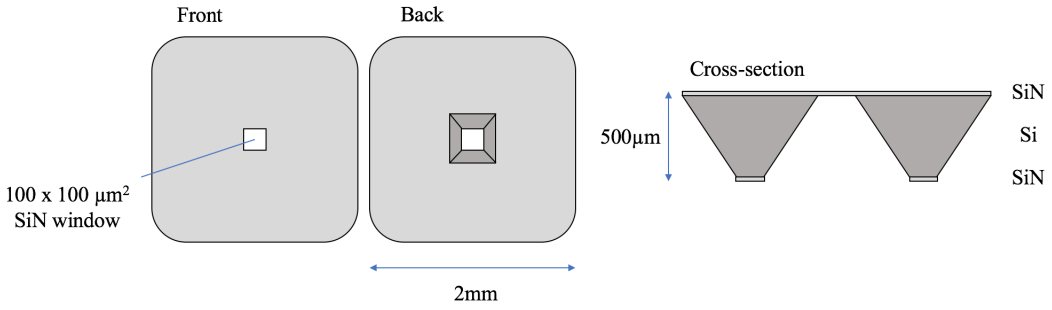

Figure 2.1: Front, back and cross-section of a single Si_3N_4 membrane used for thin film deposition. These membranes can be loaded into a sample rod which is placed within the TEM column, for sample visualisation.

2.2.2 RF Magnetron Sputtering

All samples studied in this thesis are polycrystalline thin films and are deposited using RF magnetron sputtering by collaborators in Seagate Technology, Ireland.

Radio Frequency (RF) magnetron sputtering is a commonly used deposition technique for thin films due to its uniform and dense coating with strong adhesion. [2,3] Sputtering is a process whereby atoms or molecules of some materials are ejected from a target situated in a vacuum chamber, becoming precursors for coating, due to the bombardment of accelerated high-energy inert gas ions. Repetition of this process leads to a build up of target atoms on the substrate, referred to as sputter deposition.

Figure 2.2 is a schematic showing the main components and processes of a typical RF magnetron sputtering system. In sputtering, two electrodes are used: one electrode is the target material (i.e. the material to be deposited) and the other is the substrate (i.e. the material to be deposited on). The system is held under a low

base pressure of 6 x 10^{-7} Pa, and filled with an inert gas, in this case, Argon. A high frequency (∼14 MHz) alternative current (high voltage) is applied between the cathode and the anode, to sustain the ion production. The high voltage bias ejects electrons from the cathode which ionise the argon gas atoms, creating a plasma within the chamber. The argon ions are then accelerated into the negatively charged target (cathode). This is a high energy collision which produces target atoms from the sputtering target, which then travel through the chamber towards the substrate, where they condense and produce a thin film.

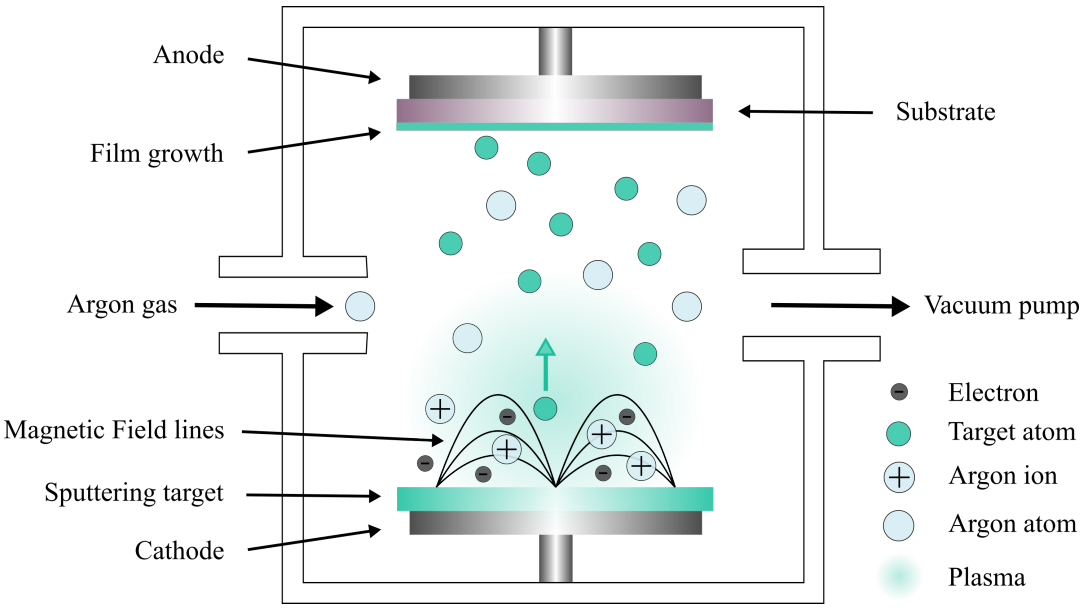

Figure 2.2: Schematic of a radio frequency (RF) magnetron sputtering system used for sample deposition.

In addition, RF Magnetron sputtering uses magnets behind the negative cathode to trap electrons over the negatively charged target material so they are not free to bombard the substrate, increasing the focusing of the ions towards the material and allowing for faster deposition rates. [4,5] The permalloy thin films were deposited a room temperature on the front surface of the Si_3N_4 substrates shown in figure 2.1.

The film thickness can be controlled by increasing or decreasing the deposition times. Furthermore, co-sputtering techniques mean multiple targets can be contained within the chamber and deposited simultaneously. Different atomic compositions

of the alloys could be achieved by taking into account the Ni and Fe density and molar mass, to give individual deposition rates and combined alloy deposition rate. In practice the alloy compositions of the films were controlled by altering the power of the magnetrons which thereby altered the deposition rate. For this work, a slight variation of percentage composition around the well known 80/20 nickel/iron permalloy was used. Samples were capped with a 5 nm layer of zirconium to avoid oxidation. Zirconium is able to provide a good shielding layer due to its slow oxidation rate and good coverage of permalloy. [6] Samples characterised in Chapter 4 contain additional Ruthenium seed layers with the aim of controlling physical properties, such as grain size.

Samples were prepared in an Anelva C-7100 sputter deposition tool, situated at Seagate Technology. Deposition rates were calibrated by x-ray fluorescence (XRF) measurement and confirmed with scanning electron microscopy (SEM) measurement of samples prepared by focused ion beam (FIB). [7] Samples were deposited on TEM substrates (Figure 2.1) by being mounted onto thermally oxidised silicon substrates with strips of Kapton tape, shown in Figure 2.3.

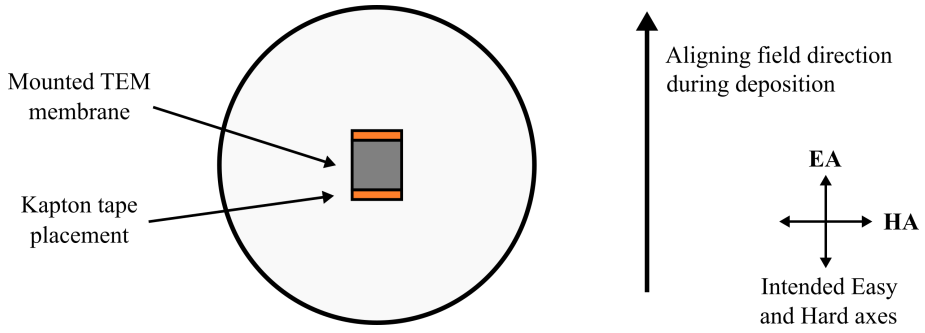

Figure 2.3: Schematic of TEM substrate mounting and axis directions for sample deposition.

2.2.3 Annealing of Samples

It is well known that the application of an external magnetic field during a heat treatment of a thin film sample can have beneficial influence on magnetic properties, such as a strong induced uniaxial anisotropy. [8] One of the most important effects

of magnetic thermal annealing is the defining of the easy axis in a ferromagnetic material.

When a ferromagnetic material is annealed at a high temperatures, the individual magnetic moments within the material will align with the externally applied magnetic field. Eventually, the system will reach an equilibrium state with the external field still applied. As the temperature is slowly reduced, the material will retain this preferred direction of magnetisation, known as the easy axis.

Following the process of thin film deposition as described in Section 1.4.5, samples were annealed for 5 hours in a vacuum at 300 degrees, with an applied field of 250 oersteds, and left to cool overnight. A high temperature was used to improve magnetic properties and a magnetic field was used to promote an easy-axis direction.

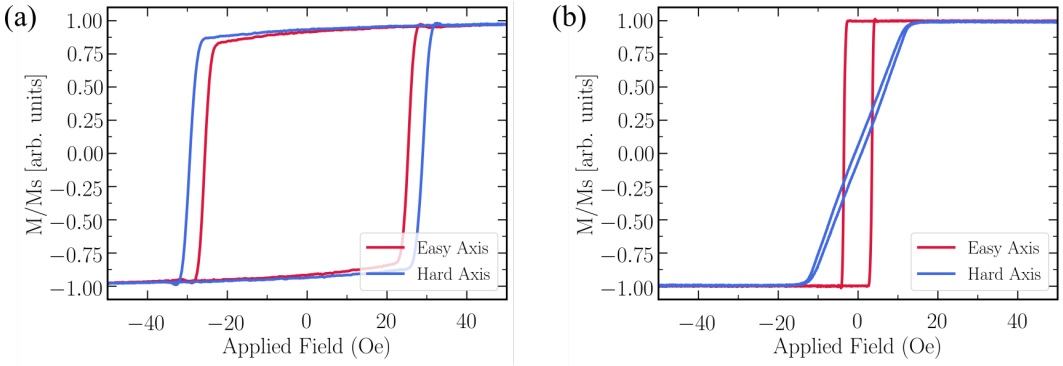

Figure 2.4: Typical hysteresis loops for a (a) weakly annealed specimen and (b) strongly annealed specimen with a strong induced uniaxial anisotropy as shown by the well defined easy and hard axis loops.

Figure 2.4 shows the difference in hysteresis loops (see Section 1.3), where the thermal magnetic annealing has been unsuccessful (a) compared to that of a successful annealing (b). The purpose of annealing is to provide a well-defined preferred direction of magnetisation. Figure 2.4(b) shows a BH loop where there is a well defined easy and hard axis magnetisation behaviour.

2.3 Bulk Characterisation

2.3.1 B-H Looper

A B-H looper provides a way of characterising the magnetic properties of bulk materials, in this case 6" silicon wafers. A material's magnetic response can be measured by inserting the sample into a magnetic field, measuring the response and analysing the resulting hysteresis loops. The benefit of using a BH looper over other techniques, such as a vibrating sample magnetometer (VSM), is that it produces and displays the samples hysteresis loop in 'real-time' i.e. quick refresh rate, allowing for in-situ sample rotation. This leads to an quick and efficient establishment of the easy and hard loops. The facilities used at the University of Glasgow include a SHB instrument, Model 109A. A B-H looper measures the magnetic properties of a thin film by producing a hysteresis loop of magnetic flux density **B** versus applied field intensity **H**. The external magnetic field applied across the sample will align the individual magnetic dipole moments in the direction of the field. Hysteresis displays how a magnet may have more than one possible magnetic moment **M** in a given magnetic field **H**, depending on how the field changed in the past (Section 1.3). Remanence occurs when some of the alignment of these magnetic dipoles is retained even when the applied field is reduced to zero. The shape and size of the hysteresis loop depends on the magnetic properties. From the resulting hysteresis loop, one can determine important magnetic properties such as magnetisation saturation, coercivity and anisotropy field.

Figure 2.5 shows a schematic of the B-H looper set-up. The B-H looper utilises Faraday's law of electromagnetic induction to measure the hysteresis relating to the specific sample. The sample is first magnetised by an AC field, leading to an induced current in a pick-up coil. The pick-up coils are configured to measure thin-film samples. The maximum field that can be applied to the sample is up to 200 Oe. This field size is more than sufficient for the samples measured in this thesis. Full details of the B-H looper by SHB instruments can be found on the company's website. [10]

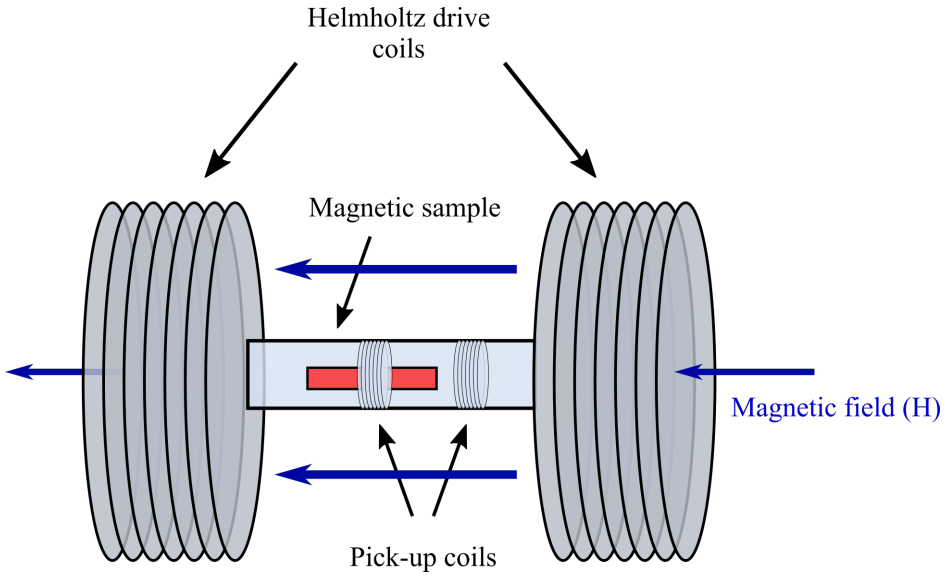

Figure 2.5: B-H looper schematic: A magnetic sample is placed within an externally applied magnetic and its magnetic response is measured by producing a hysteresis loop.

2.4 The Transmission Electron Microscope

Electron microscopy is a vital tool in material science when investigating the micro-structural properties, along with the micro-magnetic properties of a magnetic sample. It allows for the acquisition of high quality, high resolution images for interpretation and analysis. Specifically, it allows for characterisation of the granular structure and film texture, as well as using a modified TEM set-up to image the magnetic structure, as detailed in the following sections.

2.4.1 Introduction

The idea that a microscope could use electrons as an illumination source was proposed shortly after De Broglie's hypothesis was published in 1925. This revolutionary work hypothesised that all matter has a wave-like nature, where he related wavelength and momentum as $\lambda = h/p$. By 1929, De Broglie's theory was proven through interference diffraction experiments, showing that electrons can exhibit wave-like characteristics and critically displaying a wavelength much shorter than that of visible light. [11, 12] By 1933, the first transmission electron

microscope was built by German physicists Ernst Ruska and Max Knoll, allowing the study of features that have a length scale well below the optical resolution limit. [13]

The following sections will outline the basic operating principles and TEM set-up. It will then discuss the two types of imaging used in the work presented in this thesis: structural imaging and magnetic imaging.

2.4.2 Operating Principles

The main parts that make up an electron microscope are the electron source, a set of electromagnetic lenses, apertures and detectors. A beam of electrons pass through the sample and a series of electromagnetic lenses, to where they are ultimately focused at a viewing screen or camera at the bottom of the column.

TEMs consist of a column that is under a vacuum to minimise interactions between the electron beam and air molecules. At the top of the column, there is an electron emitter that generates a beam of electrons that travel down the column. The incoming electron beam, i.e. the source of illumination, can be produced by two types of electron sources: thermionic and field-emission. Field-emission sources use a large field gradient between the source and an anode to extract electrons, compared to thermionic sources which extract electrons through heating. All TEM imaging in this thesis was performed using the FEI Tecnai T20 microscope in the Kelvin Nano-Characterisation Centre in the University of Glasgow. The Tecnai T20 TEM is a standard commercial microscope, with a LaB_6 thermionic electron source.

The wavelength of electrons λ that have been accelerated by a potential difference V, can be related.

$$\lambda = \frac{h}{P} = \frac{h}{(2m_0eV)^{1/2}} \tag{2.1}$$

where h is Planck's constant, P is the momentum and m_0 and e are the rest mass

and magnitude of charge of an electron, respectively. But as most modern TEMs, including the one used in all parts of this thesis, use accelerating voltages of 200 kV, the relativistic kinetic energy of the electrons must be considered. In this case, the wavelength of an electron can be described as:

$$\lambda = \frac{h}{\left[2m_0eV\left(1+\frac{eV}{2m_0c^2}\right)\right]^{1/2}}. \tag{2.2}$$

Using equation (2.2) where c is the speed of light, the electron wavelength of 200 kV electrons is found to be 2.51 pm.

The resolution of a perfect lens system within a microscope is theoretically limited by the wavelength of the illumination source. Microscopes that achieve this theoretical resolution are described as 'diffraction limited'. Abbe's limit can be used to describe the diffraction limited resolution of a microscope:

$$d = \frac{\lambda}{2nsin(\theta)} \tag{2.3}$$

where $nsin\theta$ is the numerical aperture, λ is the wavelength of light/radiation travelling in a medium with a refractive index n, where the light radiation converges to a spot with a half angle θ, to make a spot of radius, d. Therefore one major advantage of electron optics over visible light optics is that that wavelength of 2.51 pm is five orders of magnitude smaller than visible light (typically between 450-700 nm). The decreased wavelength would control the resolution capabilities of the microscope in an ideal case, however there are other competing limiting factors which will be discussed in following sections.

After electrons are produced by the electron source at the top of the optic axis and accelerated by the electron gun, they pass through a series of electromagnetic lenses. They use magnetic fields to focus the electrons, similarly to the way convex glass lenses are used to focus light. However, electromagnetic lenses are imperfect.

These lens defects, or aberrations affect the ability of the lens to form an image. This means the lens system will be aberration limited, rather than diffraction limited (as described by Equation (2.3)).

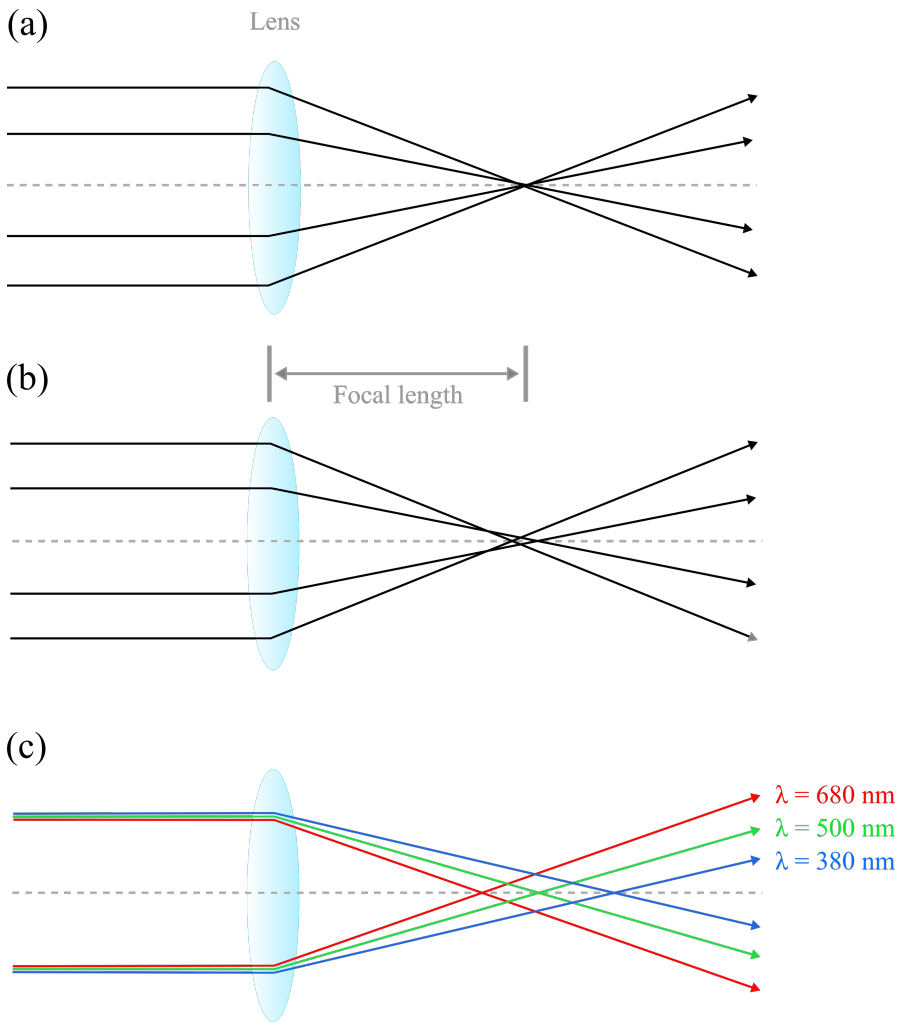

Figure 2.6: Schematic showing electromagnetic lens aberrations. (a) No aberrations: A 'perfect' lens. (b) Spherical aberration: Electrons passing through the outer portion of the lens are more strongly refracted than those passing through the central region. (c) Chromatic aberration: The variation of a lens' refractive index with changed in wavelength.

Electromagnetic lenses can have several types of aberration, which are highlighted in Figure 2.6. The most limiting aberration is referred to as spherical aberration, C_S, which causes off-axis electrons to converge more than on-axis electrons. As a result a parallel illumination is imaged as a disk of finite size surrounded by a series of diffraction rings. This ultimately will limit the resolution of the system

and the ability to magnify detail. The practical resolution r_p for a system with spherical aberrations can be given by the following equation:

$$r_p = 0.91(C_s\lambda^3)^{1/4} \tag{2.4}$$

For example, with typical values of λ and C_S of 2.5 pm and 1.2 mm respectively, a point-to-point resolution of approximately 0.34 nm is reached.
Although this is an important limiting factor in conventional TEM operation, the effect of spherical aberration will be negligible when using Lorentz imaging (Section 2.6.1) as defocus is required to generate magnetic image contrast in the Fresnel mode. Chromatic aberration C_C occurs where the convergence of the electrons varies with the electron wavelength. Most modern electron guns are capable of reducing the spread of electron energies before they hit the specimen, this is known as increasing the monochromaticity of the electron source. [14] The effects of these aberrations means the resolution of the TEM is limited to approximately 50 λ for conventional transmission electron microscopes. [15]

2.4.3 The Microscope Column

There are two ways to configure a TEM. First is conventional TEM (CTEM), and the second is scanning TEM (STEM), where the electron beam is focused into a spot and rastered across the sample. All imaging performed in this thesis was acquired using CTEM configuration on the FEI T20. Figure 2.7 shows a typical microscopy set-up of a conventional transmission electron microscope, specifically an imaging mode with positive magnification. High energy electrons (200 kV) are ejected from the electron gun at the top of the column, where they enter the condenser system. This system acts to control the electron intensity, spot size and convergence of the beam through the use of electromagnetic lenses and apertures.

The specimen is placed between the upper and lower pole pieces of the objective lenses. This is the main imaging lens of the system and determines the resolution of the microscope. Electrons are focused so they are parallel to the specimen upon

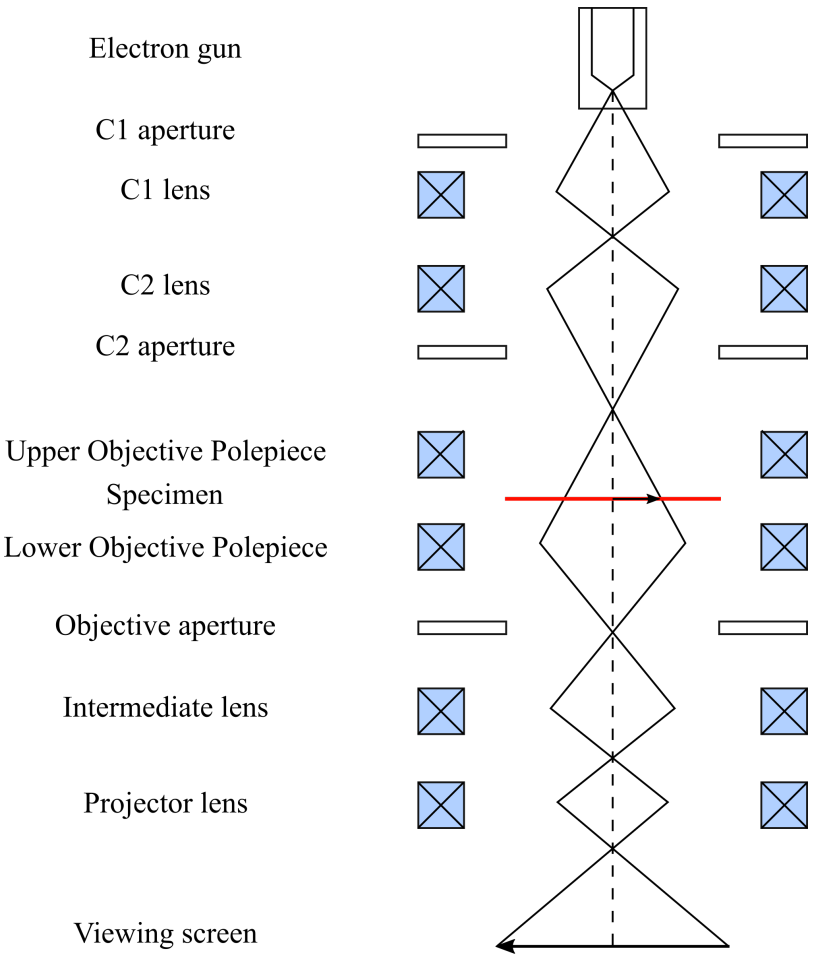

Figure 2.7: Schematic showing the typical set-up of a conventional transmission electron microscope column. The figure illustrates key parts and positions of electromagnetic lenses and apertures which are used in image formation which is finally viewed on a phosphor screen, where the central dash line is the optic axis. The TEM is composed of gun column, condensed lens, objective lens and projectors lens. The components and electron beam path are not to scale.

interaction. After transmission through the specimen, the beam is focused to a spot in the back focal plane by the lower objective lens. The objective aperture acts to restrict the angular spread of the electrons allowed to form the final image, enhancing contrast (see Section 2.5.2 bright and dark field imaging section later in chapter). Below the objective system, there are a series of intermediate and projector lenses which act to further magnify and project the image onto the viewing screen. The intermediate lens selects the mode of operation of the microscope, which is either imaging or diffraction. The FEI T20 microscope also contains

additional features, such as the Lorentz lens, which allows the imaging of magnetic materials in a low field environment. which will be discussed in more detail in Section 2.6. Below the microscope column is the Gatan Image filter (GIF), which was used for capturing CTEM images.

2.5 Structural Characterisation

There are two main modes of operation in a conventional TEM system. Electron diffraction patterns can provide information on the physical properties such as crystal structure and texture. Additionally, TEM image formation can provide information on the specimen structure, such as grain size and shape. Both methods were used in this thesis and will be described in more detail in Sections 2.5.1 and 2.5.2 respectively.

2.5.1 Diffraction

Electron diffraction is a powerful method for characterising a materials structure and composition. [16] Diffraction in a TEM can be described as the elastic scattering of waves by the arrangement of atoms in a material. Some electrons in the beam are incident on the atomic planes at a critical angle (Bragg angle). These electrons are reflected in phase with electrons from neighbouring planes, resulting in constructive interference. To obtain the maximum constructive interference, it must satisfy the Bragg condition:

$$n\lambda = 2dsin\theta \tag{2.5}$$

where n is an integer number which is the interference order, d is the spacing of the planes, θ is the incident angle and λ is the wavelength of the electrons. Figure 2.8 highlights the plane spacing and the path difference of the two waves being equal to $2dsin\theta$.

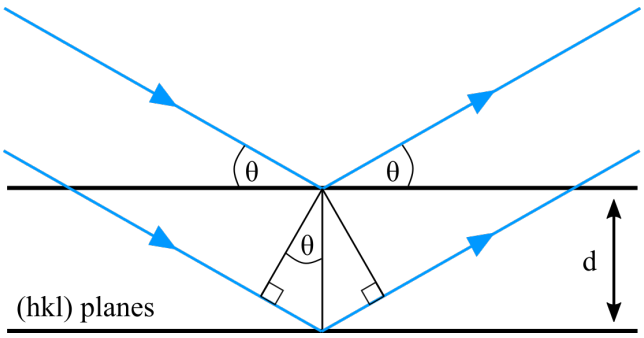

Figure 2.8: Electron diffraction in a crystal lattice. A beam incident on a pair of planes which is separated by a distance, *d*. The angle of incidence is equal to the angle of reflection, as indicated.

Within a crystal, each set of atomic planes has a different inter-plane spacing. Two systems will be studied in this thesis; cubic and hexagonal. For a cubic lattice, this spacing can be given by:

$$d = \frac{a}{\sqrt{h^2 + k^2 + l^2}} \tag{2.6}$$

where a is the lattice parameter and h,k,l are the Miller indices for the set of lattice planes.

The lattice spacing for a hexagonal crystal (hcp) in reciprocal space, in this case the Ru layer, is given by,

$$d_{hkl} = \frac{1}{\sqrt{\frac{4}{3a^2}(h^2 + k^2 + hk) + \frac{l^2}{c^2}}} \tag{2.7}$$

with a and c being the lattice constants of the crystal structure, and h,k,l are the Miller indexes.

If we consider the diffraction phenomenon in reciprocal lattice space, the spacing of (hkl) planes is given by:

$$d_{hkl} = \frac{1}{\mathbf{g}_{hkl}} \tag{2.8}$$

with $\mathbf{g}_{hkl}$ the reciprocal vector given by:

$$\mathbf{g}_{hkl} = h\mathbf{a}^* + k\mathbf{b}^* + l\mathbf{c}^* \tag{2.9}$$

where, $\mathbf{a}^*$, $\mathbf{b}^*$, $\mathbf{c}^*$ are the unit-cell translation vectors in reciprocal space, which are related to lattice constants a, b, c, and the unit-cell volume, V_c via the relation:

$$\mathbf{a}^* = \frac{\mathbf{b} \times \mathbf{c}}{V_c} \tag{2.10}$$

$$\mathbf{b}^* = \frac{\mathbf{c} \times \mathbf{a}}{V_c} \tag{2.11}$$

$$\mathbf{c}^* = \frac{\mathbf{a} \times \mathbf{b}}{V_c} \tag{2.12}$$

If we define difference vector, $\mathbf{K} = \mathbf{K}_D$ - $\mathbf{K}_I$ with $\mathbf{K}_I$, $\mathbf{K}_D$ are the incident and diffracted wave vectors, respectively. The difference vector will given by:

$$|\mathbf{K}| = \frac{2sin\theta}{\lambda} \tag{2.13}$$

As a result, Bragg's law can be rewritten in reciprocal lattice space as:

$$\mathbf{K} = \mathbf{g}_{hkl} \tag{2.14}$$

The equation 2.14 represents the Laue condition for constructive interference. The construction of diffraction spots can be understood using the Ewald sphere representation (Figure 2.9). The Ewald sphere is a sphere in reciprocal space of radius of r = $1/\lambda$. From intersections of the Ewald sphere and reciprocal space the diffraction spot can be constructed. In the TEM, electrons that pass through the specimen are brought to focus in the back focal plane of the objective lens, the diffraction pattern is produced in this plane.

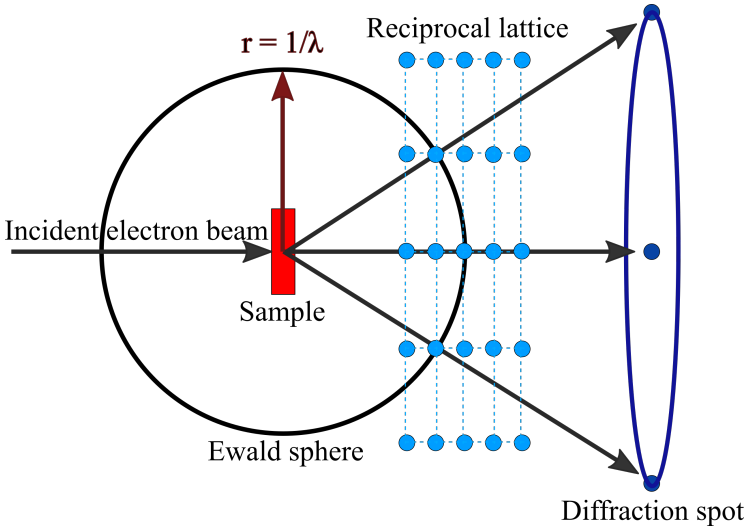

Figure 2.9: The Ewald sphere of reflection to construct the diffraction spot from reciprocal space.

In a single crystal diffraction experiment, the electron wavelength, beam direction and reciprocal planes which intersect with the Ewald sphere are fixed, resulting in a pattern with bright spots on a dark background. However, the samples studied in this thesis are exclusively polycrystalline. In the case of polycrystalline sample, all possible orientations of crystallites are present and a ring pattern is visible (Figure 2.10). This pattern appears as a superposition of many single crystal spot patterns, therefore continuous rings are formed. The brightest spot lies at the centre, due to the majority of electrons going directly through the sample, without being scattered. This central (unscattered) spot is masked for image acquisition as it can easily damage the CCD camera.

Crystalline texturing is the distribution of crystallographic orientations of the grains in a polycrystalline material, occurring in a polycrystalline sample when some preferred orientation exist [11] Moreover, in a textured-polycrystalline sample, the pattern will have broken rings, or arcs, due to the variation of the preferred orientation in the individual grains present in the sample. Despite the texturing in one direction, the grains are still randomly orientated about this direction so do retain a ring pattern. The characteristic feature of the textured specimen can be seen in a pattern by tilting the specimen. If a texturing orientation exists, diffraction

rings of some planes will appear and other ones may be disappeared because some planes deviate from the Bragg condition. This texture, or lack of, can be viewed when the sample is tilted, Figure 2.10(b) demonstrates a 30 degree tilt.

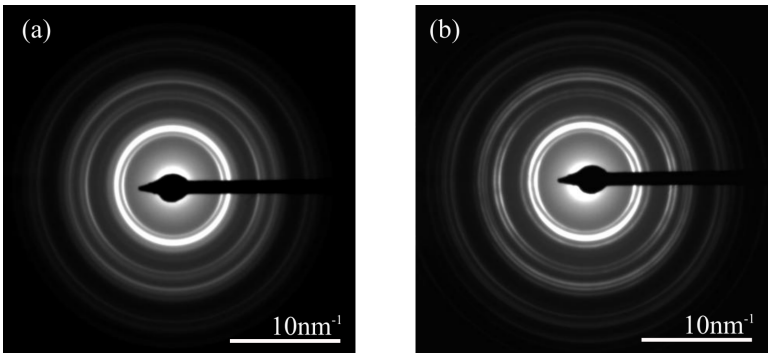

Figure 2.10: Typical electron diffraction patterns with a *fcc* structure at 30 degree tilts produced for (a) non-textured 10 nm $Ni_{45}Fe_{55}$ polycrystalline thin film and (b) a textured 10 nm $Ni_{45}Fe_{55}$ with an additional 1 nm $Ni_{79}Fe_{21}$ seed layer polycrystalline specimen.

2.5.2 Bright and Dark Field Imaging

A typical diffraction pattern for a polycrystalline sample consists of a bright central spot surrounded by rings (see Figure 2.10(a)). The central spot contains the direct unscattered electrons, whilst the rings are from the scattered electrons. The objective aperture allows you to select specific diffracted electron beams to produce either a bright-field (BF) or dark-field (DF) image.

Depending on the chosen electrons, only certain crystal orientations will contribute to the image. Images formed from the direct electron beam are referred to as bright-field (BF) images. Grains that appear dark in the bright-field image are those that satisfy the Bragg condition. If only scattered electrons are used for image formation, a dark-field (DF) image is produced.

Bright-field imaging is the most basic operational mode in the TEM. In bright-field imaging the beam is spread out at the objective lens to give broad beam illumination of a large area of the sample with electrons travelling near perpendicular to the sample plane. This illumination type is called "parallel beam illumination". An

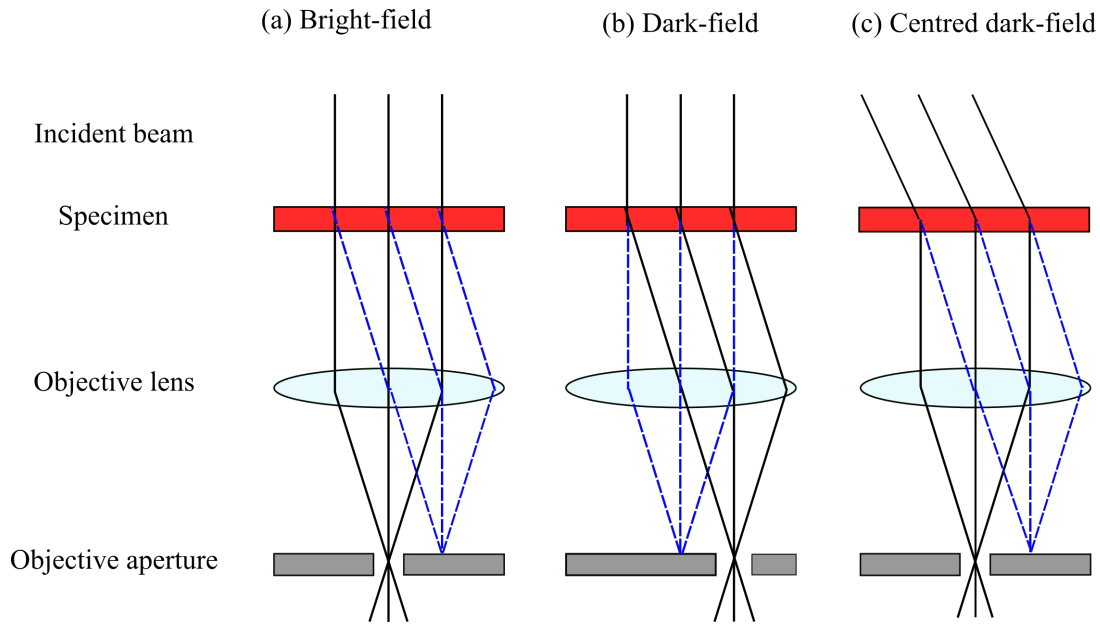

Figure 2.11: Ray diagram for the formation of (a) bright-field imaging, (b) dark-field imaging achieved by centring the objective aperture around the diffracted electron beam, and (c) centred dark-field imaging by tilting the incident beam to the Bragg angle.

aperture is inserted directly after the objective lens into the back focal plane to ensure only electrons passing parallel though the objective lens pass through to form the first image in the intermediate lenses before projection. Figure 2.11(a) shows this in the form of a ray diagram. The rays forming the bright-field image are shown in black and the rays blocked by the objective aperture are shown in blue. An example of an typical experimental bright-field image, demonstrating grains within a polycrystalline material is shown in Figure 2.12(a).

In dark field imaging, rather than only using the transmitted beam, electrons that have been scattered by the sample are imaged. This is done by using an aperture to block all but a select group of electrons by centring the aperture over a single diffraction spot. Where the electron beam is incident to the specimen the diffraction spots are located off-axis meaning the position of the objective aperture must be moved to highlight a particular spot, this is called 'off-axis' dark field imaging, shown in figure 2.11(b), i.e. looking at the image plane with apertures used to select the diffraction plane. Alternatively, tilting the beam causes the

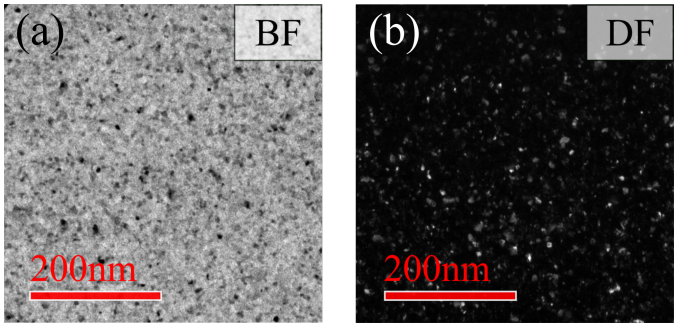

Figure 2.12: TEM (a) bright-field and (b) dark-field images of polycrystalline grains present in a 10 nm $Ni_{45}Fe_{55}$ polycrystalline thin film. A bright-field image is formed from unscattered electrons, i.e. the direct electron beam, compared to a dark field image where the image is formed from the deflected electron beam.

transmitted beam to appear off-centre to the optic axis and the diffraction spot of interest to centre on the optic axis. This method is called 'on-axis' dark field imaging, as shown in figure 2.11(c). The on-axis method is preferred as the off-axis method causes the diffracted beam to pass though the objective lens at a greater distance from the optical axis which will be more susceptible to aberrations. Selecting only one diffraction spot results in an image where intensity is dependent on crystallographic orientation. This technique is often employed when the grain size in polycrystalline materials is of interest.

2.5.3 Measurement of Grain Size Distribution

The above techniques were used to image permalloy thin films and allow for the characterisation of their physical structure, including crystal structure and grain size. In thin film polycrystalline samples, like those studied in this thesis, the magnetic properties of the material can be greatly influenced by the grain size distribution. [18] Dark field images are useful when looking at grain size distribution due to the high contrast between the grains. This makes it easier to distinguish individual grains for analysis. An example of the difference between typical bright-field and dark-field images can be seen in Figure 2.12.

The growth processes in granular systems are known to follow a log-normal distribution which is defined as: [19]

$$P(D) = \frac{1}{\sqrt{2\pi}\sigma D} exp\left[\frac{-(ln(D) - (\mu)^2)^2}{2(\sigma)^2}\right] \tag{2.15}$$

where D is the grain size, μ is the mean value of ln(D) and σ is the standard deviation of $ln(D)$.

To measure the grain size, a large number of dark-field images were acquired (> 20) to ensure statistical significance. Image analysis can be done using the software ImageJ where limits of minimum and maximum grey levels can be selected to produce a final thresholded image (Figure 2.13(b)), allowing the individual grain sizes to be measured. The calculated log-normal distribution is then plotted against the measured diameters, shown in Figure 2.13(c). To ensure good statistical results, a minimum of 10,000 grain diameters were measured for each specimen.

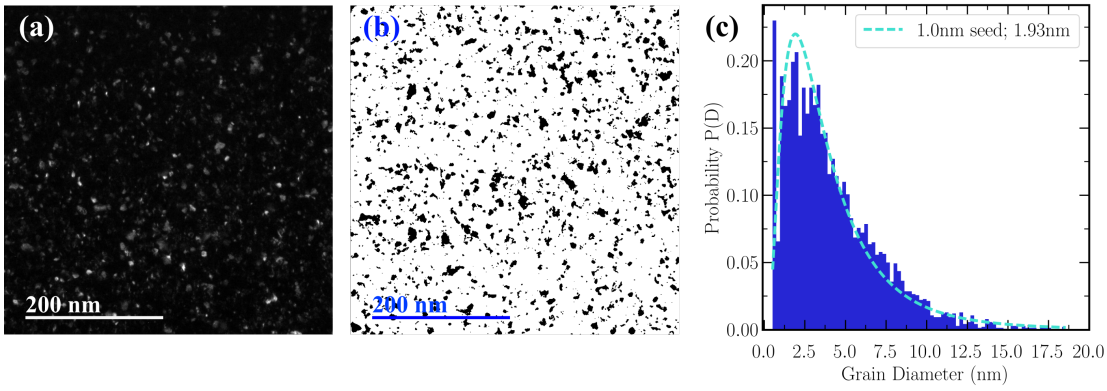

Figure 2.13: Process of determining a typical grain size distribution: (a) Dark-field TEM image showing polycrystalline granular structure, (b) Threshold image using Image J software and (c) Plotted log-normal distribution. Images were taken from an 10 nm $Ni_{45}Fe_{55}$, with a 1 nm $Ni_{79}Fe_{21}$ seed layer sample.

2.6 Magnetic Imaging

The observation of the magnetic configurations is of great interest for many applications of magnetic materials. Lorentz Transmission Electron Microscopy

(LTEM) is one of the techniques which enables analysis of the local magnetic properties, potentially down to the nanoscale. This technique also allows in-situ observations of the domain structure and micro-magnetic configuration of a magnetic material throughout different stages of the hysteresis process, which will prove vital for this project, and will be discussed in Section 2.6.3.

2.6.1 Lorentz Microscopy

In 1959, Hale et al discovered a conventional transmission electron microscope could be used to image the magnetic configuration of a specimen. They discovered that they could capture experimental TEM images featuring typical magnetic specimen characteristics, such as domain walls, simply by defocusing the imaging forming lens. [20]

Classic Lorentz microscopy is deemed an 'umbrella' term and it refers to all the methods of magnetic imaging in a transmission electron microscope. The way in which electrons interact with a ferromagnetic specimen is of great importance in this project. This interaction can be described using both classical and quantum mechanical approaches.

Classical Approach

When an electron beam passes through an area with a magnetic induction component perpendicular to its trajectory, the beam will be deflected by the Lorentz force, $\mathbf{F}_L$. The Lorentz force can be described classically by:

$$\mathbf{F}_L = -e(\mathbf{v} \times \mathbf{B}) \tag{2.16}$$

where e and $\mathbf{v}$ are the electron charge and velocity respectively, and $\mathbf{B}$ is the magnetic induction. Figure 2.14 shows electrons passing through a thin ferromagnetic film. The directions of magnetisation are in the plane of the specimen as indicated.

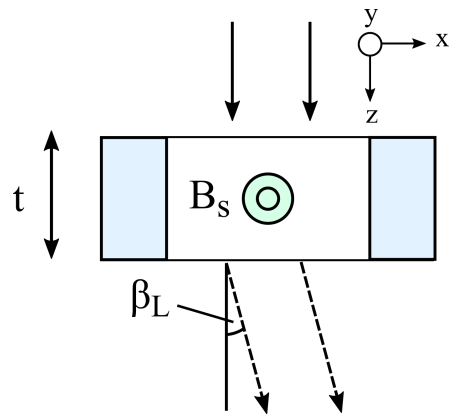

Figure 2.14: Deflection of an incoming beam of electrons, β, due to the Lorentz force when passing through a magnetic thin film.

A parallel beam, incident perpendicular to the plane of the film along the z-axis experiences a deflection in the x-direction at angle β_L is demonstrated in Figure 2.14. By integrating Equation 2.16 over the electron path, an expression for the deflection is given by:

$$\beta_L(x) = \frac{e\lambda}{h} \int_{-\infty}^{\infty} B_y(x, y) dz \tag{2.17}$$

where β_L is the magnetic induction in the x direction, h is Planck's constant, λ and e are the electron wavelength and charge respectively. It is assumed that there is an incident electron beam in the z-direction onto a thin magnetic sample that lies in the xy plane, containing domain walls. If it is assumed that the magnetisation lies along the +y and -y directions, there will be deflections of the incident beam in the +x and -x directions.

Therefore, for an untilted, uniformly in-plane magnetised specimen with a thickness, t, and a saturation induction B_S, then the magnitude of the deflection angle can be given by:

$$\beta_L = \frac{e\lambda B_S t}{h} \tag{2.18}$$

A typical value of deflection from 20 nm thick permalloy, where B_S = 1.0 T, magnetised in plane gives 12.7 μrad. This means that the magnitude of the deflection

of the electron beam due to the Lorentz force is much smaller than the typical angle of Bragg diffraction in the order of 10^{-2} rad.

Quantum Mechanical Approach

The above description is based on a classical point of view, and is sufficient to qualitatively explain the principles of Lorentz microscopy. By taking a quantum mechanical point of view, it is possible to extract quantitative magnetic information from the specimen. The interpretation of quantum mechanical approach requires a theory created by Yakir Aharonov and David Bohm, commonly referred to as the Aharonov-Bohm effect. [21]

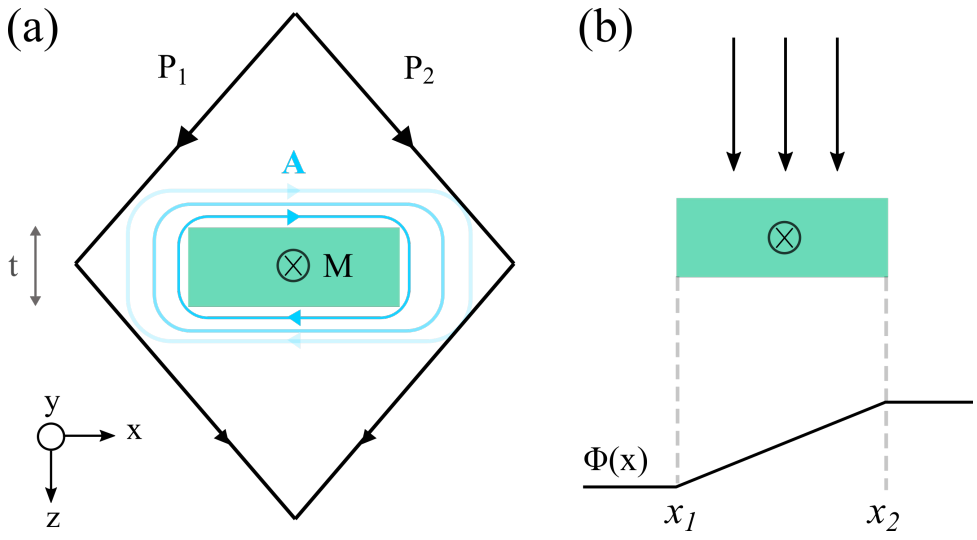

Figure 2.15: Schematic illustration of the Aharonov-Bohm effect. from a quantum mechanical approach. (a) Two electrons with the same start and end point will acquire a phase shift when travelling at different paths, P_1 and P_2 through an interaction with the magnetic vector potential (**A**). (b) The associated magnetostatic phase shift, ϕ(x).

In quantum mechanics, the electron is represented as a waveform, with the specimen and surrounding area being considered as a phase object. The image in Lorentz microscopy is constructed by considering the electron wave propagation. The Aharonov-Bohm effect states that a charged particle, in this case an electron, experiences a phase shift when passing through an electromagnetic potential, as shown in Figure 2.15.

As an electron wave passes through a specimen, any phase shift ϕ needs to be taken into account. If two electrons originating from the same point travel different, but equal distance paths, and rejoin, they may develop a phase difference due to magnetic effects. This phase difference will be proportional to the magnetic flux through the surface defined by the two paths. This phase shift $\Delta\phi$ is given by:

$$\Delta\phi = \frac{2\pi eN}{h} \tag{2.19}$$

where N is the enclosed magnetic flux. The phase shift between any two points x_1 and x_2 of an incident plane wave is given by equation 2.21:

$$\Delta\phi(x_2 - x_1) = \frac{2\pi e}{h} \int_{x_2}^{x_1} \int_{-\infty}^{+\infty} B_y(x, z) dz dx \tag{2.20}$$

$$\Delta\phi(x_2 - x_1) = \frac{2\pi et}{h} \int_{x_2}^{x_1} B_y(x) dx \tag{2.21}$$

where x_1 and x_2 are the points defining the integrated path. Hence, it can be seen that the magnitude of the phase shift is proportional to the integrated magnetic induction along the electron trajectory. This shows that ferromagnetic phase objects may be regarded as pure phase objects. [19]

Creating a field-free environment

The objective lens is the main imaging lens in most microscopes. It ultimately defines the systems resolution due to the aberrations previously discussed in Section 2.4.2. The specimen is normally located at the centre of the objective lens, meaning there is a large field present (usually in the order of 2 T), used to focus the electron beam. This makes this set-up unsuitable for magnetic imaging as the large field will overcome, and destroy any magnetic information in most areas of interest. To successfully image any magnetic materials, the objective lens set-up has to be modified to create a field-free conditions. [22] A way of achieving field-free conditions is to incorporate additional lenses, known as Lorentz lenses.

This enables the objective lens to be turned off meaning a remanent field of approximately 100 Oe remains.

One advantage of the Lorentz lens integration is that whilst imaging using the weaker Lorentz lens, the objective lens can be weakly excited, allowing it to be used as an electromagnet within the electron column. This creates a controllable field within the specimen region, allowing for in-situ magnetising experiments which will be discussed further in section 2.6.4.

2.6.2 Fresnel Imaging

The Fresnel imaging mode is a well established magnetic imaging technique due to it being a fast and easy-to-use method. Fresnel imaging consists of a parallel beam of electrons hitting a sample and being deflected by the samples magnetic induction. Depending on the direction of the magnetic induction, via domains, the electron deflection can lead to convergent or divergent electron beams, meaning an increase or decrease of the intensity in the image. This will lead to walls imaged as bright and dark lines respectively, as explained below. A Fresnel imaging schematic is shown in Figure 2.16.

Magnetic contrast is produced when the image is defocused by a distance Δz. Defocusing means that an object plane above or below the sample is imaged, depending on whether the lens is under-focused or over-focused. The value of Δ has to be carefully selected, as a larger defocus will lead to an increase in the magnetic contrast, but at the detriment of the image resolution. Lorentz imaging is unsuitable for the observation of very small details. However, it is a particularly useful method for the study of micro-magnetic behaviour over a large area of a continuous thin film, which is the region of interest in this project and discussed in the following section.

2.6.3 Imaging of Magnetisation Ripple

The Fresnel mode of Lorentz microscopy is ideal for studying continuous thin films. High contrast images are possible with Fresnel imaging which is sensitive

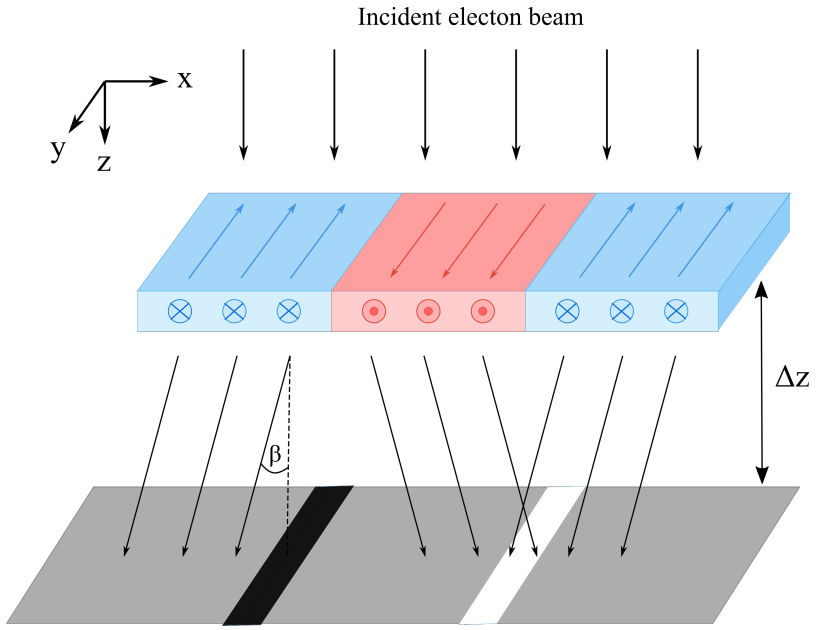

Figure 2.16: Fresnel imaging technique: An electron beam passes through a magnetic material, where the Lorentz force either converges or diverges the electron beam to create bright and dark areas in the image. This allows magnetic domains to be observed and subsequently analysed.

to the variation of the micromagnetic structure. A Fresnel image of a magnetic polycrystalline specimen provides a pattern of domain walls surrounded by a background of magnetisation ripple, shown in Figure 2.17.

As discussed previously in Section 1.7, magnetisation ripple is the small wave-like fluctuations of the magnetisation direction that occurs in thin polycrystalline ferromagnetic films. It originates from the random orientation of local anisotropies in each grain. The magnetisation ripple contrast lies perpendicular to the mean direction of the local magnetisation, and so can be used to orient the specimen with the applied field parallel to either the easy or hard axis. [23, 24, 25] Since magnetisation ripple is related to the magnetic and structural properties of the specimen, characterisation of the ripple spectrum can provide quantitative information. [26, 27] This will help with the understanding of the micromagnetic behaviour of the materials investigated in this thesis. A developed characterisation method has been produced to analyse large sets of Fresnel images displaying magnetisation ripple. A full description of this technique will be presented in Chapter 3.

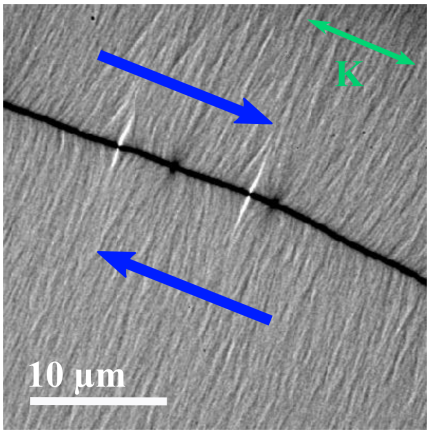

Figure 2.17: Fresnel image of a $Ni_{45}Fe_{55}$ polycrystalline thin film displaying magnetisation ripple. Imaging was taken along the hard axis, demonstrating zero field domain formation. The direction of magnetisation **M** is shown by the blue arrows.

2.6.4 In-situ Magnetising Experiments

The ability to perform in-situ magnetising experiments is an advantage of Lorentz microscopy. An external magnetic field can be applied to perform in-situ hysteresis experiments and allow for imaging of the magnetic structure at each stage.

An magnetic field, **H**, is produced at the sample when an electric current flows through the objective lens coil, which lies out of plane to the film when it is un-tilted. When a specimen is tilted at an angle θ around its central axis, it will encounter a magnetic field component which lies parallel to the specimen plane, $\mathbf{H}_{||}$, given by:

$$\mathbf{H}_{||} = \mathbf{H} \times sin(\theta) \tag{2.22}$$

where **H** is the magnetic field produced from the objective lens and θ is the tilt angle of the specimen with respect to the horizontal axis. The direction and the strength of the in-plane magnetic field can be controlled by the sign and value of the tilt angle θ.

The FEI Tecnai T20 microscope used in this work has a maximum tilt range of $\pm 30°$ determined by the tilt-rotate rod. This method will used in the following results chapters. It is important to note that the specimen will also experience

an out-of-plane magnetisation component when tilted. However this will have a negligible influence on continuous thin film specimens due to the large out-of-plane demagnetising factor. [28]

2.6.5 Lorentz Image Calculation from MuMax^3 Simulations

Calculation of simulated Fresnel images plays a vital role in all results chapters of this thesis. Fresnel images were calculated by scripts written by S. McVitie and G. White [29], which implement a software version of an original algorithm, created by M. Mansuripur. [30]

The intensity I of a Fresnel image is given by:

$$I(\mathbf{r}, \Delta) = 1 - \frac{\Delta\lambda}{2\pi}\nabla_{\perp}^{2}\phi(\mathbf{r}) \tag{2.23}$$

Where Δ is the defocus and $\nabla_{\perp}^{2}$ is the Laplacian relating to the in plane co-ordinates. The small focus limit assumes the higher order defocus terms are neglected.

The spatial frequencies in the image determine the validity of the equation for a given defocus. Ignoring conduction and displacement currents because there are no conduction currents flowing and no field changing with time, the Laplacian can be expressed as follows:

$$\nabla_{\perp}^{2}\phi(\mathbf{r}) = -\frac{e\mu_0}{\hbar}\int_{\infty}^{\infty}(\nabla \times \mathbf{M}) \cdot \hat{\mathbf{n}}dz \tag{2.24}$$

where e is the magnitude of the electronic charge, $\hat{\mathbf{n}}$ is the unit vector parallel to the beam, μ_0 is the permeability of free space, $\hbar$ is the reduced is Planck's constant, and $\mathbf{M}$ is the magnetisation.

If we consider inserting the above equation into Equation 2.23, where we take a small value for defocus Δ, and assume the magnetisation is uniform throughout the film thickness, t, the intensity can be written as:

$$I(\mathbf{r}, \Delta) = 1 - \Delta \frac{e\mu_0 \lambda t}{h} (\nabla \times \mathbf{M}(\mathbf{r})) \cdot \hat{z} \tag{2.25}$$

Therefore the final Fresnel image intensity can be calculated to a first order approximation. This helps interpretation as it only involves fields local to the film and not all of space. Equation 3.18 is simple to evaluate as we have knowledge of the microscope parameters and the out of plane component of the magnetisation curl parallel to the electron beam. A schematic illustration of the Laplacian of the phase can be seen in Figure 2.18.

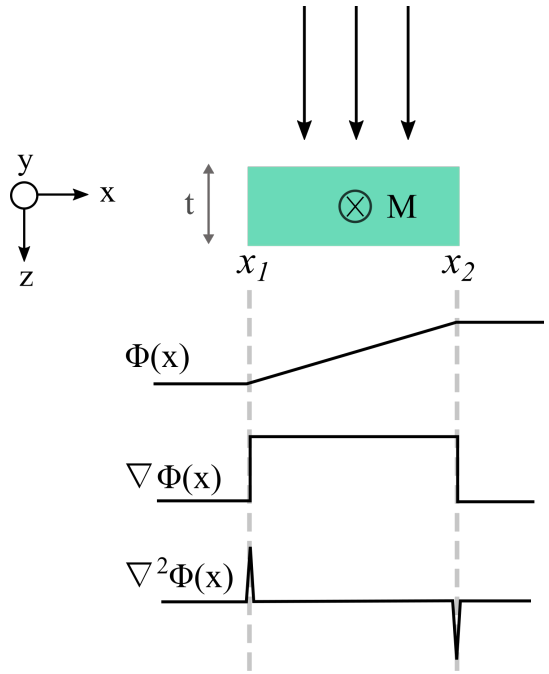

Figure 2.18: Schematic of the phases changes that electrons experience when passing through a magnetic specimen. The Fresnel mode of Lorentz imaging is sensitive to the Laplacian of the phase, $\nabla^2 \Phi$.

The advantage is this method allows for a simple calculation and interpretation of micromagnetic simulations, which can be compared to experimental images

To calculate the Fresnel image, a uniform incident electron wave with unit amplitude is assumed. The exit wave is then calculated by multiplication of the Fourier transform of the incident wave and the transfer function based on a Lorentz lens with spherical aberration term $C_s = 8000$ mm in a TEM with an operating voltage of 200 kV and $\lambda = 2.51$ pm. An inverse Fourier transform of the exit wave multiplied by its complex conjugate gives the image intensity. This process has been implemented through a script in Digital Micrograph. In practice, small values of defocus present problems with the signal to noise ratio, especially when there are non-magnetic contributions to the image contrast.

2.7 Summary

In this chapter a brief outline of the techniques used in fabrication process are outlined. This is followed by a review into the background of transmission electron microscopy (TEM). Conventional TEM procedures were discussed for physical characterisation, including grain size and crystal structure. The main method of characterisation in this thesis is Lorentz microscopy, the principle of which was described concentrating on the Fresnel mode of imaging. Lorentz microscopy is the main technique used in the presented work, used to quantitatively characterise the micromagnetic structure of the thin films as described in following chapters. Finally, simulated image calculation methods were discussed, which can be used to create successful magnetic models for specific sample structures.

2.8 Bibliography

[1] D. Weller, G. Parker, O. Mosendz et al. A HAMR media technology roadmap to an areal density of 4 Tb/in2. *IEEE Transactions on Magnetics*, 50(1), 2014.

[2] P. J. Kelly and R. D. Arnell. Magnetron sputtering: A review of recent developments and applications. *Vacuum*, 56(3):159-172, 2000.

[3] J. E. Greene. Review Article: Tracing the recorded history of thin-film sputter deposition: From the 1800s to 2017. *Journal of Vacuum Science and Technology A:Vacuum, Surfaces, and Films*, 35(5):05C204, (2017).

[4] G. Brauer. Magnetron Sputtering. *Phys. Technol.*, 19:67-75, (1988).

[5] R. Surmenev, A. Vladescum, M. Surmeneva et al. Radio Frequency Magnetron Sputter Deposition as a Tool for Surface Modification of Medical Implants. *Modern Technologies for Creating the Thin-film Systems and Coatings*, (2017).

[6] M. Gabor, C. Tiusan and T. Petrisor. The Influence of the Capping Layer on the Perpendicular Magnetic Anisotropy in Permalloy Thin Films. *IEEE Transactions on Magnetics*, 50(11):1-4, (2014).

[7] J. I. Goldstein, D. E. Newbury, J. R. Michael, N. W. M. Ritchie, J. H. J. Scott, and D. C. Joy. *SEM Microscopy and X-Ray Microanalysis*. Springer, 4 edition, (2018). ISBN 9781493966745. doi: 10.1007/978-1-4939-6676-9.

[8] K. Masahiro and Y. Kazuhiro. The effect of annealing on the magnetic properties of permalloy films in permalloy Ta bilayers, *Journal of Magnetism and*

Magnetic Materials, 147(1):213-220, (1995).

[9] J. K. Howard. Thin films for magnetic recording technology: A review. *Journal of Vacuum Science and Technology.* 4(1), (1986).

[10] "shb instruments", http://www.shbinstruments.com.

[11] G. P. Thomson and A. Reid. Diffraction of Cathode Rays by a Thin Film. *Nature*, 119(3007), (1927).

[12] C. Davisson and L. Germer. Reflection of electrons by a crystal of nickel. *Proc. Natl. Acad. Sci. U.S.A.*, 14:317-322, (1928).

[13] E. Ruska. The development of the electron microscope and of electron microscopy. *Reviews of Modern Physics*, 59(3):627-638, (1987).

[14] B. Freitag, S. Kujawa, P. M. Mul, J. Ringnalda, and P. C. Tiemeijer. Breaking the spherical and chromatic aberration barrier in transmission electron microscopy. *Ultramicroscopy*, 102(3):209-214, (2005).

[15] O. L. Krivanek, T. C. Lovejoy, and N. Dellby. Aberration-corrected STEM for atomic-resolution imaging and analysis. *Journal of Microscopy*, 259(3):165-172, (2015).

[16] L.A. Bendersky and F.W. Gayle. Electron diffraction using transmission electron microscopy. *Journal of Research of the National Institute of Standards and Technology*, 106(6):997-1012, (2001).

[17] D. Litvinov, T. O'Donnell and R. Clarke. In-situ thin film texture determination *Journal of Applied Physics*, 85(4):2151-2156, (1999).

[18] Y.T. Chen, J.Y. Tseng et al. Effect of grain size on magnetic properties and microstructure of $Ni_{80}Fe_{20}$ thin films *Thin Solid Films*, (2013).

[19] M.Fatima Vaz, M.A.Fortes. Grain size distribution: The lognormal and the gamma distribution functions. *Scripta Metallurgica* 22:1, 35-40, (1988).

[20] S. McVitie and G. S. White. Imaging Amperian currents by Lorentz microscopy. *Journal of Physics D: Applied Physics*, 37(2):280-288, (2004).

[21] Y Aharonov and D Bohm. Significance of electromagnetic potentials in the quantum theory. Physical Review, 115(3):485, (1959).

[22] A. Kohn and A. Habibi. Adapting a JEM-2100F for magnetic imaging *JEOL News*, 47(1):17-22, (2012).

[23] K. J. Harte. Theory of magnetisation ripple in ferromagnetic films. *Journal of Applied Physics*, 30(5):789, (1959).

[24] H. Hoffmann. Quantitative calculation of the magnetic ripple of uniaxial thin permalloy films. *Journal of Applied Physics*, 35(6):1790-1798, (1964).

[25] H. Hoffmann. Theory of Magnetisation Ripple. *IEEE Transactions on Magnetics*, 4(1):32-38, (1968).

[26] T. Suzuki and C. H. Wilts. Quantitative Study of the Magnetisation Ripple in Ferromagnetic Ni-Fe Alloy Films. *Journal of Applied Physics*, 39(2):1151-1153, (1968).

[27] R. Ploessl, J. N. Chapman, and A. M. Thompson et al. Investigation of the micromagnetic structure of cross-tie walls in permalloy. *Journal of Applied Physics*. 73(5):2447-2452, (1993).

[28] S. McVitie and J. N. Chapman. Coherent Lorentz Imaging of Soft, Magnetic Materials. *MRS Bulletin*, (October 1995):55-58, (1995).

[29] S. McVitie and M. Cushley. Quantitative Fresnel Lorentz microscopy and the transport of intensity equation. *Ultramicroscopy*, 106(4-5):423-431, (2006).

[30] M. Mansuripur. Computation of electron diffraction patterns in Lorentz electron microscopy of thin magnetic films. *Journal of Applied Physics*, 69(8):5890, (1991).

3

Developing Methods for the Characterisation of Magnetisation Ripple using Lorentz Microscopy

Contents

3.1 Introduction

As previously noted in Chapter 1.7, magnetisation ripple is a well known phenomenon that occurs in ferromagnetic polycrystalline thin films. It occurs over large areas of thin films, where the properties such as ripple wavelength λ and angle of deviation from the mean direction of magnetisation θ can vary. These variations occur even without any external effects, such as applied fields and stress. A single experimental Fresnel image, such as that shown in Figure 3.1(d), displaying magnetisation ripple consists of a range of spatial frequencies. Analysis of such images allow the possibility of ripple characterisation through careful interpretation.

This chapter includes a detailed review into previous characterisation methods used to determine key parameters such as ripple dispersion and wavelength. Work presented includes a newly developed characterisation methodology which allows for convenient and reliable parameter determination by using automated data analysis techniques. This chapter will include in-depth comparisons between old and new methods, followed by discussions as to why the developed methodology is an improvement on previous methods for both accuracy and measurement time.

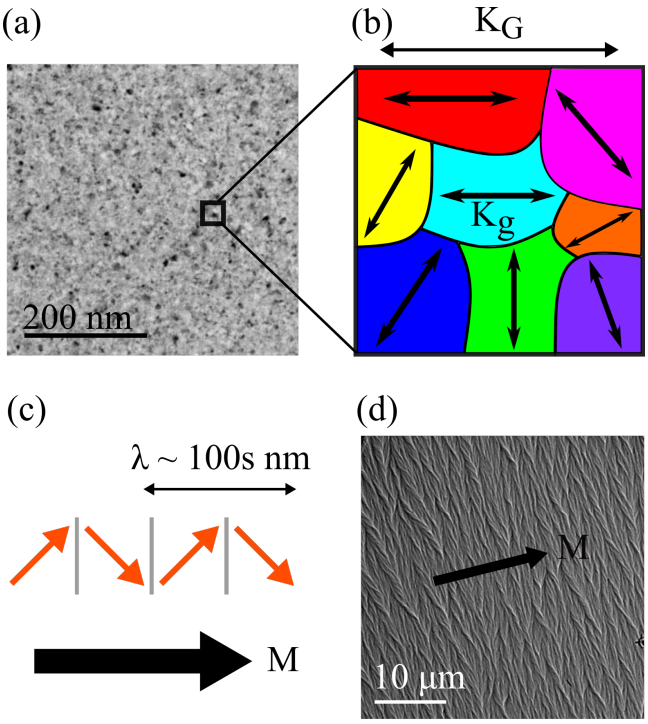

Figure 3.1: Schematic of magnetisation ripple origin. (a) $Ni_{45}Fe_{55}$ bright field TEM image, showing a granular structure, expected from a polycrystalline thin film. (b) The random direction of the granular crystalline anisotropy K_g, with an additional global uniaxial anisotropy K_G. (c) Schematic of the magnetisation fluctuations, producing low-angle domain walls, commonly referred to as magnetisation ripple, where the length scale is in the order of 100s nm. (d) Lorentz TEM image displaying strong magnetisation ripple of a $Ni_{45}Fe_{55}$ permalloy thin film. The arrow indicates the mean direction of magnetisation **M**.

3.2 Relevant Literature Summary

This section will provide a timeline and a brief overview on developments in the characterisation of magnetisation ripple, specifically focusing on the methodology involved in experimental characterisation.

Research into experimental quantification of magnetic ripple properties has been somewhat limited since it was first observed in 1959. Fuller and Hale, and E. Fuchs were among the first to produce publications which used an electron-optical method of viewing magnetisation contributions in thin films, using a standard transmission electron microscope. [1,2,3,4] They both produced experimental TEM images displaying magnetisation ripple. Fuller and Hale named the phenomenon 'magnetisation ripple' and made the first attempt to approximate the ripple

wavelength by averaging the measured wavelength values [2]. This is a relatively simplistic method of wavelength determination which will be discussed in great detail in Section 3.4.

In the same year, E. Feldtkeller observed the rotation of the magnetisation direction, featuring magnetisation ripple, through a hard axis hysteresis sequence, however no characterisation was made. [5] In 1968, T. Suzuki measured ripple characteristics over a range of permalloy alloy composition, substrate deposition temperature and measurement temperature. [6] An estimate for ripple wavelength was made from the spacing between fluctuations in experimental Fresnel images. The amplitude of the angular spread of the magnetisation direction was then estimated. [7]

Gaigher followed this in 1969 using the same method as Fuller and Hale, where the mean long range wavelength was obtained from direct measurements on the experimental ripple images. [8]

In 1994, advances in characterisation techniques were made by Herrmann, Zweck and Hoffmann who produced the first publication where a 2D Fourier transform was taken of experimental Fresnel images. [9] This imaging processing technique is used to decompose an image into its spatial frequency components. They defined the average ripple wavelength as the distance between the central peak and the mode peak in the FFT. This method improved the reliability of ripple wavelength measurements when compared to real-space measurements and will be discussed in greater detail in Section 3.5.

L.J Heyderman, also in 1994, studied ferromagnetic multilayers through easy and hard axis reversal processes. [10] She improved upon the FFT analysis used by Herrmann. She was the first to use a power spectrum i.e. (the square of the modulus) to display the data within the Fourier transform. This significantly reduced noise in FFT spectrum measurements to improve the accuracy of line profile measurements. She also defined contour plots of relative FFT intensities, and used these to define ripple characteristics, such as dispersion angle and ripple wavelength.

In 2002, Hosson presented a new method for magnetic ripple characterisation using rotational averaging processes of the FFT images. [11] This method will be studied in greater detail in Section 3.6.1 and 3.7.1 for dispersion angle and dominant ripple wavelength respectively.

Some of the previous work was from the University of Glasgow and includes visualisation of magnetisation ripple through Lorentz microscopy. Chapman used the same methodoloy used as T. Suzuki [12, 13]. Others defined the ripple dispersion as the FFT angle where the intensity falls by 75% of the value at the origin. [14, 15] C. Brownlie, also from the University of Glasgow, characterised ripple properties using the method devised by Fuller and Hale, by using real-space measurement techniques. The average wavelength was estimated by taking a line trace parallel to the axis of magnetisation, counting the number of intensity peaks and averaging the distance between the peaks. [16] The limitations of this methodology will be discussed in greater detail in Section 3.4. D. Ngo characterised the ripple wavelength by using a large integrated box profile over a FFT structure. [17, 18] This process will be also be described in Section 3.7.1, in comparison to the rotational average.

3.3 Overview

This chapter describes how using image processing to produce data in Fourier space can lead to more information being acquired about a specimens magnetic configuration during magnetisation reversal processes. It will include a description and discussion of quantification methods used in previous publications including real space measurements (3.4) and using reciprocal space measurements (3.5). This is followed by a discussion into previous methods used for dispersion angle θ characterisation (3.6.1). A new and improved processing method for dispersion angle θ characterisation has been developed and will be detailed in Section 3.6.2. The same outline is applied for characterisation of dominant ripple wavelength λ_{Dom} where previous and new methods are discussed in Sections 3.7.1 and 3.7.2 respectively. Two additional new methods of characterisation have been developed; ripple image

intensity I (3.7.3) and spectroid ripple wavelength $\theta_{Spectroid}$ (3.8). Ripple image intensity allows for mapping of ripple contrast variation as a function of field. The most subtle changes in image intensity of a sequence of Fresnel images can be picked up. Magnetisation ripple consists of a range of wavelength frequencies. Unlike the dominant ripple wavelength determinations, which characterises the mode peak, the spectroid method has been developed to measure the weighted average wavelength value in the full FFT spectrum. This is generally a more consistent method of ripple determination with both strong and weak ripple properties. All methods can be used in conjunction to maximise characterisation of ripple properties. A comparison of ripple wavelength characterisation methods will be discussed in Section 3.9, followed by an example Fresnel image sequence which highlights how these characterisation methods can be utilised for hysteresis mapping (3.10).

3.4 Real Space Measurements

Real space line profiles of magnetisation ripple are easy to acquire from experimental TEM images using software such as Digital Micrograph and ImageJ. [18,19] Figure 3.2 shows four separate samples of experimental Fresnel TEM images with varying degrees of magnetisation ripple present at an applied field of $\approx$ 30 Oe, heading toward the magnetisation saturation state. The compositions are all 10 nm $Ni_{45}Fe_{55}$ with increasing $Ni_{80}Fe_{20}$ seed layer thickness's. (Note, these are the samples which will be studied in greater detail in Chapter 4). Example 1 exhibits a large variation in **M**, where as in Example 4 the ripple is more suppressed. The differences in magnetic ripple configurations are observable by the eye, however acquiring quantitative information is the key to characterisation.

One method of achieving quantitative outputs is to take a simple line profile through the image, integrated over a defined area. This was used by H. L. Gaigher in 1969 [7]. This method was used for the example images shown in Figure 3.2. where the white box highlights the integrated area used for the line profiles with a width of 100 pixels, and the line traces from the equivalent images in 3.2 are

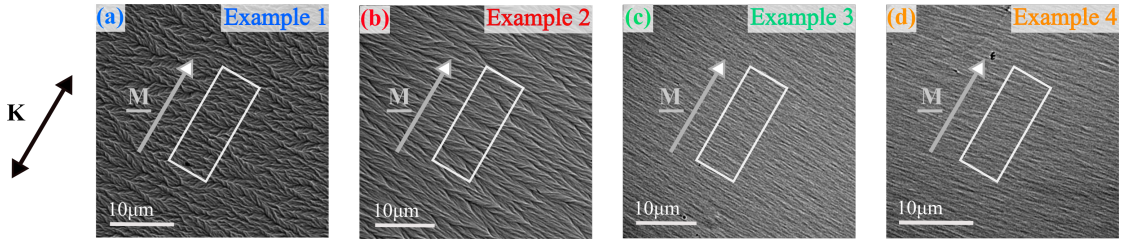

Figure 3.2: Examples of experimental Fresnel TEM images of polycrystalline thin films with varying degrees of magnetisation ripple present. Images (a-d) show a 10 nm $Ni_{45}Fe_{55}$ thin film with increasing $Ni_{80}Fe_{20}$ seed layer thickness. The white box highlights the integrated area of 100 pixels width used for the line profiles, with the white arrow indicating the mean direction of magnetisation of the film **M**. These materials will be studied in greater detail in Results Chapter 4.

plotted in Figure 3.3(a,c,e,g). The average distance between the peaks represents the characteristic length scale, in this case average ripple wavelength. Additionally, the 1D transforms of these line traces are displayed in Figure 3.3(b,d,f,h).

The distance between the peaks does decrease from Example 1 through to Example 4 as seen from the images, however the distances between the peaks is not uniform. It is also somewhat variable on the location of the line trace over the Lorentz image. Table 3.1 shows the approximated average wavelength values determined from the average peak-to-peak distance, which has been manually measured, and the associated estimated standard error. This method gives a quick output for an average wavelength value and is useful when looking at images with a large variation in ripple strength. Due to the large deviation in the spread, it wouldn't be a reliable method when looking at images displaying ripple with subtle differences.

Sample	Average wavelength λ (μm)
1	0.9 ± 0.1
2	0.5 ± 0.1
3	0.3 ± 0.1
4	0.2 ± 0.1

Table 3.1: Real space measurement technique used to determine the average magnetisation ripple wavelength λ value. This technique will work to obtain an approximate value when comparing images with a large variation in ripple strength. However, there is a large deviation in the spectrum and a significant standard error associated with this method.

It is clear that there isn't a single harmonic wavelength value in all example images. This is confirmed when a 1D Fourier transform is taken of the line traces shown in Figure 3.3(b,d,f,h). It reiterates that the signal is made up of a range of frequencies, with decreasing amplitude. Examples 1 and 2 have larger lower spatial frequency contributions. Examples 3 and 4 have significantly smaller lower spatial frequency components and look almost like experimental image noise contributions. The goal in this chapter is to develop an updated methodology for extracting an average wavelength value and its corresponding deviation.

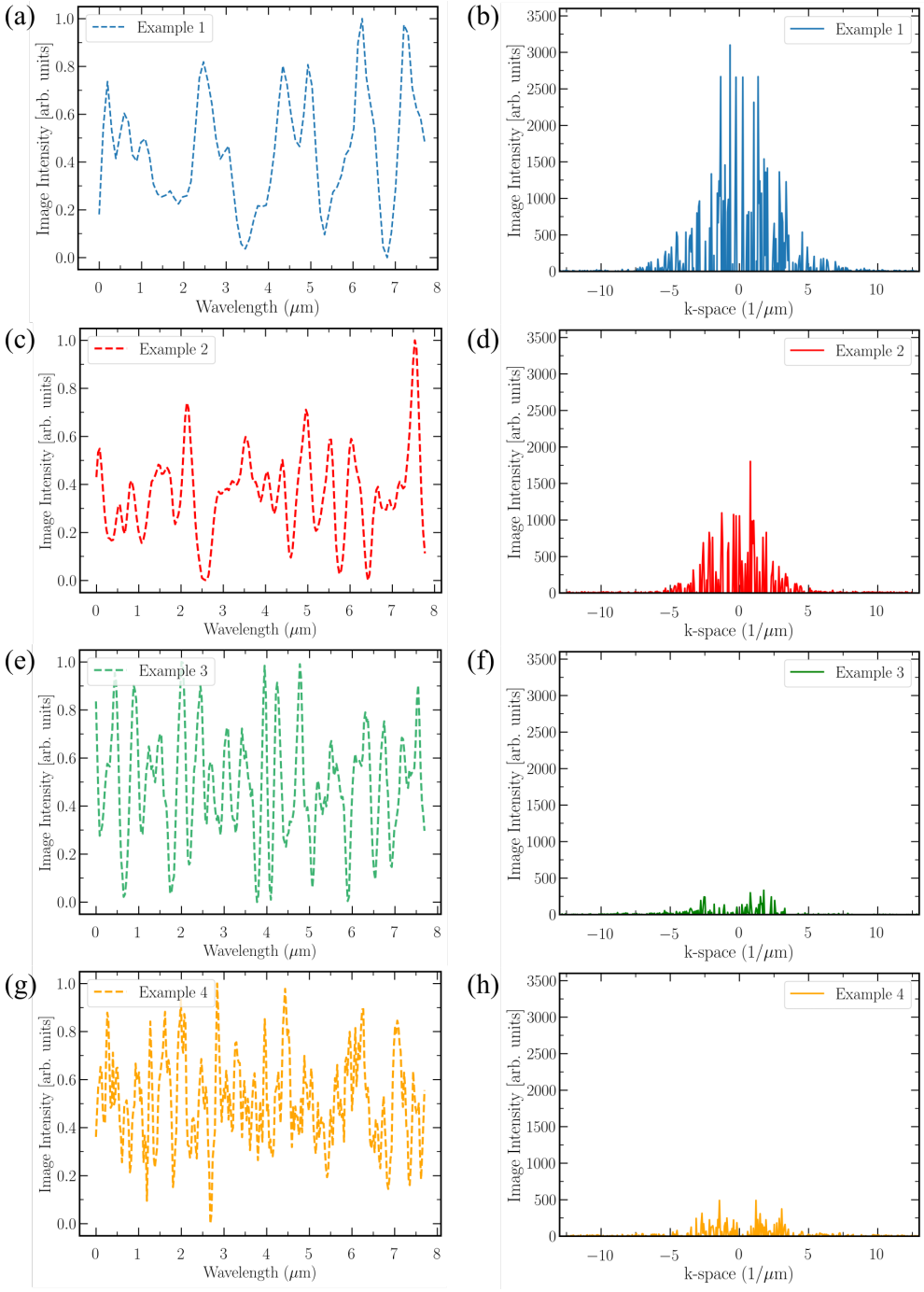

Figure 3.3: Real space ripple measurements; an integrated line profile is taken over an experimental real-space Fresnel image (a,c,e,g for Examples 1-4). Although there are observable differences between the line profiles, it is more difficult to extract one final value for ripple wavelength λ. 1D Fourier transforms of the line traces shown in Figure 3.3(b,d,f,h). Confirms the presence of a range of wavelength values in an experimental Fresnel image displaying magnetisation ripple. A weaker magnetisation ripple, as shown in (f,h) has a smaller amplitude when compared to (b,d).

3.5 2D Fast Fourier Transform

A fast Fourier transform, or FFT, is a well-known image processing technique used to decompose an image into its spatial frequency components. It can be applied to a 2D image to convert it from a spatial domain, to a spatial frequency domain. In a frequency (or Fourier) domain image, each point represents a particular spatial frequency contained in the spatial domain image.
First, a Fresnel image displaying magnetisation ripple is needed such as the example given in Figure 3.4(a) i.e. a single domain region. A fast Fourier transform (FFT) image can then be acquired, implemented in Digital Micrograph (Gatan software). [19] The 2D Fourier transform will display data in k-space against intensity I.

Figure 4.4(a) highlights the difference in a single wavelength distribution, like that of a sine wave compared to that of a distribution of magnetisation ripple components in (b). The FFT is the spectrum of the ripple, each point in k space is effectively the amplitude of that harmonic component. Therefore a FFT of a single component will result in 2 sharp peaks like that shown in (c). Magnetisation ripple has many contributions. Areas of high signal means there is a large amount of ripple with a specific characteristic wavelength value. Typical magnetisation ripple produces a 'bow-tie' structure, as shown in Figure 3.4(d). Integrated line traces can be taken over the area of interest, highlighted by the blue box. This confirms there is a single wavelength in (e) and a flat peaked distribution, representing a range of wavelengths in (f).

The bow-tie structure consists of two lobe-like features. A more detailed schematic is shown in Figure 3.5(b). There is a 2-fold symmetry associated with the structure. A number of magnetic ripple characteristics can be determined and will be described in the following paragraph.

The net orientation of the magnetisation, $\mathbf{M}$ can be determined from the mean direction of the magnetisation ripple. This is given by the direction of a line through the centre of the two symmetric lobes, shown by the red line in Figure 3.5(b). For example, this is a useful characterisation technique when determining

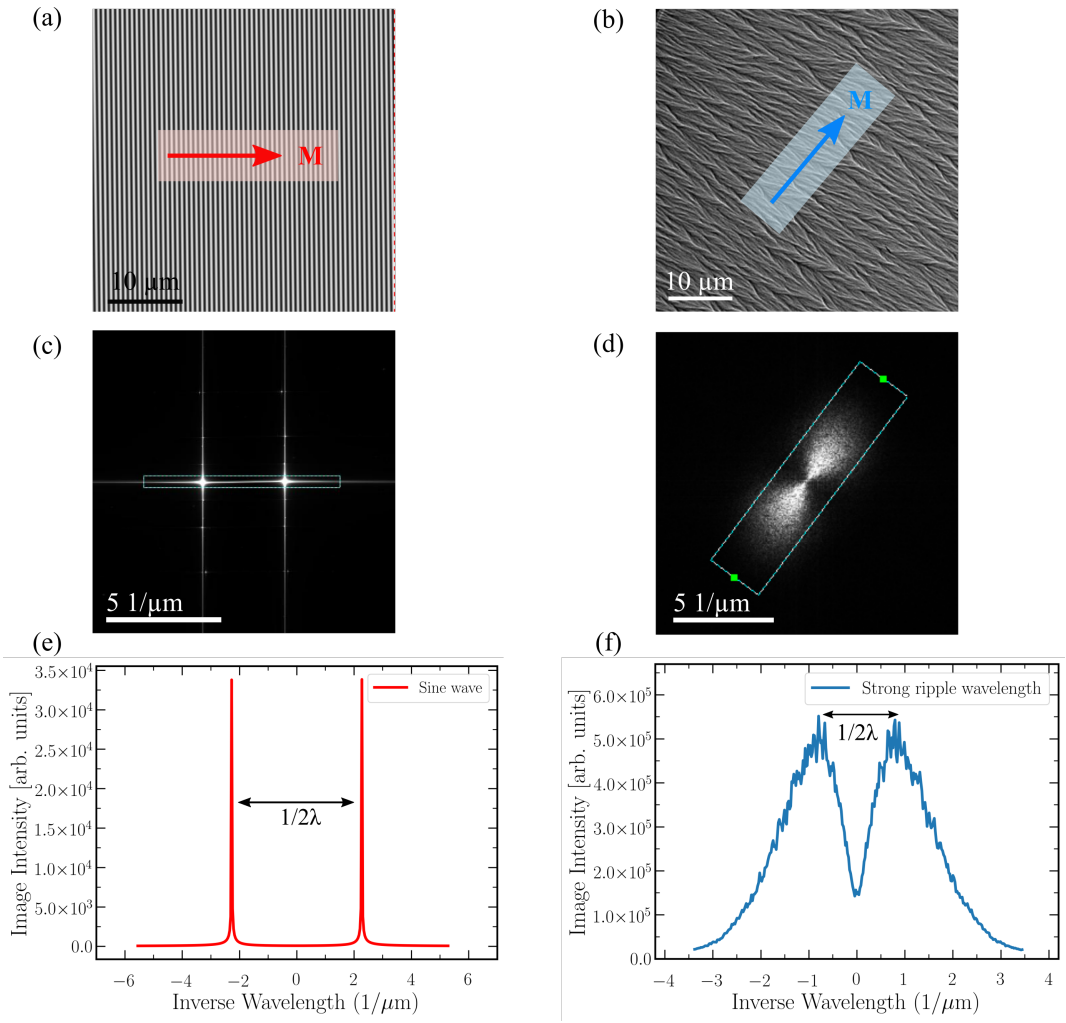

Figure 3.4: Single sine wave wavelength distribution compared to a magnetisation ripple distribution. (a) Single wavelength sine wave simulated Fresnel image, (b) Experimental 10 nm $Ni_{45}Fe_{55}$ Fresnel image displaying magnetisation ripple. (c,d) are the corresponding FFT images, where the blue box highlights the location of the integrated line profile. (e,f) show the plots of the line profiles, where the distance between the origin and either measured peak represents the inverse ripple wavelength value.

the changes of magnetisation direction in hard axis hysteresis rotation during the application of an applied field.

Secondly, Hoffmann first described magnetic ripple dispersion as the local deviation of the magnetisation from its mean direction. [21, 22] It assumed that all fluctuations of the magnetisation from its spatial average are small i.e. the sample is nearly single domain. The magnetic ripple dispersion, θ can be determined by measuring the spread of the angle of the lobes from the mean direction of magnetisation. This gives

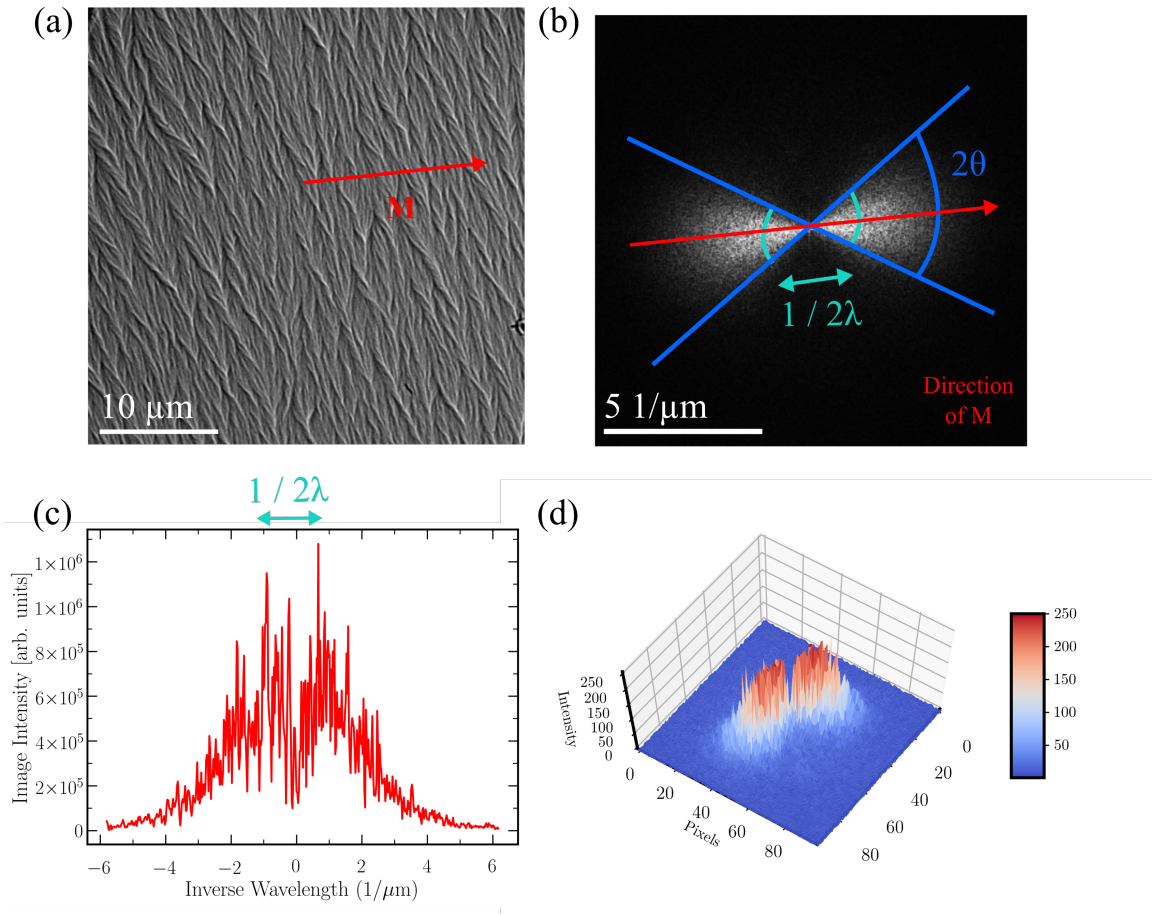

Figure 3.5: (a) Experimental Lorentz TEM image of magnetisation ripple. (b) FFT of Fresnel image produces an image in the frequency domain, commonly referred to as a 'bow-tie' structure. It can be used to determine the following ripple parameters: the direction of magnetisation **M**, the magnetic ripple dispersion angle, θ, and the ripple wavelength, λ. (c) A line profile of one pixel width can be taken through the origin of the bow-tie structure (along red arrow) to display a range of wavelength frequencies. (d) 3D surface plot of FFT structure shown in (b), highlighting the spread of frequencies present in the image.

information about the range of magnetic ripple orientations. A visual estimation of the ripple dispersion angle was made in Figure 3.5(b) and is highlighted by the angle between the 2 blue lines, 2θ. These lines can visually be defined by the region where the white FFT structure stops. Figure 3.5(d) shows a 3D representation of the FFT structure, where there is a gradually decrease in signal at the FFT edges. Therefore this visual definition is an approximation. A large increase in the angular spread is seen during the easy axis reversal processes, when an applied field is reduced from magnetisation saturation to just before the coercive field H_C. In

Section 3.6.1 the methods used by previous publications to determine the magnetic ripple dispersion will be outlined. This is followed by a discussion into an improved, and more reliable method for characterisation in Section 3.6.2.

Thirdly, a value for ripple wavelength, λ can be determined. In Hoffmann's ripple theory publication, he discussed how there would be 'one dominant periodicity' of magnetic ripple. However, when defining an equation for theory he defined the ripple wavelength value as the 'mean wavelength of the ripple along the mean direction of the magnetisation'. Fuller and Hale also interpreted the fine structure lines in terms of a 'mean wavelength'. [1]

As mentioned earlier, Herrmann produced one of the first publications to successfully quantify magnetic ripple properties from experimental TEM images. [8] He defined the ripple wavelength from the peak-to-peak intensity (or the mode value) of the frequency spectrum. It is given by the inverse distance between the origin and either point of highest intensity in each lobe. This distance can be acquired using a single line profile (Figure 3.5(c)), and the corresponding measured distance is highlighted by the green arrow in Figure 3.5(b). The ripple wavelength is inversely proportional to the distance from the origin to the intensity peaks. For example, a larger ripple wavelength will shift the intensity peak towards the centre of the image. This is not an unreasonable method of characterisation, however is limited through only using the peak intensities, rather than the full range of the spectrum shown in Figure 3.5(d). For example, the regions of peak intensities should occur at equal distances from the centre of the bow-tie structure. However in the example shown in (c), there is an asymmetry with the measurement technique. This asymmetry is a result of random noise in the image, and difficultly in determining an accurate orientation of $\mathbf{M}$ from visual inspection. This method, along with others will be described in Section 3.7, where the individual method limitations will be discussed followed by how they can be improved upon.

3.6 Dispersion Angle

In the following sections, a single experimental Fresnel image displaying strong magnetisation ripple properties will be analysed as an example. Section 3.6.1 discusses using a previous publication method produced by Hosson. Section 3.6.2 describes a new method developed as part of the this project, and for purposes of this thesis.

3.6.1 Previous Methods

As discussed previously, the dispersion angle is equal to the spread of the magnetisation from the mean direction. Hosson devised an improved method of determining a value for the ripple dispersion angle from experimental Fresnel images. [10] A schematic description of the quantification method is displayed in Figure 3.6.

The first step involves using the modulus of the FFT of an experimental Fresnel image with single domain magnetisation ripple like that shown in Figure 3.6(a). Hosson's method involves applying a radial band pass mask to the FFT image where the maximum intensity peak lies. This is illustrated in Figure 3.6(b) and (c) where a line profile is taken through the origin of the bow-tie structure, and is plotted in (c). An approximation of the first order maximum is made, i.e. the highest pixel intensity. A radial band pass mask can be applied onto the FFT, so that it contains the highest pixel intensity. This is shown in Figure 3.6(d). A definition for the appropriate width of the band pass mask was not given, but for the purposes of this example, the width equalled 50% of the full lobe length, centred around the highest intensity pixel (where the full lobe length is defined as the distance from the FFT origin through the centre of the bow-tie structure until the furthest edge.) This is followed by an azimuthal projection of the masked FFT image, giving Figure 3.6(d) as a function of azimuthal angle in Figure 3.6(e). Integrated line profiles are summed over the red box. Figure 3.6(f) shows when the profile is plotted, the ripple dispersion angle was determined by locating the angular distance where the peak intensity reduces by a root mean square value

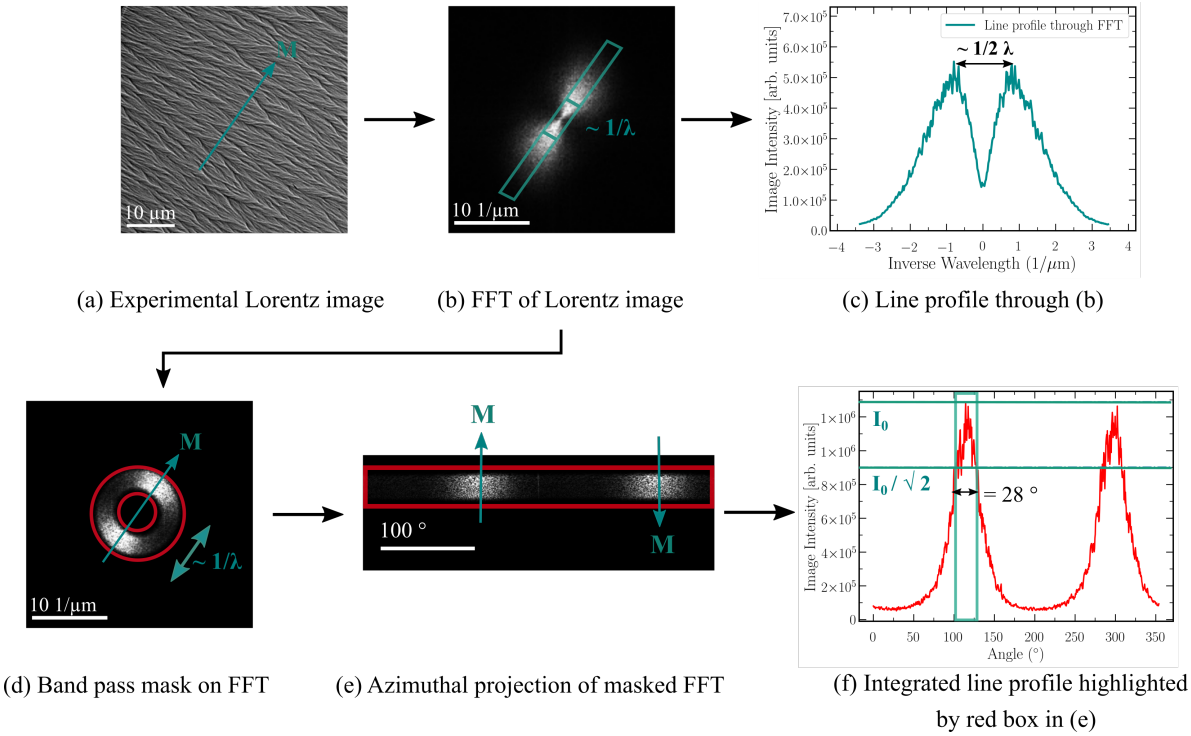

Figure 3.6: Schematic description of the quantification method in determining the dispersion angle θ of an image displaying magnetisation ripple, developed by Hosson [10]. A radial band pass mask is applied to a selected region on the FFT modulus (d) which is an estimate of the (c) dominant wavelength value (i.e. region of highest intensity), followed by an azimuthal projection of the image (e). An integrated line profile is taken in the region of interest, highlighted by the red box in (e). This is plotted in (f) as integrated intensity against angle. The FFT dispersion angle corresponds to when the peak intensity reduces to approximately 70%. The determined angle of 2 θ gave a final value of 14° ± 1.5 as the FFT dispersion angle.

$(1/\sqrt{2} \approx 70\%)$. This is an arbitrary decision as defined in the publication. This region is highlighted by the green box in (f). Using Hosson's method, a value of 28 degrees was determined as the FFT width, giving a final value of 14° ± 1.5 as the FFT dispersion angle θ for the experimental image shown in Figure 3.6(a). This measured deviation in magnetisation direction is highlighted in Figure 3.7 on both the experimental Lorentz image (a) and the corresponding FFT (b).

Having a standard percentage intensity drop is a good method of determining changes in ripple, however, this is based on the highest intensity value. This peak value may not lie centrally in the noisy distribution. Figure 3.6(f) is a good example of this, as it shows that there can be an asymmetry associated with the

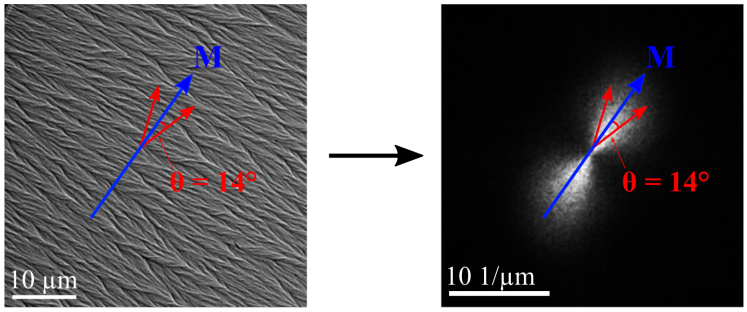

(a) Experimental Lorentz image (b) FFT of Lorentz image

Figure 3.7: (a) Experimental Fresnel image and (b) corresponding modulus of the FFT. Highlighting the determined angle of 2 θ given by the angle between the two red arrow and the direction of magnetisation **M**. This gives a final value of 14 $\pm$ 1.5 degrees as the FFT dispersion angle, when using the methodology developed by Hosson [10] and described in Figure 3.6.

peaks, if we consider the 2nd peak distribution relative to the first peak. The highest intensity value can also be much larger than the intensity values in the surrounding pixels, which will skew the profile and create an overall smaller FFT angle measurement. Even Figure 3.6(f) has a somewhat noisy profile, making the measurement of angular width more difficult to accurately determine. These factors decrease the reliability of this measurement technique. Another drawback is that this is a subjective measurement technique. The location of the dominant wavelength value and the appropriate width of the band pass mask is somewhat subjective. Additionally, by applying such a large mask to the FFT, vital information is lost about the full ripple spectrum.

3.6.2 New Method for θ determination

In this section a new method is proposed for measuring the dispersion angle θ. Unlike the method discussed earlier by Hosson, all data from the FFT modulus image will be used in the analysis process. The following process uses the Python programming language to implement the steps described. Python scripts were written and developed for the purpose of this thesis.

Figure 3.8 displays the initial steps. The first step is to take intensity profiles from the FFT of the ripple. This is shown in Fig 3.8(a). As an example, one

is taken from the centre of the FFT along the symmetry axis of the distribution (blue). The other is taken at the edge of the distribution (red). It is clear there is a significant difference in the intensity profiles, where by the intensity through the centre is much larger, as expected and shown in Figure 3.8(b).

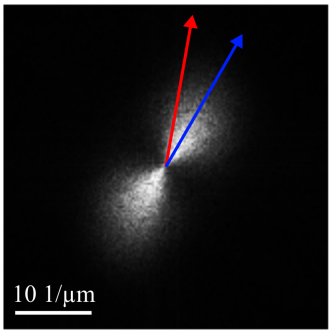

(a) Example lineprofiles taken through the bow-tie centre (blue) and edge (red)

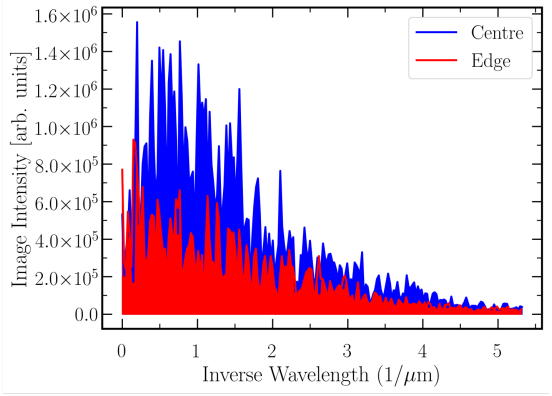

(b) Example lineprofiles are plotted demonstrating intenstiy changes

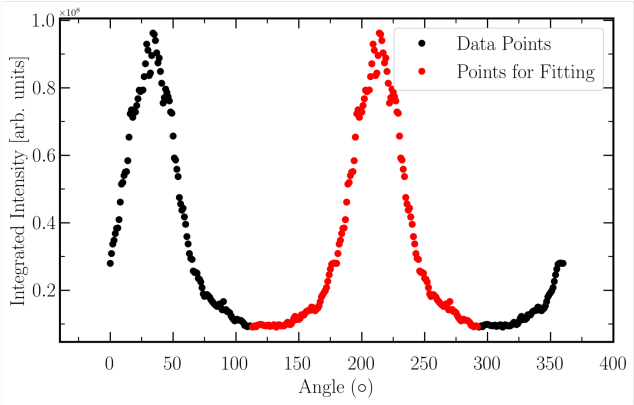

(c) Integrated intensity can be plotted against radial angle (black line)

Figure 3.8: Schematic of a proposed improvement in measuring the dispersion angle θ of magnetisation ripple. Intensity line profiles are taken from the image origin for a full 360 degree rotation. 2 line profile examples are shown in (a,b) where the blue and red lines represent profiles taken through the bow-tie centre and edge respectively. The average integrated intensity value for each profile can then be plotted as a function of angle, and is shown by the black points in (c). It is assumed that both peaks are of equal distribution. Therefore the peak with an unbroken 180 degree curve will be used for further analysis, represented by the points in red.

For full analysis the script takes intensity line profiles are taken for a full rotation of 360 degrees (2π) from the image origin. Each line profile is integrated to get the total intensity, so in the case of the two lines shown in (a) and (b) the blue

line will have a larger value than the red. This is plotted for lines at all angles as shown in Fig 3.8(c). Two peaks are generated, which represent the two symmetric lobes on the FFT. It is assumed that the 2 peaks will be symmetric and equal (as there is no misalignment error like described earlier), so only one will be used for further analysis purposes. This is highlighted in Figure 3.8(c) where the red dots represent the region used in any further analysis. There are 360 dots in total to represent the 360 degrees, with equal angle spacing of one degree.

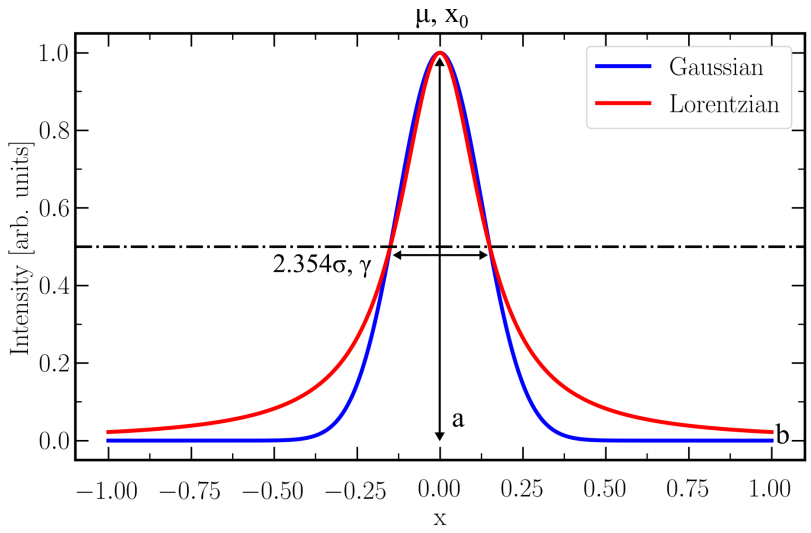

Figure 3.9: Comparison of Gaussian (blue) and Lorentzian (red) standardised distributions, where they both feature the same full-width half maximum (FWHM). Lorentzian peak tails are typically wider than that of Gaussian's. Key points of both distributions are highlighted, which are used in Equations 3.1 and 3.2.

The angle associated with the distribution of the peak can give information on the spread of the magnetic ripple orientation. The desired quantitative output is the full-width half maximum (FWHM) of the peak. However, when using the unfitted data, and using the largest intensity point as the centre of the peak, it can lead to an associated asymmetry when measuring the LHS and RHS of the FWHM from the mode peak. A way to improve the data set is to use either a Gaussian or Lorentzian curve fitting technique with typical examples shown in Figure 3.9. The equations of the Gaussian $I_G(\theta)$ and Lorentzian $I_L(\theta)$ functions used are as follows:

$$I_G(\theta) = a \exp \frac{-(x-\mu)^2}{2\sigma^2} + b \tag{3.1}$$

where a is the amplitude, b is the offset (in this case equal to zero), σ is the standard deviation and μ is the mean of the distribution.

$$I_L(\theta) = \frac{a\gamma^2}{\gamma^2 + (x - x_0)^2} + b \tag{3.2}$$

where a is the amplitude, b is a constant, γ and x_0 is the width and the centre of the distribution.

The Gaussian and Lorentzian curves plotted in Figure 3.9 show these formulae with μ and x_0 equal to zero, as is b. The FWHM of these functions, given by $2.345 \times \sigma$ and γ, are both equal and represent the distance of the curve when the intensity drops by 50%. These 2 values are the key parameters for characterisation of ripple dispersion.

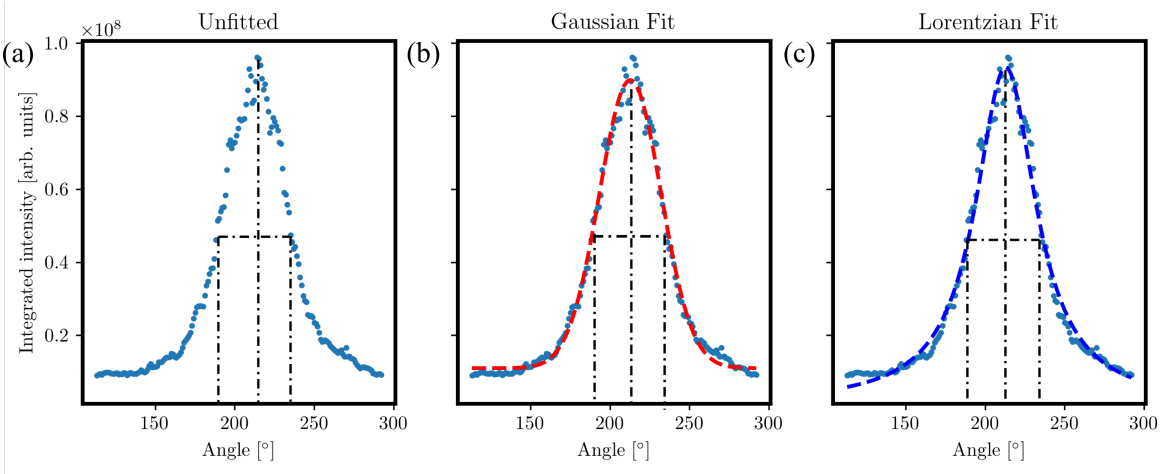

Figure 3.10: Figure demonstrating three different methods of determining the dispersion angle of a FFT image. All methods determine the FWHM as the dispersion angle value. The first option (a) is to use the raw integrated intensity values. An improved solution is to fit a best fit curve, using either a (b) Gaussian or (c) Lorentzian fit.

The best fit peak also gives an associated angle for the mean direction of magnetisation θ_M, which is useful for mapping hard axis reversal behaviour. A comparison of outputs for the different FWHM determination techniques is summarised in Table 3.2. All three methods are in good agreement with a variation of as little as half a degree.

Analysis OutPuts	Unfitted	Gaussian	Lorentzian
Dispersion θ (°)	23 ± 1.0	22.9 ± 0.5	23.1 ± 0.5
M angle θ_M (°)	214 ± 1.0	212.7 ± 0.5	212.8 ± 0.5

Table 3.2: Comparison of techniques for magnetisation ripple dispersion angle and direction of magnetisation determination.

Residual plots are a method of visualising how much a best-fit line vertically misses a data point. These are shown for the Gaussian and Lorentzian fits in Figure 3.11(a) and (b) respectively. The averaged residual value for the Gaussian plot was in fact smaller than that of the Lorentzian, meaning it had a slightly overall better fit to the raw data. Figure 3.9 shows that both fitting methods produce good and reliable results and both could be used for successful analysis in upcoming sections. However, the Lorentzian had a better fit at the region of interest (the peak). Therefore, for the following results Chapters (4,5,6), the Lorentzian fit method was selected for determining the dispersion angle θ and direction of **M** θ_M, however either option would work well.

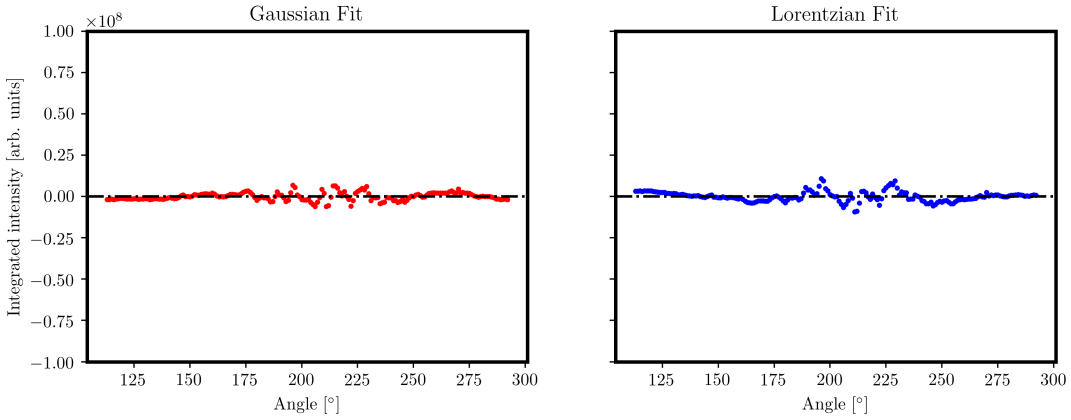

Figure 3.11: Data point residuals for the (a) Gaussian and (b) Lorentzian fit, highlighted in red and blue respectively. They represent a measure of how much a best fit-line misses the raw data point. Both fits produce small residual values, confirming both methods produce reliable fitting.

3.6.3 Discussion

A comparison can be made of the measured dispersion angle θ values using the methodologies described. Hosson's method measured the dispersion angle at a 70% drop of intensity, compared to the new method which measures the corresponding angle at the FWMH i.e. 50%. For the purposes of method comparison, all measurements were taken at a drop of 50% intensity. The Hosson method and the new developed method were used on all 4 example images previously shown in Figure 3.2, as all images have varying amounts of magnetisation ripple present. The outputs for both methods are shown in Table 3.3. Both methods are in good agreement. The main difference in the two methods is the consistency of each measurement. As previously mentioned, Hosson's method is a subjective measurement technique. Additionally, by applying such large mask to the FFT structure, information will be lost. The steps described for the new method can be automated, so there is no bias in the analysis technique. It also proves to be a more accurate measurement, mostly due to the lack of human biasing and measurement errors. Hosson's method is a viable option for an estimation of the dispersion angle. However when analysing a large amount of experimental (or simulated) Fresnel images, the new method will produce quicker, and more precise outputs.

Example Image	Hosson Method (°)	New Method (°)
1	32 ± 1.5	37.5 ± 0.5
2	21 ± 1.5	23.1 ± 0.5
3	13 ± 1.5	12.2 ± 0.5
4	14 ± 1.5	14.0 ± 0.5

Table 3.3: Comparison of previous techniques developed by Hosson and a new proposed methodology for magnetisation ripple dispersion angle determination.

3.7 Dominant Ripple Wavelength

In the following Section 3.7.1, previous published methods are discussed for determining dominant ripple wavelength value. For this section, two example Fresnel

images with varying magnetisation ripple will be used, to discuss the breakdown of previous methods with weaker ripple properties. This is followed by Section 3.7.2, where a proposed new method for determining the dominant wavelength through curve fitting is presented, which will be referred to as λ_{Dom}. This methodology will be discussed for experimental images of both strong and weak ripple properties. A new additional characterisation parameter of integrated intensity I is introduced in Section 3.7.3. This is particularly useful for mapping variations in Fresnel TEM image contrast when taking a sample through a hysteresis sequence.

3.7.1 Previous Methods

Important ripple characteristic length scales are the mean, dominant and the deviation of the ripple wavelength.

The inverse spatial frequency with the maximum intensity (or the mode value) can be found in Fourier space by measuring the distance between pixels of highest intensity and the FFT origin. This method has been seen as the standard, and most widely used parameter in publications involving magnetic ripple characterisation. However, although the original theoretical paper discussed in Section 1.7 acknowledges that there is usually a dominant wavelength value, the *mean or average* wavelength value is used for the theoretical derivation of the ripple wavelength λ. The asymmetric distribution of the spatial frequency spectrum means the mode value (which represents the dominant λ) will be different from the mean, where the dominant wavelength value is usually significantly larger than the mean. This is due to the mean including all lower frequencies in the spectrum. The dominant wavelength refers to just one value. Methods for determining the dominant ripple wavelength λ_{Dom} value will be discussed below, with an explanation into how these methods can be improved upon.

The idea of using a rotational average method for accurate determination of the dominant ripple wavelength λ_{Dom} was first used by Hosson in 2002. [10] Another method used in several other publications to obtain this value involves taking an

integrated intensity line profile over a region limited to the bow-tie structure. [16,17] Both methods are outlined and compared in Figure 3.10 when used on experimental Fresnel images displaying (a) strong and (b) weak magnetic ripple wavelength properties. These methods will be discussed in detail below.

Hosson's method consists of taking a rotational average (360 degrees) of the modulus of the FFT. A single pixel width line profile can then be taken in any direction from the image origin (e,f). This will result in a plot of image intensity against k-space distance, where the distance from 0 to the first order maximum is equal to $1/\lambda$. This method works well with images displaying larger ripple wavelengths, giving rise to higher contrast, as demonstrated in Figure 3.12(i). However, when the ripple is weak, the dominant wavelength peak becomes harder to determine due to reduced contrast variation, as highlighted by the red line plot. Additionally, the rotational averaging effect leads to a lack of area specific information. It includes a large amount of unnecessary background noise which makes the changes in contrast within the area of interest, i.e. the bow-tie structure, less prominent and therefore more difficult to measure.

Another common dominant ripple wavelength λ_{Dom} characterisation method is outlined in Figure 3.12(g,h), originating from a University of Glasgow publication [15]. It involves similar steps to Hosson's method, but rather than taking a rotational average of the FFT, it involves taking a line profile through the centre of the bow-tie structure, and integrating over a selected area that is larger than the full width of the structure (the width of the integration is variable on the spread of the FFT). The corresponding line profiles for both strong and weak ripple wavelengths are plotted in (j).

This produces plots of integrated intensity against k-space. The measured distance between the two highest intensity points is measured, which is equal to $1/2\lambda$. Line profile plots are shown in Figure 3.12(h), for both strong and weak ripple wavelength properties respectively. This proved to be a successful characterisation

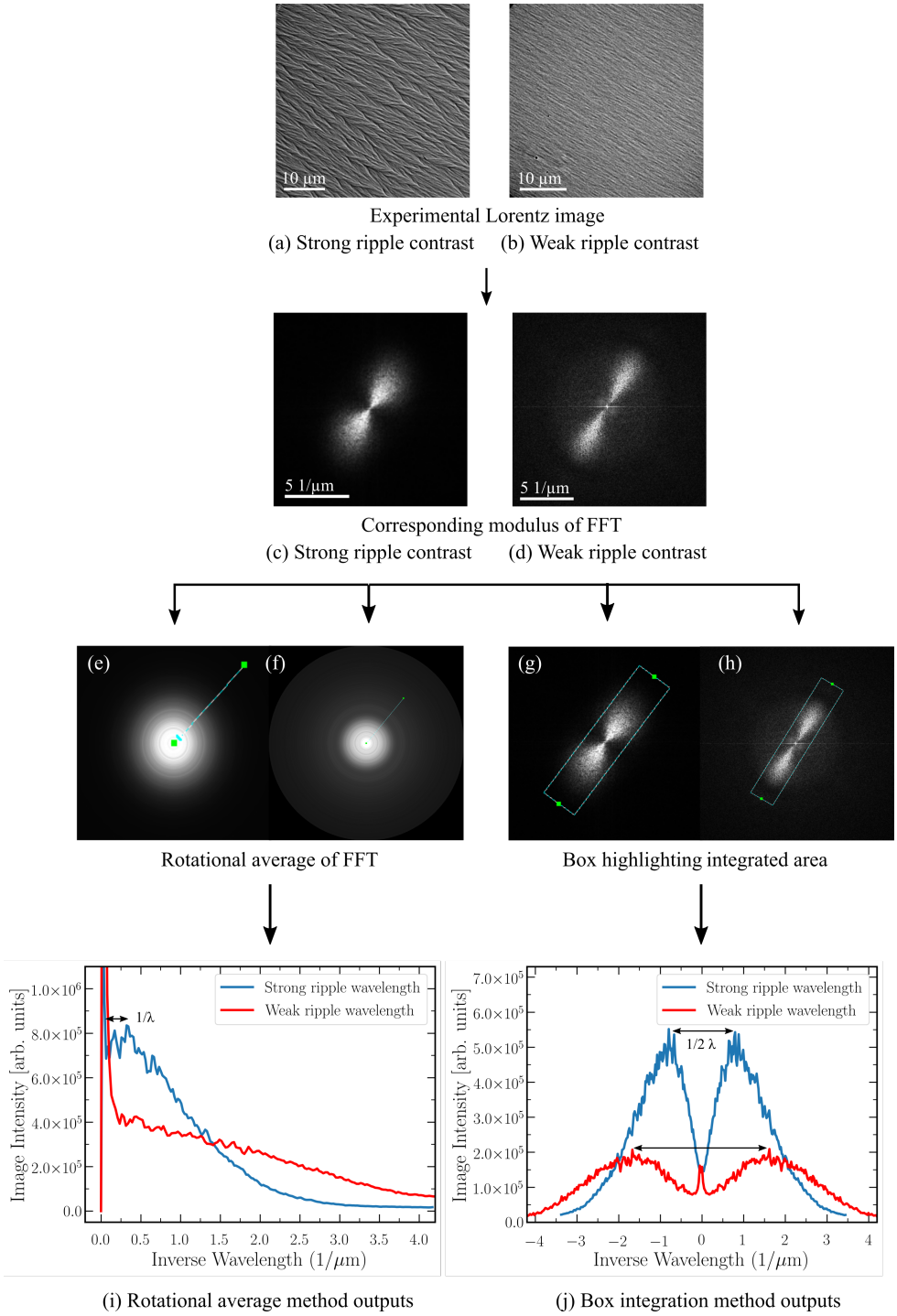

Figure 3.12: Schematic of previous methods used in determining the dominant ripple wavelength from the FFT modulus data of an experimental 10 nm $Ni_{45}Fe_{55}$ single domain Fresnel image displaying (a) strong and (b) weak magnetic ripple characteristics and corresponding FFTs. The first method (e,f) is to take a rotational average of the FFT (around 2π)and take a single pixel width line profile from the origin, measuring the Fourier distance from the origin to the peak. The second method (g,h) is to choose a large integrated intensity area, which covers the full FFT and measure the Fourier space distance between the peaks. The corresponding line profiles are plotted in (i,j). The rotational average method becomes less effective with weaker ripple wavelength λ, unlike that of large integrated area.

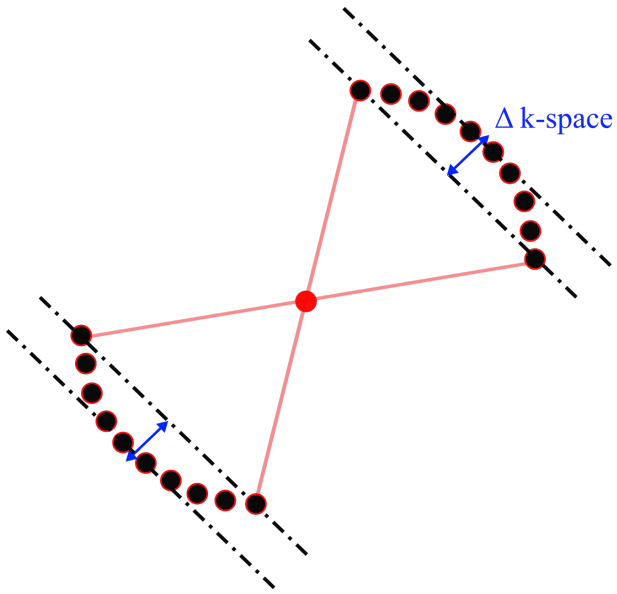

Figure 3.13: Box integration methods of dominant ripple wavelength determination have an associated error with the final output. The integration area doesn't take into consideration that the ripple wavelength varies radially. This will create an error in the k-space measurement, Δ k-space.

method for both variations of ripple properties, unlike that of Hosson's which struggled with weaker ripple.

The bow-tie structure is lobed, and the intensities can partially vary radially from the origin . This means when using a simple average integration technique, in this case in the shape of a rectangle, it comes with an associated error range.

A simplified schematic is shown in Figure 3.13, which denotes a ripple structure which is truly radial. We assume all the black dots lie at equal distances from the origin, but in varying orientations. It is important to note that this is an exaggerated effect. Although there is some radial variation, there is no basis to suggest that the structure is fully radial. When integrating over a box as shown in Figure 3.12(f), the intensities will be averaged creating an associated error range in k-space. The effect of this can be investigated using simple geometry rules and the results are presented in Figure 3.14. As expected, an increase in the dispersion angle increases the measurement error range in k-space. Similarly, if the distance between the highest intensity peak increases, so does the measurement range error. As previously discussed, this measurement range error is only valid if the distribution

is truly radial. In reality, there will only be partial radial effect,therefore the use of a rectangle integration will be less than the quantities seen in Figure 3.14.

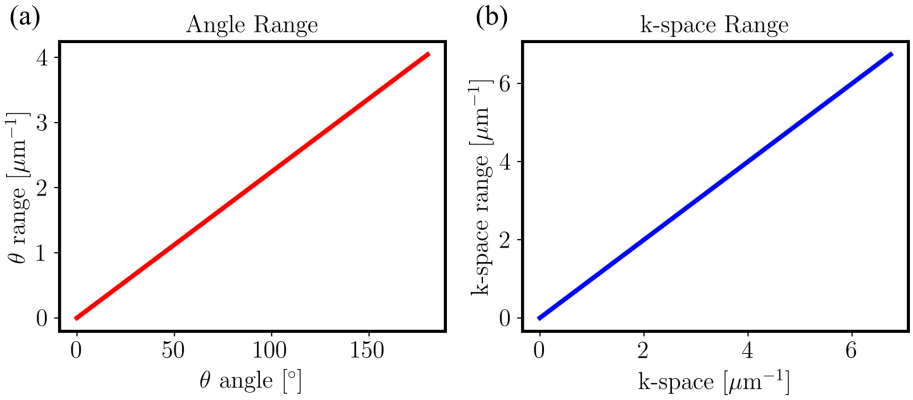

Figure 3.14: The associated range error with dominant ripple wavelength can be plotted as a function of (a) increasing dispersion angle and (b) increasing ripple wavelength. The error is directly proportional to the angle and wavelength.

Discussion

Table 3.4 shows a comparison of the outputs for dominant ripple wavelength determination. This includes taking a single line profile through the origin of the FFT, like the example shown in Figure 3.5(c), and the two methods described (rotational average and box integration.

It is clear that the rotational average method is completely inconsistent for both strong and weak ripple properties when compared to the other two methods. Both the single line trace and box integration are in good agreement with each other. This would be as expected. By integrating a line profile over a defined area, it has the effect of averaging the data, resulting in the measurement error being reduced, as highlighted in Table 3.4.

There is an order of magnitude increase when using the rotational average method compared to the other methods. A ripple wavelength value that is larger than a micron is usually only found when imaging along the easy axis and very close to the coercive field i.e. where the ripple properties would be largest. The rotational average method also completely breaks down when measuring smaller

wavelengths, demonstrated in Figure 3.12(i). It can therefore be assumed that for the experimental images used in this body of work, the rotational average wavelength values would not be reliable. A quick real-space wavelength approximation can be made, which confirms that a wavelength value larger than a micron, for both the strong ripple and weak ripple cases, would not be correct. The box integration method produces much more sensible outputs and works successfully for both strong and weak ripple, as shown in Figure 3.12(j).

However, as described previously, and highlighted in Figure 3.13 and 3.14, there is some discrepancy when using a box integration for a bow-tie FFT structure which displays radial variations. An improvement to this would be creating a methodology that uses the most successful aspects of the methods discussed here. It is proposed that using a rotational average over a limited angular range (specifically the dispersion angle) could yield a more accurate determination of the dominant ripple wavelength. A method has been devised and will be discussed in the following section.

Method Outputs	Strong ripple λ_{Dom}	Weak ripple λ_{Dom}
Single line trace (μm)	1.2 ± 0.1	0.6 ± 0.1
Box Integration (μm)	1.24 ± 0.03	0.60 ± 0.03
Rotational Average (μm)	3.0 ± 0.1	2.4 ± 0.2

Table 3.4: Comparison of outputs for dominant ripple wavelength determination λ_{Dom} using previously used analysis techniques.

3.7.2 New Method: λ_{Dom}

An improvement to both methods described in the previous section is proposed. Rather than rotationally averaging the full FFT image like the Hosson method, a partial rotational average can be used over a limited angular range, followed by a radial integration. Using the information gathered from the previous ripple dispersion analysis, the FFT cone with the corresponding measured dispersion angle, can be defined as the sole area being used to find the dominant wavelength value. Then a partial integration technique can be used, as highlighted in Figure 3.15.

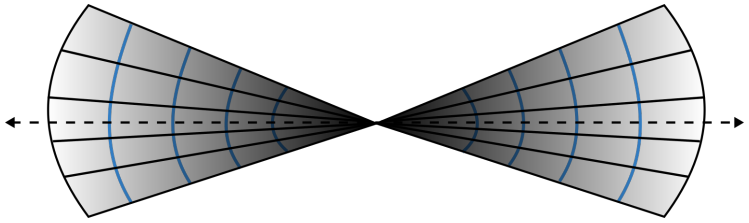

Figure 3.15: A solution to the error is to calculate the average radial integration of the bow-tie structure. The blue lines indicate the radial lines of integration, usually over a distance of 1 pixel. The intensities that lie along these lines are summed and averaged. These values can be plotted against distance from the origin.

This process includes integrating radially, by a width of a pixel, specifically in the region previously determined by the dispersion angle i.e. a limited angular range. This eliminates the discrepancy associated with measuring the distance of the peak from the origin. The blue lines indicate the radial lines of integration, usually over a distance of 1 pixel. The intensities that lie along these lines are summed and averaged. These values can be plotted against distance from the origin.

These values can be plotted against distance from the origin, i.e. plot the radial averaged integrated intensity against k-space and are shown in Figure 3.16. The area of interest is solely the dominant value i.e. the mode value, so the data set is cropped remove data points outside of the bow-tie structure. Three different data sets can be used from our dispersion angle determination discussed previously: Raw data points, Gaussian and Lorentzian i.e. The dispersion angle value determines the region used for the partial rotational average, with the value shown in Table 3.3. Therefore there will be some variation, although small (< 1.5 degrees), in the plots shown in Figure 3.16.

A Gaussian distribution function (Equation 3.1) can then be applied to the raw averaged radial integration data. This figure displays how successful the fitting is to the raw data, even with weak ripple properties. This method doesn't breakdown unlike that of previous methods described. The peak of the Gaussian fit can be extracted with an associated error, the results of which are compared in Table 3.4. Even though 3 different dispersion angles were used to determine a final dominant wavelength λ_{Dom} value, there is a variation of less than 2% between

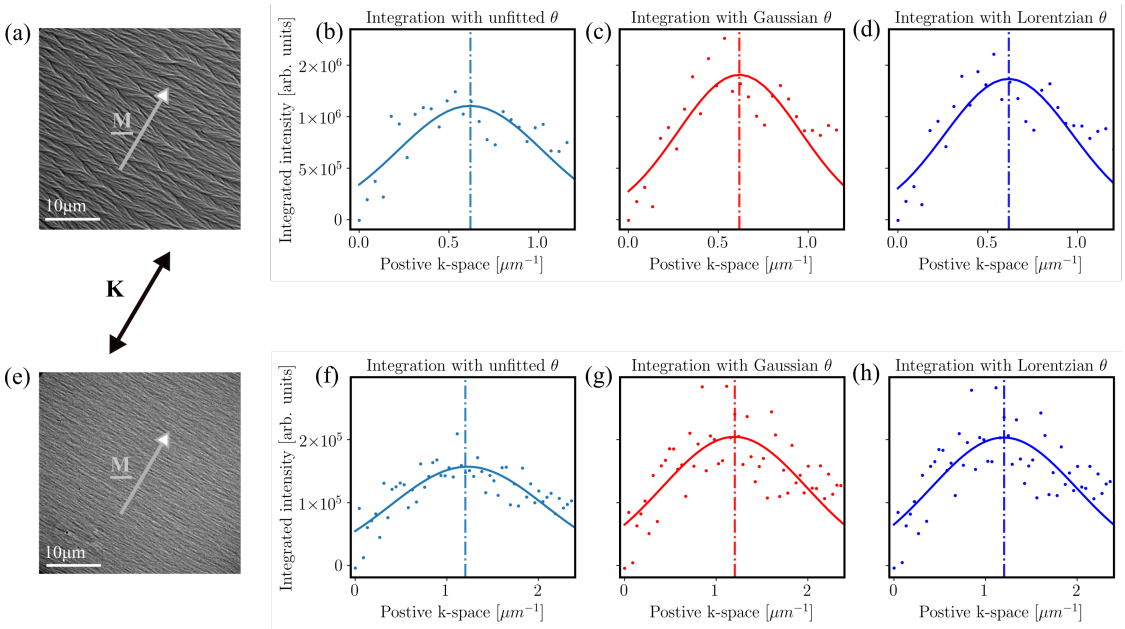

Figure 3.16: Schematic of dominant ripple wavelength plots. (a) and (e) are example experimental Fresnel images displaying strong and weak ripple properties respectively. The radial integrated intensity is plotted against k-space distance. A Gaussian distribution be fitted to the data, where the peak corresponds to the dominant ripple wavelength value. (b,f), (c,g), (d,h) represented the raw, Gaussian or Lorentzian dispersion angle integration points respectively, described in the previous section. The results are summarised in Table 3.4.

the three methods when measuring weak ripple properties, meaning we can be confident in the final output results.

Analysis Outputs	Unfitted	Gaussian	Lorentzian
Strong ripple λ_{Dom} (μm)	1.62 ± 0.02	1.62 ± 0.02	1.62 ± 0.02
Weak ripple λ_{Dom} (μm)	0.82 ± 0.02	0.84 ± 0.02	0.84 ± 0.02

Table 3.5: Outputs for dominant ripple wavelength determination λ_{Dom} using the newly proposed analysis methodology.

Discussion

Table 3.6 summarises the outputs of dominant ripple wavelength λ_{Dom} using the 3 different methods discussed in this section; a rotational average, a box integration, and an improved proposal of a partial rotational average.

As discussed earlier, the full rotational average method does not produce an accurate determination of the dominant ripple values. It also fails when characterising images displaying weak magnetic ripple properties, such as Figure 3.12(i). Due to these reasons, the rotational average outputs are not a good representation of ripple wavelength.

The outputs for the proposed method and the box integration method are in better agreement with the expected output. However, there is a still a variation of nearly 400 nm between both methods for the strong ripple case. The partial rotation methods yields results which are quite larger than the box method. This difference arises from the range of data which is being used. The box integration method uses more signal from lower spatial frequencies, and more noise from regions outside the lobes. The partial integration techniques removes significantly more of these lower spatial frequencies. Therefore, the weighting of spatial frequencies is therefore different in these methods. Each method represents different distribution of the intensities in the FFT. No distribution will have a very clear peak (like the example sine wave in Figure 3.4(e), so it makes sense for each method to give a different answer. Another difference could be attributed to the box integration method being a manual technique based on direct visualisation of the FFT image. The associated error with the measurement also has to be considered. The partial rotational average technique process has been developed and automated to reduce the measurement error.

	Method	Strong Ripple λ_{Dom} (μm)	Weak Ripple λ_{Dom} (μm)
New	Partial Rotational Average	1.62 ± 0.02	0.84 ± 0.02
Old	Rotational Average	3.0 ± 0.1	2.4 ± 0.2
	Box Integration	1.24 ± 0.03	0.60 ± 0.03

Table 3.6: Comparison of old and new techniques for dominant magnetic ripple wavelength λ_{Dom} determination.

3.7.3 New Method: Reciprocal Space Image Intensity Variation *I*

A second output can be extracted from the graphs shown in Figure 3.16. It shows the peak of a curve, which when measured along the x-axis represents the dominant ripple wavelength. However, the height of these curves, i.e. the integrated intensity along the y-axis, changes with ripple properties. As ripple properties increase, such as wavelength and dispersion, this leads to a higher integrated intensity value. This change in intensity is particularly useful for the mapping of ripple contrast variation as a function of field. For example, the image intensity will be lessened towards magnetisation saturation due to a reduction in magnetisation ripple, and therefore image contrast, when directly compared to images at remanence. This method of characterisation involves measuring the changes in the dominant wavelength peak height (i.e. integrated intensity) as a function of field.

The physical output values measured from this characterisation method are not meaningful in isolation. This method is useful when being used in conjunction with other characterisation methods described, such as dispersion angle and dominant ripple wavelength. It allows for the visualisation of trends in the variation in ripple properties throughout a hysteresis sequence. This should follow the same trend as other characterisation methods. This will be studied in greater detail in Section 3.10.2, when it is used on 5 examples images during an easy axis hysteresis sequence.

3.8 New Method: Spectroid Wavelength

When Hoffmann proposed his theory for magnetisation ripple wavelength, he acknowledged that the ripple would be made up of a broad range of wavelengths, and therefore defined the ripple wavelength as the 'mean' value. However, as any approximation of experimental ripple wavelength would have been evidenced through real-space measurements at this time, it follows that this 'mean' value was more than likely the dominant ripple value. As mentioned previously, the spectrum of values can consist of lots of low frequency components. When the true *mean*

wavelength value was determined for Figure 3.17(a), it gave an output of 306 nm for the full FFT image, or 424 nm when just using the area of the lobes as determined by the dispersion angle. These values are considerably lower than other wavelength characterisation outputs, that instead look for the dominant wavelength value λ_{Dom}.

Here, an alternative method of determining a value for the specimens *mean* ripple wavelength has been developed and proposed for the purposes of this thesis. The spectral centroid, commonly referred to as a spectroid, is a measure used to characterise a spectrum. It indicates where the centre of mass of the spectrum is located. It is calculated as the weighted mean of the frequencies present in the signal, determined using a Fourier transform, with their magnitudes as the weights. In this case, the spectrum consists of a range of magnetic ripple wavelengths. The spectroid of the spectrum is measured through relative intensities and their distances in k-space. It can be written as:

$$\lambda_{Spectroid} = \frac{\sum k \cdot I(k)}{\sum (I)k} \tag{3.3}$$

where *I(k)* represents the weighted frequency value and k represents the centre frequency of that bin.

The same raw radial integrated intensity plots acquired for the dominant ripple wavelength analysis are used in this method (Figure 3.16) for determining the wavelength spectral centroid. The difference here is that the data set is not cropped around the peak, but all intensity points within the radial integration area are used. Note that the partial rotational average area was used, similar to the dominant wavelength determination. This ensures that lots of additional low-frequency components won't be included in the measurement, which would act to decrease the final ripple output significantly. These plots are shown in Figure 3.17.

The spectroid wavelength will differ from dominant ripple wavelength value. This is expected as it tells us information about where the centre of mass of the ripple spectrum is present, rather than the highest integrated intensity value. The spectroid wavelength is highlighted by the bold vertical lines in Figure 3.17, where all 3 varying

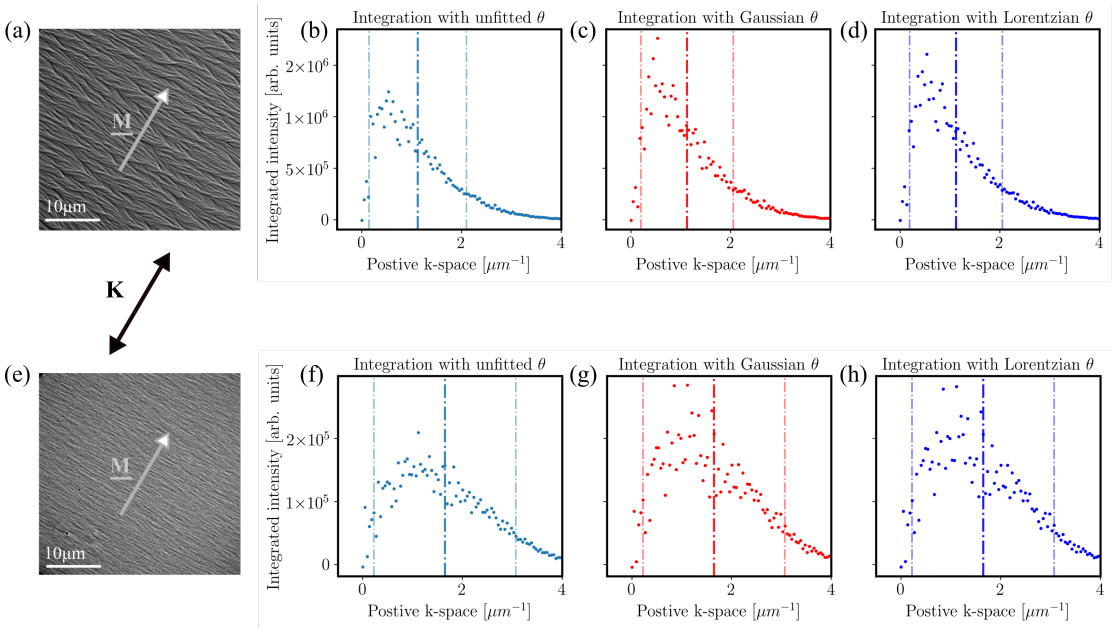

Figure 3.17: Schematic of dominant ripple wavelength plots. (a) and (e) are example experimental Fresnel images displaying strong and weak ripple properties respectively. An alternative method to determine a value for ripple wavelength is to determine the spectral centroid of the FFT, also refers to as the weighted centre of mass $\lambda_{Spectroid}$. This value is highlighted by the bold vertical line. The corresponding standard deviation σ, is shown on either side.

integration areas are in good agreement. The spectral standard deviation, σ, can also be acquired, which tells us about the spread of the ripple wavelength values. This value is highlighted on Figure 3.17 by the lines on either side of the spectroid value.

Discussion

Outputs are summarised in Table 3.7. There is good agreement in all 3 plots for both the spectral centroid ($\approx 1\%$ deviation) and spectral standard deviation values ($\approx 5\%$) for both strong and weak ripple properties. All 3 analysis techniques could be used, but for the purposes of this project, the Lorentzian fitting methods will be used for the results presented in the following results chapters.

The spectroid wavelength is proposed as an additional method of determining a single quantitative output for a samples magnetisation ripple value, along with the dominant wavelength value. As shown in Figure 3.5(d), the distribution of the intensities present in the FFT can vary greatly from case to case. A weighted

Analysis Outputs	Unfitted	Gaussian	Lorentzian
Strong ripple $\lambda_{Spectroid}$ (μm)	0.90 ± 0.01	0.88 ± 0.01	0.90 ± 0.01
Strong ripple σ (μm)	1.02 ± 0.01	1.08 ± 0.01	1.08 ± 0.01
Weak ripple $\lambda_{Spectroid}$ (μm)	0.60 ± 0.01	0.60 ± 0.01	0.60 ± 0.01
Weak ripple σ (μm)	0.66 ± 0.01	0.72 ± 0.01	0.70 ± 0.01

Table 3.7: Comparison of results for fitted and unfitted spectroid ripple wavelength $\lambda_{Spectroid}$ determination.

average favours using all ripple wavelength values present in the image, rather than concentrating on one dominant value. It provides values that tell us information about the full intensity distribution in the FFT structure.

Both methods are viable options of characterising ripple properties and are best used in conjunction with each other. The dominant wavelength gives information solely on the mode peak wavelength, and the spectroid tells us more about the wavelength distribution. Both methods will be used as characterisation methods in the following results Chapters 4, 5 and 6.

3.9 Ripple Wavelength Method Comparison

A comparison can be made of the outputs from different wavelength determination methods, focusing only on 1 example image for simplicity. The outputs for the example image displaying strong ripple properties are shown in Table 3.8.

As discussed in Section 3.7.1, is clear that the rotational average method does not produce sensible outputs. An estimate in real-space tells us that the dominant ripple wavelength will lie under 1 μm. This method produces a wavelength value that is significantly larger than the real space measurement. This is reiterated when both box integration and λ_{Dom} methods produce outputs much closer to the real-space approximation.

It is important to note that there is almost a 50% difference in wavelength when using the dominant wavelength method when compared to the spectroid method.

This is expected as the spectroid factors in all the smaller wavelength frequencies within the bow-tie structure from the Fourier transform. As this is a new technique, measuring the distribution of the wavelength spectrum, rather than the dominant value, the values obtained for this can not be directly compared to other methods which aim to identify the mode peak.

Ultimately, all methods other than the rotational average method can be used for determining a final output. However, in thin films with a more pronounced uniaxial anisotropy, the ripple properties will be more suppressed and there will be a much smaller variation across the film. More suppressed ripple increases the associated measurement error when using the box integration method, therefore highlighting a disadvantage of this method. The new methods developed in this body of work for acquiring values for dominant wavelength λ_{Dom} and weighted wavelength $\lambda_{Spectroid}$ reduces the human bias and measurement error when acquiring outputs. When these methods are used in conjunction, it allows for an insight into both the dominant ripple wavelength, and an insight into the wavelength distribution through the spectroid measurements. For this reason, these methods will be used for ripple characterisation in all following results chapters.

	Method	Wavelength Output (μm)
Old	Rotational Average	3.0 ± 0.1
	Box Integration	1.24 ± 0.03
New	Partial Rotational Average	1.62 ± 0.02
New	$\lambda_{Spectroid}$	0.9 ± 0.01

Table 3.8: Ripple wavelength method comparison. This table compares old methods and new methods, of dominant λ_{Dom} and $\lambda_{Spectroid}$ outputs.

3.10 Hysteresis Mapping

Hysteresis mapping can be undertaken by analysing images in a range of applied fields, throughout a hysteresis sequence. Example images were chosen which correspond to an easy axis hysteresis with a reducing field, displaying strong ripple properties.

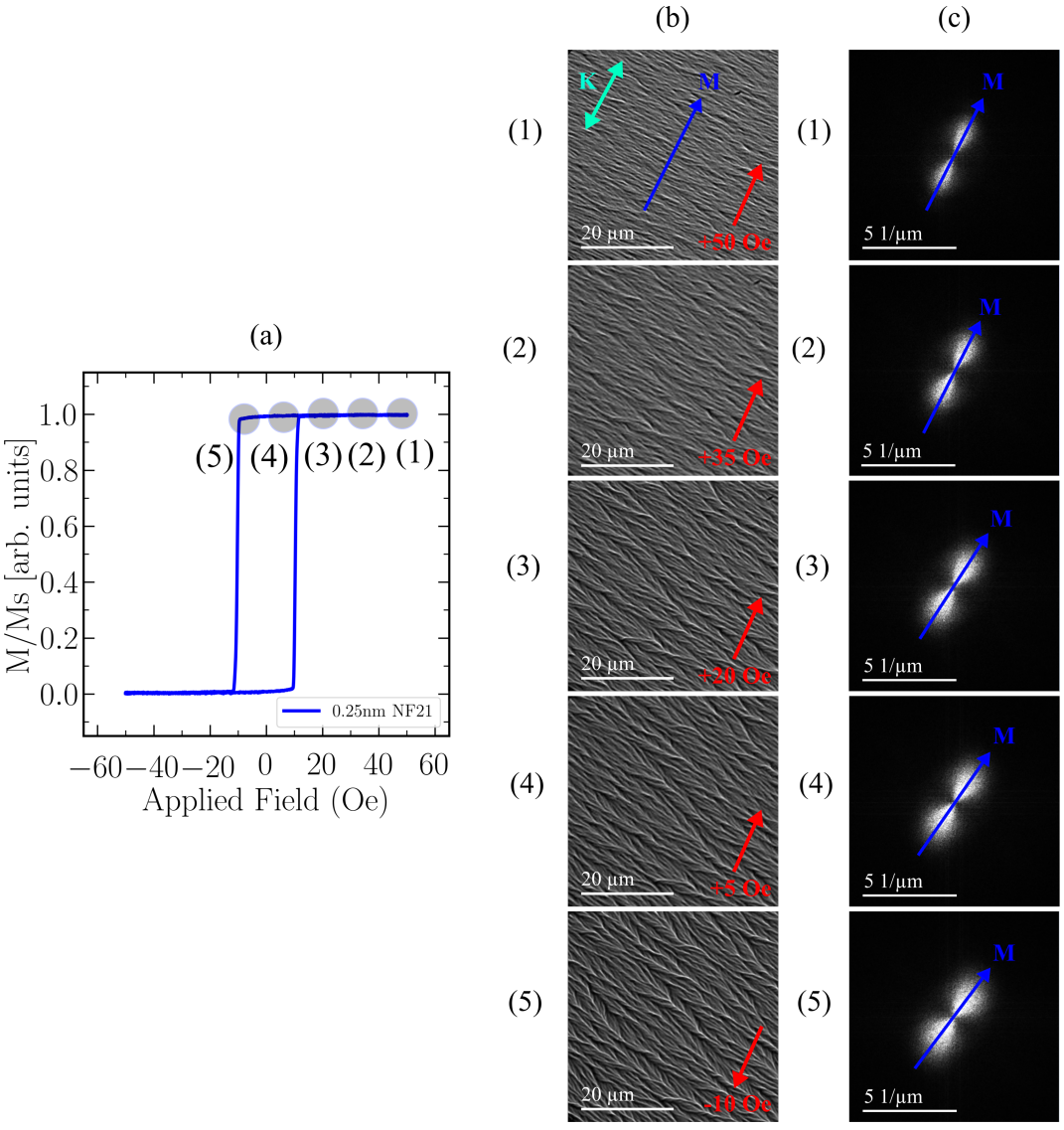

Figure 3.18: Schematic displaying the variation in FFT intensity with increasing ripple wavelength and dispersion. (b) 1-5 display experimental Fresnel images of a 10nm $Ni_{45}Fe_{55}$, 0.25 nm $Ni_{79}Fe_{21}$ seeded sample (sample used as strong ripple example) taken in an easy axis hysteresis sequence, where their location is highlighted on the hysteresis loop (a). The corresponding modulus of the FFT is also shown in 1-5(c).

These images were taken on a 10 nm $Ni_{45}Fe_{55}$ thin films, with a 0.25 nm $Ni_{45}Fe_{55}$

seed layer. This is one of the samples which will be investigated in Chapter 4. The corresponding easy axis M-H loop is shown in Figure 4.18 (a). There is a reduction in M/M_s from 0.99 in (1) to 9.3 in (5). (b) displays a range of experimental Fresnel images in an easy axis hysteresis sequence with their corresponding modulus of the FFT images shown in (c). Images (1) through (5) visibly show increasing magnetic ripple properties, such as dispersion and wavelength. The following subsections will use example images 1-5 to demonstrate changes in analysis outputs as a function of field. These measured variations are vital when trying to understand micromagnetic dynamics, such as how field effects magnetic ripple properties. Dispersion angle θ, dominant ripple wavelength λ_{Dom}, integrated intensity I and spectroid wavelength $\lambda_{Spectroid}$ examples will be given in the following sections used the example images shown in Figure 3.18.

3.10.1 Dispersion Angle

Dispersion angle relates to the range of magnetisation orientations, which manifests itself as the spread of the FFT lobes. The spread of the lobes increases with decreasing field (Figure 3.18(1c) to (5c)). When the analysis detailed in Section 3.6.2 is used on these example images, it produces results which are plotted in Figure 3.19.

The dispersion angle θ is equal to half the angle measured at the FWHM of the normalised Lorentzian fitted peak. Outputs for the example images are shown in Table 3.9. The following figure reference refer to those shown in Figure 3.18. 1(b) at a field of 50 Oe along the easy axis, has a measured dispersion angle of 16.3°. 5(b) visibly has a much larger ripple dispersion and this is confirmed with a measured angle of 21.5° at a field of -10 Oe. It is important to note that the larger the externally applied field, the smaller the measured dispersion angle will be, if the field is applied along the direction of the magnetisation. 1(b) may have a reduced ripple dispersion when compared to 5(b), but still has some strong ripple properties present.

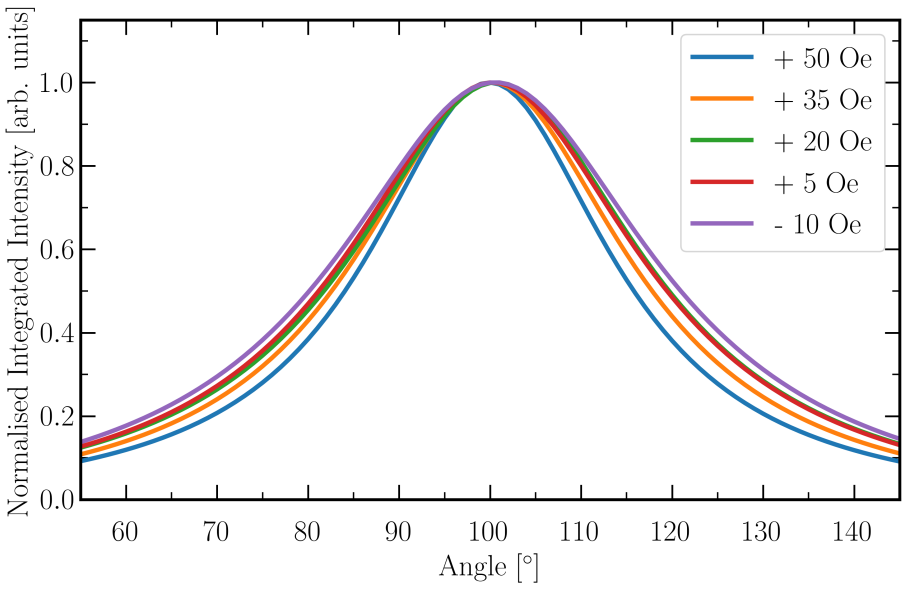

Figure 3.19: Lorentzian fitted plots displaying intensity as a function of angle through a reduction in applied field. The dispersion angle relates to the FWHM of the normalised peaks.

Field (Oe)	Dispersion Angle θ (°)
+ 50	16.3 ± 0.5
+ 35	18.3 ± 0.5
+ 30	19.7 ± 0.5
+ 5	20.0 ± 0.5
- 10	21.5 ± 0.5

Table 3.9: Dispersion angle θ outputs as a function of applied field along the easy axis.

3.10.2 Dominant Ripple Wavelength and Integrated Intensity

This method of characterisation involves using the radial integration data used for dominant ripple wavelength analysis as described in Section 3.7.2 (Figure 3.14). To determine the dominant ripple wavelength, the variation of the peak in terms of the y-axis (integrated intensity) was used.

This method involves measuring the changes in the peak height as a function of field. Results are recorded as a power spectral density (PSD), i.e. the power contained in that frequency range at the λ_{Dom} value. This is a particularly useful

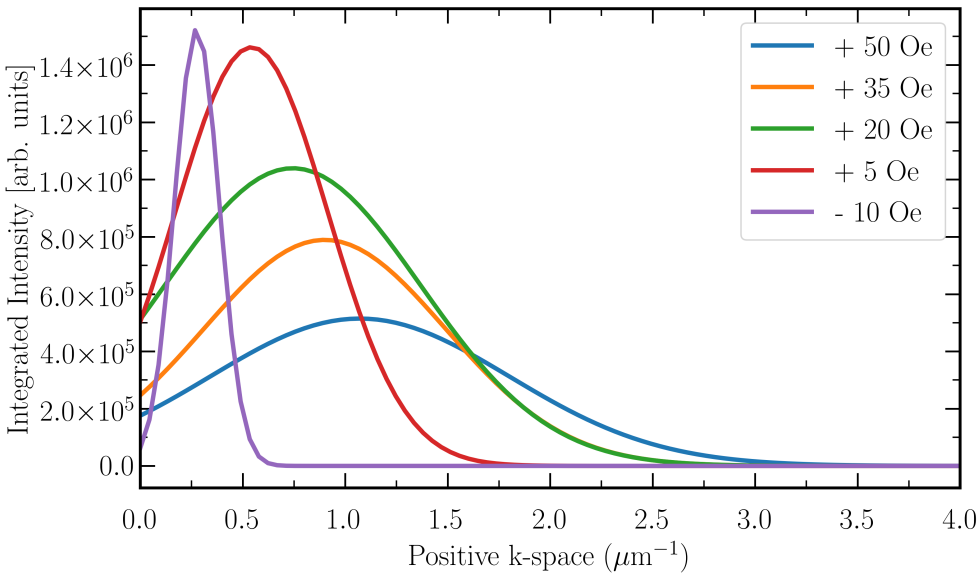

Figure 3.20: Modulus of FFT intensity characterisation results, using the images displayed in Figure 4.16. Image (1b) shows a Fresnel TEM with a large amount of ripple dispersion, compared to that in Example (5b). The curves are taken from the analysis of dominant wavelength value (Figure 4.16). The peak intensity values from their corresponding FFT images can be measured and compared. A larger ripple dispersion creates more contrast and increased integrated intensity.

method of characterisation when looking at a set of Fresnel images from a hysteresis sequence. The resulting plot of the example images is shown in Figure 3.20, with the outputs recorded in Table 3.10.

Field (Oe)	λ_{dom} (μm^{-1})
+ 50	0.24 ± 0.02
+ 35	0.28 ± 0.02
+ 30	0.34 ± 0.02
+ 5	0.46 ± 0.02
- 10	0.91 ± 0.02

Table 3.10: Dominant ripple wavelength λ_{Dom} as a function of applied field along the easy axis.

The results are in agreement with what can be seen visually from the experimental Fresnel images. The image with the weakest ripple has the lowest peak intensity, and this value increases with strengthening ripple. There is also a significant reduction in the spread of wavelength values with strengthening ripple properties, as shown

by the reduction in fitted peak spread along the x axis (k-space).

3.10.3 Spectroid Wavelength

The weighted average (spectroid) analysis was used on the example images shown in Figure 3.18, in which Image 1(b) has the weakest ripple properties, compared to Image 5(b) which exhibits the strongest. This is confirmed when taking the weighted average of the raw integrated intensity points as shown in Figure 3.21. The vertical lines represent the measured weighted average point. There is a shift of this measured output towards the zero point origin with increasing ripple properties (a smaller number in reciprocal space means a larger real space value, in this case ripple wavelength). Analysis on Image 1(b) gives an inverse spectroid wavelength value of 1.34 μm^{-1} compared to 1.07 μm^{-1} for Image 5(b). Real-space spectroid wavelength values are shown in Table 3.11 which show follow typical behaviour where there is a decrease in ripple properties with increasing applied field.

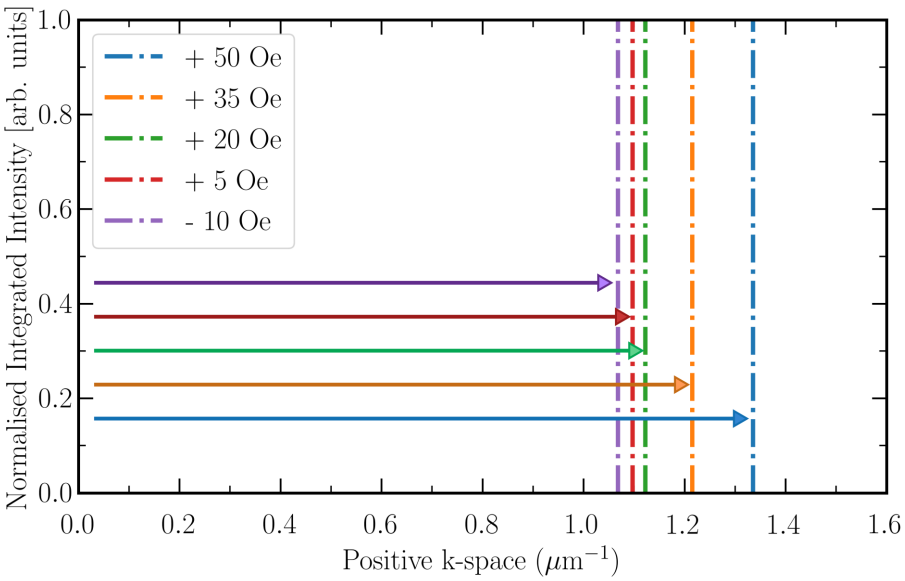

Figure 3.21: Spectroid wavelength characterisation results, using the images displayed in Figure 3.18. Image 1(b) shows a Fresnel TEM with a large amount of ripple dispersion, compared to that in image 5(b). The raw data is plotted from the analysis of the weighted average wavelength value. The measured spectroid values from their corresponding FFT images can be measured and compared. Increasing ripple properties, in this case wavelength, shifts the weighted average peak towards the zero-point origin.

Field (Oe)	$\lambda_{Spectroid}$ (μm^{-1})
+ 50	1.34 ± 0.01
+ 35	1.22 ± 0.01
+ 30	1.14 ± 0.01
+ 5	1.09 ± 0.01
- 10	1.07 ± 0.01

Table 3.11: Measured spectroid wavelength outputs as a function of field. There is a suppression of ripple properties with increasing applied field along the easy axis.

3.11 Summary

This chapter involves an in-depth discussion into both old and new steps implemented when characterising magnetic ripple properties. Magnetic ripple is well known phenomenon that occurs in ferromagnetic polycrystalline thin films, and can be easily visualised using Lorentz microscopy techniques. A publication in the 1960s by H. Hoffmann produced a theoretical model for predicting two parameters; the mean magnetic ripple wavelength and the ripple deviation from the mean direction. [20,21]

Different experimental publications have used varying methods to produce a single output for a materials magnetic ripple properties. Magnetic ripple can be thought of as a wave-like fluctuation. Due to this, all methods discussed have a common denominator; they all do their characterisation in reciprocal space through a 2D Fourier transform. It produces what is commonly referred to as a 'bow-tie' structure and is described in Section 3.5.

The corresponding FFTs of real space images displaying magnetisation ripple show spatial frequency spectras that are quite varied in both shape and distribution. Whilst recognising this, it can be seen that different methods can be used to characterise the magnetic ripple properties and extract useful numbers to quantify the samples behaviour on the micromagnetic scale.

Section 3.6 discusses methods used to characterisation the magnetic ripple dispersion angle θ. It is defined as the spread of the lobes in the bow-tie structure from the mean direction of magnetisation $\mathbf{M}$. Previous methods have used selective

masking of regions within the bow-tie structure. A proposed improvement is to use all information available with the bow-tie structure. An averaged integrated intensity line profile is taken over 360 degrees of the FFT image. This can be plotted as a function of angle producing two symmetric peaks. The full-width half maximum of the fitted peaks can then be extracted to produce 2θ.

The second parameter to be discussed is the dominant ripple wavelength λ_{Dom}. Although theory defines ripple wavelength as the mean value, there is usually an obvious dominant ripple wavelength value within the spectrum, and this parameter was used a lot in many experimental ripple publications. Previous methods discussed in Section 3.7.1 were a rotational average method, and a box integrated intensity method. Problems arising from these characterisation methods are discussed in detail. An improved method was proposed using a combination of the benefits of both old methods, featuring a partial rotational averaging method and is described in Section 3.7.2. Section 3.7.3 discusses a new method of characterising the 2D FFT image intensity, specifically the peak intensity value. This has proved to be particularly useful when characterising subtle changes within a hysteresis sequence.

Section 3.8 discusses a new method of determining a value for the centre of mass of a ripple spectrum, referred to as the $\lambda_{Spectroid}$. It is calculated as the weighted mean of the frequencies present in the spectrum. The advantage of this method is that it uses all wavelengths present in bow-tie structure, rather than one single dominant value.

These new proposed methods, of (a) ripple dispersion angle θ, (b) dominant ripple wavelength λ_{Dom}, (c) weighted mean of the wavelength spectrum $\lambda_{Spectroid}$ and (d) FFT image intensity I, will be used for ripple analysis in the following three results chapters. Examples of how they can be used for hysteresis mapping are shown in Section 3.10.

3.12 References

[1] H. W. Fuller, M. E. Hale and H. Rubinstein. Magnetic domain observations by electron microscopy. *Journal of Applied Physics.* 30(5):789, (1959).

[2] H. W. Fuller and M. E. Hale. Determination of magnetisation distribution in thin films using electron microscopy. *Journal of Applied Physics.* 31(238), (1960).

[3] E. Fuchs and Z. Angew. The magnetisation of thin nickel iron films along the hard axis. *Journal of Physics.* 13, 157, (1961)

[4] E. Fuchs and W.Zinn. Isotropic Permalloy Films. *Journal of Applied Physics.* 34(9):2557-2562, (1963).

[5] E. Feldtkeller. Ripple hysteresis in thin magnetic films. *Journal of Applied Physics.* 34, 2646, (1963).

[6] T. Suzuki and C. H. Wilts. Quantitative study of the magnetisation ripple in ferromagnetic nife alloy. *Journal of Applied Physics.* 39(2):1151-1153, (1968).

[7] N. G. Chechenin. Effects of topography on the local variation in the magnetisation of ultrasoft magnetic films: a Lorentz microscopy study. *Philosophical Magazine.* 83(2): 2899-2913, (2003).

[8] H. L. Gaigher. The Wavelength of the Magnetization Ripple of Electrodeposited Ni-Fe Films. *Z. Physik.* 223:257-266, (1969).

[9] Herrmann, M., Zweck, J. and H. Hoffmann(1994). Observation and characterization of micro-magnetic structures. *International Conference of Electron Microscopy.* 13, 245-249, (1994).

[10] L. J. Heyderman. TEM investigation of the magnetisation processes in exchange coupled multilayer films. *Journal of Magnetism and Magnetic Materials.* 138:344-354, (1994).

[11] J. T. Hosson. Ultrasoft Magnetic Films Investigated with Lorentz Tranmission Electron Microscopy and Electron Holography. *Microscopy and Microanalysis.* 8:4(274-287), (2002).

[12] J. N. Chapman and G. R. Morrison. Quantitative determination of magnetisation distributions in domains and domain walls by scanning transmission electron microscopy. *Journal of Magnetisation and Magnetic Materials.* 35: 254-260, (1983).

[13] J. N. Chapman. The investigation of magnetic domain structures in thin foils by electron microscopy. *Journal of Physics D* 17:623-647, (1984).

[14] M Fulton. Thesis: An investigation of the magnetic properties of spin- valves using transmission electron microscopy. (1995).

[15] B. R. Craig. Transmission electron microscopy study of CoFe films with high saturation magnetisation. *Journal of Applied Physics.* 100:053915, (2006).

[16] Craig Brownlie. A TEM investigation of controlled magnetic behaviour in thin ferromagnetic films. PhD thesis, University of Glasgow. (2007).

[17] D-T. Ngo. Nanoscale physical microstructure and micromagnetic behaviour of CoIr film with negative anisotropy. *Journal of Physics D: Applied Physics*. 44:095001, (2011).

[18] D-T. Ngo. In-situ transmission electron microscopy for magnetic nanostructures. *Journal of Physics D: Applied Physics*. 44:9(095001), (2011).

[19] D. R. G. Mitchell, B. Schaffer. Scripting-customised microscopy tools for DigitalMicrograph. *Ultramicroscopy*. 103:319-332, (2005).

[20] Schneider, C.A., Rasband, W.S., Eliceiri, K.W. NIH Image to ImageJ: 25 years of image analysis. *Nature Methods* 9, 671-675, (2012).

[21] H. Hoffmann. Quantitative calculation of the magnetic ripple of uniaxial thin permalloy films. *Journal of Applied Physics*. 35(6):1790-1798, (1964).

[22] H. Hoffmann. Theory of Magnetisation Ripple. *IEEE Transactions on Magnetics*, 4(1):32-38, 1968.

4

Effect of ultra-thin $Ni_{79}Fe_{21}$ seed layers on magnetic properties of $Ni_{45}Fe_{55}$

Contents

4.1 Introduction

In order to keep pace with the digital storage demands, it is necessary that the capacity of storage devices increases while reducing cost per GigaByte and meeting device reliability requirements. Hard Disk Drives (HDDs) remain an integral and necessary part of the digital storage landscape with continuing demand for increased storage density capability. In order to maintain this, reductions in individual bit sizes are necessary to improve the systems areal density capability (ADC). Read-write head development to support these system requirements benefits from high moment, permeable ferromagnetic materials in both the write element and read sensor components of the head for increased write field and improved shielding characteristics respectively.

Bulk magnetic measurements, such as vibrating-sample magnetometer (VSM) and magneto-optic Kerr effect (MOKE) measurements are well established techniques for characterising a samples average magnetic behaviour. However, as read-write head critical dimensions decrease, it is more important than ever to pay particular attention to local, nano-scale magnetic effects as new materials are developed and optimised. Transmission electron microscopy (TEM) is well known for its high spatial resolution and can be used to characterise a materials granular structure, with grain sizes as small as a few nanometres. [1,2] In addition to imaging a materials structure, magnetic imaging can be achieved by using Lorentz TEM where the objective lens is turned off, allowing for the visualisation of the micromagnetic distribution. The films investigated in this Chapter will exhibit magnetisation ripple, where a new characterisation method, as discussed in Chapter 3 is used for analysis of magnetisation ripple properties in this results chapter.

In HDD read-write head design $Ni_{45}Fe_{55}$ has long been a high moment alternative for $Ni_{80}Fe_{20}$, however lack of a well-defined uniaxial anisotropy and higher coercive fields have limited its widespread adoption. [3,4] Table 4.1 highlights and compares

key parameters from bulk magnetic measurements of unseeded 1 μm thick $Ni_{80}Fe_{20}$ and $Ni_{45}Fe_{55}$ thin films. It highlights bulk magnetic properties such as the magnetic flux density saturation B_{Sat}, the anisotropy field H_k, the coercive field H_c and magnetostriction λ. (Definitions for these properties can be found in Chapter 1).

Parameter	$Ni_{80}Fe_{20}$	$Ni_{45}Fe_{55}$
B_{Sat} (T)	1	1.6
H_k (Oe)	2.5	9.5
H_C (Oe)	0.3	0.4
λ	-1 x 10^{-6}	20 x 10^{-6}

Table 4.1: Comparison of properties of 1 μm thick $Ni_{80}Fe_{20}$ and $Ni_{45}Fe_{55}$ thin films. Values quoted from High Performance write heads using $Ni_{45}Fe_{55}$ [5].

As can be seen in Table 4.1 the $Ni_{45}Fe_{55}$ thin film shows significantly increased saturation magnetisation M_s. $Ni_{80}Fe_{20}$ has a B_{Sat} value of 1 T (equivalent to M_{Sat} = 10 kG), compared to an increased vale of 1.6 T (equivalent to M_{Sat} = 16 kG) for $Ni_{45}Fe_{55}$ thin films. A higher M_{Sat} value results in higher write fields, and is an important factor for switching higher coercivity media. It also increases permeability in shielding structures, which provide better protection from unwanted stray fields during read back processes. $Ni_{45}Fe_{55}$ also exhibits a reasonable coercivity (slightly more than $Ni_{80}Fe_{20}$ but lower than higher percentage composition Fe alloys). Higher Fe alloys (>55%) are subject to corrosion in head manufacture and operation in the drive, so are not a viable option.

The disadvantages of $Ni_{45}Fe_{55}$ are also highlighted in Table 4.1, where there is a both a switch of sign, and an $\approx$ 20 fold increase in magnetostrictive effects. HDD devices aim for little to no magnetostiction present in the read/write head materials. Magnetostriction effects on permalloy thin films will be investigated in greater detail in Chapter 6. There is also a significant increase in the anisotropy field, H_k from 2.5 to 9.5 Oe, resulting in an increase in uniaxial anisotropy from 100 J/m^3 to 600 J/m^3 respectively.

Use of extremely thin seed layers, and ferromagnetic seed layers in particular, are of interest to control the microstructure and stress in such films to achieve soft magnetic

properties while maintaining a high magnetic moment density. The chapter aims to provide a clearer understanding on the physical and magnetic effect of seed layers. Magnetisation ripple properties are investigated and proposed as a viable additional experimental characterisation technique for sample comparison throughout a full hysteresis sequence. Additionally, the Hoffmann model for theoretical magnetisation ripple (Section 1.7) will be tested.

Results presented in this Chapter are in collaboration with Seagate Technology, located in Londonderry. The sample preparation and bulk magnetic measurements were undertaken by Kevin McNeill and Muhammad Bilal Janjua using tools located at Seagate. All remaining imaging and analysis was undertaken as part of this project at the University of Glasgow.

4.2 Sample Deposition

Four polycrystalline films of similar total thickness, 15 nm, were investigated. All films included a 10 nm $Ni_{45}Fe_{55}$ layer, followed by a 5 nm Ru capping layer to prevent subsequent oxidation. Figure 4.1 shows a schematic illustration of the film structure. In addition to an unseeded sample, thin $Ni_{79}Fe_{21}$ seed layers of 0.25, 0.5 and 1.0 nm were also investigated. All layers were grown through radio frequency (rf) magnetron sputter deposition (as previously described in Section 2.2.2) using an Anelva c-7100 tool situated at Seagate Technology. A static 100 Oe aligning field was applied in the plane of the film to help induce an uniaxial anisotropy. Deposited films were then annealed in a 0.3 T applied field at 225 degrees (along the same direction as the deposition field). Deposition rates were calibrated by a X-ray fluorescence (XRF) measurement and confirmed with scanning electron microscopy (SEM) measurement of samples prepared by focused ion beam (FIB). The films were deposited onto 100×100 μm^2 electron transparent Si_3N_4 membranes for TEM measurements, as well as bulk Si substrates.

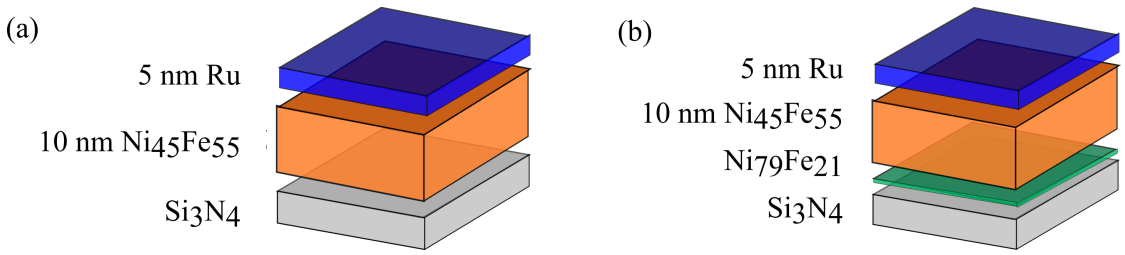

Figure 4.1: Cross section schematic showing the structures of samples (a) unseeded, (b) seeded samples with the following seed layer thickness; 0.25 nm $Ni_{79}Fe_{21}$, 0.5 nm $Ni_{79}Fe_{21}$ and 1.0 nm $Ni_{79}Fe_{21}$. All samples consist of a 10 nm $Ni_{45}Fe_{55}$ layer, and are capped wit a 5 nm Ru layer. All samples were deposited on electron transparent Si_3N_4 membranes.

4.3 Bulk Magnetic Measurements

The influence of very thin $Ni_{79}Fe_{21}$ seed layers on the bulk magnetic properties of 10 nm thick films of $Ni_{45}Fe_{55}$ has been investigated. As stated earlier, bulk magnetic measurements were undertaken by Kevin McNeill and Muhammad Bilal Janjua using tools located at Seagate Technology, UK. To obtain a large enough signal to measure a B-H hysteresis loop, samples were also deposited onto larger bulk Si wafers. Easy and hard axis hysteresis loops for each film were determined using a commercial SHB model 109S hysteresis loop tracer, operating at a maximum applied field of 200 Oe.

Figure 4.2 shows the normalised easy and hard axis hysteresis loops from the B-H loop measurements on the four unseeded and seeded films. The red and blue loops represent the applied field along the easy and hard directions respectively. The unseeded film, shows near isotropic behaviour with a large coercivity of 29.1 Oe along the easy axis (as defined by the deposition and annealing fields), and little change when applied along the hard direction. Therefore, the fields used during deposition and annealing have not resulted in anisotropic behaviour. Uniaxial behaviour improves with increasing seed layer thickness, as can be seen from the loops of the other $Ni_{79}Fe_{21}$ seeded films, with decreasing easy axis coercivities of around 10.3 Oe, 3.8 Oe and 3.5 Oe respectively. There is also a marked increase in uniaxial anisotropy, as evidenced by the increase in H_K from 2.0 Oe to around 12.8 Oe through the addition of 1 nm seed layer.

It is notable that the effect of improved anisotropic behaviour of the films occurs at just 0.25 nm seed layer thickness. This improved behaviour increases with seed layer thickness, with a seed layer thickness of 0.5 nm 1.0 nm showing little difference. It appears that an further increase in seed layer thickness will not improve the magnetic properties further, however there are no thicker films to prove this hypothesis. Key points in the hysteresis sequence are highlighted in Table 4.2.

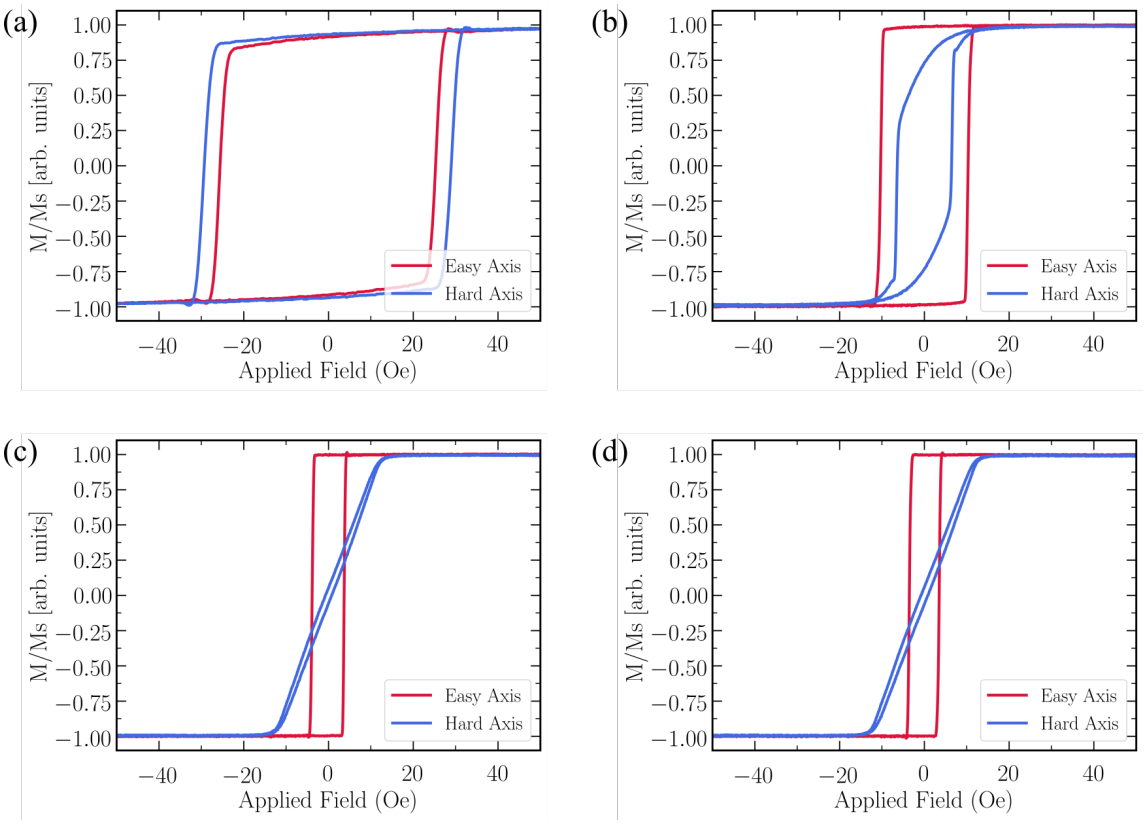

Figure 4.2: Hysteresis loops for 10 nm $Ni_{45}Fe_{55}$ sample (a) unseeded, (b) 0.25 nm $Ni_{79}Fe_{21}$ seed layer, (c) 0.5 nm $Ni_{79}Fe_{21}$ seed layer and (d) 1.0 nm $Ni_{79}Fe_{21}$ seed layer, with the field applied along the easy and hard axis, represented by the red and blue loops respectively.

As discussed previously, $Ni_{79}Fe_{21}$ seed layers were introduced as a way of controlling physical and micro-magnetic properties of a higher moment $Ni_{45}Fe_{55}$ thin film. The addition of increasing thickness seed layer increased the magnetic moment of the film. Magnetic flux density values increased from 1.42 to 1.57 for the unseeded to 1.0 nm seeded sample, measured in Teslas. This was calculated using

Seed layer Thickness (nm)	B (T)	Easy Axis H_C (Oe)	Hard Axis H_C (Oe)	Hard Axis H_K (Oe)
0.00	1.42	29.1*	25.8*	-
0.25	1.46	10.3	6.4	10.2
0.50	1.52	3.8	0.7	12.7
1.00	1.57	3.5	0.8	12.8

Table 4.2: Key parameters from bulk B-H looper magnetic measurements, with increasing $Ni_{79}Fe_{21}$ seed layer thickness. A seed layer of $Ni_{79}Fe_{21}$ improves uniaxial anisotropy properties, as shown through a decrease in the coercive field H_C along the easy axis, and increase in the anisotropy field H_K along the hard axis. *Indicates measurements are made for the intended easy and hard axis. However a well defined easy axis has clearly not been induced in these films.

bulk measurements and sample geometry. There is quite clearly a significant improvement in magnetic properties, such as the reduction in H_C and an increase in H_K through the addition of $Ni_{79}Fe_{21}$ seed layers when investigating larger, bulk magnetic thin films. The following sections will investigate how this relates to microstructure (4.4) and micromagnetic (4.5) properties.

4.4 Physical Microstructure

4.4.1 Crystal Structure

NiFe alloys used in the seeded layer, with a composition of 79/21 have a *fcc* (face-centred cubic) structure. The 10nm NiFe alloy with a composition of 45/55 has a *bcc* (body-centred cubic) crystal structure. The Ru layer is a *hcp* structure. These crystal structures are known for these compositions. Experimental diffraction images allow for these structures to be confirmed with SAED measurements. The lattice spacing for cubic and hexagonal systems can be determined using the following equations.

$$d_{hkl} = \frac{a}{\sqrt{(h^2 + k^2 + l^2)}} \tag{4.1}$$

$$d_{hkl} = \frac{1}{\sqrt{\frac{4}{3a^2}(h^2 + k^2 + hk) + \frac{l^2}{c^2}}} \tag{4.2}$$

with a and c being the lattice constants of the crystal structure, and h,k,l are the Miller indexes.

The crystal structure of a film can be determined using electron diffraction. However, care is needed in analysing and indexing electron diffraction patterns when imaging multi-layer stacks. Figure 4.3 shows selected area electron diffraction (SAED) images for films that are (a) unseeded and untilted, following by samples tilted by 20 degrees for: (b) unseeded, (c) 0.25 nm $Ni_{79}Fe_{21}$ seeded, and (d) 1.0 nm $Ni_{79}Fe_{21}$ seeded.

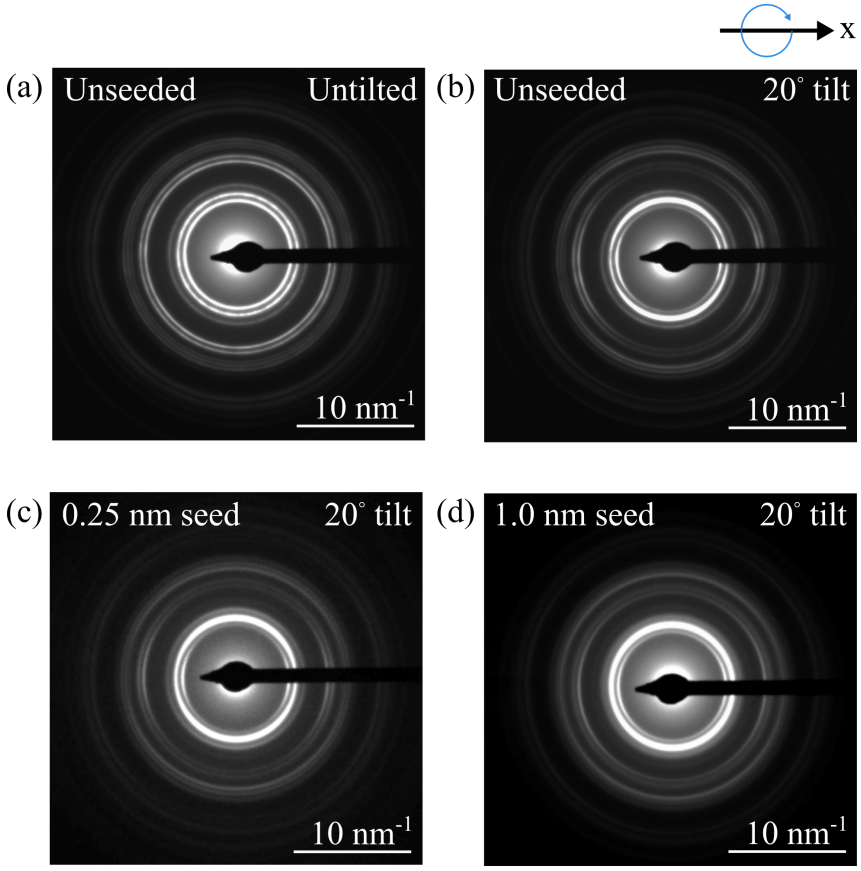

Figure 4.3: SAED patterns for an unseeded and (a) untilted sample, and (b) a 20 degree tilt angle sample. Frames (c) and (d) show the SAED patterns for the (c) 0.25 nm $Ni_{79}Fe_{21}$ seeded sample, and (d) shows the 1.0 nm $Ni_{79}Fe_{21}$ seeded sample, both at a tilt angle of 20 degrees.

The uniform circular diffraction rings surrounding a single central spot obtained from an un-tilted sample confirms that the sample is polycrystalline.

The combination of several crystal structures results in the rings overlapping, creating rings with larger widths, as shown in Figure 4.3. Figure 4.4(a,b) are intensity line profiles from the origin of the diffraction patterns shown in Figure 4.3(a,d).

This is also highlighted in Figure 4.4(a,b), where the red line trace (b) which represents the tilted 1.0 nm $Ni_{79}Fe_{21}$ seed layer sample is less defined when compared to the tilted unseeded sample shown in (a). This makes specific ring determination more challenging, due to the overlap of allowed reflections.

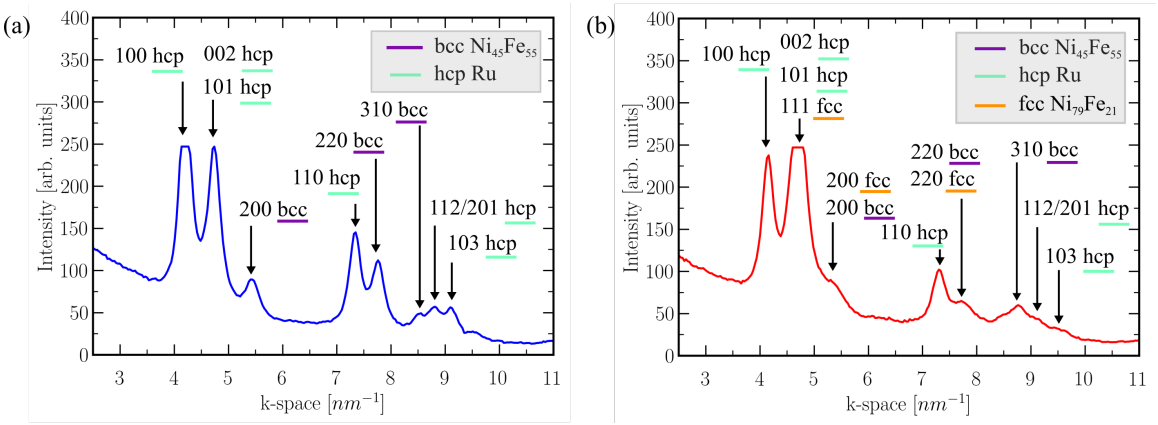

Figure 4.4: (a) Line profiles from origin of experimental SAED images, comparing un-tilted unseeded and 1.0 nm $Ni_{79}Fe_{21}$ seed layer samples. Indexing diffraction rings from SAED patterns (b) unseeded and (c) 1.0 nm $Ni_{79}Fe_{21}$ seed layer.

The diffraction rings for the unseeded and 1.0 nm $Ni_{79}Fe_{21}$ seed layer sample have been calculated and are shown to be consistent with experimental results. The indexing of the SAED, as shown in Figure 4.4 confirms that for a Ru crystal, $a =$ 0.270 nm and $c = 0.428$ nm. It also confirms that for $Ni_{45}Fe_{55}$, $a = 0.358$ nm, and for $Ni_{79}Fe_{21}$, $a = 0.360$ nm. This is in agreement with expected values.

Experimental SAED images allows for crystal texture determination. When tilting a non-textured polycrystalline specimen, the diffraction pattern rings maintain their uniform intensity. In a textured polycrystalline film, the pattern will have broken rings, or arcs i.e. the intensity of some rings is either enhanced or reduced. This indicates that the grains in the film are not randomly oriented but in fact display a preferred orientation. The results shown in Figure 4.3 show that there

is texture present in the unseeded and 0.25 nm $Ni_{79}Fe_{21}$ seed layer sample. This texture is seen in the index HCP rings of 100, 002 and 101. This corresponds to texture along the [010] direction. The addition of the $Ni_{79}Fe_{21}$ reduces the texture in the thin film, demonstrated by the unbroken diffraction rings present in the 1.0 nm seed layer sample.

Often, seed layers are usually used to promote a crystal texture direction, whereas the opposite effect is seen here. [6,7,8] However, as the seed layers used in this investigation are ultra-thin ($\leq$ 1 nm), it is proposed that they in-fact don't act like conventional seed layers, but provide nucleation sites for the growing film, leading to a reduced average grain size and more randomised texture directionality. This is explored in the next section.

4.4.2 Grain Structure

In thin film polycrystalline samples, the magnetic properties of the material can be greatly influenced by the grain size distribution and orientation. Bright-field (BF) and dark-field (DF) TEM images were used to analyse the grain size distribution of the film. Dark field images are particularly useful when looking at grain size distribution due to the high contrast between the grains. This makes it easier to distinguish individual grains for analysis. An example of the difference between typical bright-field and dark-field images can be seen in Figures 4.5 and 4.6 respectively. (See Section 2.5.2). Note the examples given are taken in different areas of the sample. Bright field and dark field TEM images were taken to analyse the granular structure within the polycrystalline thin films, using a FEI Tecnai T20 microscope.

Figure 4.5(a) of the unseeded film displays a large grain size with a large size variation. Figure 4.5(b,c,d) visually demonstrate the reduction in grain size with the addition of increasing $Ni_{79}Fe_{21}$ seed layer thickness. A seed layer as thin as 0.25 nm has a dramatic effect on the samples average grain size. Not only do the grains appear

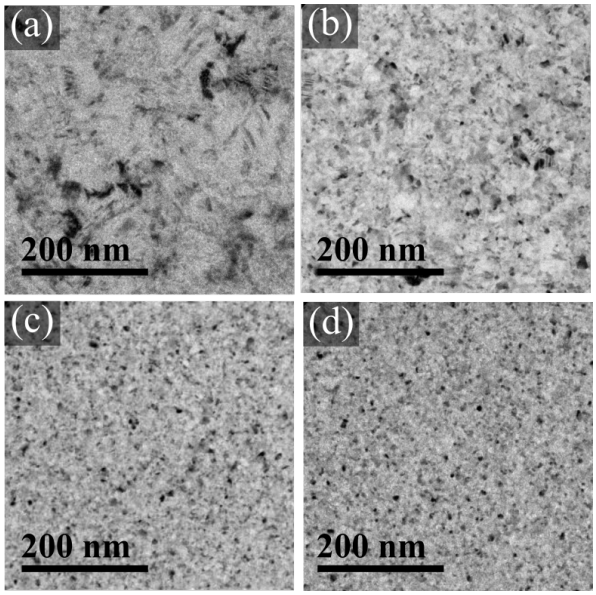

Figure 4.5: Experimental bright-field TEM images, displaying the grain size distribution for a 10 nm $Ni_{45}Fe_{55}$ sample (a) unseeded, (b) 0.25 nm $Ni_{79}Fe_{21}$, (c) 0.5 nm $Ni_{79}Fe_{21}$ and (d) 1.0 nm $Ni_{79}Fe_{21}$ seed layer.

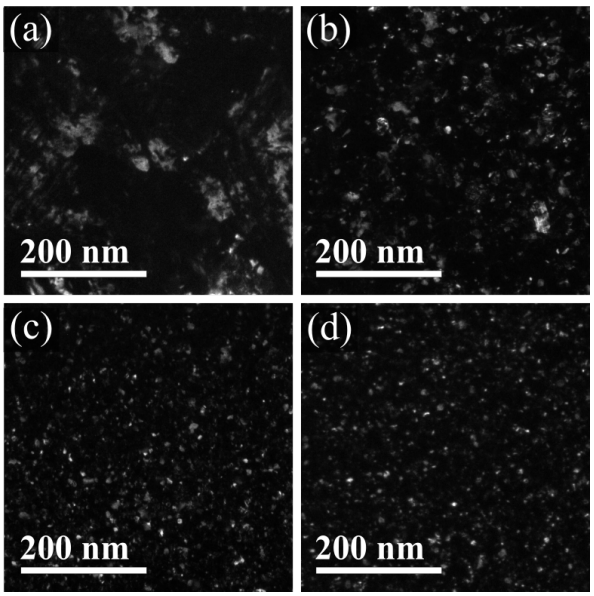

Figure 4.6: Experimental dark-field TEM images, displaying the grain size distribution for a 10 nm $Ni_{45}Fe_{55}$ sample (a) unseeded, (b) 0.25 nm $Ni_{79}Fe_{21}$, (c) 0.5 nm $Ni_{79}Fe_{21}$ and (d) 1.0 nm $Ni_{79}Fe_{21}$ seed layer.

to decrease in size, but the spread of the sizes observed is greatly reduced. The same grain size variation was confirmed through dark-field imaging shown in Figure 4.6.

Figure 4.7 highlights key steps in average grain size determination. To measure the grain size, a large number of dark-field images were acquired (> 20 images), like

the example shown in (a). Image processing can be carried out using the software Image J, where limits of minimum and maximum grey levels can be selected to produce a threshold image (b). Individual grain areas can then be measured using ImageJ software, which have been highlighted through the threshold image, and an approximation of the grain diameter can be made.

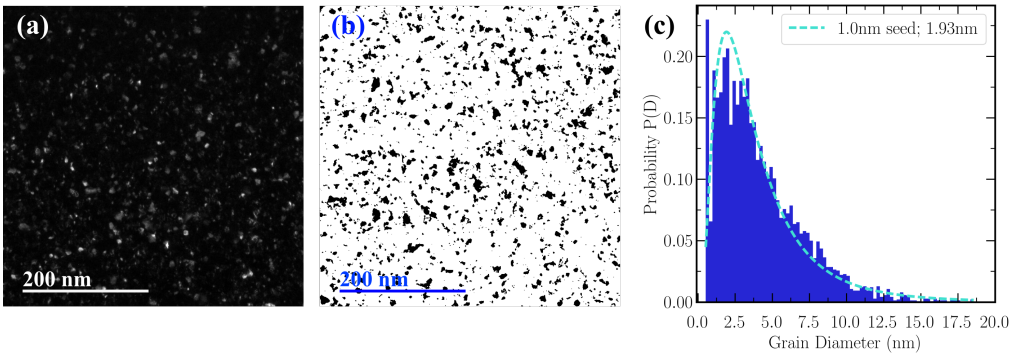

Figure 4.7: Average grain size determination using Image J. (a) Experimental dark-field image for 0.5 nm $Ni_{79}Fe_{21}$ seed layer sample. (b) Image thresholding, where black regions represent image grains. (c) Histogram of measured grain size diameter with fitted log-normal distribution represented by the dashed line.

These results can be can be plotted as a histogram as shown in Figure 4.8. The calculated log-normal distribution was determined using Python analysis and was then plotted against the measured diameters, shown in Figure 4.9. (a) represented the probability distribution for all samples, compared to the normalised log-normal plots shown in (b). To ensure good statistical results, a minimum of 10,000 grain diameters were measured for each specimen.

Table 4.3 demonstrates that the addition of ultra-thin seed layers has a pronounced effect on the samples grain size distribution. Not only do the grains appear to decrease in size, the range of measured grain sizes also reduces. The measured log-normal peak decreases from a grain size diameter of 10.2 nm in the unseeded film, to 7.5 nm in the 0.25 nm $Ni_{79}Fe_{21}$ seed layer sample, then proceeds to saturate at just under 2 nm for 0.5 nm seed layer. The narrow distribution of grains confirms homogeneity of nano-grains existing in the film. It appears that the addition of thicker seed layers will not reduce the grain size any further. It is suggested that by reducing the grain size below the exchange length, typically 5-10 nm, it will

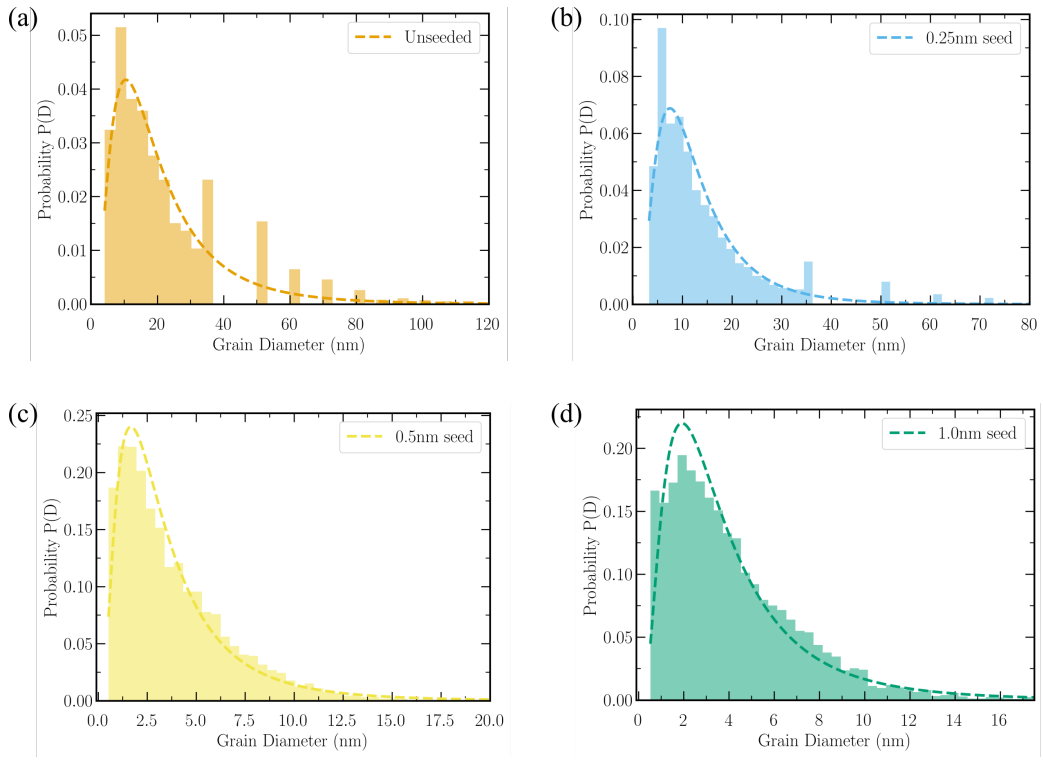

Figure 4.8: Log-normal distributions fitted to histograms, displaying the grain size distribution for a 10 nm $Ni_{45}Fe_{55}$ sample (a) unseeded, (b) 0.25 nm $Ni_{79}Fe_{21}$, (c) 0.5 nm $Ni_{79}Fe_{21}$ and (d) 1.0 nm $Ni_{79}Fe_{21}$ seed layer.

lead to more efficient in-plane exchange coupling between the individual grains. An effect of a stronger granular exchange coupling might be expected to suppress the magnetisation ripple in the film. This will be investigated by imaging the micromagnetic structure as described in the following section.

Seedlayer Thickness (nm)	Mean Diameter (nm)	Standard Deviation (nm)	Log-normal Peak (nm)
0.00	17.3	2.0	10.2
0.25	11.2	1.9	7.50
0.50	2.9	2.1	1.7
1.00	3.2	2.1	1.9

Table 4.3: Grain size distribution analysis outputs.

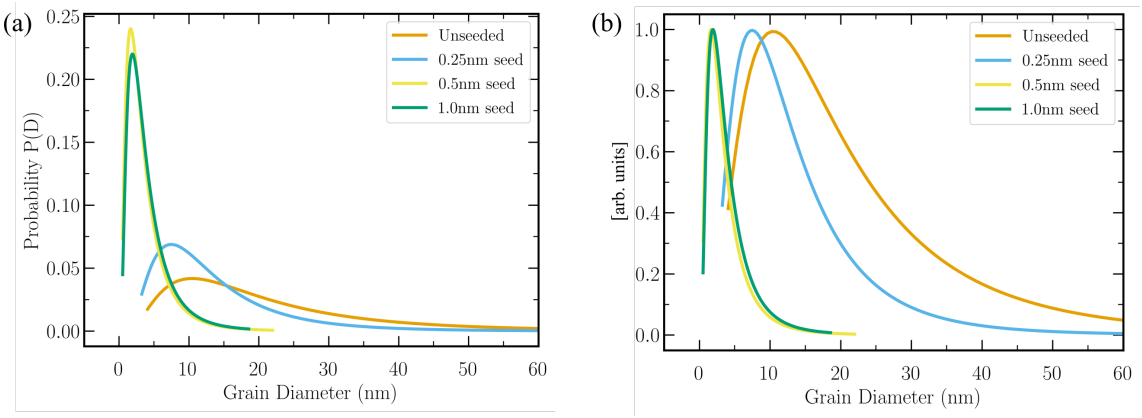

Figure 4.9: Measured grain size distribution results; (a) Log-normal grain size distribution, and (b) Normalised log-normal curves for for a 10 nm unseeded $Ni_{45}Fe_{55}$ sample and 0.25 nm, 0.5 nm and 1.0 nm $Ni_{79}Fe_{21}$ seed layer samples.

4.5 Micromagnetic Visualisation

The aim of this section is to provide an understanding of the micromagnetic behaviour of a $Ni_{45}Fe_{55}$ thin film, and how the addition of ultra-thin $Ni_{79}Fe_{21}$ seed layers can usefully influence the magnetic properties. In order to fully understand the specimens micromagnetic structure and magnetisation reversal processes of the film, the Fresnel mode of Lorentz microscopy was employed for magnetic TEM imaging. All films investigated in this section exhibit magnetisation ripple due to their polycrystalline grain structure (discussed in Section 1.7). In-situ measurements were carried out by sample tilting, resulting in applying a magnetic field using the remanent field present in the electron column (previously described in Section 2.6.4). The magnetising experiments involved easy and hard axis field application using a tilt rotate rod in the TEM. In-plane fields were applied to a near magnetisation saturation state, then the reversal process was recorded by varying the field from maximum positive field to negative field, also known as hysteresis behaviour.

4.5.1 Magnetisation Reversal

The evolution of the magnetisation distribution of the unseeded and seeded thin films have been investigated for orthogonal directions of the applied field. The

easy and hard axis can be found by varying the direction of the applied field, by rotation of the sample. For hard axis measurements, the sample is rotated until purely magnetisation rotational behaviour is observed. This behaviour is consistent with typical hard axis dynamics, an example of which is shown in Figure 4.10, where the rotation of the magnetisation **M** direction as a function of applied field is highlighted by the blue arrow.

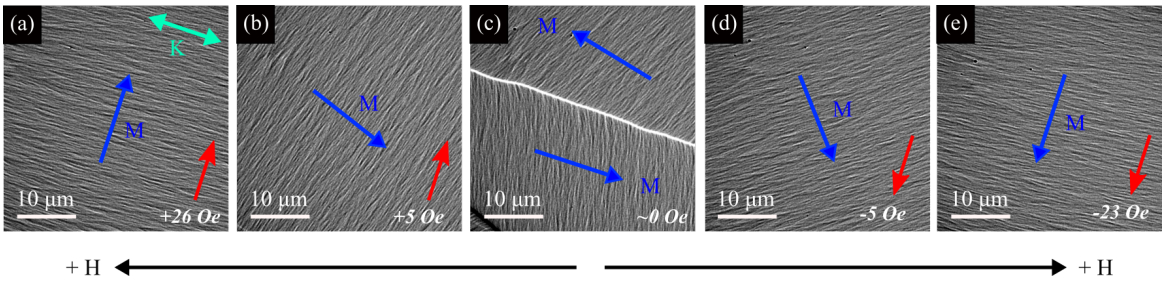

Figure 4.10: Simplified example of experimental Fresnel images (a-e) of the 0.5 nm $Ni_{79}Fe_{21}$ seed layer sample during a hard axis hysteresis reversal. Highlights the rotation of the magnetisation **M** direction with a reduction of field, and an application in the opposing direction. The red arrows represent the direction of the applied field, **H**, and K is the uniaxial anisotropy direction.

An external field can be applied by simply tilting the sample, and using the remanent field in the microscope. The field was taken from +30 Oe to - 30 Oe (which corresponds to the remanent field and the tilt range used) to ensure magnetisation saturation was reached. At a field of +30 Oe, and -30 Oe, the magnetisation aligns parallel to the applied field. The outward path and return path were in agreement with reversal occurring entirely through magnetisation rotation. The component of magnetisation **M** along the hard axis is assumed be be proportional to $\cos\theta$, where θ is the angle between **M** and the in-plane component of the applied field. Therefore at saturation, when the magnetisation lies at 0, or 180 degrees, the normalised magnetisation should be at 1 and -1 respectively. As the magnetisation rotates as the field is reduced, the increase in the angle results in the normalised magnetisation reducing towards zero. The final $\cos\theta$ value is plotted against the external field applied through tilting. This can then be used to deduce the net moment of the film, and in turn used to plot a M-H loop.

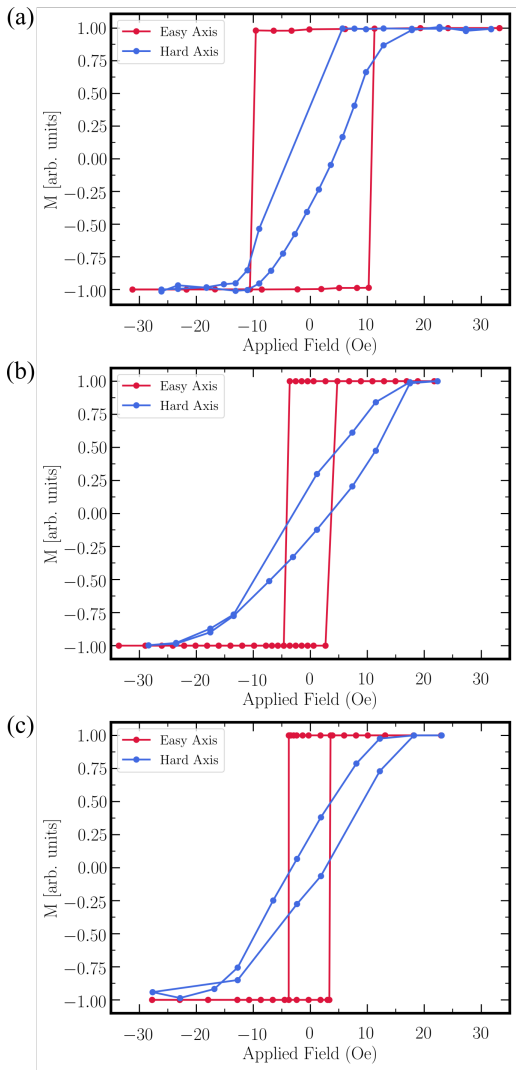

Figure 4.11: Measured M-H loops from Fresnel TEM images with the external field applied along the easy axis and hard axis for (a) 0.25 nm $Ni_{79}Fe_{21}$ seed layer, (b) 0.5 nm $Ni_{79}Fe_{21}$ seed layer and (c) 1.0 nm $Ni_{79}Fe_{21}$ seed layer.

Figure 4.11 shows the M-H loop results for easy axis and hard axis field application. The unseeded sample did not exhibit any measurable hysteresis behaviour due to limitations of applying a large enough in-situ field, so will be ignored in results shown in Figure 4.11.

The easy axis behaviour shows a reduction in the coercive field with an increase in seed layer thickness, that saturates with thickness over 0.5 nm. This is in good agreement with bulk magnetic measurements described in Section 4.3. All hard axis plots also show typical hard axis behaviours, with 0.5 nm and 0.1 nm seed layer

samples producing similar loops as expected. The 0.25 nm seed layer has a more open loop, with a smaller anisotropy field value, H_K when compared to the other samples.

Although the M-H loops exhibit the typical easy and hard axis configurations respectively, there is some discrepancy when compared to the bulk magnetic measurement outputs. This can be attributed to a discrepancy in measuring such a small field present in the TEM. This difference is highlighted in Table 4.4.

Seedlayer Thickness (nm)	Bulk BH H_C (Oe)	Lorentz H_C (Oe)	% Diff	Bulk BH H_k (Oe)	Lorentz H_k (Oe)	% Diff
0.25	10.3	10.2	-1%	-	-	-
0.5	3.8	3.9	+3%	13	16.8	+30%
1.0	3.5	2.1	-40%	13	13.8	+6%

Table 4.4: Easy axis coercive field H_C value comparison of bulk measurements compared to micro-magnetic methods. All three samples show consistent trends when comparing bulk and micro-magnetic measurements.

Table 4.4 highlights how both bulk and micromagnetic measurements exhibit the same trends with increasing seed layer thickness. i.e. a reduction in H_c and H_k. The magnetic properties are relatively consistent between the bulk and TEM samples.

4.5.2 Easy Axis Reversal

In this section, Fresnel images will be shown of easy (Section 4.5.2) and hard axis (Section 4.5.3) hysteresis reversals, to show differences in micromagnetic behaviour followed by quantitative analysis which will be presented later in this chapter, in Section 4.6.

For an applied field lying parallel to the easy axis of the magnetic thin film, magnetisation reversal normally proceeds by a single 180° domain wall sweeping across the sample within the field of view. In reality, the wall was rarely/never imaged for easy axis reversal, however a rapid “event" was observed at the coercive field H_C. The applied field was increased slowly to get in close approximation to the coercive field H_C of the sample. Each Fresnel image is recorded in the same region of the sample, and the applied field direction is indicated by the red arrow.

Unseeded

Figure 4.12 shows the Fresnel images of the easy axis magnetisation reversal of the unseeded 10 nm $Ni_{45}Fe_{55}$ sample. These images are of higher contrast and are much more irregular compared to the other seeded thin films. The acquired images are consistent with the bulk magnetic measurements, in that there is visibly a large amount of ripple dispersion. It was observed that there was little to no difference between the 'easy' and 'hard' axis loops, confirming the bulk measurements which showed a lack of a defined anisotropy axis.

0.25nm $Ni_{79}Fe_{21}$ Seed Layer

The observed magnetisation ripple behaviour in the seed layer samples depends strongly on the seed layer thickness. The magnetisation ripple showed greater transverse coherence and preferred directionality when compared to the unseeded sample. Figure 4.13 shows images of the reversal mechanism along the easy axis of 0.25 nm $Ni_{79}Fe_{21}$ seed layer sample, and their corresponding location on the bulk BH hysteresis loop. On reduction of the applied field from + 30 Oe (a) to - 14 Oe (c), there was a visible increase in ripple dispersion and wavelength. A domain wall flash was observed at a switching field of approximately -15 Oe.

It is important to note the large changes of ripple properties between (c) and (d). The applied field is almost the same with a small increase of only 2 Oe, but that has causes a switch in magnetisation **M** direction (d) which lies parallel to that in (c). The latter also has much more reduced dispersion and contrast. Any further increase of field resulted in a slight suppression of the magnetisation ripple, as seen in the comparison of Figure 4.13 (d) and (e) taken at -16 Oe and -30 Oe respectively.

0.5 and 1.0 nm $Ni_{79}Fe_{21}$ Seed Layer

Bulk magnetic measurements described in Section 4.3 showed that there was minimal variation between the magnetic properties of the 0.5 nm and 1.0 nm $Ni_{79}Fe_{21}$ seed layer samples. Both samples followed typical easy axis behaviours. This was

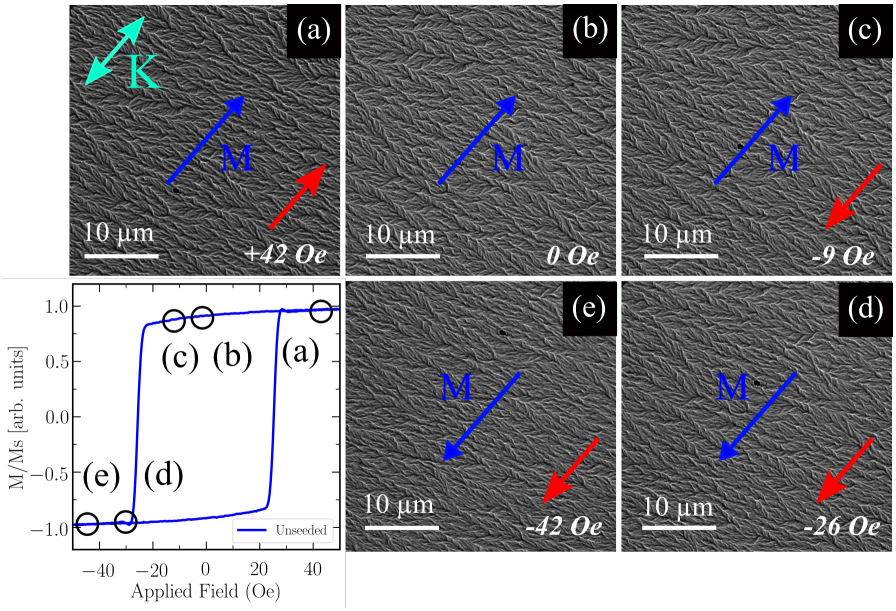

Figure 4.12: Fresnel images demonstrating the magnetisation reversal process along the easy axis of an unseeded 10 nm $Ni_{45}Fe_{55}$ thin film. The red arrows represent the direction of the applied field, H, and K is the uniaxial anisotropy direction. The corresponding location of the Fresnel image is highlighted on the bulk BH hysteresis loop. Note that this film exhibits isotropic behaviour so there is little to no variation between images taken at various applied fields.

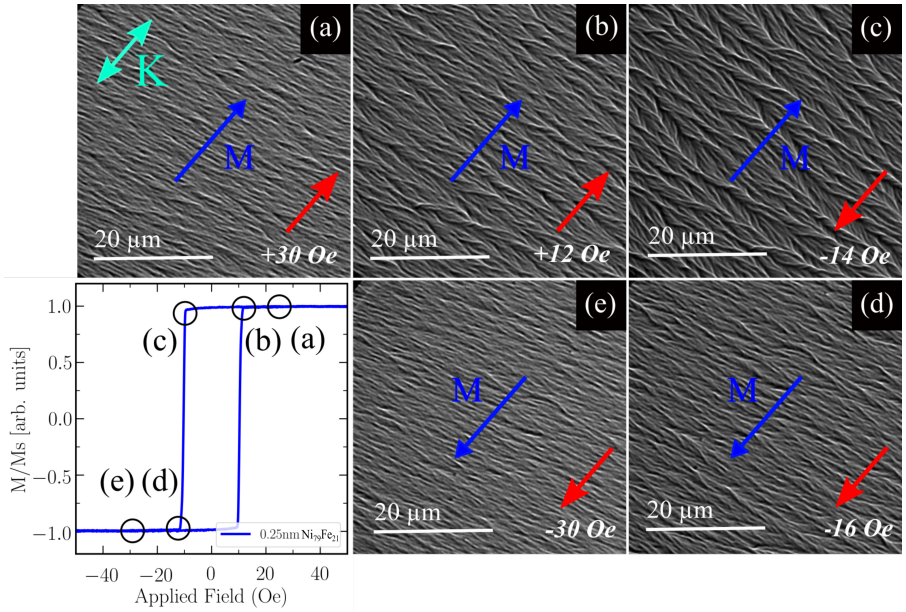

Figure 4.13: Fresnel images demonstrating the magnetisation reversal process along the easy axis of 10 nm $Ni_{45}Fe_{55}$ thin film with 0.25 nm $Ni_{79}Fe_{21}$ seed layer. There is a visible increase in magnetisation ripple contrast until the coercive field H_C, which is approximately -15 Oe, is reached, and the direction of magnetisation rapidly switches.

confirmed when visually inspecting experimental Fresnel images along the easy axis. Figures 4.14 and 4.15 demonstrate key points in an easy axis hysteresis sequence with the use of Fresnel images, for the 0.5 nm and 1.0 nm samples respectively. Similarly to the 0.25 nm seeded sample, there was a expansion of the magnetisation ripple dispersion with a reduction of the applied field from the magnetisation saturation state, seen in (a)-(c). There are significant changes from (c) to (d), which represent only an increase of a few Oe and a reverse of magnetisation direction from anti-parallel to parallel with **H**. This is also less noticeable changes in ripple properties such as dispersion. This was followed by a suppression after the coercive field was achieved. (d)-(e). However, there is visually a substantial suppression of magnetisation wavelength and dispersion angle when compared to the unseeded and 0.25 nm seeded sample. Experimental images of the various samples at the same applied field will be compared in the following section.

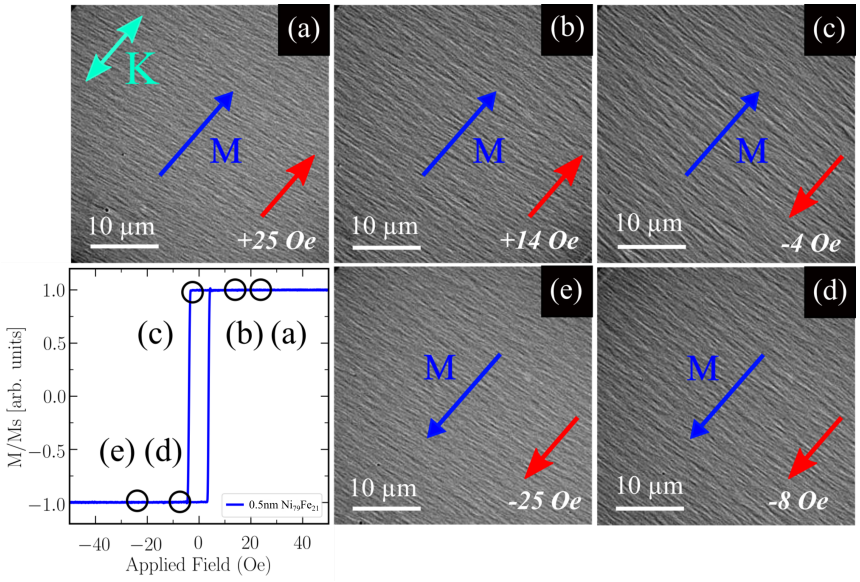

Figure 4.14: Fresnel images demonstrating the magnetisation reversal process along the easy axis of 10 nm $Ni_{45}Fe_{55}$ thin film with 0.5 nm $Ni_{79}Fe_{21}$ seed layer. There is a visible suppression in magnetisation ripple properties when compared to Figure 5.12 and 5.13.

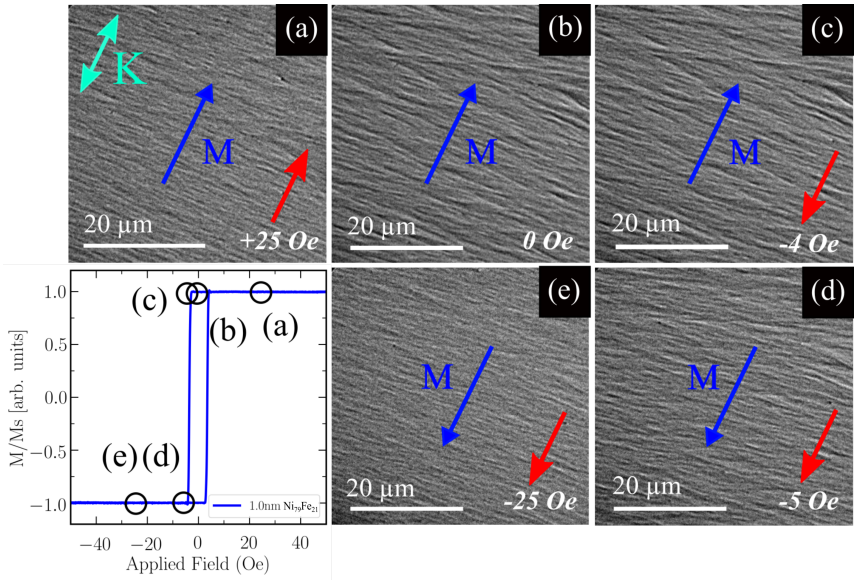

Figure 4.15: Fresnel images demonstrating the magnetisation reversal process along the easy axis of 10 nm $Ni_{45}Fe_{55}$ thin film with 1.0 nm $Ni_{79}Fe_{21}$ seed layer. The corresponding location of the Fresnel image is highlighted on the bulk BH hysteresis loop.

Easy Axis Fresnel Image Comparison

Figure 4.16 shows an example of how bulk magnetic measurements don't tell us the full picture of a samples micro-magnetic behaviour. All experimental Fresnel images were taken at equivalent applied fields, in this case + 24 Oe, highlighted by the black dot in (a). The B-H loop denotes that all the 3 samples have nearly the same M/M_s value, measuring at 0.933, 0.991 and 0.997 respectively. However, when visually compared with increasing seed layer thickness (b,c,d), there is a large suppression of magnetic properties such as ripple dispersion angle and wavelength, leading to an overall decrease in image contrast. Fresnel imaging allows for additional characterisation of micro-magnetic properties that wouldn't be possible with just bulk magnetic measurements. These changes in magnetic ripple properties can be characterised to produce quantitative outputs for sample comparisons, using the methodology discussed in Chapter 3, and results will be given in Section 4.6.

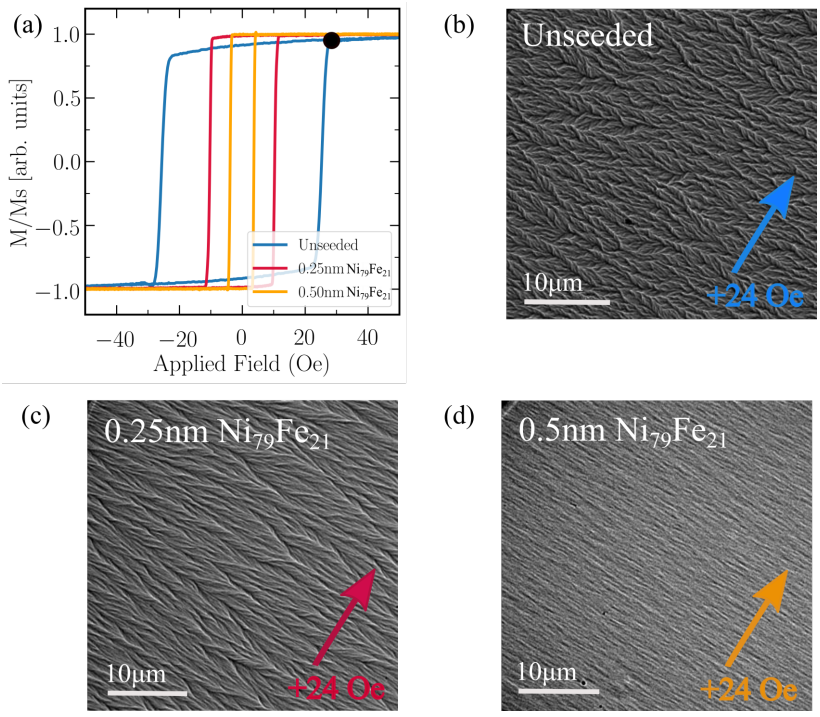

Figure 4.16: (a) B-H easy axis hysteresis plot for unseeded, 0.25 nm $Ni_{79}Fe_{21}$ seed layer and 0.5 nm $Ni_{79}Fe_{21}$ seed layer, 10 nm $Ni_{45}Fe_{55}$ thin films. Corresponding experimental Fresnel TEM images showing the suppression of magnetisation ripple are shown in (b,c,d). All images were acquired with an externally applied field of +24 Oe, shown by the black dot on the hysteresis plot. Visually displays the suppression of magnetisation ripple through the addition of ultra thin $Ni_{79}Fe_{21}$ seed layers.

4.5.3 Hard Axis Reversal

Hard axis behaviour typically involves rotation of the magnetisation and formation of domain walls with reducing applied field, assuming the field lies exactly along the hard axis. Experimental images from a hard axis hysteresis sweep will be shown in the following sections. As the unseeded sample showed isotropic behaviour, therefore meaning it did not exhibit any significant uniaxial anisotropy (i.e. an easy/hard direction), it will be omitted from the discussion below.

0.25nm $Ni_{79}Fe_{21}$ Seed Layer

Experimental Fresnel images were acquired from the hard axis of the 0.25 nm $Ni_{79}Fe_{21}$ seed layer sample. Typical hard axis hysteresis behaviour was observed and is shown in Figure 4.17. Ripple dispersion and wavelength was increased with

a reduction of the applied field, until the formation of low-angle domain walls (Néel-type wall), displayed in Figure 4.17(b,c). These domains then rotate with varying field, until the walls lie perpendicular to the hard axis (or parallel to the easy axis). An increase in field in the opposing direction will rotate the domains by 90 degrees until the magnetisation lies parallel to the field. On the reverse path, similar behaviour was observed.

Although the 0.25 nm $Ni_{79}Fe_{21}$ seed layer sample has clear variation in easy and hard behaviour, the uniaxial anisotropy present in the film is much weaker than that of the thicker seed layer samples. This manifests itself when studying the micro-magnetic behaviour shown in Figure 4.17. The reversal process reveals a clear low angle wall formation that starts at a field of + 9 Oe (b), and remains until a reverse field of - 17 Oe (d) is applied. The low angle domain walls become higher in angle from (b) to (c), where the angle is then reduced again in (d).

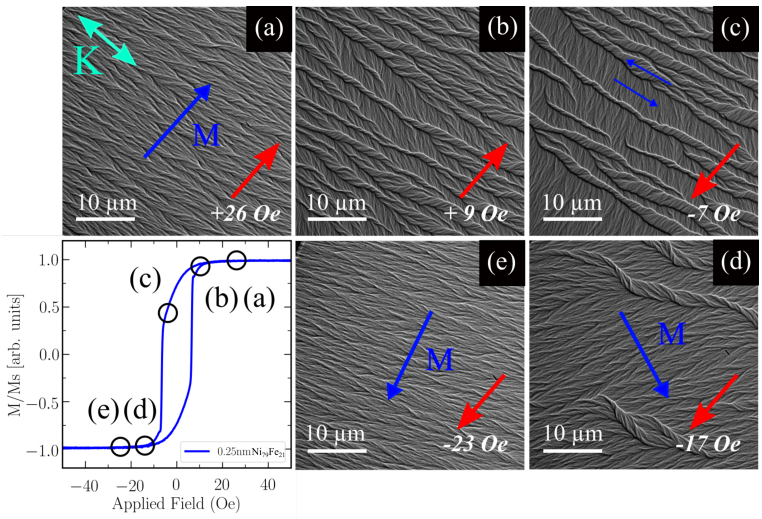

Figure 4.17: Fresnel images demonstrating the magnetisation reversal process along the hard axis of 10 nm $Ni_{45}Fe_{55}$ thin film with 0.25 nm $Ni_{79}Fe_{21}$. The red arrows represent the direction of the applied field, H, and K is the uniaxial anisotropy direction. The corresponding location of the Fresnel image is highlighted on the bulk B-H hysteresis loop. The acquired images show typical hard axis behaviour with a rotation of the magnetisation direction by 90 degrees with a reduced applied field, followed by domain formation which lies parallel to the easy axis.

0.5 and 1.0 nm $Ni_{79}Fe_{21}$ Seed Layer

Similar hysteresis processes were observed for 0.5 nm and 1.0 nm $Ni_{79}Fe_{21}$ seed layer films. There is minimal difference between the two films, so the following discussion will be an overview of both films behaviours. Fresnel images confirm an improvement in magnetic properties with respect to anisotropy. Due to an increase in the films uniaxial anisotropy, there was a reduction in the samples coercive field, and anisotropy field values, as expected from bulk measurements.

In Figures 4.18(b) and 4.19(b), the applied field is reduced to +11 and +8 Oe respectively. Both images show the ripple dispersion becoming greater, and magnetisation direction beginning to rotate, before domain wall nucleation in Figures 4.18 and 4.19(c). When there is no field present on the sample, a single domain wall appeared. The magnetisation of the domains lies parallel to the easy axis direction, which is typically hard axis behaviour for a thin film with a strong uni-axial anisotropy present (unlike that of the 0.25 nm seed layer sample exhibiting less ordered domain behaviour). The top domains seen in Figures 4.18 and 4.19(c) both increased in size with increasing field (in the opposing direction), gradually covering the whole area of the membrane, through the movement of the domain wall. A larger applied field forces the magnetisation direction from the easy axis direction, to the perpendicular hard axis like in Figures 4.18(d,e) and 4.19(d,e).

Hard Axis Fresnel Image Comparison

Figure 4.20 shows a direct comparison of hard axis behaviour between the seed layer samples. All experimental images shown here are taken at near zero applied field, having been reduced from a $+M_{Sat}$ field. The region is highlighted by the dots placed on the normalised BH loops presented in (a). The red arrows represent the direction of the magnetisation **M**. At near zero field, for all 3 samples shown in Figure 4.20(b,c,d), the magnetisation direction has rotated to lie parallel to the easy axis. The direction of the easy axis is highlighted by the green arrow, K. The addition of 0.5 and 1.0 nm $Ni_{79}Fe_{21}$ seed layers (Figure 4.20(c,d)) greatly reduces the

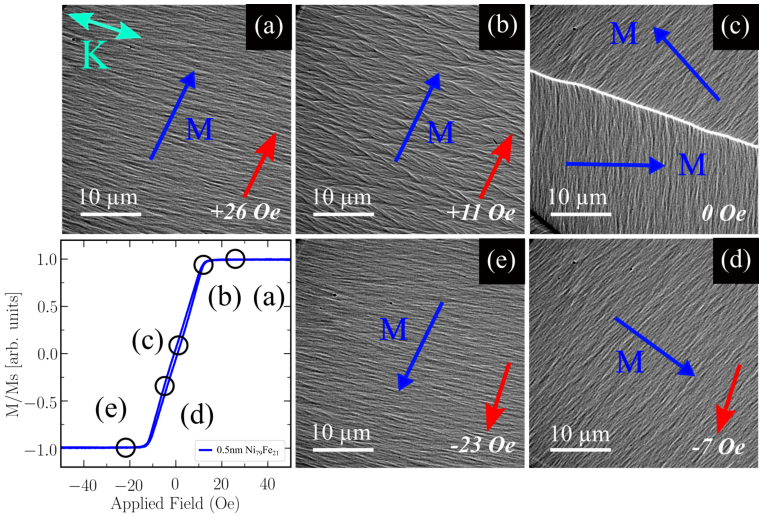

Figure 4.18: Fresnel images demonstrating the magnetisation reversal process along the hard axis of 10 nm $Ni_{45}Fe_{55}$ thin film with 0.5 nm $Ni_{79}Fe_{21}$. This followed typical hard axis behaviour with a rotation of the magnetisation direction by 90 degrees with a reduced applied field, with domain formation.

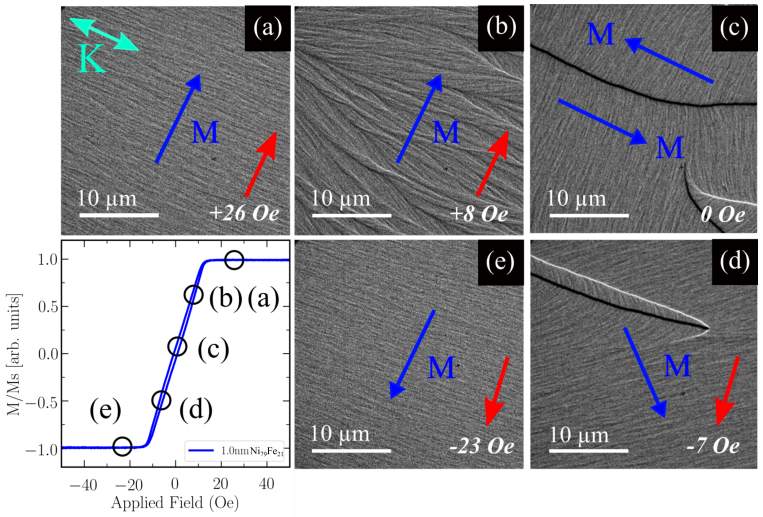

Figure 4.19: Fresnel images demonstrating the magnetisation reversal process along the hard axis of 10 nm $Ni_{45}Fe_{55}$ thin film with 1.0 nm $Ni_{79}Fe_{21}$. This followed typical hard axis behaviour with a rotation of the magnetisation direction by 90 degrees with a reduced applied field, with domain formation.

domain formation noise, and the ripple appears reduced when compared to 0.25 nm $Ni_{79}Fe_{21}$ seed layer sample (Figure 4.20(b)). Although, it is important to note the change in scale between Figure 4.20(b) and (c,d). This reiterates the improvement in magnetic properties, such as uniaxial anisotropy K_u and anisotropy field, H_K.

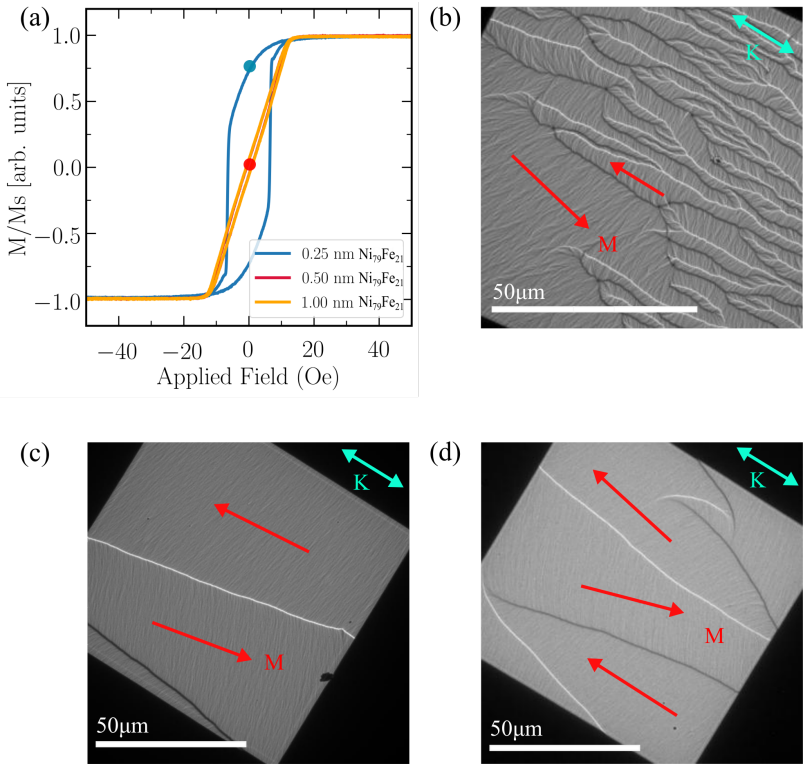

Figure 4.20: (a) Normalised B-H hard axis hysteresis plot for (b) 0.25 nm $Ni_{79}Fe_{21}$ seed layer, (c) 0.5 nm $Ni_{79}Fe_{21}$ seed layer, (d) 1.0 nm $Ni_{79}Fe_{21}$ seed layer 10 nm $Ni_{45}Fe_{55}$ thin films. Corresponding experimental Fresnel TEM images showing domain formation. All images were acquired at a near zero applied field when sweeping down from magnetisation saturation, highlighted by the dot on the hysteresis plot. Red arrows indicate the direction of magnetisation of individual domains. Green arrow indicates the easy axis direction, *K*. Visually displays the suppression of domain formation noise through the addition of ultra thin $Ni_{79}Fe_{21}$ seed layers.

4.6 Easy Axis Fourier Transform Analysis

Chapter 3 detailed a newly developed methodology for magnetisation ripple characterisation. It described how image processing techniques could be used to produce data in the Fourier space, which lead to more information being acquired about a specimens micromagnetic structure during magnetisation reversal processes.

The properties discussed in the following section are as follows: Dispersion angle θ, dominant ripple wavelength λ_{Dom}, spectroid ripple wavelength $\lambda_{Spectroid}$, and ripple image intensity *I*. All of the seed layer samples will be individually investigated as a function of applied field along the easy axis in the following sections. This will include a discussion into limitations of the automated analysis technique.

Outputs at key points in the hysteresis sequence will be directly compared for all samples in Section 4.6.5.

Section 4.7 provides further analysis and comparison between the seed layer samples when considering the change in properties as a function of field, specifically the exponent of easy axis trends going from the maximum applied field, up until just before the coercive field. This will be investigated for all seed layer samples (other than the unseeded isotropic film), and will also be compared to Hoffmann's theory for magnetisation ripple (Section 1.7).

4.6.1 Unseeded

Bulk magnetic measurements presented in Section 4.3 tell us that the unseeded $Ni_{45}Fe_{55}$ sample exhibits isotropic behaviour. This means it has little to no uniaxial anisotropy, with little variation between easy and hard axis behaviours. It has a measured coercive field, H_C of 18 Oe.

Fourier transform analysis for the unseeded sample as a function of field is shown in Figure 4.21. Dark and light purple refer to the sweep up and sweep down hysteresis sweeps respectively. The shaded area refers to the measured coercive field value H_C.

A FFT dispersion angle as large as 45° reflects the large dispersion visible from the experimental images previously shown (Figure 4.12). There is a gradual decrease in dispersion angle with increasing applied field, for both sweep up and sweep down loops, with the lowest value being at approximately 36°. This means the applied field was not large enough to reach a magnetisation saturation state as there is still substantial ripple present in the film. This is reflected through a maximum M/M_s value of 0.95 at a field of 26 Oe. Other analysis methods described in Chapter 3, such as dominant wavelength (Figure 4.21(b)), spectroid ripple wavelength (c,d), and image intensity (e), don't show significant changes between the ripple properties throughout a hysteresis sweep. The sample still shows significant micromagnetic ripple structure even at relatively high fields.

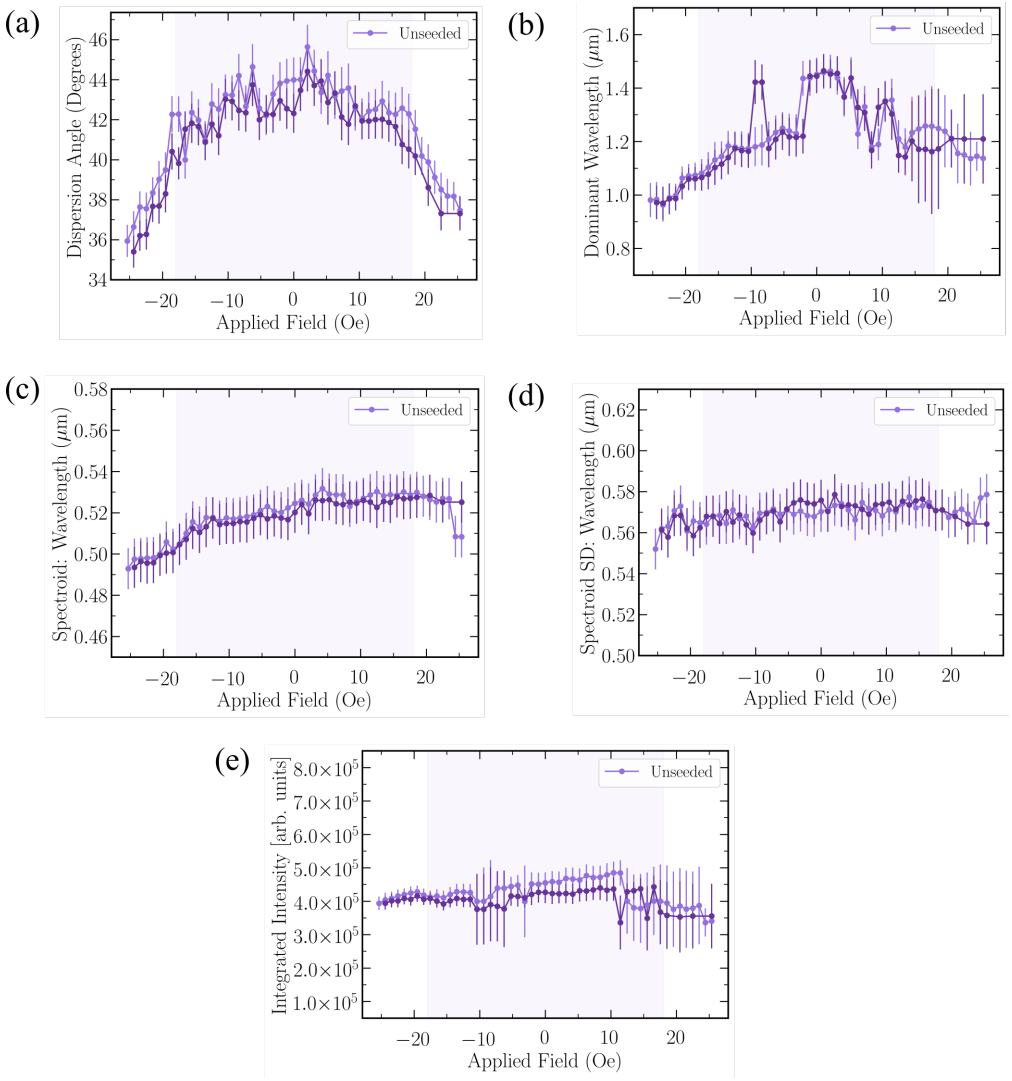

Figure 4.21: Ripple analysis outputs for a 10 nm $Ni_{45}Fe_{55}$ unseeded sample. The shaded area refers to the coercive field, H_C value. The two lines represent hysteresis loops that sweep up and down from M_{Sat}. Outputs are plotted against field for (a) dispersion angle θ, (b) dominant ripple wavelength λ_{Dom}, (c,d) spectroid ripple wavelength $\lambda_{Spectroid}$ and standard deviation respectively, and (e) ripple image intensity I.

4.6.2 0.25nm $Ni_{79}Fe_{21}$ Seed Layer

Fourier transform analysis outputs for the 0.25 nm $Ni_{79}Fe_{21}$ seed layer sample are presented in Figure 4.22. Results presented in (a)-(e) show similar characteristic behaviour with discontinuities observed at coercive fields. This is recognised by a sudden suppression of magnetic ripple properties as the coercive field H_C is reached and the magnetisation direction rapidly switches to the opposite direction. All analysis techniques showed the same distinctive steps at the coercive field of the

film. This region of $+H_C$ and $-H_C$ is highlight by the coloured blue box.

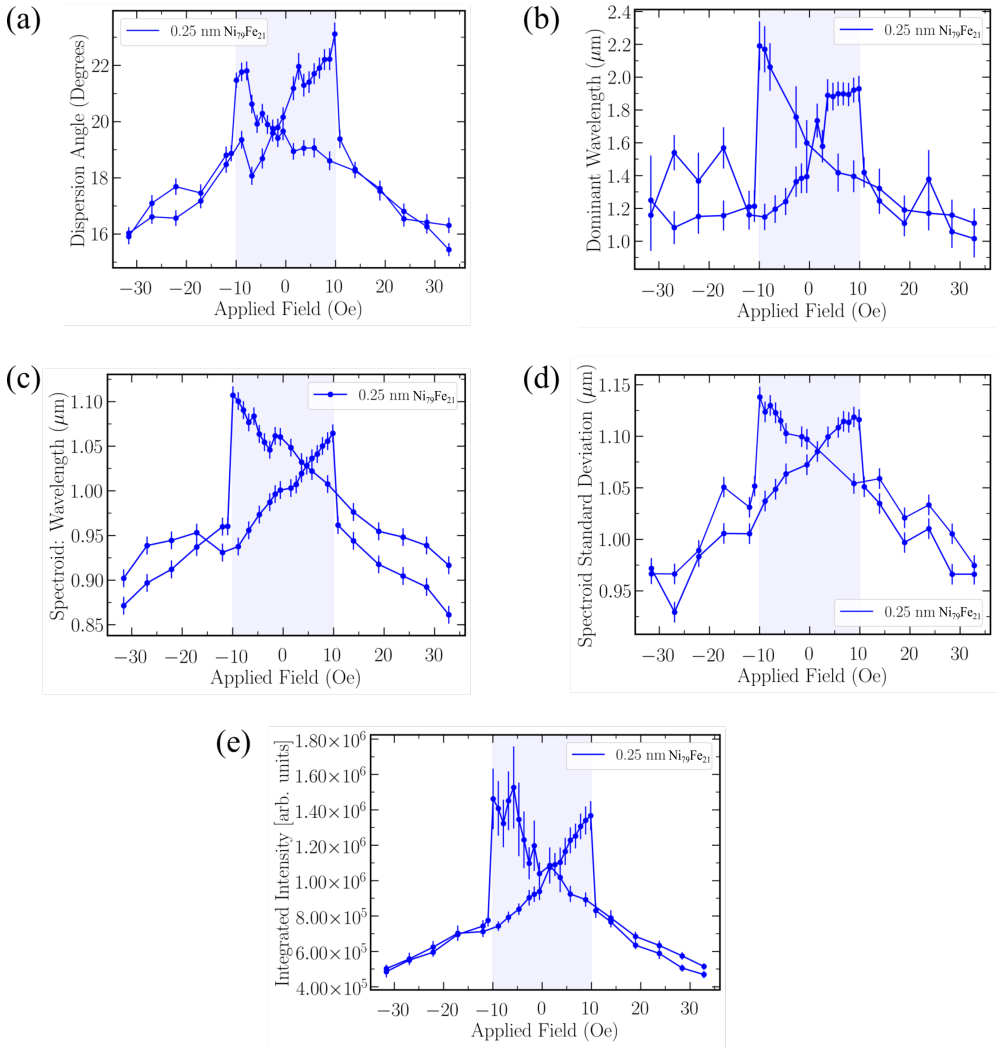

Figure 4.22: Analysis outputs for a a 10 nm $Ni_{45}Fe_{55}$ sample with a 0.25 nm thick $Ni_{79}Fe_{21}$ seed layer. Shaded area represents the experimental switching field H_C. The two lines represent sweep up and sweep down plots taken from -ve Msat to +ve Msat or the reverse, respectively. (a) FFT dispersion angle θ, (b) dominant ripple wavelength λ_{Dom}, (c) spectroid wavelength $\lambda_{Spectroid}$, (d) spectroid wavelength standard deviation and (e) integrated intensity I.

Figure 4.22(a) plots dispersion angle θ as a function of field for both a up and down hysteresis sweep. Results show a dispersion angle suppression from approximately 22° just before the switching field, to approximately 16° at an applied field that is larger than 30 Oe. This shows a significant suppression from the unseeded sample, roughly in the order of 50%. The dominant ripple wavelength results plotted in (b) show the same trend, whereby the ripple wavelength increases to

approximately 1.1 μm before switching, compared to a suppression of ripple to 0.55 μm at a field of $\approx$ 30 Oe. The spectroid ripple wavelength $\lambda_{Spectroid}$ plot shown in Figure 4.22(c) was a successful characterisation technique when measured as a function of field as it follows the same trend seen by other methods. The coercive field value for both sweeps is consistent, with both sweeps exhibiting a sudden drop off once a larger field is applied. An average spectroid wavelength value of 1.08 μm was measured at H_C, where is it reduced to 0.88 μm at a field of approximately 30 Oe, exhibiting a $\approx$ 20% drop.

The integrated intensity plot shown in Figure 4.22(e) confirms the trends shown by other characterisation methods with a significant reduction in the intensity with increasing applied field. At H_C, the integrated intensity has a maximum value in the order of 1.5 x 10^6, which reduces to 5 x 10^5 (arb. units) with an applied field of $\approx$ 30 Oe, a substantial drop of 67%. This dramatic change in values can be analysed further and results will be presented in Section 4.7.

4.6.3 0.5nm $Ni_{79}Fe_{21}$ Seed Layer

The same analysis techniques were use on 0.5 nm $Ni_{79}Fe_{21}$ seed layer sample, and are shown in Figure 4.23. For samples with weak ripple contrast, the dispersion angle measurements break down. Figure 4.23(a) seems to indicate that the dispersion angle decreases as the coercive field is approached. This is the opposite of what is expected and seen in the experimental Fresnel images themselves (Figure 4.14(a-c)). Therefore it can be concluded that this measurement is unreliable for this sample. However, the results show there is still a significant reduction in the measured dispersion angle, of approximately 50% when compared with the 0.25 nm sample, with a ripple angle in the range of 11 to 13°.

Other measurements were successful. We see a suppression of dominant ripple wavelength from 0.86 μm at H_C, to $\approx$ 0.6 μm at a field of 30 Oe in Figure 4.23(b). This also shows an approximate suppression of 50% when compared to the 0.25 nm seed layer sample results. Figure 4.23(c) gives a spectroid ripple wavelength

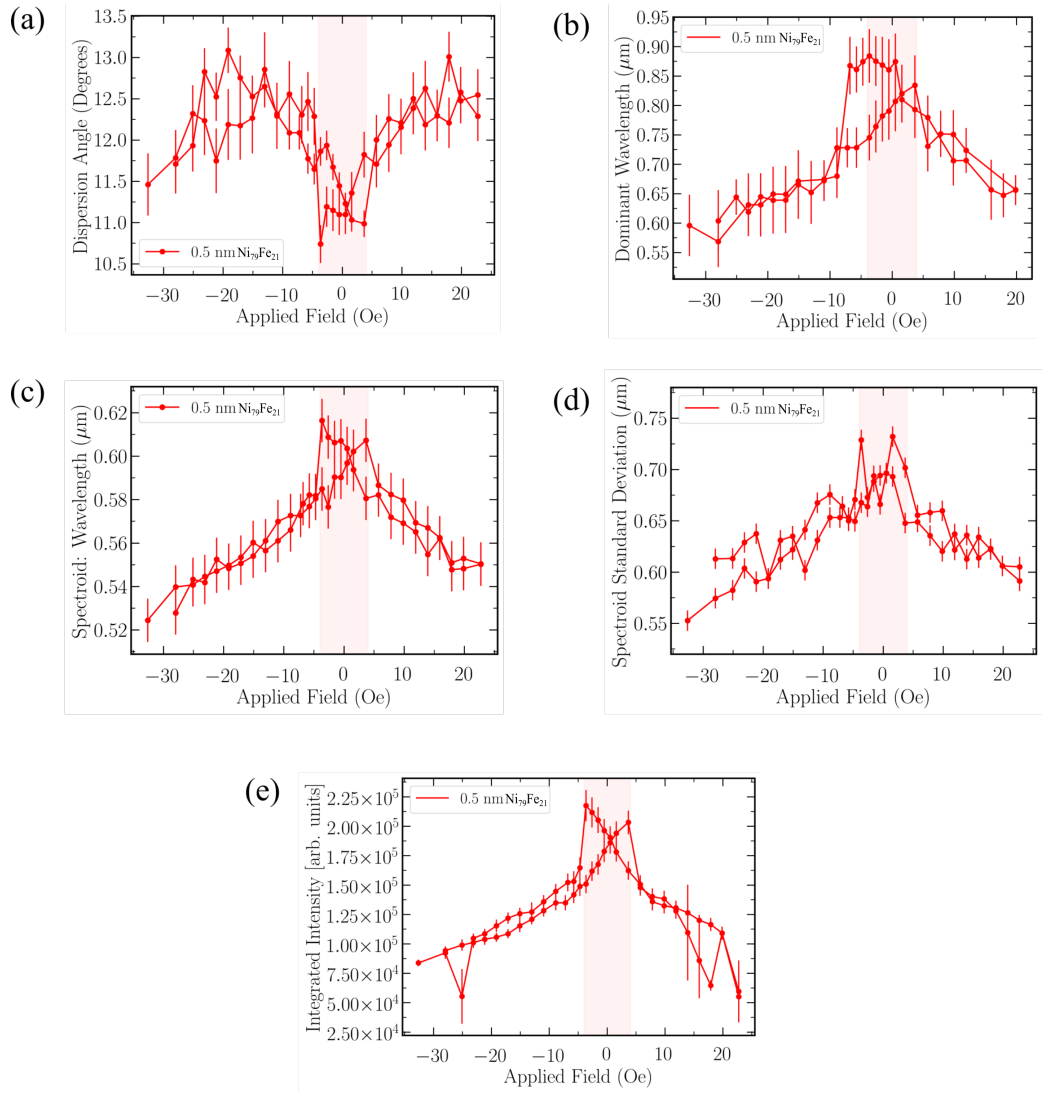

Figure 4.23: Analysis outputs for a 10 nm $Ni_{45}Fe_{55}$ sample with a 0.5 nm thick $Ni_{79}Fe_{21}$ seed layer. Shaded area represents the switching field H_C. The two lines represent sweep up and sweep down plots taken from -ve Msat or +ve Msat respectively. (a) FFT dispersion angle θ, (b) dominant ripple wavelength λ_{Dom}, (c) spectroid wavelength $\lambda_{Spectroid}$, (d) spectroid wavelength standard deviation and (e) integrated intensity I.

$\lambda_{Spectroid}$ of 0.62 μm at the coercive field that reduces to 0.55 μm at an applied field of approximately 30 Oe. This results in $\approx$ 40% suppression of spectroid ripple properties when compared to the 0.25 nm seed layer sample results.

The image integrated intensity results shown in Figure 4.23(e) arguably show the most successful outputs due to the smooth line plots when compared to other methods presented even when analysing images of low ripple contrast (towards magnetisation saturation). The gradual increase of ripple contrast with reducing

applied field is as expected. It also shows an overall reduction when compared to the 0.25 nm sample. However, all outputs shown are in agreement with the measured H_C value or +/- 4 Oe, as highlighted by the red box.

4.6.4 1.0nm $Ni_{79}Fe_{21}$ Seed Layer

The results shown in Figure 4.24 are outputs from the experimental images exhibiting the weakest, or most suppressed magnetisation ripple properties. This is reflected in outputs, (a) - (e), as the variation between the images is harder to determine.

Generally, the measured dispersion angle is slightly smaller than that of the 0.5 nm $Ni_{79}Fe_{21}$ seed layer sample. However, similarly to the 0.5 nm results, there appears to be a breakdown of the analysis of the magnetisation ripple as the film gradually reaches a more saturated state with larger applied fields (larger than 30 Oe) as shown in Figure 4.24(a). This again highlights that there is a limit to a successful dispersion angle determination, whereby the contrast and angle must be large enough to gain accurate outputs. Figure 4.24(b) shows that the dominant wavelength determination also became more difficult to measure with weaker ripple properties. The associated errors also increase with decreasing ripple properties. The spectroid wavelength analysis presented in (c,d) and the integrated intensity (e) appear to be successful methods even with reduced ripple properties. There is a subtle suppression of 10% when comparing the 0.5 and 1.0 nm spectroid wavelength outputs. This is reiterated by a subtle suppression between the two samples when looking at the integrated intensity values. More details of these exact values for direct comparison will be discussed in the following section.

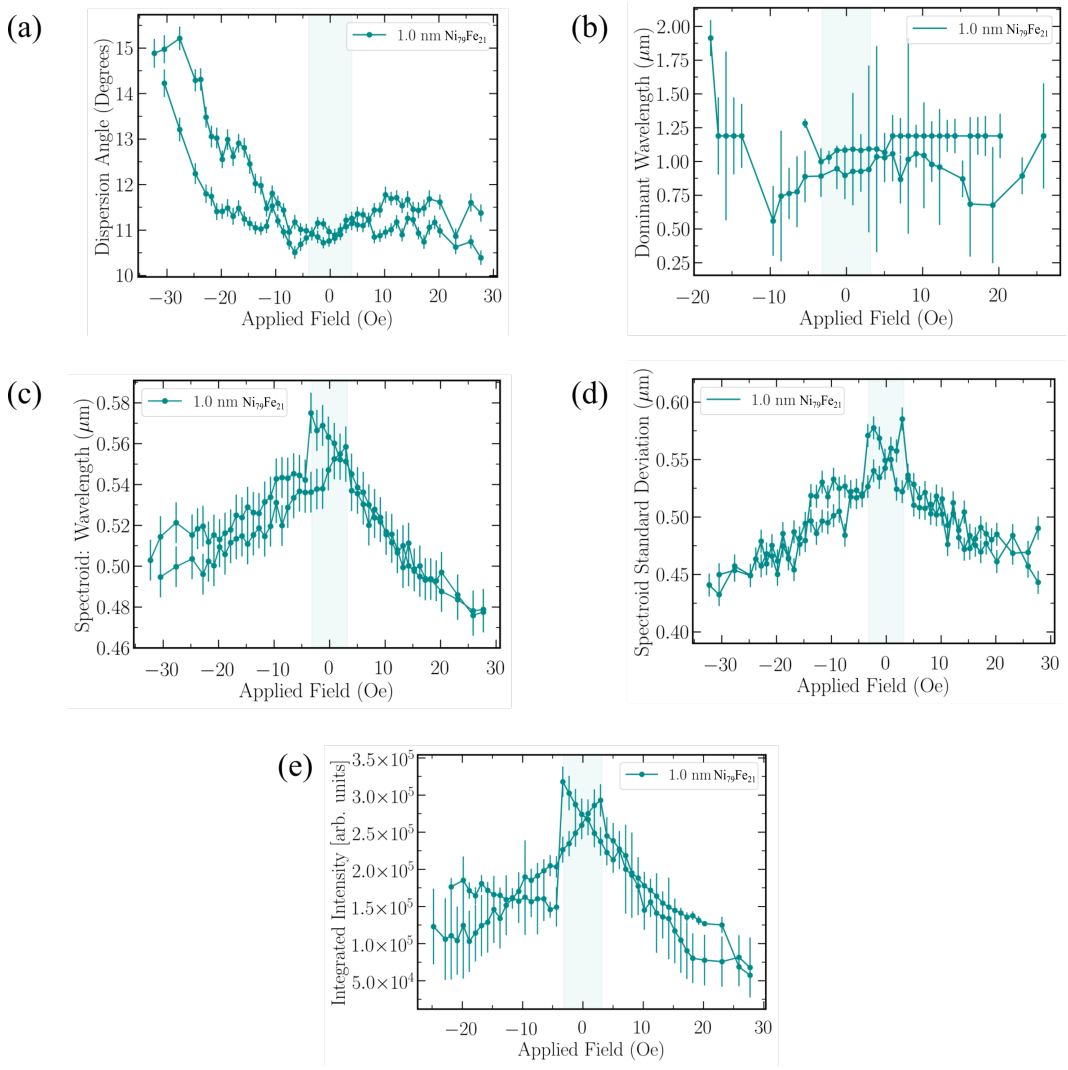

Figure 4.24: Analysis outputs for a a 10 nm $Ni_{45}Fe_{55}$ sample with a 1.0 nm thick $Ni_{79}Fe_{21}$ seed layer. Shaded area represents the experimental switching field H_C. The two lines represent sweep up and sweep down plots taken from -ve Msat to +ve Msat or the reverse, respectively. (a) FFT dispersion angle θ, (b) dominant ripple wavelength λ_{Dom}, (c) spectroid wavelength $\lambda_{Spectroid}$, (d) spectroid wavelength standard deviation and (e) integrated intensity I.

4.6.5 Comparison of Magnetisation Ripple for increasing $Ni_{79}Fe_{21}$ seed layer thickness

Figures 4.25 and 4.26 show a direct comparison of the $Ni_{79}Fe_{21}$ seed layer samples properties along the easy axis at (a) the coercive field and (b) at an applied field of 24 Oe, for dispersion angle θ and spectroid ripple wavelength $\lambda_{Spectroid}$ respectively. A field of 24 Oe was chosen as it is the largest applied field, and therefore closest

to a magnetisation saturation state.

Figure 4.25 shows that there is a gradual decrease in dispersion from the mean magnetisation direction with increasing seed layer thickness. This is consistent for both measurements taken at the coercive field value (a) and an applied field of 24 Oe (b). Additionally, there is a suppression of the dispersion angle for each sample from H_C to 24 Oe. It is important to note that the 0.5 nm and 1.0 nm dispersion outputs are equal for 24 Oe measurements as there appears to be a minimum dispersion angle that can be determined accurately. Exact values are shown in Table 4.5.

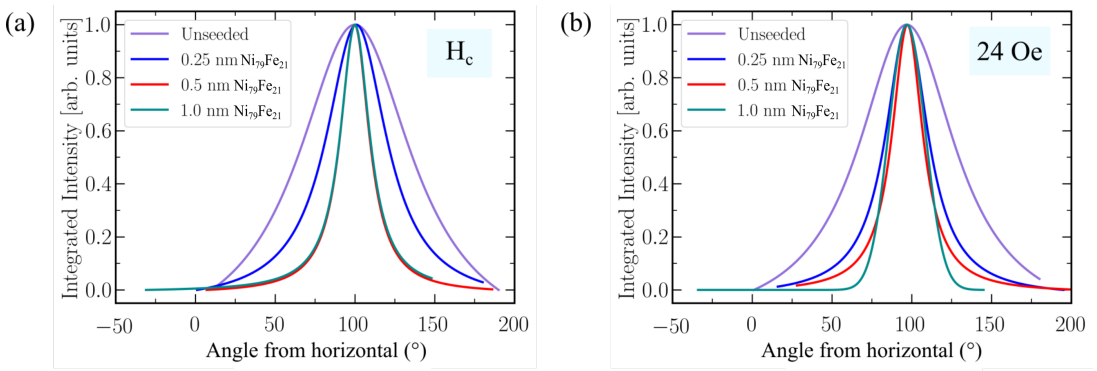

Figure 4.25: FFT analysis comparison for varying thickness of $Ni_{79}Fe_{21}$ seed layers. Figures (a,b) display the suppression of the dispersion angle from the magnetisation **M** direction with increasing seed layer thickness, using the Lorentzian fitting method as described in Chapter 3.6.2. (a) is measured at the samples coercive field H_C before switching, where as (b) is measured at a field of +24 Oe approaching magnetisation saturation.

Figure 4.26 shows the integrated intensity outputs at the same conditions. The spectroid weighted average value is indicated by the coloured vertical line. Both figures in (a) and (b), which represent the coervice field and an applied field of 24 Oe respectively, follow the same trend. There is an increase of the weighted average wavelength value (in Fourier space) with increasing seed layer thickness. Additionally, there is an increase in the k-space output with increasing field i.e. smaller ripple wavelength. There also is a decline in the image integrated intensity (y-axis), which is expected due to the reduced image contrast. The quantitative outputs of these plots are highlighted in Table 4.5, including magnetic ripple properties at remanence.

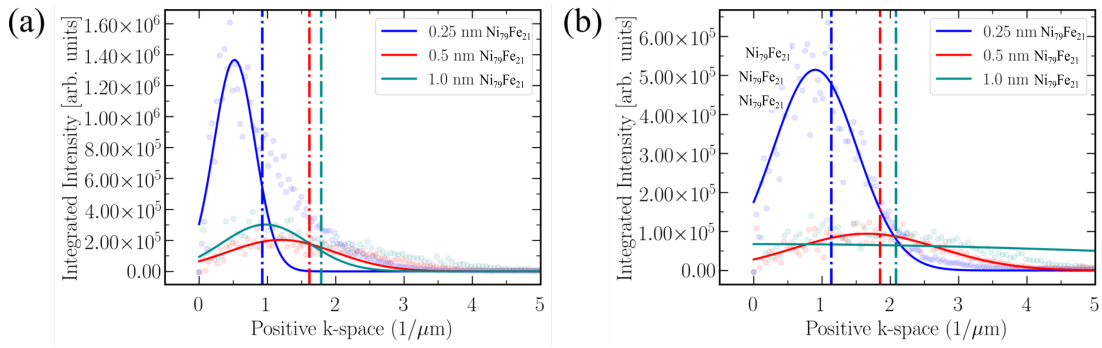

Figure 4.26: FFT analysis comparison for varying thickness of $Ni_{79}Fe_{21}$ seed layers. (a) is measured at the samples coercive field H_C before the switch in magnetisation direction, where as (b) is measured at a field of 24 Oe approaching magnetisation saturation. Figures (a,b) show the shift of the central spectroid in k-space with increasing field. There is also a note-able decrease in the images integrated intensity peak with increasing seed layer thickness.

The addition of a 1.0 nm thick $Ni_{79}Fe_{21}$ seed layer can suppress the ripple wavelength from 1.08 μm to 0.56 μm when comparing 0.25 and 1 nm thick seed layers, both measured at the films coercive field (>50% decrease). The same trends were seen for the dispersion angle measurements, seeing a reduction from 42.5° to 11.0° with a 0.5 and 1.0 nm seed layer. However, with a reduction of FFT dispersion angle, the analysis technique breaks down when determining accurate angle outputs, and therefore produces larger associated errors. This is possibly due to two reasons: (a) Reduced contrast in the FFT image and (b) difficulty in measuring variations in a reduced width bow-tie structure. It is suggested there is possibly a limiting angle factor when measuring the FWHM values successfully. For results presented here, there is a breakdown of dispersion angle determination at approximately $<$ 11 degrees.

Seedlayer Thickness (nm)	Dispersion Angle θ (∘)			Spectroid Wavelength λ (μm)		
	H_C (Oe)	0 Oe	30 Oe	H_C (Oe)	0 Oe	30 Oe
0.00	42.5	42.0	36.5	1.10	1.10	1.08
0.25	22.5	19.0	16.0	1.08	1.00	0.88
0.50	11.0	11.0	11.5	0.62	0.60	0.54
1.00	11.0	11.0	11.0	0.56	0.54	0.48

Table 4.5: Key outputs from ripple analysis. The ripple dispersion angle and wavelength was investigated as a function of field, applied along the easy axis. Table includes outputs for each seed layer sample at an applied field of 24 Oe, remanence and at the corresponding coercive field H_C before the switch in magnetisation direction.

4.7 Discussion

As previously discussed in Section 1.7, Hoffmann derived a theoretical model for magnetisation ripple properties [9]; Dispersion angle θ and dominant ripple wavelength λ.

Hoffmann determined that the dispersion of the magnetisation depends on the dispersion of the anisotropy, on the magnetic constants of the film, on the thickness of the film and on the applied field. He predicted that an estimate of the mean value of magnetisation dispersion when applying a field along the easy direction, θ, can be given by:

$$\theta = \frac{1}{4\pi^{\frac{1}{2}}} \frac{DK}{(2t)^{\frac{1}{4}} M^{\frac{1}{2}}} \cdot \frac{1}{(AK_u(h+1))^{\frac{3}{8}}} \tag{4.3}$$

Where D is the mean grain size of the polycrystalline film, t is the film thickness, K is the crystal anisotropy constant, M is the saturation magnetisation, K_u is the uniaxial anisotropy constant, and $h = H/H_k$, which is referred to as the reduced field. Therefore Hoffmann predicted there would be a increase in ripple dispersion with increasing grain size and overall uniaxial anisotropy amongst other factors.

Hoffmann used the following theoretical formula for determining the longitudinal ripple wavelength when an external field is applied along the easy axis:

$$\lambda_E = 2\pi \left(\frac{A}{K_U}\right)^{\frac{1}{2}} (h+1)^{-\frac{1}{2}} \tag{4.4}$$

where A is the exchange constant, $K_u = MH_k/2$ is the uniaxial anisotropy constant. It can therefore be predicted that a film would exhibit increased magnetisation ripple wavelength with decreased uniaxial anisotropy.

Seedlayer (nm)	D (nm)	t (nm)	K (J/m^3)	M (A/m)	A (J/m)	K_u (J/m^3)
0.00	10	10.00	1×10^3	11.1×10^5	1.3×10^{-11}	116
0.25	5	10.25	1×10^3	11.4×10^5	1.3×10^{-11}	250
0.50	3	10.50	1×10^3	11.6×10^5	1.3×10^{-11}	766
1.00	2	11.00	1×10^3	11.6×10^5	1.3×10^{-11}	796

Table 4.6: Values used in Hoffmann's equations (4.3) and (4.4) for different seed layer samples. All inputs were acquired from sample data and experimental measurements, except the exchange constant A which is assumed from literature.

These two theoretical predictions can be plotted as a function of the reduced field, h, using the experimental values obtained from previously discussed sections. The examples given in Figure 4.27 relate to easy axis behaviour.

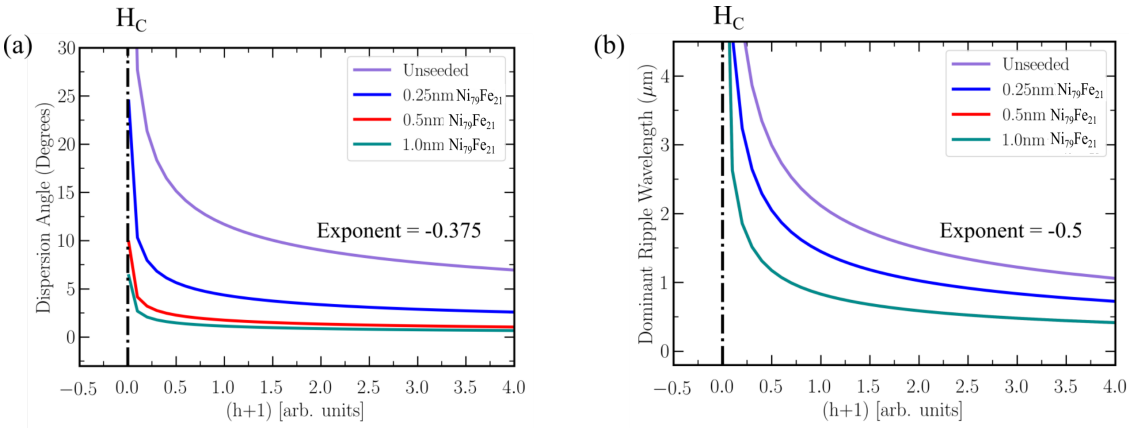

Figure 4.27: Predictions of Hoffmann's theory using parameters in Table 4.6 for seed layer samples. (a) dispersion angle θ and (b) dominant ripple wavelength λ. Note, in (b) the red and green plots overlap. These plots refer to a reduction in applied field from near magnetisation saturation, until the coercive switching field is reached.

Hoffmann's ripple theory is a fairly simple model and predicts simple behaviour. In this work an empirical study was undertaken for magnetisation ripple for films of different physical and magnetic properties.

Values given through theoretical models often aren't consistent with experimental results. This is because they don't consider real-world physical problems that come with experimental procedures, such as measurement limitations. An example of this is the difficulty of imaging a Fresnel image along the easy axis, before the switch of magnetisation direction at the coercive field H_C. A simple correction involves shifting the reduced field to start at 0.5 (h+1) rather than zero. This equates to approximately 1 degree tilt (or around 1 Oe) away from the switching field value. As discussed earlier, the remanent field of the objective lens present in the microscope is 60 Oe. However, there is a good agreement with Hoffmann's theory in that there is a reduction in magnetisation ripple properties with increasing applied field. A way to investigate the trends of the experimental results presented in Section 4.6 is to measure the exponents of the curves, and compare them to that of the theory. These curves relate to the transition from magnetisation saturation to the coercive switching field through a reduction in applied field. The unseeded sample showed isotropic behaviour so does not fit the criteria for this theoretical model and will be omitted from the following discussion. As the dispersion angle results for the more suppressed ripple present in the 0.5 and 1.0 nm seed layer samples was not reliable at higher fields, they will also be omitted from the discussion.

Figure 4.28 shows fitting to experimental results for the dispersion angle θ of the 0.25 nm $Ni_{79}Fe_{21}$ seed layer sample. (a) Shows the best fit exponent of -0.17, which gives the best fit to the data, but with half the exponent predicted by theory (-0.375).

The exponent line in Figure 4.28 can be compared to that predicted of theory, displayed by the blue line in Figure 4.27. There is a substantial increase in the experimental measurements for dispersion angle, with a near 200% increase when comparing at a reduced field (h+1) of 4. Hoffmann's theory predicts a dispersion angles < 5 degrees when inputting with experimental values. It has been shown in Section 4.5.2 from experimental Fresnel images that the predicted value is incredibly small and not realistic. Simulations presented in Chapter 5 aims to investigate how changes in parameters such as grain size, anisotropy and exchange constant can change dispersion angle outputs. The goal for this will be to fine-tune the

simulation input parameters to best match the experimental results, and then to discuss how the theory can be modified to produce similar predictions.

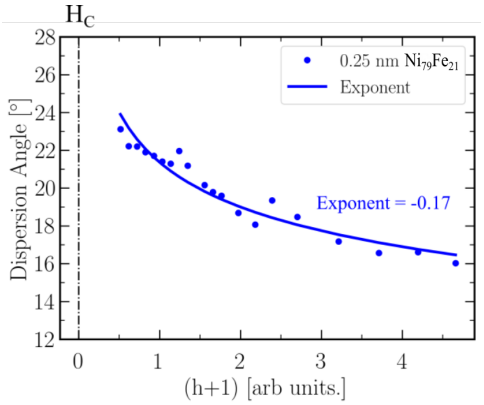

Figure 4.28: Best-fit exponent analysis for dispersion angle of the 0.25 nm $Ni_{79}Fe_{21}$ seed layer sample.

Figure 4.29 shows the measured exponents from the best fit lines for (a) spectroid wavelength and (b) dominant wavelength. Out of the 2 outputs presented in Figure 4.29, the ripple spectroid (a) produced exponents that were the furthest away from theory predictions. The wavelength approximations were an order of magnitude less. This is as expected as predictions made by Hoffmann are approximations for the dominant ripple wavelength value, and not the weighted average. The spectroid results have less of a variation with field, and behave more like a linear trend.

There is relatively good agreement when directly comparing Hoffmann's theory to experimental outputs for dominant ripple wavelength. When comparing at a reduced field (h+1) of 4 for the 0.25 nm seed layer sample, the wavelength value is measured as 1.2 μm and 0.75 μm for experiment and theory respectively. For the 0.5 and 1.0 nm seed layer samples who exhibit similar properties, the wavelength value is 0.7 μm and 0.4 μm for experiment and theory respectively. Similarly to dispersion angle, a simulation investigation into how input parameters such as anisotropy and the exchange constant can vary ripple wavelength will be presented in Chapter 5.

Figure 4.29(a,b) reiterates the large suppression of ripple wavelength through the addition of seed layers. There is little variation between results presented for the 0.5 and 1.0 nm seed layer samples, highlighted by the lines in green and red. This

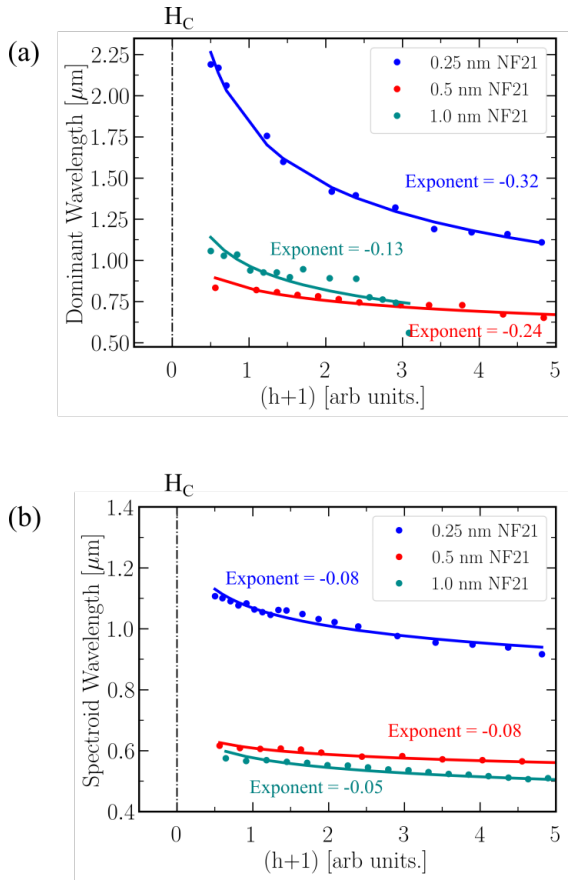

Figure 4.29: Curve fitting of experimental results (a) spectroid ripple wavelength and (b) dominant ripple wavelength, with measured exponents on plots.

confirms seed layers of additional thickness (larger than 1 nm) are less likely to suppress magnetisation ripple properties further. Generally, the exponent outputs were further from theory for the 0.5 and 1.0 nm seed layer samples. This would be expected, as it has been confirmed from both bulk and micro-magnetic measurements that the coercive field is much lower ($\approx$ 3 Oe) than that of the unseeded and 0.25 nm seed sample. This means it is more challenging to successfully acquire Fresnel images before the switching field is reached.

Micromagnetic simulation of magnetisation ripple will be a useful tool when trying to gain better understanding of how specific parameters effect ripple properties. For example, Hoffmann's theory of magnetisation ripple has given a single value for a materials exchange constant. This assumes 100% coupling between the grains. In reality this percentage could be much lower. This is something that will

investigated through simulations presented in Chapter 5. Other parameters used in Hoffmann's theory, such as grain size, and anisotropy will also be investigated in detail will the aim of producing simulation outputs that match experimental results presented in this chapter.

4.7.1 Comparison of magnetisation ripple along the hard and easy axis

An additional observation was the variation in the magnetisation properties along the hard and easy axis. Hoffmann's theory for magnetisation ripple also predicts that there will be a subtle suppression of ripple properties along the easy axis, when compared to the hard axis with the same exact applied field. This theory could easily be empirically investigated for films of different physical and magnetic properties, in this case seed layers of different thickness's. Magnetisation ripple analysis was completed along both the easy and hard axis sequences, at an applied field of $\approx$ 24 Oe for all seed layer samples with a defined uniaxial anisotropy. The unseeded sample exhibited isotropic behaviour so will be omitted from the discussion. Table 4.7 summarises the results. Hoffmann's theory of a slight hard axis suppression was confirmed experimentally by all 3 seed layer samples, through all 5 characterisation methods. Specifically, Hoffmann predicted a 30% reduction in easy axis dominant ripple wavelength values, when compared to hard axis values at the same field. Experimentally, this reduction was slightly lower, at 12% and 24% for the 0.25 and 0.5 nm samples respectively. However, overall theory and experiment are in relatively good agreement.

Table 4.7 also summarises main result outputs, with a direct comparison between the seed samples and their corresponding ripple properties. All analysis techniques display the same conclusions: there is a large suppression of ripple properties when increasing seed layer thickness from 0.25 nm to 0.5 nm, and this effect seems to plateau with the addition of a thicker seed layer, in this case 1.0 nm.

Analysis OutPuts	0.25 nm seed		0.5 nm seed		1.0 nm seed	
	EA	HA	EA	HA	EA	HA
θ (°)	16.3	16.2	11.7	11.0	11.0	11.0
Spectroid (μm)	0.92	0.96	0.52	0.58	0.48	0.5
Spectroid SD (μm)	2.18	2.30	1.22	1.40	0.98	1.08
Intensity [arb. units]	5.1 x 10^5	6.5 x 10^5	9.4 x 10^4	2.0 x 10^5	5.8 x 10^4	1.9 x 10^5
Wavelength (μm)	1.08	1.28	0.60	0.74	0.58*	0.66

Table 4.7: Ripple analysis outputs; Easy axis and hard axis comparison for all seeded $Ni_{45}Fe_{55}$ samples at an applied field of 24 Oe. Theory predicts a suppression of magnetisation ripple along the easy axis, when compared to the same field applied along the hard axis. *Automated analysis failed to characterise wavelength values smaller than 0.3 μm. This value was taken from a field of 20 Oe.

4.8 Summary and Conclusions

This chapter shows the influence of ultra-thin $Ni_{79}Fe_{21}$ seed layers on the microstructure of thin $Ni_{45}Fe_{55}$ films with soft magnetic properties. Different stack thickness's were observed to vary in both physical and magnetic structures. Dark-Field TEM images show that the co-sputtered films follow a typical log-normal distribution. An addition of ultra-thin seed layers drastically reduces the average grain size of the film from 10.2 nm to 1.7 nm, and reduces grain size variation. Crystal structure and film texture could be detected from the splitting of the diffraction rings in SAED images. The addition of seed layer reduces texture in the film, meaning the films grains are randomly oriented in 3 dimensions. Bulk magnetic measurements were taken using a B-H looper. The unseeded sample showed near isotropic behaviour. The addition of seed layers produced well-defined uni axial hysteresis loops, with decreasing easy axis coercivities H_C, and an increase in the anisotropy field H_K.

We have demonstrated how the Fresnel mode of Lorentz microscopy can be used to provide a detailed description of the magnetisation reversal processes of four different NiFe thin films. It allows for direction visualisation of micromagnetic processes during magnetisation reversal, allowing for a more detailed insight when being compared with standard bulk B-H measurements.

Polycrystalline thin films exhibit a phenomenon called magnetisation ripple. A method was proposed for characterisation in two ways; the ripple dispersion and

wavelength. The unseeded 10 nm $Ni_{45}Fe_{55}$ sample exhibited very pronounced ripple with large amount of dispersion and a large ripple wavelength. The addition of $Ni_{79}Fe_{21}$ seed layers as thin as 0.25 nm can suppress the ripple wavelength by 50% when measured at the films coercive field. The addition of a thicker seed layer, 1.0 nm, suppresses the ripple wavelength by another 50% when compared to the 0.25 nm sample. The 0.5 nm and 1.0 nm samples had a very subtle suppression of magnetic properties, suggesting a thicker seed layer sample would not improve magnetic properties further (such as a reduction the coercive field). The same trends were seen for the dispersion angle measurements. There was a suppression of the magnetic ripple properties along the hard axis when being compared to easy axis measurements at the same applied field. This is consistent with classical ripple theory proposed by Hoffmann. The dramatic effect of seed layer addition suggests that the film is a good candidate for controlling both the physical and magnetic properties of $Ni_{45}Fe_{55}$ thin films, whilst maintaining a high magnetic moment density.

4.9 References

[1] G. Herzer, Grain size dependence of coercivity and permeability in nanocrystalline ferromagnets, Magn. IEEE Trans. On, vol. 26, no. 5, pp. 1397-1402, (1990).

[2] C. L. Platt, A. E. Berkowitz, D. J. Smith, and M. R. McCartney, Correlation of coercivity and microstructure of thin CoFe films, J. Appl. Phys., vol. 88, no. 4, p. 2058, (2000).

[3] R. M. Bozorth, Ferromagnetism, Reissue. New York: IEEE Press, pp. 109, (1993)

[4] P. C. Andricacos and N. Robertson, Future directions in electroplated materials for thin-film recording heads, IBM J. Res. Dev., vol. 42, no. 5, pp. 671-680, (1998).

[5] N. Robertson, H. L. Hu, and Ching Tsang, High performance write head using NiFe 45/55, IEEE Trans. Magn., vol. 33, no. 5, pp. 2818-2820, (1997).

[6] Y. Fu, T. Miyao, J. W. Cao, Z. Yang, M. Matsumoto, X. X. Liu, and A. Morisako, Effect of Co underlayer on soft magnetic properties and microstructure of FeCo thin films, J. Magn. Magn. Mater., vol. 308, no. 1, pp. 165-169, (2007).

[7] H. S. Jung, W. D. Doyle, and S. Matsunuma, Influence of underlayers on the soft properties of high magnetization FeCo films, J. Appl. Phys., vol. 93, no. 10, p. 6462, (2003).

[8] H. S. Jung, W. D. Doyle, J. E. Wittig, J. F. Al-Sharab, and J. Bentley, Soft anisotropic high magnetization Cu/FeCo films, Appl. Phys. Lett., vol. 81, no. 13, p. 2415, (2002).

[9] H. Hoffmann. Theory of Magnetisation Ripple. *IEEE Transactions on Magnetics*, 4(1):32-38, (1968).

5

Simulation Modelling of Magnetisation Ripple

Contents

5.1 Introduction

Magnetisation ripple is a phenomenon possessed by ferromagnetic polycrystalline thin films, that can be studied through visual inspection of Fresnel images. [1,2,3]

Usually, simulations are used alongside experimental images to help gain an understanding of the micromagnetic properties. However, simulation of this phenomenon has been somewhat limited. [4,5] The work presented in this chapter details development of micromagnetic models with the aim of replicating magnetisation ripple effects in a permalloy thin film.

It must be noted that although micromagnetic simulations act as a guide in conjunction with experimental results, they do not provide a reliable predictive tool. For example, finite difference simulations use geometrically perfect elements (cells) of uniform thickness, where as in reality the granular structure will be irregular. Another difference is the simulation of hysteresis loops, whereby the field changes in defined step sizes rather than a gradual change during experiments. As a result it is expected that the micromagnetic simulations will differ at some level. Despite this, simulations are a useful tool in understanding observed behaviour and determining trends.

The aim for this project is to implement MuMax^3 for modelling of local grains in a polycrystalline film exhibiting their own randomly orientated anisotropy. In addition to this, the film should also possess its own uniaxial anisotropy K_u in order to simulate the effect of magnetisation ripple.

Two different models have been developed to simulate magnetisation ripple properties, with the aim of replicating the experimental trends between samples of increasing seed layer thickness presented in Chapter 4. Section 5.2 introduces a 'Granular Magnetocrystalline Anisotropy Axis Variation model', which has a limited directionality variation about a fixed axis, whilst Section 5.3 introduces a more sophisticated magnetisation ripple model which has two independent contributions for global and granular anisotropy. As described in Section 1.7, the interaction of the granular magnetocrystalline anisotropy K_g and the global uniaxial anisotropy K_G gives rise to magnetisation ripple effects. A reminder of the magnetisation ripple origin schematic is shown in Figure 5.1. This chapter will investigate the merits of both the models described. The latter model exhibits a more realistic

set-up but the former may give some insight and introduction into the effect of local variations of magnetocrystalline anisotropy on micromagnetic structures. This chapter will investigate the validity of both the models described.

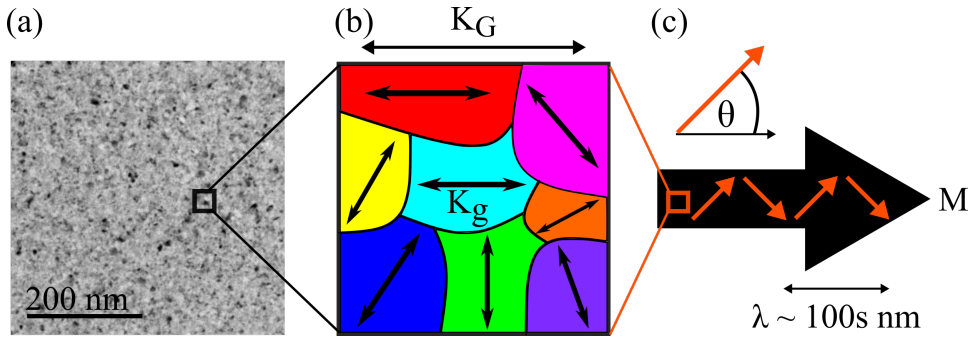

Figure 5.1: Schematic of magnetisation ripple origin. (a) $Ni_{80}Fe_{20}$ bright field TEM image, showing a granular structure, expected from a polycrystalline thin film. (b) The random direction of the granular crystalline anisotropy K_g, with an additional global uniaxial anisotropy K_G. (c) Schematic of the magnetisation fluctuations, producing low-angle domain walls, commonly referred to as magnetisation ripple, where the length scale is in the order of 100s nm.

5.2 Granular Magnetocrystalline Anisotropy Axis Variation

5.2.1 Simulation Method

Figure 5.1 is a simplified schematic of the physical origin of magnetisation ripple. It is formed by 2 independent anisotropy factors: first a granular anisotropy that is present in each grain and can be in any direction, and a global uniaxial anisotropy that is along a specified direction. The former is inherent and relates to the magnetocrystalline anisotropy of the material (Section 1.4.4), whereas the latter is induced during the material growth or annealing processes (Section 1.4.5). Anisotropies are key factors in determining the magnetisation state of the thin film. In this proposed model we consider the resultant anisotropy in each grain, where all grains will have the same magnitude of K, where K varies with direction. K acts more like the larger and dominant induced anisotropy K_G for the experimental

films seen in Chapter 4. A modified schematic of Figure 5.1(b) highlighting the simulation of anisotropy contributions for each grain is shown in Figure 5.2.

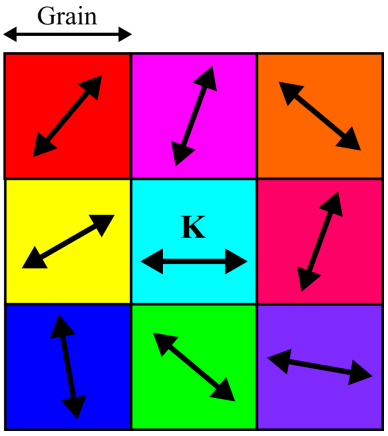

Figure 5.2: MuMax[3] simulation set-up for the granular magnetocrystalline anisotropy axis variation model. Each grain is assigned a fixed K value. The orientation of the anisotropy directionality is controlled using the angular variation parameter.

Simulation Set-Up

This model is based on creating a deviation of the magnetisation from a specified direction. It is important to note that this is a 2D simulation model, so there will be no contribution in the z-direction i.e. only simulated for the in-plane anisotropy components. The initial mean direction was set as a constant, and refers to the x-axis, or along the (100).

The parameter that introduces the directional deviation, is referred to as the angular anisotropy variation. This can be set in the range of 0 to 100%, and is multiplied by a constant of 2π. The 2π represents the radius of a circle, and all possible directions in the x and y. Figure 5.3 provides a simplified schematic for the simulation set-up.

For example, an angular variation of 0%, will produce zero deviance from the initial magnetisation. A variation of 100% will produce a completely disordered simulation, where the direction of anisotropy in each grain could lie anywhere in the 2π region. A random normal distribution term is also used to draw from a

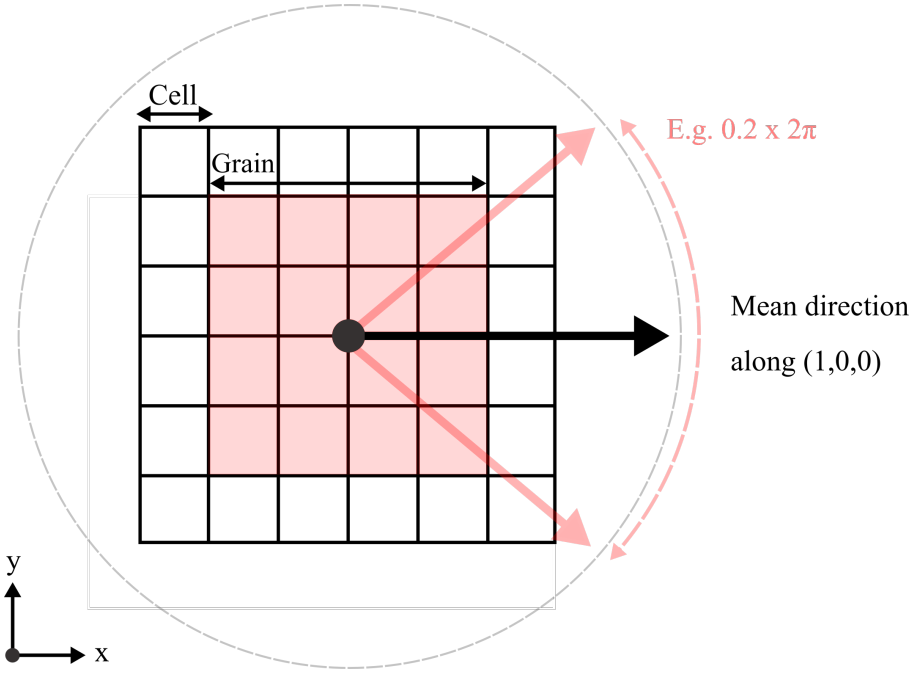

Figure 5.3: MuMax^3 simulation set-up. Each square represents a cell. A grain is made up of a group of cells, here indicated by the red region. Each grain is assigned an anisotropy value, in which the direction can lie randomly within a defined region, in this case highlighted by the red arrows which represent a region of 20% of 2π.

normal Gaussian distribution. This is inbuilt in the MuMax^3 software. An equation for determining the anisotropy vector in a grain is defined as:

$$\text{Random vector orientation} = RandNorm() \times AngularVariation \times 2\pi \quad (5.1)$$

Figure 5.4 highlights how the angular variation parameter varies the anisotropy directionality. Three example angular variation inputs are presented: 2, 10 and 20% (equivalent to $\pi/25$, $\pi/5$ and $2\pi/5$ respectively). Figure 5.4 (a,c,e) show the granular structure present in each simulation, to represent a polycrystalline thin film. The magnitude of K is equal in each grain but lies along different directions. The colours in these images represent the directionality of the anisotropy associated with that grain, using the colour wheel shown in (g). For example, light green regions represent the anisotropy in the +y direction, and red regions represent the +x direction. However, it is important to note that the anisotropy in each grain is not

unidirectional, but uniaxial. This means that the red and blue grains have equivalent uniaxial anisotropies. Therefore for any given angle, angle + π is equivalent.

Figure 5.4 (b,d,f) are plots of the x and y components of the granular anisotropy vector. It provides a way of visualising the distribution of anisotropy vectors. Note, the anisotropies plotted are uniaxial so have equivalent distributions at the vector angle + π. For the example figures presented here, only 30 grains were taken into account, in one specific direction (rather than uniaxial) to prevent overcrowding in the plot. In reality, there are approximately 2500 grains in each simulation. A low angular variation, like in Figure 5.4(a,b), it is intended to represent a situation where a sample has been annealed to give a strong in-plane easy axis. As the angular variation is increased to 20%, for example in Figure 5.4(e,f), it increases the random distribution of the grains, although the majority of the granular anisotropy directions are still concentrated in the +x direction. This is intended to represent a sample which has had a less successful annealing treatment but still exhibiting easy and hard axis behaviour.

Simulation Parameters

Parameters were chosen for a standard 80/20 permalloy composition as this chapter aims to investigate trends rather than direct experimental sample comparisons:

- Bulk exchange constant A = 13 x 10^{-12} J/m (for both intergranular and intragranular exchange)
- Saturation magnetisation M_s = 8.6 x 10^5 A/m
- Grid size = 1000 x 1000 x 1 cells
- Cell size = 5 nm x 5 nm x 20 nm
- Simulation size = 5 μm^2 x 5 μm^2 x 20 nm
- Grain size = 20 nm using Voronoi tessellation
- Periodic boundary conditions = 32 x 32 x 0 repetitions
- Anisotropy constant K = 1000 J/m^3

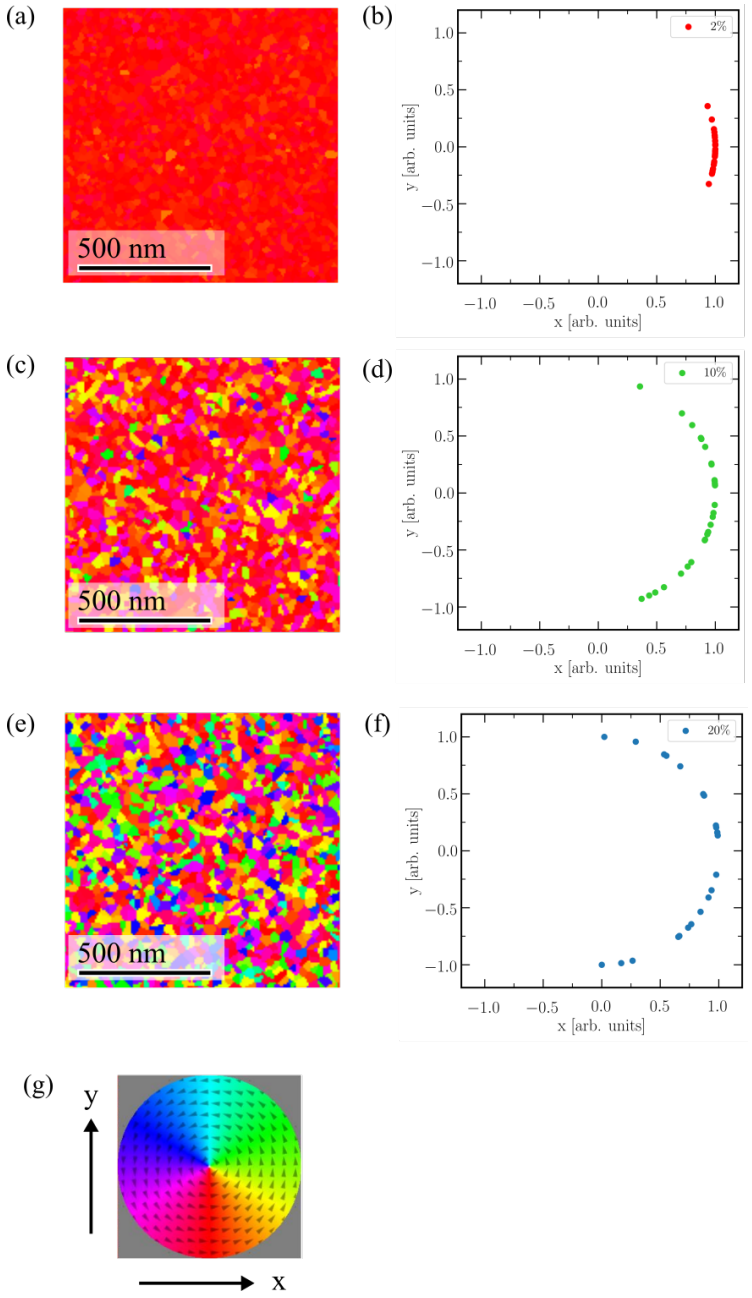

Figure 5.4: Effect of the angular variation parameter on the granular anisotropy of 1000 J/m^3 of a simulated polycrystalline thin film. (a,c,e) show the granular structure of the simulation, where the colours refer to the directionality of the anisotropy as defined by the colour wheel in (g). (b,d,f) are plots of the x and y components of the anisotropy vector, showing deviation for the specified mean direction $+x$. (a,b) show angular distribution of granular anisotropy when set at 2%, where red grains denote anisotropy in the + x-direction, therefore a non-random system. It represents a sample which has a strong induced anisotropy that is much larger than that in the grains. (c,d) and (e,f) represent 10% and 20% angular range respectively.

The anisotropy constant of $K = 1000\ J/m^3$ is the anisotropy assigned to each grain, the direction of this anisotropy depends on the angular variation value used in Equation 5.1. This equals an equivalent anisotropy field H_k of 25 Oe, which is of the order seen experimentally in seedlayer samples.

The grain size diameter of 20 nm was selected to ensure the grain size was sufficiently larger than the cell size (of 5 nm) without being completely unrealistic. These sizes were chosen to improve simulation computing time, whilst still retaining a large simulation dimensionality. In reality, the average grain size seen experimentally for permalloy thin films (For example in Chapter 4) is less than 10 nm. This is a factor that will be discussed later. Both the cell and grains exhibit the same exchange coupling value A. The only difference between grains are the anisotropy directions.

It should be noted that in MuMax^3 the cells and grains are box shaped which will be different form real grains seen in sputtered materials, which will have more irregular surfaces. However it does allow for structures which can be matched to the granular length scales, where the magnetic properties can be given realistic values.

Periodic boundary conditions were used at to eliminate any edge effects (or to make the simulation more like an infinite one). [7,8] The simulations discussed here used $32 \times 32 \times 0$ repetitions i.e. the simulation reflects an area of 32 additional cells in each in-plane direction. This means the demagnetising field behaves as if there are 32 extra repetitions along the x- and y-directions.

Using the parameters defined above, the effect of anisotropy angular variation was investigated for simulations run at 2, 5, 10, 15 and 20% of 2π.

In order to obtain a hysteresis sequence for each simulation, the magnetisation of the ferromagnetic material, in this case permalloy, was initialised to a single domain state along a given direction (x- or y-direction). A strong magnetic field can be applied along the same direction for an in-plane easy axis behaviour, or at 90° rotation for an out-of-plane hard axis behaviour. For the following simulations a maximum field H_{max} of 30 Oe was applied, from $+H_{max}$ to $-H_{max}$ for one hysteresis

sweep. This field was chosen to ensure a near magnetisation saturation state was reached, whilst keeping simulation running time within reason.

5.2.2 Simulated M-H Loops

The influence of anisotropy angular variation on magnetic properties of a 20 nm thick $Ni_{80}Fe_{20}$ simulated sample was investigated. Figure 5.5 shows normalised easy and hard hysteresis loops for angular variation of 2, 5, 10, 15 and 20%. By decreasing the angular variation, the anisotropy is strengthened in one defined direction. A result of this is a clearly more well defined uniaxial behaviour, in this case in the x-direction. These results have some similarities with experimental results presented in Section 4.3 (Figure 4.2), which showed a dramatic increase in uniaxial anisotropy from an initial isotropic sample, through the addition of ultra-thin seed layers.

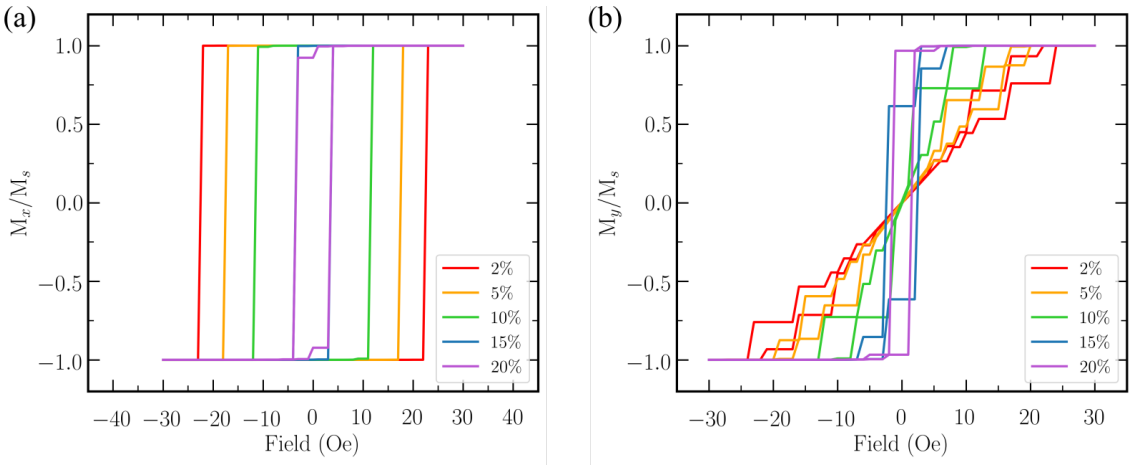

Figure 5.5: Simulated MH hysteresis loops for a 20 nm $Ni_{80}Fe_{20}$ sample with varying amounts of angular directionality variation: 2, 5, 10, 15 and 20%. (a) Easy axis outputs and (b) hard axis outputs.

All outputs produce easy axis behaviours, however there is a substantial variation in the measured coercive field value. There is an increase of the easy axis coercive field from $\approx$ 4 Oe to 23 Oe. This means a larger field is needed to overcome the energy barrier, where the magnetisation direction switches by 180 degrees. There is also a marked increase in measured uniaxial anisotropy K_u with a reduction in angular variation. This is measured from results presented in Figure 5.5(b) by

the increase in H_k from 2 to 24 Oe ($K_u = M_S H_k/2$). Note, that these values are approximations for 15% and 20% outputs, which still retain some magnetisation at zero field. Key hysteresis outputs are summarised in Table 5.1.

Angular Variation (%)	Easy Axis H_C (Oe)	Hard Axis H_K (Oe)	Hard Axis M_R Normalised M	K_u J/m^3
2	23	24	0	950
5	18	20	0	780
10	12	13	0	520
15	4	7*	0.61	280*
20	4	2*	0.97	80*

Table 5.1: Key parameters from simulated MH magnetic measurements, with increasing angular variation. Results presented from both easy axis and hard axis outputs. *Indicates an approximation value, as hard axis behaves more like typical easy axis behaviour.

Measured K_u can be investigated as a function of angular variation percentage. Results are presented in Figure 5.6 with a linear line of best-fit. All simulations were run with an uniaxial anisotropy constant $K_u = 1000$ J/m^3. Measured outputs from simulations are in good agreement. It can be approximated that measured K_u would also equal 1000 J/m^3 if granular anisotropy deviation was set to zero.

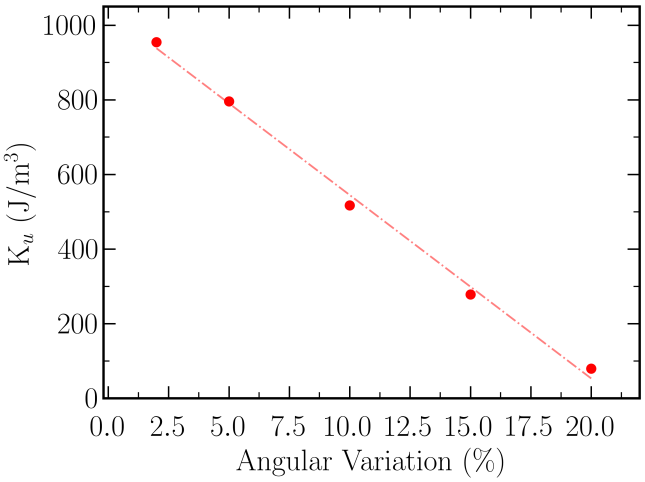

Figure 5.6: Measured simulated uniaxial anisotropy K_u as a function of angular variation % with a linear line of best-fit. Increasing the angular variation creates an increasing y-component of magnetisation, decreasing the effective K_u.

An increase in angular range reduced the simulated films uniaxial properties until their behaviour was isotropic. This results in near isotropic behaviour for the 15

and 20% simulations, whereby the corresponding easy and hard axis loops are the very similar, if not the same. This would indicate the material has lost most of its directionality and is now a completely disordered (or randomly distributed) system.

5.2.3 Simulated Fresnel Images

MuMax^3 simulations were set to produce magnetisation outputs in the x, y and z -directions, throughout a full hysteresis sweep. These files can be fed into Digital Micrograph, where a script developed by S.McVitie et al (which implemented a software version of an original algorithm, created by M. Mansuripur), can be used to create a simulated Fresnel image from magnetisation components. [9,10] An example is shown in Figure 5.7, of (a) M_x, (b) M_y and (c) M_x components respectively. When limits are set to $+M_s$ to - M_s (i.e. +1 to -1) there is reduced contrast in the image. This is due to the fact that the magnetisation dominates along the x-direction for easy axis behaviour. A smaller contrast range allows for visualisation of the magnetisation fluctuations for both M_x and M_y components. Note that the M_z components is grey as this component is equal to zero. All simulations are essentially 2D systems, as the thin film is only one cell in thickness.

We investigate the dependence of magnetisation ripple structure on the angular directionality variation of the granular anisotropy. Fresnel images will be shown of easy and hard axis hysteresis reversals, to investigate differences in micromagnetic behaviour, followed by quantitative analysis which will be presented later in Section 5.2.4.

Easy Axis

For an applied field lying parallel to the easy axis of a magnetic thin film with strong uniaxial anisotropy, the experimental magnetisation reversal processes consist of a rapid domain wall sweep across the sample, at the switching field. As seen experimentally in Chapter 4, the magnetisation ripple properties such as dispersion and wavelength, are expected to increase up until this switching/coercive field is

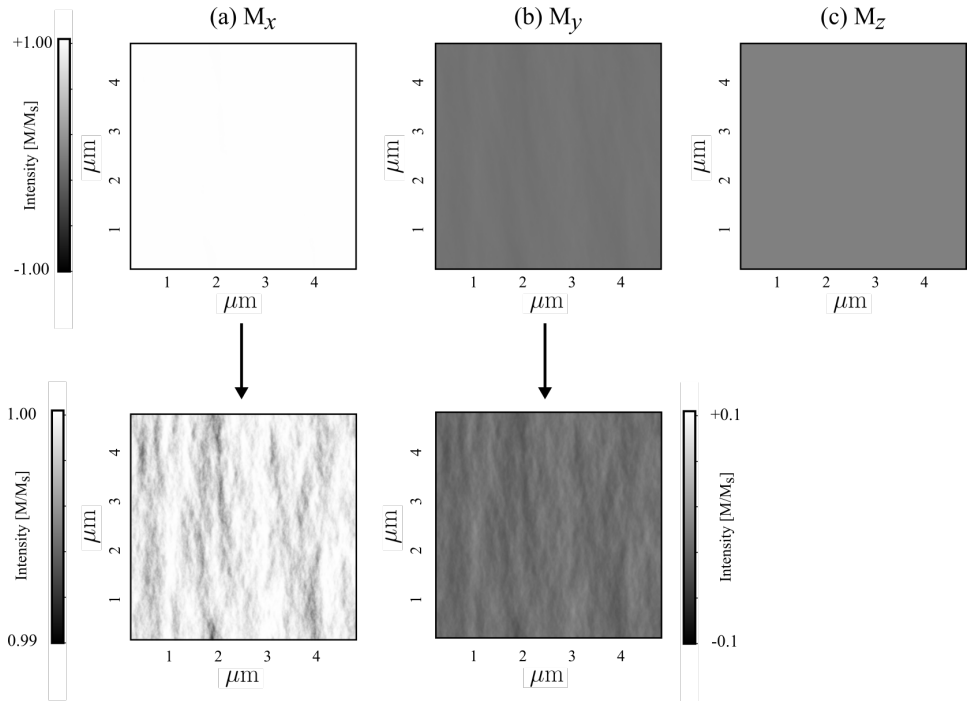

Figure 5.7: Example magnetisation components: (a) M_x, (b) M_y and (c) M_x respectively. Images acquired from a 20% angular variation using the parameters described in Section 5.2.1. Images are taken at a field of +30 Oe applied along the easy axis.

reached, at which the direction of field and net magnetisation become parallel. Any field larger than this will suppress both the dispersion and wavelength until the full magnetisation saturation is reached.

Figure 5.8 and 5.9 show a sequence of simulated Fresnel images of the easy axis magnetisation reversal for an angular variation of 2% and 20% respectively. Simulated Fresnel images were acquired using a defocus value of 500 μm. Note the contrast limits are equal in both sets of images for direct comparison. The simulated images visually resemble the experimental images obtained from real permalloy thin films (Section 4.5.2 and 4.5.3).

The applied field direction is indicated by the red arrow. The fine structure that is present in all images is simulated magnetisation ripple. It allows the orientation of the magnetisation to be determined through FFT analysis. The direction of magnetisation is highlighted by the blue arrow. The images presented range from near magnetisation saturation at a field of + 30 Oe (a), until just before the switching field at H_C (c) in each case. One difference between images Figure 5.8(c)

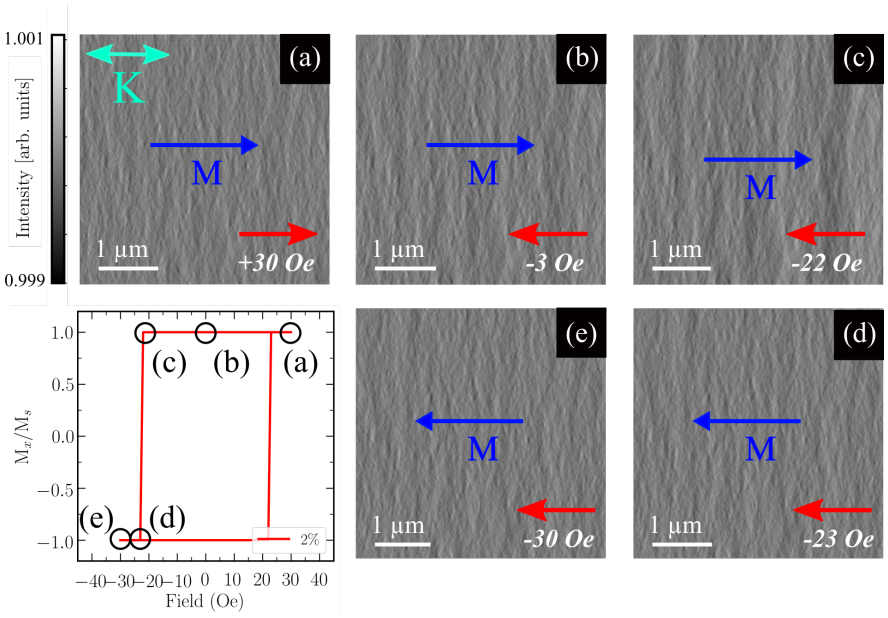

Figure 5.8: Simulated Fresnel images with a defocus of 500 μm, demonstrating the magnetisation reversal process along the easy axis of a 20 nm $Ni_{80}Fe_{20}$ thin film, with an angular variation of 2%. A full list of simulation parameters are described in Section 5.2.1. The red arrows represent the direction of the applied field, H, and K is the uniaxial anisotropy direction. The blue arrow represents the mean direction of the magnetisation.

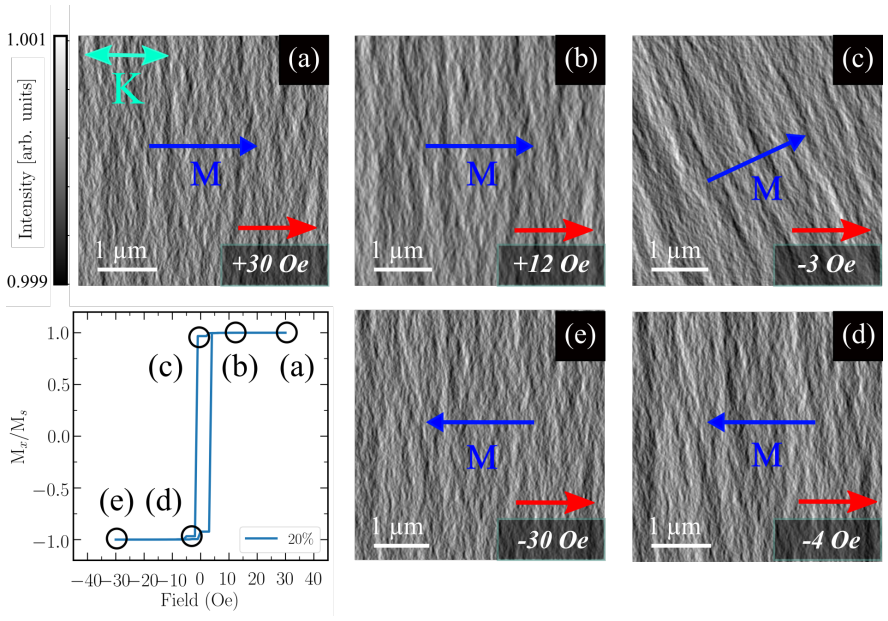

Figure 5.9: Simulated Fresnel images with a defocus of 500 μm, demonstrating the magnetisation reversal process along the easy axis of a 20 nm $Ni_{80}Fe_{20}$ thin film, with an angular variation of 20%. A full list of simulation parameters are described in Section 5.2.1.

and 5.9(c) is what appears to be a rotation of the magnetisation direction for the latter image. This shows the simulation is not showing true easy axis behaviour and is a sign of less defined uniaxial anisotropy, when compared to the 2% image.

The observed magnetisation ripple behaviour from the simulated Fresnel images depends on the angular variation value. Images 5.8(a,e) and 5.9(a,e) can be directly compared as they are simulated Fresnel images at the same applied fields. The most obvious difference is the contrast present in the images. There is higher contrast present with the 20% angular variation images. This indicates there is a larger deviation in the magnetisation from the mean direction. This can be confirmed by comparing M_y component images, as shown in Figure 5.10.

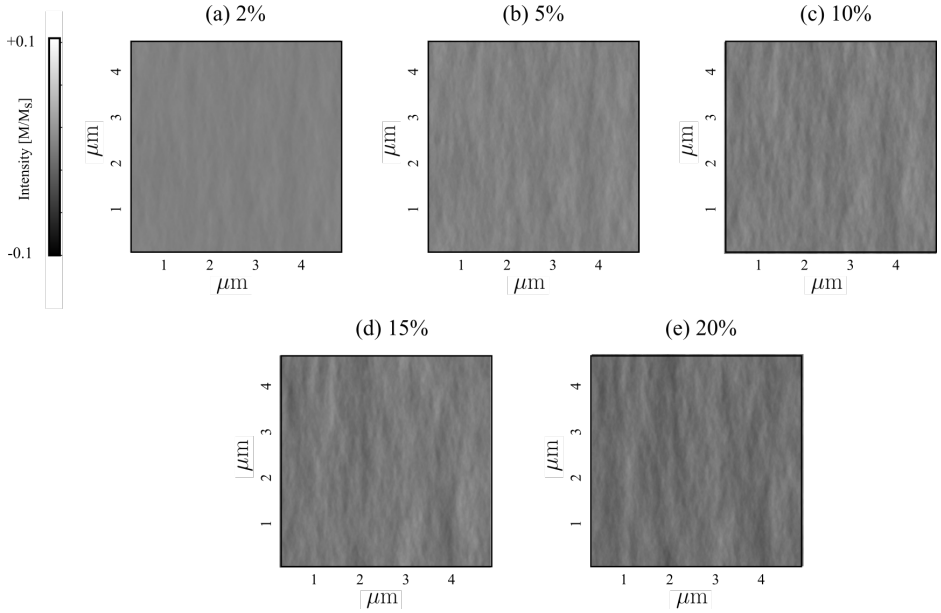

Figure 5.10: Simulated M_y components at a field of +30 Oe applied along the easy axis for (a) 2%, (b) 5%, (c) 10%, (d) 15% and (e) 20% simulations. All images have equivalent contrast limits. Lighter and darker contrast indicates a larger deviation in the y-component directionality.

There is a gradual increase in contrast variation (light and dark regions) within the image, signifying a larger deviation of the y-component. This increase in M_y dispersion confirms that there is an increase in magnetisation ripple dispersion, that can be visually observed in the corresponding Fresnel images. These characteristics will be quantitatively assessed in Section 5.2.4.

Hard Axis

Typical hard axis behaviour involves rotation of the magnetisation direction on a reduction of the applied field. Figure 5.11 and 5.12 show a sequence of simulated Fresnel images of the hard axis magnetisation reversal for an angular variation of 2% and 20% respectively. Figure 5.11 exhibited almost idealised hard axis behaviour with the rotation of the magnetisation **M** with decreasing field.

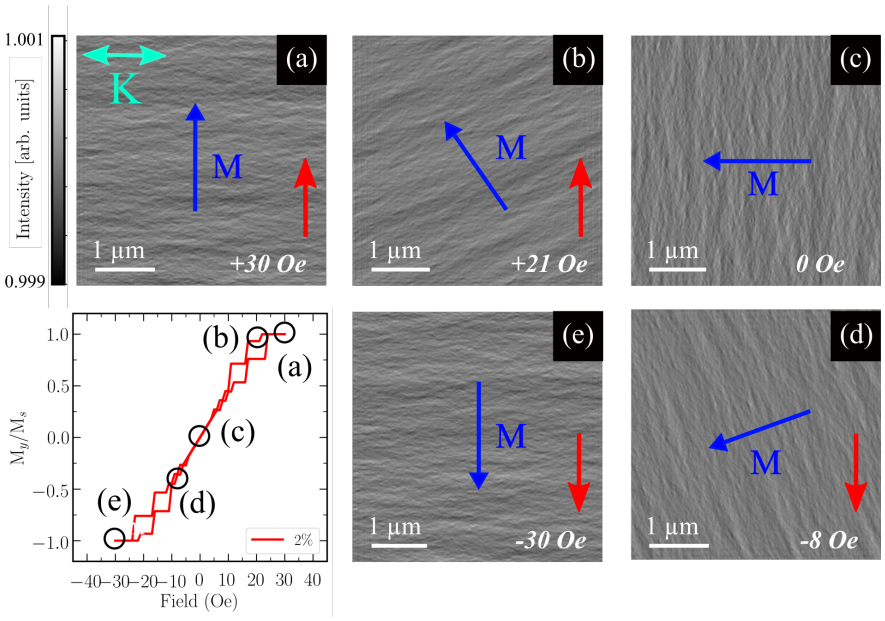

Figure 5.11: Simulated Fresnel images with a defocus of 500 μm, demonstrating the magnetisation reversal process along the hard axis of a 20 nm $Ni_{80}Fe_{20}$ thin film, with an angular variation of 2%.

Similarly to the easy axis results, the magnetisation ripple dispersion and wavelength appear much larger for the 20% angular variation simulation when compared to the 5%. The 20% simulation 'hard axis' loop (Figure 5.12) exhibits something much more closely related to easy axis behaviour. This indicates that there is a dispersed anisotropy resulting in a reduction in K_u i.e. isotropic behaviour. However, these images are only qualitative impressions, therefore further analysis is needed to quantify ripple properties. These will be quantified with the techniques discussed in Chapter 3 in the following section.

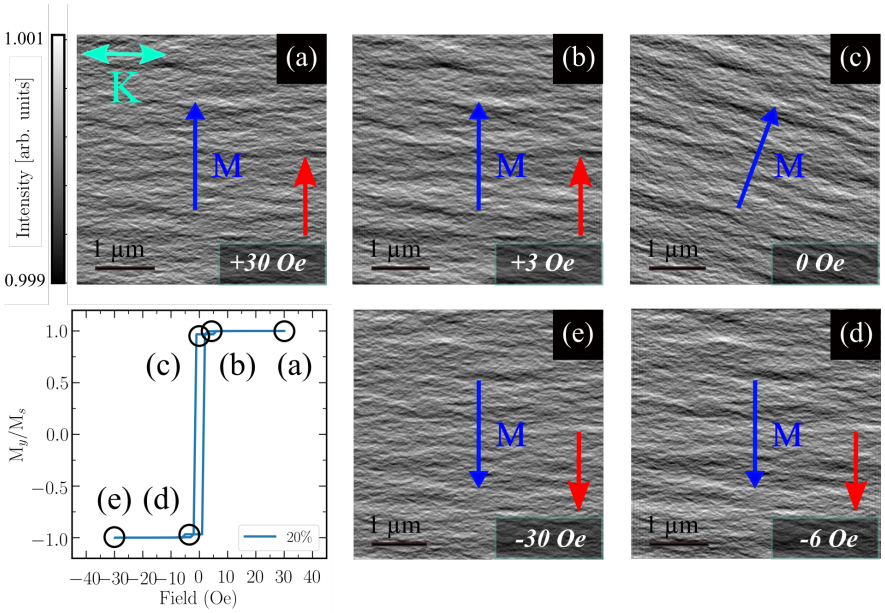

Figure 5.12: Simulated Fresnel images with a defocus of 500 μm, demonstrating the magnetisation reversal process along the hard axis of a 20 nm $Ni_{80}Fe_{20}$ thin film, with an angular variation of 20%.

5.2.4 Magnetisation Ripple Characterisation

Just like the experimental Fresnel images presented in Chapter 4, 2D FFT images can be taken of the simulated Fresnel images created through MuMax[3] outputs. Visually, the magnetisation and Fresnel images confirm that there is an increase in the ripple dispersion with increasing angular variation, however analysis is needed to produce quantitative outputs. The properties discussed in the following section are as follows: Dispersion angle θ, dominant ripple wavelength λ_{Dom}, spectroid ripple wavelength $\lambda_{Spectroid}$. Additionally, the resultant **M** component can be determined by the modulus of M_y/M_x outputs. All simulation outputs of increasing angular variation have been individually investigated as a function of applied field along both the easy and hard axis.

From a visual inspection of both the M_y component and simulated Fresnel images presented in the previous sections, it is clear to see the ripple properties strengthen with increasing angular variation, through the increased contrast due to larger deviation of the magnetisation direction.

This was confirmed for all simulations using ripple analysis techniques described in Chapter 3. Tables 5.2 and 5.3 present ripple analysis results from an applied field of + 30 Oe applied along the easy and at a remanent state respectively. Simulation outputs produced a suppression of ripple properties with increasing applied field. Dominant wavelength λ_{Dom} appears to be most 'sensitive' measurement, when compared to $\lambda_{Spectroid}$, which has considerably lower outputs when compared to experimental results. This will discussed in the following section. All characterisation methods for the easy axis analysis are in agreement, that there is a suppression of magnetisation ripple properties with decreasing angular variation. Similar trends were seen in the hard axis analysis, with increased ripple properties with increased angular variation.

Angular Variation %	M_x/M_s [Normalised M]	$\lambda_{Spectroid}$ (nm)	λ_{Dom} (nm)	Dispersion θ °	M component °
2	0.999998	90 ± 5	380± 20	36 ± 1	0.11
5	0.999991	100 ± 5	380 ± 20	40 ± 1	0.20
10	0.999985	100 ± 5	380 ± 20	41 ± 1	0.26
15	0.999968	100 ± 5	500 ± 20	41 ± 1	0.38
20	0.999902	100 ± 5	560 ± 20	42 ± 1	0.72

Table 5.2: Key outputs from easy axis ripple analysis. Table includes outputs for each angular variation simulation at an applied field of +30 Oe along the easy axis, towards magnetisation saturation.

Angular Variation %	M_x/M_s [Normalised M]	$\lambda_{Spectroid}$ (nm)	λ_{Dom} (nm)	Dispersion θ °	M component °
2	0.999992	100 ± 5	620 ± 20	40 ± 1	0.21
5	0.999974	100 ± 5	640 ± 20	40 ± 1	0.35
10	0.999940	110 ± 5	880 ± 20	41 ± 1	0.56
15	0.999158	120 ± 5	920 ± 20	40 ± 1	2.71
20	0.995082	120 ± 5	1060 ± 20	42 ± 1	22.63

Table 5.3: Key outputs from easy axis ripple analysis. Table includes outputs for each angular variation simulation at zero field.

5.2.5 Discussion

This simplified micromagnetic model proved to be successful for producing sensible magnetisation reversal processes. The simulated Fresnel images resemble the

experimental Fresnel images acquired from other chapters (4 and 6) within this thesis. We have also seen changes in behaviour by varying parameters. However physical values, for example ripple wavelength, are much lower than seen experimentally. However this is not necessarily surprising due to the difference in grain size. Additionally, the observed contrast in simulated Fresnel images is very weak. This will be discussed in this section.

The field dependence for (a) dominant and (b) spectroid ripple wavelength values are presented in Figure 5.13 for increasing angular variation. This relates to the region of an applied field of + 30 Oe along the easy axis, that is reduced to just before the switching field. This is why each plot cuts off at different negative field values, relating to the measured coercive field H_c value for each simulation. All lines show good agreement with both theory and experimental observations, whereby the ripple wavelength reduces when increasing field where field and magnetisation directions are parallel.

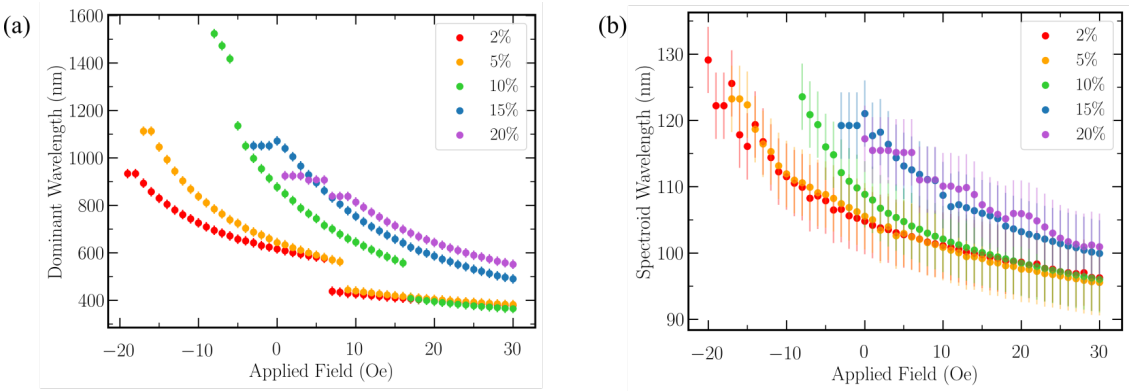

Figure 5.13: (a) Dominant ripple wavelength and (b) spectroid wavelength results measured from a field of + 30 Oe to just before the measured coercive field H_C value, when applied along the easy axis for increasing angular variation.

It is important to note the discontinuities in Figure 5.13(a) unlike the smooth variation in (b) with increased applied field. These are analysis artefacts due to reduced contrast in simulated Fresnel images with highly suppressed ripple properties as the magnetisation saturation is approached. The best-fit exponent of each plot

can be fitted from results presented in Figure 5.13(a), with the discontinuities removed. These exponent values are shown in Table 5.4.

Generally, the best-fit power dependence agrees well with Hoffmann's theory of magnetisation ripple (Section 1.7), which predicts a negative exponent (a decrease in ripple wavelength with increased field) which approximates to $\lambda_{Dom} = H^{-0.5}$ [11].

Angular Variation %	Exponent [arb. units]
2	-0.3
5	-0.3
10	-0.5
15	-0.3
20	-0.3

Table 5.4: Key outputs from easy axis ripple analysis. Table includes best-fit exponent outputs for each angular variation simulation, calculated for results plotted in Figure 5.14(a).

Simulated outputs can be compared to experimental ripple analysis results, which can be found in Chapter 4. One of the samples under investigated (specifically the 1 nm $Ni_{79}Fe_{21}$ seed layer sample, had a measured uniaxial anisotropy of $\approx$ 800 J/m^3. From Table 5.5, this is comparable with the simulation with an angular variation of 5%, which exhibited a simulation uniaxial anisotropy of 796 J/m^3. Another experimental sample from Chapter 4 (unseeded sample) exhibited isotropic behaviour, which is comparable to the 20% angular variation simulation. Table 5.5 shows direct comparisons between experimental and simulated ripple analysis for samples exhibiting strong and weak uniaxial anisotropy, at an applied field of + 30 Oe along the easy axis.

The first positive was that the experimental results for the unseeded and 1 nm seed layer sample have features that the simulation model was able to successfully reproduce with regards to lack of anisotropy and a well defined anisotropy, determined from hysteresis loops. Although the simulation used a different approach using angular variation, it successfully reproduced aspects of magnetic behaviour seen experimentally. Chapter 5 detailed how the uniaxial behaviour could be

manipulated through grain size variation. In the simulations, it is varied through a range of anisotropy direction. However both show anisotropic to isotropic behaviour.

The behaviour of the simulated magnetisation ripple matched the experimental trends very well. As seen from results presented in Chapter 4, a thin film with stronger uniaxial anisotropy will experience a suppression of magnetisation ripple properties (both wavelength and dispersion) when compared to a film with weak uniaxial anisotropy. In this case, the unseeded sample and 20% sample both exhibited isotropic behaviour. This was confirmed through a consistent increase of properties, such as those shown in Table 5.5, with an increase in dispersion angle and wavelength from the 5 to 20% simulation.

Parameter	Experimental Outputs		Simulated Outputs	
	1 nm $Ni_{79}Fe_{21}$	Unseeded	5%	20%
K_u (J/m^3)	800	Isotropic	796	Isotropic
θ (°)	13 ± 1	37 ± 1	40 ± 1	42 ± 1
$\lambda_{Spectroid}$ (nm)	480 ± 10	1080 ± 10	96 ± 5	104 ± 5
λ_{Dom} (nm)	600 ± 20	1200 ± 20	380 ± 20	600 ± 20

Table 5.5: Comparison of experimental results for a 1 nm $Ni_{79}Fe_{21}$ seed layer sample (presented in Chapter 4) with 5% angular variation simulated results, at an applied field of + 24 Oe along the easy axis. Both experimental and simulated results exhibited a uniaxial anisotropy of approximately 800 J/m^3. Additionally, the experimental unseeded sample and 20% angular variation simulation can be compared as they both exhibited isotropic properties.

It is important to remember the limitations of simulating a realistic polycrystalline granular structure. The granular structure for the experimental results consisted of a distribution of grain sizes, with a mean diameter ranging from 3-10 nm. A grain size of 20 nm was chosen for the simulations presented in this section to ensure a large enough simulation dimensionality, without excessive simulation running times. This grain size is obviously significantly larger than the 3 nm grain size diameter measured experimentally, which will strongly contribute to the discrepancy in simulated results results. Additionally, the simulated cells/grains are regular box shaped with abrupt flat surfaces, unlike that of real grains which are irregular. It is expected that further work would be required to explain the small scale

effects seen here, which could offer an explanation as to why such small spectroid values are observed in the simulations.

Whilst this model is limited, by reasons outlined above, it has proved to be a reasonable start. It has produced simulated Fresnel images which show magnetisation ripple that does show a good resemblance to aspects seen experimentally (for example, in Chapter 4). It also allowed for successful characterisation of magnetisation properties. The model allowed for simulations which represented both highly ordered and disordered systems without physical changes in simulated grain size. This model was successful is producing trends which replicate what was seen experimentally in Chapter 4, whereby a material with a larger uniaxial anisotropy exhibits a suppression of ripple dispersion and wavelength. Decreasing the angular variation acted to strengthen the uniaxial anisotropy and thereby decreasing the ripple properties.

The Anisotropy Axis Variation model assigned each grain a set magnetocrystalline anisotropy value, which refers to the combination of K_G and K_g in each grain. In reality, there will be a number of anisotropy terms to consider. However, there is a direction variation from grain to grain which has produced at least visually good images of ripple. The following section will consider a model which allows for control over individual anisotropy contributions.

5.3 Individual Anisotropy Contributions Model

5.3.1 Simulation Method

A more physically realistic micromagnetic model is also proposed which allows direct control over individual anisotropy contributions rather than an overall effect as seen in the Anisotropy Axis Variation model. In this model we aim to independently set the local individual grain anisotropy K_g, and overall global (induced) anisotropy K_G.

The anisotropy values for an induced uniaxial anisotropy can be significantly larger than the individual crystalline anisotropy, depending on the materials properties.

For example, a typical value for K_G for a permalloy material deposited in a field with subsequent annealing in a field would be 800 J/m^3, compared to 100 J/m^3 for magnetocrystalline anisotropy K_g. [12] This simulation model improves upon the angular variation model by allowing the independent control of these two anisotropy constants, replicating a more realistic simulation set-up. It represents much more accurately the granular orientation in the films studied experimentally. Figure 5.14 shows a simplified schematic of the simulation set-up. The same limitations of grain size, discussed in the previous section, will still remain an issue when trying to model realistic structures. However, even with the grain limitations and trade off of modelling realistic length scales, this should prove a useful exercise.

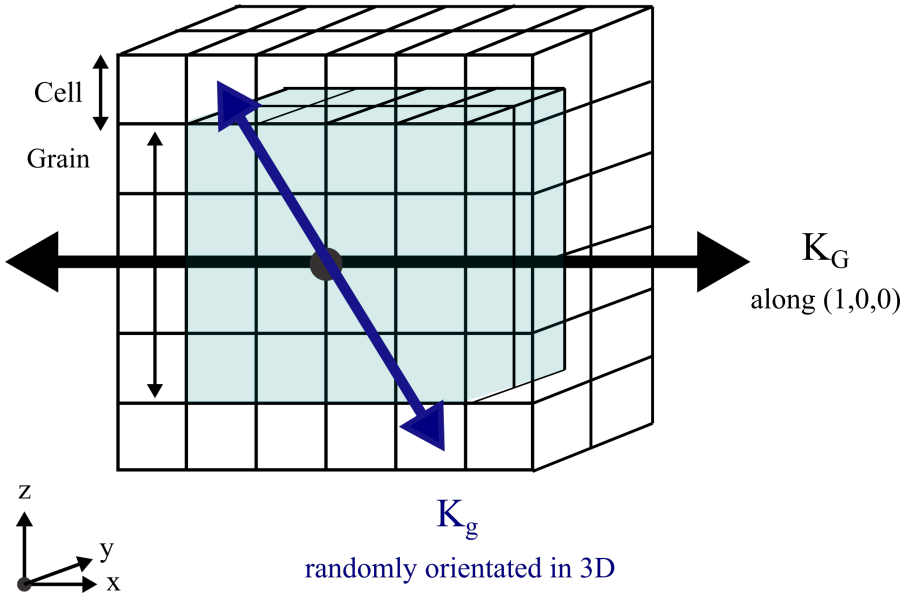

Figure 5.14: MuMax^3 simulation set-up. Allows for control of individual anisotropy components for a global uniaxial component K_G and a granular magnetocrystalline anisotropy component K_g, whereby the former is in a set direction and the latter can be randomly orientated in the x, y and z directions.

The micromagnetic model was developed to simulate polycrystalline permalloy thin films exhibiting magnetisation ripple. Creation of the micromagnetic model encompasses several parts: setting up the material parameters and sample geometry. An identical physical set-up to the previous model was also used here.

- Bulk exchange constant A = 13 x 10^{-12} J/m
- Saturation magnetisation M_s = 8.6 x 10^5 A/m

- Grid size = 1000 x 1000 x 1 cells
- Cell size = 5 nm x 5 nm x 20 nm
- Simulation size = 5 μm^2 x 5 μm^2 x 20 nm
- Grain size = 20 nm using Voronoi tessellation
- Periodic boundary conditions = 32 x 32 x 0 repetitions
- Global anisotropy K_G = 800 J/m^3 (H_k = 20 Oe)
- Granular anisotropy K_g = 100 J/m^3 (H_k = 2.5 Oe)

The global K_G and granular K_g anisotropy values were chosen as they best represent permalloy polycrystalline thin films that have been experimentally studied in this project, allowing for a direct comparison. It is important to note that the granular anisotropy is randomly orientated in 3D, unlike the previous model where all anisotropies were confined in-plane. An external in-plane magnetic field H was applied along the easy and hard axis of the material.

Figure 5.15 highlights the effect of the additional granular anisotropy contribution to the global anisotropy, which was originally set as 800 J/m^3 in the x-direction.

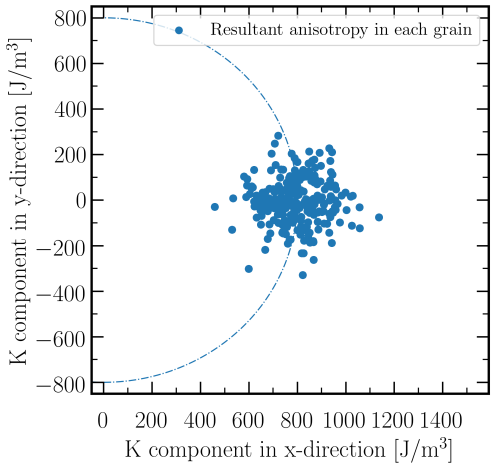

Figure 5.15: Simulated K-components in the x and y-directions. Dashed circle indicates radius of 800 J/m^3 resultant anisotropy. Dots shows the deviation from the initial 800 J/m^3 with the addition of the randomly orientated granular anisotropy K_g contribution. Note the anisotropy in only one direction is shown here, there will be an equivalent anisotropy in the opposite direction as it represents uniaxial anisotropy.

It highlights how there is both a change in direction, and a change of magnitude of the resultant anisotropy (compared to the previous model which just had an angular deviation). Similarly to Figure 5.4, the anisotropy in only one direction is shown here, there will be an equivalent anisotropy in the opposite direction as it represents uniaxial anisotropy. Despite the completely random grain orientation there is a clear angular range which is similar to the lower angular range seen in the previous model (Figure 5.4). The range of angles seen in Figure 5.15 range from 0 to 26 degrees, which is comparable to the 2 and 5% angular variation ranges.

5.3.2 Simulation M-H Loops and Fresnel Images

Figures 5.16 and 5.17 show normalised hysteresis loops with the external field applied along the easy and hard axis respectively.

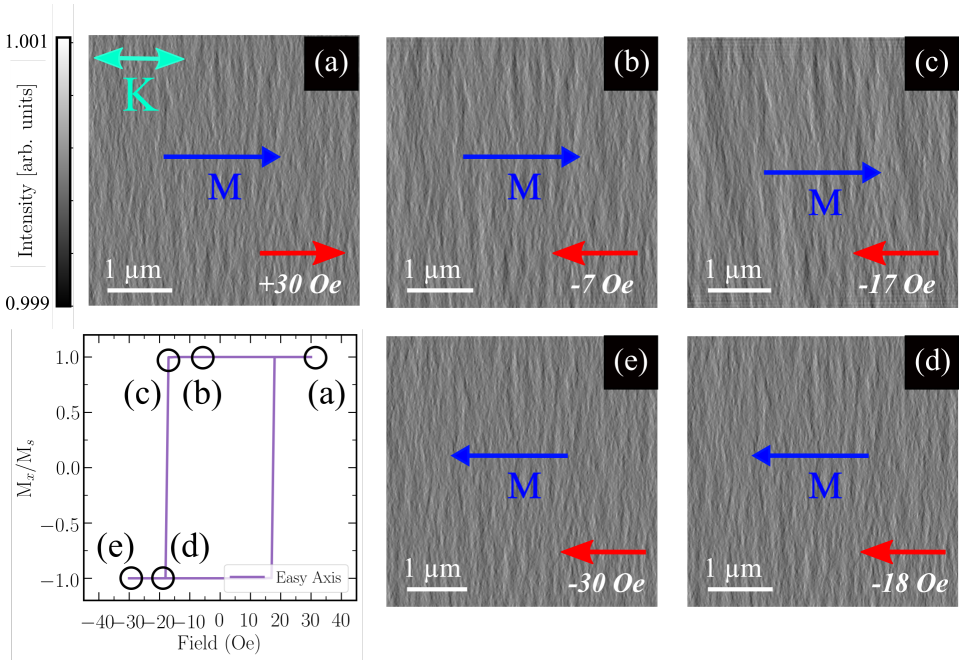

Figure 5.16: Simulation Fresnel images with a defocus of 500μm, demonstrating the magnetisation reversal process along the easy axis of a 20 nm $Ni_{80}Fe_{20}$ thin film. Parameters of the simulation include a global anisotropy of K_G of 800 J/m^3, a granular anisotropy of K_g of 100 J/m^3 and a grain size diameter of 20 nm.

Results produced typical easy and hard axis behaviours. There is a measured coercive field of 18 Oe. The measured anisotropy field H_k was measured to be 20

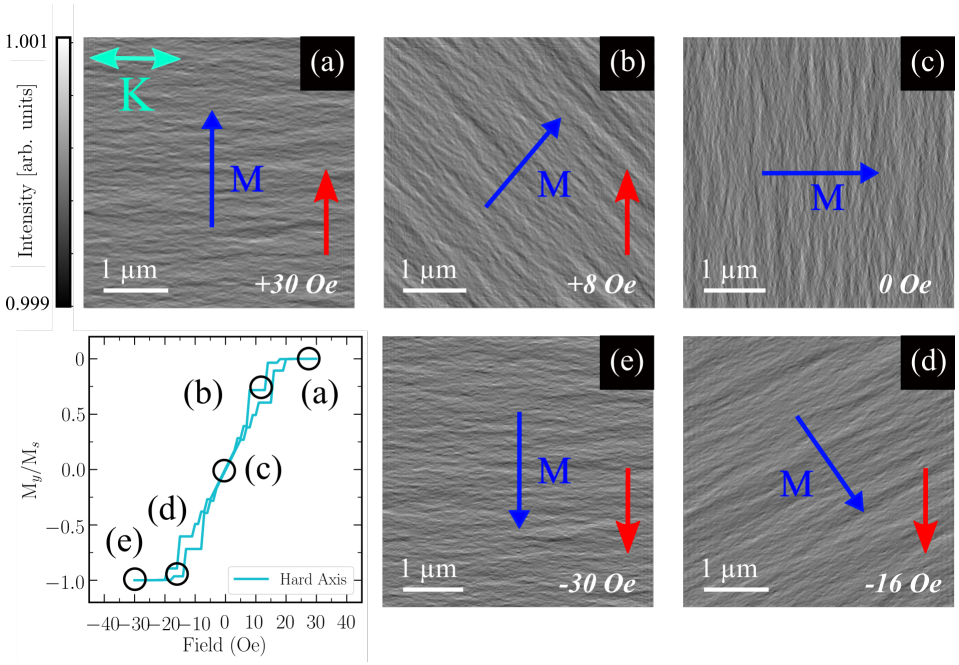

Figure 5.17: Simulation Fresnel images with a defocus of 500μm, demonstrating the magnetisation reversal process along the hard axis of a 20 nm $Ni_{80}Fe_{20}$ thin film. Parameters of the simulation include a global anisotropy of K_G of 800 J/m^3, a granular anisotropy of K_g of 100 J/m^3 and a grain size diameter of 20 nm.

Oe, producing an uniaxial anisotropy of 800 J/m^3 for the simulated thin film. As expected this is consistent with the input uniaxial anisotropy of the film. These simulated M-H loops are a reasonable match for the 1.0 nm thick seed layer in Chapter 4 (Fig.4.2), even with the variation in experimental (3 nm) and simulated (20 nm) grain size.

Similar steps to section 5.2.3 were used, whereby MuMax^3 magnetisation components can be used to produce simulated Fresnel images using Digital Micrograph. Fresnel images are shown in Figures 5.16 and 5.17 for easy and hard axis hysteresis sequences respectively. Visually, all images presented do exhibit magnetisation ripple properties. Both outputs also produced typical hysteresis trends that have been seen experimentally. Figure 5.16 (a) to (c) shows an increase in contrast which can be attributed to a visual increase in dispersion before the coercive field. The variation in ripple wavelength is less obvious and will need further analysis to determine any changes (Section 5.3.4). (d) and (e) shows a more obvious reduction in ripple dispersion, wavelength and image contrast following a switching

in magnetisation direction. Figure 5.17 shows typical hard axis behaviour with a rotation of the magnetisation direction with reducing field. When the field is reduced to zero, as shown in (c), the magnetisation direction has rotated by 90° to lie along the easy axis direction. The magnetisation continues to rotate with a field applied in the opposite direction, until the magnetisation lies 180° from its original direction (e). This is in good qualitative agreement visually with the observations of the experimental films in previous chapter.

5.3.3 Magnetisation Ripple Characterisation

Further analysis is needed to characterise ripple properties of a large number of simulated Fresnel images in a hysteresis sequence. The methodology developed in Chapter 3 was used, resulting in outputs for both ripple wavelength and dispersion. Figure 5.18 shows ripple analysis for (a) spectroid and (b) dominant ripple wavelength as a function of field from +30 reduced to -30 Oe. Analysis confirms what was seen visually in Figure 5.16, with an increase in ripple wavelength with decreasing field, reaching a maximum ripple wavelength just before the coercive field. After a switch of magnetisation direction, the ripple wavelength suppresses with increasing field.

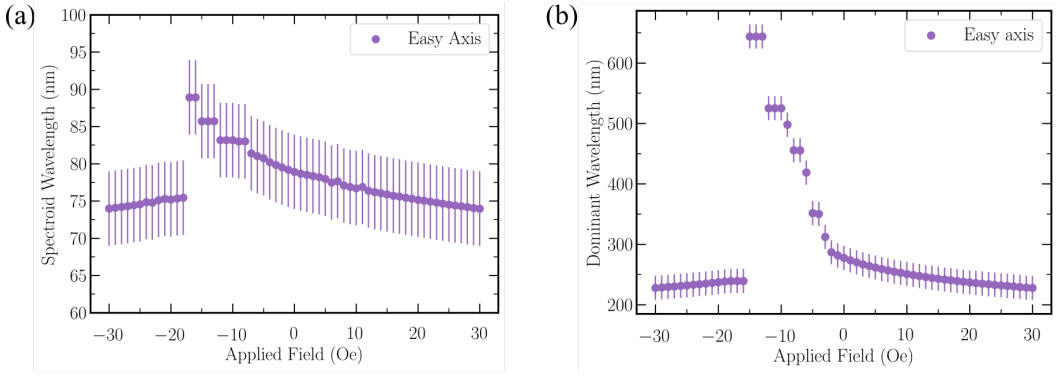

Figure 5.18: Simulated magnetisation ripple wavelength analysis outputs from a field of + 30 Oe to - 30 Oe, applied along the easy axis. (a) Spectroid wavelength $\lambda_{Spectroid}$ and (b) dominant wavelength λ_{Dom} as a function of field.

Visually, both simulation methods created similar simulated ripple structures. Comparisons can be made between experimental results from Chapter 4 and the

two simulations models. Specifically the 1.0 nm seed layer sample, which exhibited strong uniaxial anisotropy of 800 J/m^3. This is compared with the 5% angular variation simulation presented in the previous section, which also exhibited a measured uniaxial anisotropy of 800 J/m^3. Key points are highlighted in Table 5.6 for both the coercive field and at an applied field of 30 Oe.

Both simulation models produced similar outputs for all 3 parameters. However, there was a reduction in ripple wavelength parameters from the angular axis model to the individual anisotropy model. It could be attributed to the reduction in the granular anisotropy. The first model had a magnetocrystalline anisotropy of 1000 J/m^3, compared to 100 J/m^3 in the second model. However, there is a slight increase in measured dispersion angle in the individual anisotropy model. A reason for this could be that the magnetocrystalline anisotropy direction was completely randomised. The former model had strong directionality which could in turn have reduced ripple dispersion.

Parameter	Output	H_C	30 Oe
M_x/M_S (Normalised M)	Experimental	0.9173	0.9923
	Angular Axis Model	0.9993	0.9999
	Anisotropy Model	0.9977	0.9999
Dispersion θ °	Experimental	13 ± 1	11 ± 1
	Angular Axis Model	40 ± 1	40 ± 1
	Anisotropy Model	46 ± 1	48 ± 1
$\lambda_{Spectroid}$ (nm)	Experimental	540 ± 10	480 ± 10
	Angular Axis Model	120 ± 5	100 ± 5
	Anisotropy Model	90 ± 5	80 ± 5
λ_{Dom} (nm)	Experimental	840 ± 20	600 ± 20
	Angular Axis Model	1040 ± 20	380 ± 20
	Anisotropy Model	660 ± 20	240 ± 20

Table 5.6: Comparison of easy axis experimental results for a 1.0 nm $Ni_{79}Fe_{21}$ seed layer sample presented in Chapter 4 with results of both simulation models. Both experimental and simulated results exhibited a uniaxial anisotropy of approximately 800 J/m^3.

Whilst the simulation images look similar to those seen experimentally, it is clear that there are significant differences in the ripple spectrum. Figure 5.19 shows a FFT spectrum comparison of experimental results and the 2 simulation models. A

smoothed intensity plot can be taken through the centre of the FFT structures, for a better understanding of the frequency contributions. (Note, variation in mode peak *k-space* distance are expected as the dominant wavelength results showed variation between experimental and simulated outputs). Results show there is a significant variation between the experimental and simulated contributions. Both simulations had large high spatial frequency components (mode peak), but also had a substantially larger low frequency region, which appears to decrease much more gradually when compared to the experimental intensity. Both simulation models had significantly lower values for spectroid wavelength values (i.e. large k values) indicating that the short wavelength contributions were much more prominent. The reciprocal space intensity plots shown in Figure 5.19 could offer an observation as to why the weighted average values are so different in simulations when compared to what is measured experimentally.

Both models were successful in producing typical hysteresis behaviours, and trends in magnetisation ripple properties. As the simulation spectrum is quite different to what is seen experimentally, it allows for modifications of the model to improve on quantitative outputs. This will be investigated in the following sections.

5.3.4 Effect of Grain Size

Results presented in Chapter 4 detailed the inclusion of an ultra-thin $Ni_{79}Fe_{21}$ seed layer resulted in a decrease in average grain size diameter. Magnetic properties, such as magnetisation ripple, vary with grain size. As discussed previously, the models developed in this project allow for the mapping of trends. Therefore, an investigation was undertaken to simulate the dependence of grain size on magnetic behaviour. The initial simulations, like those discussed previously, started with a 20 nm grain size as a compromise between creating a large scale simulation which could run in a reasonable amount of time. We therefore wanted to explore how the grain size could be adjusted to investigate the effect on the ripple spectrum. The selected grain sizes ranged from 10 - 40 nm in 10 nm steps. The global anisotropy

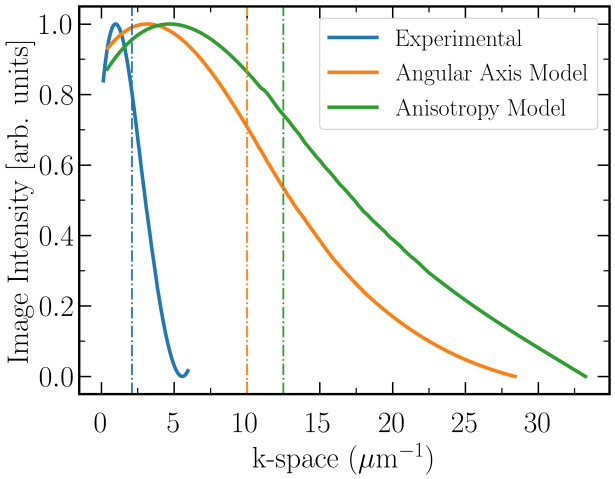

Figure 5.19: Smoothed integrated line traces through the centre of FFT for Fresnel images at a field of +30 Oe. Highlighting the difference in spectrum frequency contributions for both experimental and simulation outputs. Blue line refers to the 1.0 nm $Ni_{79}Fe_{21}$ seed layer sample. Orange line refers to the 5% Angular Axis Model with a K = 1000 J/m^3 and the green line refers to the Anisotropy Contribution Model using a global anisotropy of K_G = 800 J/m^3, granular anisotropy of K_g = 100 J/m^3. The respective vertical dash lines refer to the measured spectroid wavelength values $\lambda_{Spectroid}$ and shown in Table 5.7.

K_G of 500 J/m^3 and a granular anisotropy K_g of 100 J/m^3 were used. (Note the K_G has been reduced from the previously used 800 J/m^3 with the aim of producing simulations with greater ripple variations to better match experimental values). The physical parameters like grid/cell size and material constants remained unchanged. Simulated M-H loops are presented in Figure 5.20 with the applied field lying along the (a) easy axis and (b) hard axis.

The resulting loops show a dramatic variation in bulk magnetic properties through an increase in grain size. An increase of grain size from 10 to 40 nm produces a reduction in uniaxial anisotropy present in the thin film. Only the 10 nm grain size loops show typical easy and hard axis behaviours for a film exhibiting strong uniaxial properties. Increasing the grain size from 10 nm to 40 nm reduces the measured uniaxial anisotropy so much so that the loop exhibits near isotropic behaviour. This is indicated by the little variation between the easy and hard axis loops. Decreasing the grain size, produces a reduction in the easy axis coercive field. Similarly, a reduction in grain size closes the hard axis loop for the 10 nm simulation. These outputs are in good agreement with what was seen experimentally, in terms

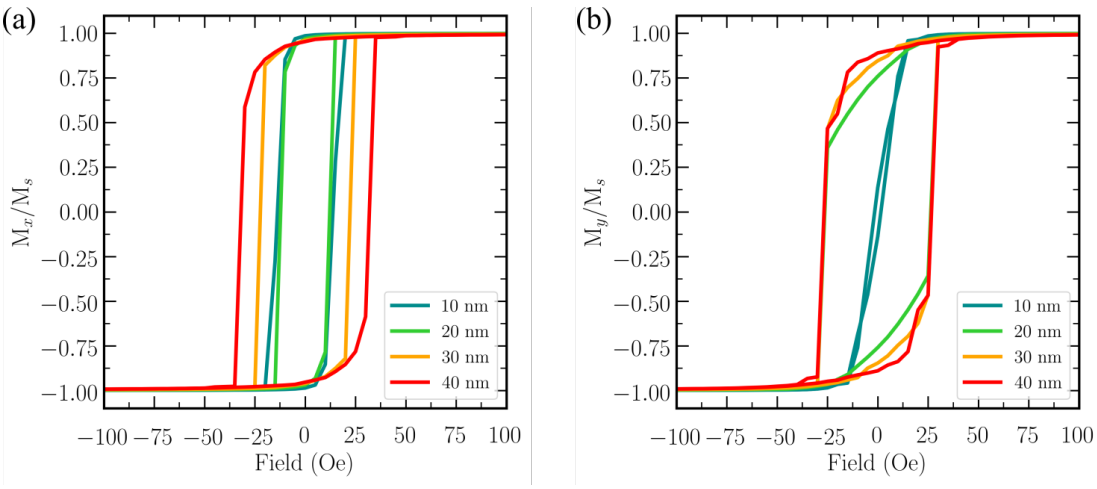

Figure 5.20: Simulated M-H hysteresis loops, with the field applied along the (a) easy axis and (b) hard axis, demonstrating the effect of increasing grain size on bulk magnetic properties.

of comparison to seed layer samples presented in Chapter 4. Key points in the hysteresis sequence are highlighted in Table 5.7. Note that the hard axis H_k, and corresponding uniaxial anisotropy K_u values are left blank for simulations with isotropic behaviour. Instead, an alternative hard axis H_c value can be measured, to emphasis the isotropic behaviour. Only the 10 nm grain simulation has a measured uniaxial anisotropy K_u in an agreement with the original input value.

Angular Variation (%)	Easy Axis H_C (Oe)	Hard Axis H_C* (Oe)	Hard Axis H_K (J/m^3)	K_u
10	20	5	12.5	500
20	20	25	-	-
30	25	25	-	-
40	35	25	-	-

Table 5.7: Key parameters from simulated M-H magnetic measurements, with increasing grain size. Results presented from both easy axis and hard axis outputs. The effective K_u value is determined from the measured H_k where $K_u = M_S H_k/2$. *Indicates a hard axis coercive measurement, indicating near isotropic behaviour i.e. when there is little difference between the easy and hard axis behaviours.

The variation in bulk magnetic properties is reflected in simulated Fresnel images shown in Figure 5.21, where (a) is a 10 nm grain simulation which increases in 10 nm steps until a 40 nm grain simulation shown in (d). These images were acquired for an applied field of +50 Oe along the easy axis, being reduced from a 200 Oe

maximum applied field. Visually, there is a substantial increase in both ripple wavelength and dispersion properties with increasing grain size and visually look more like the experimental ripple seen in Chapter 4.

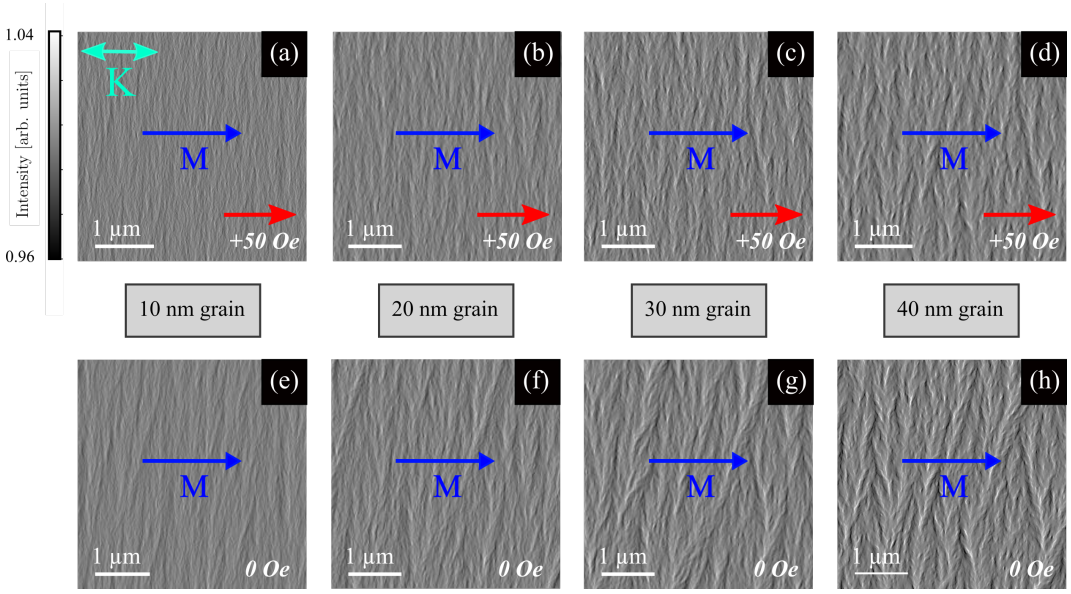

Figure 5.21: Simulated Fresnel images at a 500μm defocus, demonstrating the effect of changing the grain size on the simulated magnetisation ripple properties. (a - d) represent images taken along the easy axis at a field of 50 Oe with increasing grain size from 10 - 40 nm in steps of 10 nm. (e -h) are the equivalent images for modelled grain sizes at the remanent state.

Figure 5.21 (e-h) shows a comparison at the remanent state. This highlights the clear increase in ripple wavelength and dispersion with increasing grain size, but also the increase in these properties when compared to the images at +50 Oe (a-d).

This is reiterated when magnetisation ripple analysis is undertaken for all simulations, for a full easy axis hysteresis sweep (from +M_{Sat} to -M_{Sat}). However, for direct comparison, key points will be compared in Tables 5.8 and 5.9. These refer to magnetisation components and ripple analysis outputs for the images presented in Figure 5.21. All analysis parameters follow these same trend, whereby increasing the grain size increases the magnetisation ripple present. The magnetisation ripple wavelength at the remanent state (Table 5.9) was larger than at an applied field of 50 Oe (Table 5.8) for equivalent grain sizes.

Grain diameter (nm)	M_x/M_s [Normalised M]	$\lambda_{Spectroid}$ (nm)	λ_{Dom} (nm)	Dispersion θ °	M component °
10	0.998	30 ± 5	70 ± 20	46 ± 1	2.8
20	0.995	35 ± 5	90 ± 20	54 ± 1	4.3
30	0.992	40 ± 5	110 ± 20	55 ± 1	5.6
40	0.987	45 ± 5	170 ± 20	57 ± 1	7.4

Table 5.8: Key outputs from magnetisation ripple analysis. Table includes outputs for increasing grain size diameter at an applied field of +50 Oe along the easy axis.

Grain diameter (nm)	M_x/M_s [Normalised M]	$\lambda_{Spectroid}$ (nm)	λ_{Dom} (nm)	Dispersion θ °	M component °
10	0.986	45 ± 5	240 ± 20	49 ± 1	8.4
20	0.970	50 ± 5	280 ± 20	55 ± 1	11.9
30	0.961	50 ± 5	300 ± 20	53 ± 1	13.0
40	0.954	50 ± 5	460 ± 20	55 ± 1	14.2

Table 5.9: Key outputs from magnetisation ripple analysis. Table includes outputs for increasing grain size diameter at a remanent state

The simulation outputs produced here provide a useful tool for investigating trends. Results presented are in excellent agreement with trends seen both experimentally (for seed layer samples in Chapter 4) and with trends predicted by theory (Section 1.7), whereby grain size and ripple dispersion are proportional. The experimental results showed an increase in average grain size lead to an increase in ripple dispersion and wavelength and a reduction in K_u. These exact trends have been presented using the Anisotropy Contribution Model.

5.3.5 Effect of inter-granular exchange coupling

An investigation was undertaken to control the inter-granular exchange coupling strength $A = 13 \times 10^{-12}$ J/m, in an attempt to produce a ripple spectrum that better matches what was seen experimentally. At grain boundaries the crystal order is disrupted and so the exchange coupling between atoms is expected to have some reduction. This parameter allows for the variation in strength of the coupling between the grains. For example, 0% would mean exchange decoupled grains (fully independent and randomly distributed), and 100% would mean all grains are fully coupled. Simulations were run with the same parameters detailed in the previous

section, with a global anisotropy K_G of 500 J/m^3 and a granular anisotropy K_g of 100 J/m^3. The grain size was set to 10 nm as results shown in the previous section exhibited good easy and hard axis behaviour. Simulations were run for easy and hard axis hysteresis sequences with the exchange interaction coupling strength set as: 0, 5, 15, 50, 100%. (Note values were chosen as most variation occurred with reduced strength). Simulated M-H loops are presented in Figure 5.22 with the applied field lying along the (a) easy axis and (b) hard axis.

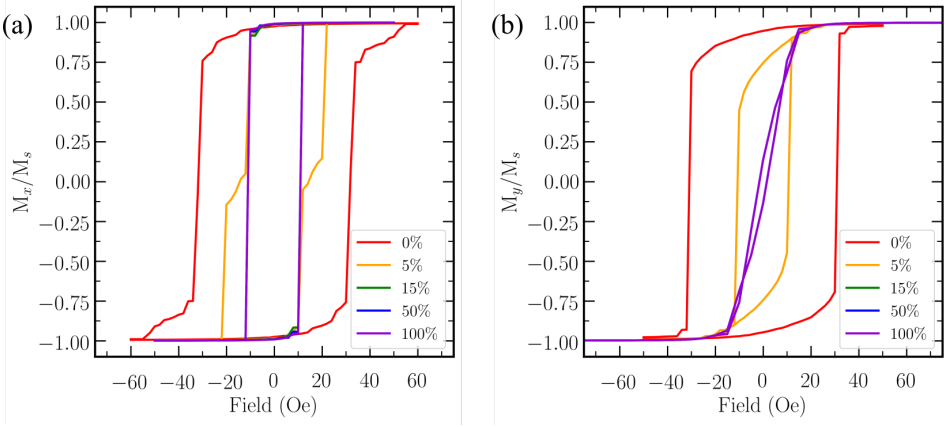

Figure 5.22: Simulated M-H hysteresis loops measured along the (a) easy axis and (b) hard axis, demonstrating the effect of changing the intergranular exchange coupling strength on the simulated bulk magnetic properties. Note, the 15, 50 and 100% plot lie on top of each other.

An increase in intergranular exchange coupling strength results in behaviour which can be identified as that for a film with well defined uniaxial anisotropy. When the strength is reduced to 0%, the behaviour is isotropic, where there is little to no variation between the easy and hard axis loops. There is a slight improvement when the strength is increased to 5%. The M-H loops exhibit typical easy and hard axis behaviour for simulations ran at 15% coupling strength or higher. Key points in the hysteresis sequence at shown in Table 5.10.

Note that the hard axis H_k, and corresponding uniaxial anisotropy K_u values are left blank for simulations with isotropic behaviour. Instead, an alternative hard axis H_c value can be measured, to emphasis the isotropic behaviour. The 15, 50 and 100% simulations have a measured uniaxial anisotropy K_u in an agreement with the original input value.

Coupling Strength (%)	Easy Axis H_C (Oe)	Hard Axis H_C* (Oe)	Hard Axis H_K J/m^3	K_u
0	30	30	-	-
5	20	10	-	-
15	10	-	12.5	500
50	10	-	12.5	500
100	10	-	12.5	500

Table 5.10: Key parameters from simulated M-H magnetic measurements, with increasing granular exchange coupling strength. Results presented from both easy axis and hard axis outputs. The effective K_u value is determined from the measured H_k where $K_u = M_s H_k/2$. *Indicates a hard axis coercive measurement, indicating near isotropic behaviour i.e. when there is little difference between the easy and hard axis behaviours.

Simulated Fresnel images are presented in Figure 5.23, acquired at a field of +50 Oe and at remanence. The most obvious difference between the images is the increase in contrast with reduced coupling strength. There also appears to be an increase in ripple dispersion with decreasing coupling strength. Magnetisation ripple characterisation was applied using the methods described in Chapter 3. Results are shown in Tables 5.11 and 5.12 which represent results acquired at +50 Oe and remanence respectively.

All simulations were in agreement, that there is a reduction in ripple properties with increasing applied field. Ripple dispersion and M component analysis both resulted in a increase in dispersion with decreasing coupling confirming what was seen visually in Figure 5.23. This is in good agreement with what is predicted by theory, which shows that dispersion angle and exchange constant are inversely proportional (Equation 1.26).

As previously discussed, the simulated FFT spectrum can provide better understanding of the frequency components. Figure 5.24 highlights the difference in FFT spectrum between 0% and 100% coupling strength at remanence. It shows a reduction in low-frequency components in the FFT spectrum with increasing coupling strength i.e. the spread of the frequency components is significantly smaller. This provides an explanation as to why measurements showed an increase in ripple

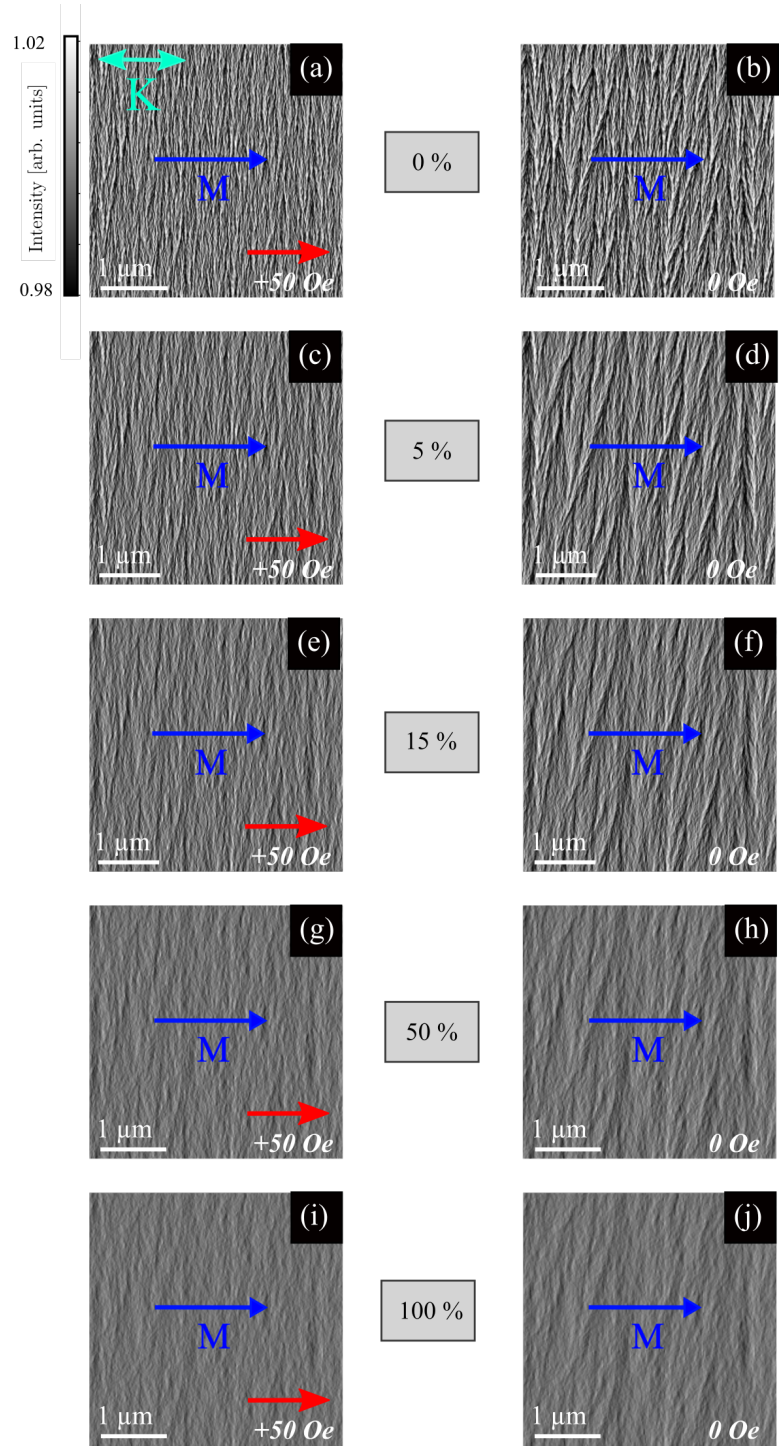

Figure 5.23: Simulated Fresnel images at a 500μm defocus, demonstrating the effect of changing the intergranular exchange coupling strength on the simulated magnetisation ripple properties. (a - e) represent images taken along the easy axis at a field of 50 Oe with increasing coupling strength from 0 to 100%. (f -j) are the equivalent strengths at the remanent state.

wavelength with increased coupling strength. This again is in agreement with theory which predicts a proportional relationship between the two. [11]

Coupling Strength (%)	M_x/M_s [Normalised M]	$\lambda_{Spectroid}$ (nm)	λ_{Dom} (nm)	Dispersion θ °	M component °
0	0.9941	25 ± 5	50 ± 20	56 ± 1	4.95
5	0.9970	30 ± 5	60 ± 20	55 ± 1	3.54
15	0.9981	30 ± 5	75 ± 20	54 ± 1	2.82
50	0.9988	35 ± 5	170 ± 20	46 ± 1	2.2
100	0.9991	40 ± 5	180 ± 20	43 ± 1	1.97

Table 5.11: Key outputs from magnetisation ripple analysis. Table includes outputs for increasing intergranular coupling strength at an applied field of +50 Oe along the easy axis.

Coupling Strength (%)	M_x/M_s [Normalised M]	$\lambda_{Spectroid}$ (nm)	λ_{Dom} (nm)	Dispersion θ °	M component °
0	0.9819	30 ± 5	370 ± 20	57 ± 1	8.96
5	0.9839	30 ± 5	380 ± 20	58 ± 1	8.69
15	0.9889	35 ± 5	380 ± 20	55 ± 1	7.34
50	0.9917	40 ± 5	460 ± 20	46 ± 1	6.54
100	0.9911	50 ± 5	500 ± 20	43 ± 1	6.8

Table 5.12: Key outputs from magnetisation ripple analysis. Table includes outputs for increasing intergranular coupling strength at a remanent state

Increased coupling strength did improve dominant wavelength values by increasing them to better match what was seen experimentally. For example, experimental results for the 1 nm seed layer sample showed a dominant ripple wavelength of approximately 600 and 900 nm at near M_{Sat} and remanence respectively. This is a relatively good match for the 50 and 100% simulation outputs. Although spectroid wavelength values did increase, it still remains that the wavelength values are considerably smaller, by nearly an order of magnitude. Changing key parameters like grain size and exchange coupling strength made little difference to improve spectroid wavelength outputs. Therefore, it can be concluded that the spectrum of simulated ripple for both models described, has different spatial contributions to experimental magnetisation ripple. However this is not unreasonable as the simulation set-up is not fully realistic in terms of physical set-up of cell/grain size.

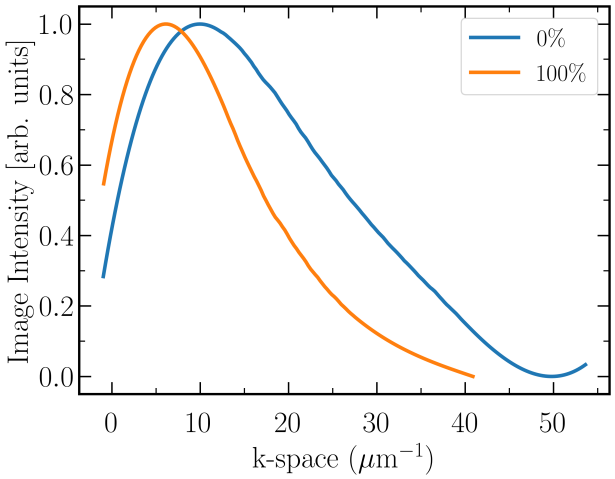

Figure 5.24: Smooth line intensity profile measured at remanence for (a) 0% (b) 100% exchange coupling strength where $A = 13$ x 10^{-12} J/m. Anisotropy contribution model using a global anisotropy of K_G of 500 J/m^3, a granular anisotropy of K_g of 100 J/m^3 and a grain size of 10 nm.

5.4 Discussion and Conclusions

The micromagnetic simulation program MuMax^3 is a finite difference software that allows for the computation of magnetisation dynamics as well as the magnetisation response to an applied magnetic field. The results presented in this chapter show that it is instructive to use numerical micromagnetic modelling for the investigation of the magnetisation reversal processes and the magnetic structure in polycrystalline thin films. Specifically focusing on trends found from quantitative analysis of magnetisation ripple properties.

Two models were presented, with the goal of replicating the phenomenon of magnetisation ripple which is a property exhibited by materials studied experimentally in this work (Chapter 4 and 6). Experimental results presented in Chapter 4 showed a large variation in magnetisation ripple properties through the addition of seed layers. The two models were used to replicate trends using differing approaches.

The first model was referred to as the 'Anisotropy Axis Variation' model. This worked by assigning each simulated grain its own magnetocrystalline anisotropy value. However, the directionality of these anisotropies could be controlled. This simulation model can replicate a sample ranging from a randomly distributed

granular anisotropy to a system with a strong uniaxial anisotropy. This model was successful in creating simulated Fresnel images which are visually very similar to that seen experimentally, for example in Chapter 4 that saw an increase in magnetisation ripple properties with increased grain size). The Fresnel images also exhibited typical easy and hard axis behaviour, with coercive field switching and magnetisation rotation respectively (for simulations with strong uniaxial anisotropy). Magnetisation ripple analysis developed and described in Chapter 3 was tested on simulated Fresnel images. Results confirmed there was a decrease in ripple properties, such as wavelength and dispersion with decreasing angular variation (and degree of global anisotropy observed). The observed magnetisation ripple was visually very good in terms of qualitative appearance. The model proved useful for predicting trends of magnetisation ripple properties, however it is simplistic in it's control over specific parameters, such as a anisotropies.

To improve on this, a second model was presented which allows for the control over individual anisotropy parameters. It is referred to as the 'Individual Anisotropy Contributions Model'. This was thought to be a more realistic model of the actual anisotropy contributions in the material, though with caveat about grain shape. In this model there were 2 inputted anisotropy parameters: (a) the individual magnetocrystalline anisotropy, that would lie in a random direction in 3D and (b) a global induced anisotropy that would lie in one specific direction, in this case along the x-axis. These two inputs could be individually controlled, along with other parameters. This model was used to investigate the effect of grain size. It proved to have a significant change effect on magnetic properties. There was a dramatic effect on the simulated M-H loops on both the easy and hard axis. A smaller grain size appeared to give better uniaxial anisotropy definition, through an increase in H_k, as defined by measurement from hysteresis loop. All magnetisation ripple properties, such as wavelength and dispersion, increased with increasing grain size. This confirmed the trends seen experimentally in Chapter 4. The effect of intergranular exchange coupling had a more subtle effect when compared to the grain size variation. However, it did produce an increase in ripple dispersion with

decreasing coupling, which in turn produced a reduction in the observed uniaxial anisotropy measured from the simulated M-H loop. There is also a decrease in wavelength with decreasing coupling. Both properties (dispersion and wavelength) follow trends predicted by magnetisation ripple theory.

Both models were successful in producing qualitatively excellent simulated Fresnel images which visually replicated magnetisation ripple properties. The magnetisation ripple characterisation methodology developed and described in Chapter 3 also worked successfully on simulated Fresnel images.

The ripple spectrum for both models had a much greater high spatial frequency contribution when compared to an experimental spectrum. This provides an explanation as to why the spectroid wavelength values are significantly lower (by nearly an order of magnitude) to what was seen experimentally. However, the dominant ripple wavelength outputs were much more realistic, in the order of 100s of nanometres.

Limitations of the models means differences in values are to be expected. The main issue being the realistic modelling of grains for the length scales required to produce ripple effects. This certainly provides a problem for future work. An improvement might be to use finite element (FE) modelling techniques. FE modelling is not restricted by uniform square cell sizes, so would allow for a more accurate representation of the polycrystalline granular structure, as seen experimentally through bright-field images. This would allow for simulation of granular shapes that are non-uniform.

5.5 References

[1] A. Gentils and J. N. Chapman. Variation of domain-wall structures and magnetization ripple spectra in permalloy films with controlled uniaxial anisotropy. *Journal of Applied Physics*, 98, 053905, (2005).

[2] A. Kohn and A. Habibi. Adapting a JEM-2100F for magnetic imaging by Lorentz TEM. *Jeol News*, 43(3): 17 - 22, (2012).

[3] D-T. Ngo. In-situ transmission electron microscopy for magnetic nanostructures. *Journal of Physics D: Applied Physics*. 44:9(095001), (2011).

[4] B. A. Belyaev. Numerical simulation of magnetic microstructure in nanocrystalline thin films with the random anisotropy. *Journal of Siberian Federal University. Mathematics and Physics*, 10(1), 132-135, (2017).

[5] D. V. Berkov and N. L. Gorn. Numerical simulation of remagnetisation processes in polycrystalline magnetic thin films with random anisotropy. *physica status solidi (a)*, 161, (1997).

[6] M. Dvornik M. Helsen F. Garcia-Sanchez A. Vansteenkiste J.Leliaert and B. Van Waeyenberge. The design and verification of mumax3. *AIP Advances*, 4(10):107133, (2014).

[7] A. L. Wysocki. Micromagnetic simulations with periodic boundary conditions: Hard-soft nanocomposites. *arXiv Condensed Matter*, 1510.08543, (2015).

[8] K. M. Lebecki. Periodic boundary conditions for demagnetization interactions in micromagnetic simulations. *Journal of Physics D: Applied Physics*, 41(17), (2008).

[9] S. McVitie and M. Cushley. Quantitative Fresnel Lorentz microscopy and the transport of intensity equation. *Ultramicroscopy*, 106(4-5):423-431, (2006).

[10] M. Mansuripur. Computation of electron diffraction patterns in Lorentz electron microscopy of thin magnetic films. *Journal of Applied Physics*, 69(8):5890, (1991).

[11] H. Hoffmann. Theory of Magnetization Ripple. *IEEE Transactions on Magnetics*. 4(1):32-38, (1968).

[12] C. Hill. Whole wafter magnetostriction metrology for magnetic films and multilayers. *IOP Science, Meas. Sci. Technol.*, 24:45601, (2013).

6

Characterisation of Magnetostriction with Observation of Magnetic Ripple using Lorentz TEM

Contents

6.1 Introduction

The effect of magnetostriction (Figure 6.1) is an important, though less intensively studied, effect in magnetic data storage technology. Although the presence of magnetostriction in device materials may be a small effect it is recognised as potentially significant. [1-3] Previous bulk measurement techniques showed how it can have a significant effect on the magnetic properties, particularly in the presence of tensile and compressive forces [4-8]. The effects of magnetostriction for materials without such applied external stresses but under normal operating conditions are less well understood. In this project we are interested in a micromagnetic study to investigate this from an experimental and modelling perspective. This project focuses on one of the most commonly used materials in data recording, permalloy with a composition varying around the 80/20 nickel to iron ratio. Details of the sample deposition can be found in Section 6.2. The reason for choosing this value is that the magnetostriction constant changes from negative to positive around this composition as the elemental ratio changes (as discussed in Section 1.5.4). We aim to identify the subtle effects magnetostriction has on continuous thin films of permalloy with three different compositions by studying their physical (Section 6.3) and magnetic behaviour (Section 6.4). Experimentally we have observed the micromagnetic behaviour in terms of magnetic ripple using Lorentz transmission electron microscopy (LTEM) for different magnetostrictive samples, with results shown in Section 6.5. This nano-scale visualisation of the magnetisation ripple structure allows for not only the mapping of hysteresis behaviour, but quantitative characterisation of the material. Section 6.6 details how it might be possible to quantitatively asses the magnetic effect magnetostriction has on the hysteresis behaviour of these samples in the absence of strain. Simulations can be performed in conjunction with these studies using the package MuMax^3 [9], in order to compare simulated trends with experimental results. Simulated results are shown

in Section 6.7. Lastly, a preliminary in-situ heating experiment was carried out to determine the relationship between magnetisation ripple and temperature, with results presented in Section 6.8.

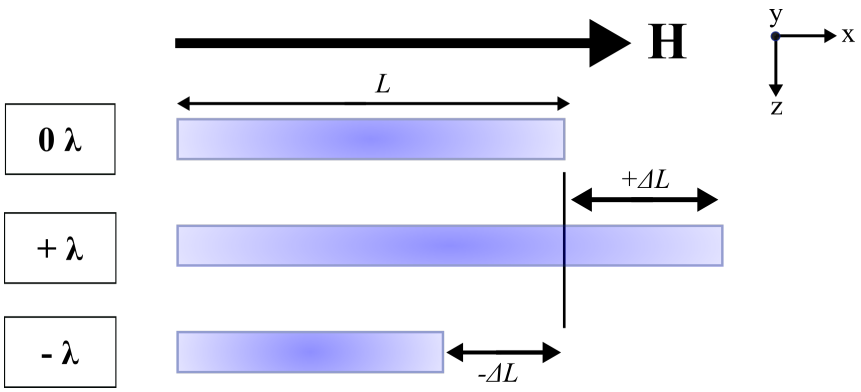

Figure 6.1: Simplified schematic of the effect of magnetostriction. A material of length L will exhibit a length change in the presence of an applied field **H**. A positive magnetostrictive (+λ) sample will experience an increase of length +ΔL along the direction of **H**. The opposite occurs for a negative magnetostrictive sample -λ.

Results in this chapter were produced in collaboration with Seagate Technology, UK. The sample preparation and bulk magnetic measurements were undertaken by Kevin McNeill and Muhammad Bilal Janjua using tools located at Seagate. All remaining imaging and analysis was undertaken by myself at the University of Glasgow.

6.2 Sample Deposition

As mentioned previously, magnetostriction strength and sign in permalloy is highly dependent on the composition values of the nickel and iron in the alloy. The crossover of magnetostrictive properties as a function of sample composition is a well published effect. [10,11] This crossover is the main focus area of results presented in this Chapter. Table 6.1 summarises how small compositional variations change the magnetostrictive signs.

Figure 6.2 shows a schematic illustration of the deposited thin film structures. Three Nickel/Iron polycrystalline films of equal thickness were investigated. All samples consisted of a 2 nm seed layer of Ru, followed by a 20 nm Ni_xFe_{100-x} layer

% Ni	λ_s
77.5	4×10^{-6}
80	1×10^{-6}
82.5	-2.5×10^{-6}

Table 6.1: Summary of composition of samples fabricated in this study. Magnetostrictive sign and value as a function of nickel composition in permalloy measured from bulk thin films. [7]

with composition values given in Table 6.1. Additionally, all films were capped with a 2 nm Ru layer to prevent subsequent oxidation.

Radio frequency (rf) magnetron sputter deposition took place at Seagate Technology, UK using an Anelva c-7100 tool. Deposition conditions were identical to those used on the set of seed layer samples described in Chapter 4.2. This includes a 100 Oe external field being applied in-plane during deposition to help induce uniaxial anisotropy. Deposited films were then annealed in a 0.3 T applied field at 225 degrees for 2 hours (along the same direction as the deposition field). This is a vital step in the deposition process as a well defined easy and hard axis is essential for the definition of good uniaxial behaviour. Films were deposited onto 100×100 μm^2 electron transparent Si_3Ni_4 membranes for TEM measurements, as well as larger Si substrates for bulk magnetic measurements.

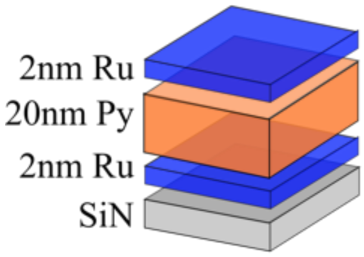

Figure 6.2: Cross section schematic showing the structure of samples under investigation. All samples consist of a 20 nm permalloy layer of varying composition. All samples are capped with a 2 nm Ru layer with an additional 2 nm Ru seed layer. All samples were deposited on electron transparent Si_3Ni_4 membranes.

6.3 Physical Microstructure

6.3.1 Crystal Structure

The same experimental characterisation methods described in Chapter 4 were also carried out on the set of magnetostrictive samples. This includes using electron diffraction images to determine a thin films crystal structure. Figure 6.3 shows untilted selected area electron diffraction (SAED) images for (a) $Ni_{77.5}Fe_{22.5}$ (b) $Ni_{80}Fe_{20}$ and (c) $Ni_{82.5}Fe_{17.5}$ permalloy alloys.

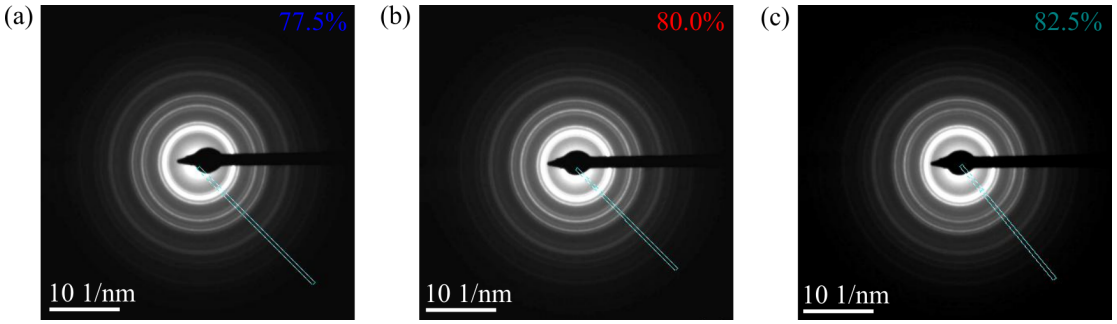

Figure 6.3: Experimental SAED patterns for (a) $Ni_{77.5}Fe_{22.5}$ (b) $Ni_{80}Fe_{20}$ and (c) $Ni_{82.5}Fe_{17.5}$ permalloy thin films. Images were acquired at zero tilt. Blue box represents the location of the integrated line profile which is shown in Figure 6.4, with an integration width of 0.4 nm^{-1}.

The uniform circular diffraction ring pattern confirms that all three samples are polycrystalline. When tilted the circular rings retained their uniformity. This indicates that the grains in the film are randomly orientated and there is no texture present in any of the films.

The Nickel/Iron alloys for all compositions have a *fcc* (face-centred cubic) crystal structure. To recap, the lattice spacing for cubic systems can be determined by the following equation:

$$d_{hkl} = \frac{a}{\sqrt{(h^2 + k^2 + l^2)}} \tag{6.1}$$

The Ruthenium cap and seed layer has a different crystal system to the Nickel/Iron permalloy. Ru has a hexagonal crystal (*hcp*) structure. The lattice spacing for this system is given by:

$$d_{hkl} = \frac{1}{\sqrt{\frac{4}{3a^2}(h^2 + k^2 + hk) + \frac{l^2}{c^2}}} \tag{6.2}$$

with a and c being the lattice constants of the crystal structure, and h,k,l are the Miller indexes.

Each diffraction ring can be successfully indexed by taking an integrated line profile from the origin of the diffraction pattern and analysing the patterns of peaks. The area of this integrated profile is highlighted on Figure 6.3 by the blue box, with an integration width of 0.4 nm^{-1}. All three line profiles are plotted and shown in Figure 6.4. The three profiles overlap, meaning all 3 samples have identical crystal structures.

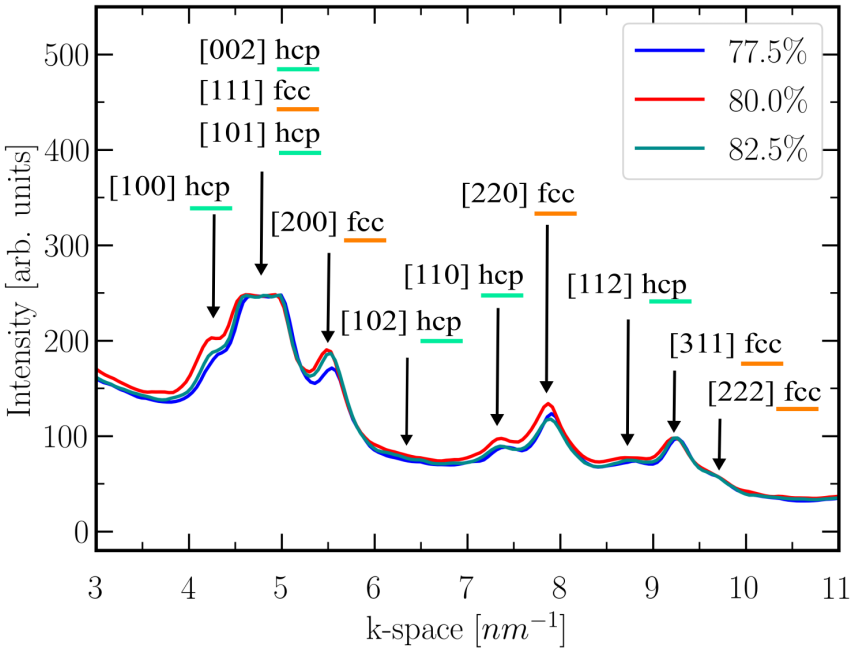

Figure 6.4: Indexed diffracton rings from SAED patterns for (a) $Ni_{77.5}Fe_{22.5}$ (b) $Ni_{80}Fe_{20}$ and (c) $Ni_{82.5}Fe_{17.5}$ permalloy thin films. Images were acquired at zero tilt. Both *hcp* and *fcc* crystal structures are successfully indexed, showing negligible changes in peak position between the 3 samples.

By assuming crystal structures (a and c parameters) for permalloy and Ru, each ring can be individually identified. The corresponding locations are highlighted in Figure 6.4. By assuming the peaks associated with the relevant crystal structures, it was approximately calculated for a Ru crystal, $a = 0.3$ nm and $c = 0.4$ nm. It

also confirmed that for all permalloy specimens, a = 0.4 nm, which is consistent with the expected structures. Therefore it can be said all 3 samples in effect have the same crystal structure with only a very small variation in the lattice parameters of the permalloy.

6.3.2 Grain Size Distribution

Bright-field and dark-field TEM images allow for the visualisation of a polycrystalline thin films granular structure. Figures 6.5 and 6.6 show experimental bright-field and dark-field images respectively for various permalloy compositions. Visually there is no significant difference between the 3 samples. All samples appear to have a uniform distribution of grain sizes.

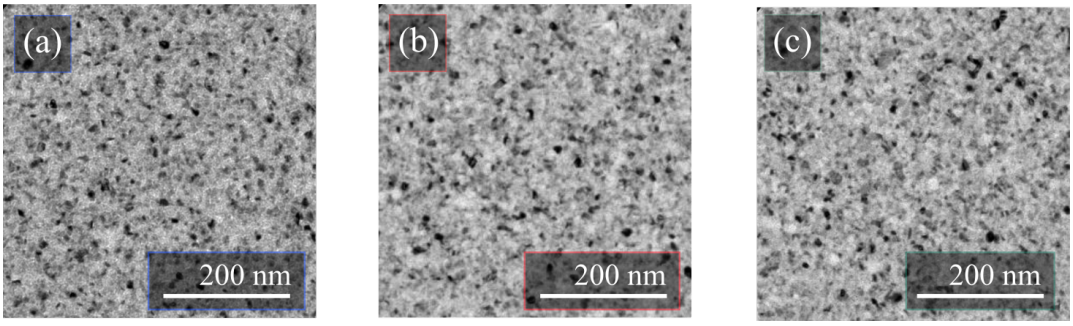

Figure 6.5: Experimental bright-field TEM images, displaying the grain size distribution for a (a) $Ni_{77.5}Fe_{22.5}$ (b) $Ni_{80}Fe_{20}$ and (c) $Ni_{82.5}Fe_{17.5}$ permalloy alloy. Note, image pixel size of 0.47 nm.

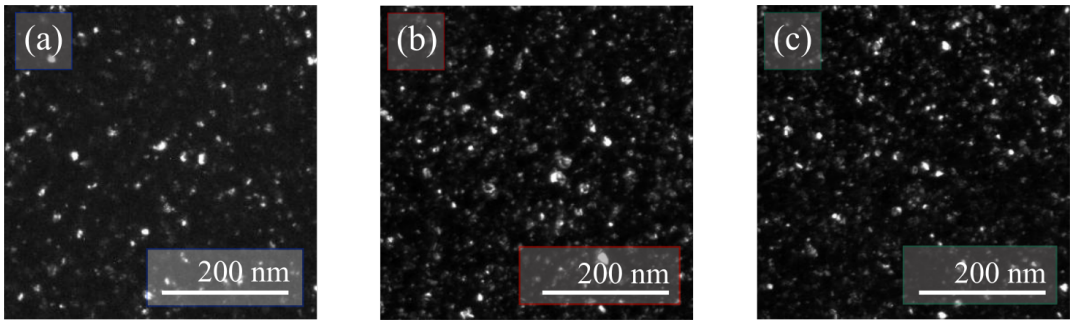

Figure 6.6: Experimental dark-field TEM images, displaying the grain size distribution for a (a) $Ni_{77.5}Fe_{22.5}$ (b) $Ni_{80}Fe_{20}$ and (c) $Ni_{82.5}Fe_{17.5}$ permalloy alloy. Note, image pixel size of 0.47 nm.

A large number of experimental dark-field images were taken for each sample ($\approx$ 20). The produced over 3000 grains (per sample) for measurement. The

same grain size distribution measurement process that was used in Chapter 4 was used on the magnetostriction samples (See Section 6.4.2 for a more detailed description). The calculated log-normal distribution can then normalised and plotted against measured grain diameters. Results are shown in Figure 6.7, with key outputs highlighted in Table 6.2.

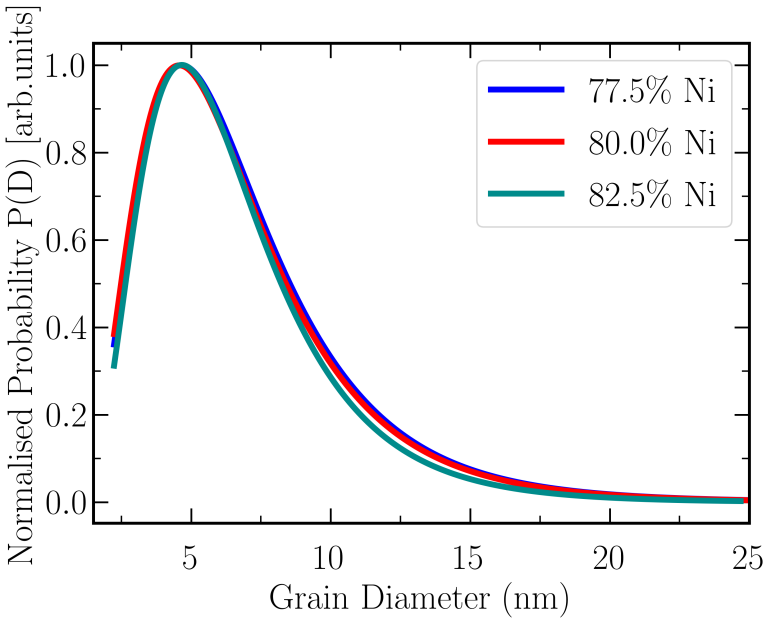

Figure 6.7: Measured grain size distribution results; normalised best-fit log-normal grain size distribution for (a) $Ni_{77.5}Fe_{22.5}$ (b) $Ni_{80}Fe_{20}$ and (c) $Ni_{82.5}Fe_{17.5}$ samples.

Results show that the change in permalloy composition has a negligible effect on the overall grain size distribution. All samples have a measured log-normal peak of approximately 4.6 $\pm$ 0.5 nm. The narrow distribution of the grains also confirms homogeneity of the grain sizes, which is consistent over all samples. Results confirm that the grain size is lower than the samples exchange length (l_{ex} = 5.3 nm for $Ni_{80}Fe_{20}$), meaning it is expected that there will be strong coupling between the grains. As shown in results presented in Chapter 4, a small grain size results in a suppression of the magnetisation ripple wavelength and dispersion when compared to grains of larger diameter. Magnetisation ripple properties will be investigated using Lorentz TEM in Section 6.5, which allows for micromagnetic visualisation. In order to achieve improved magnetic properties (such as larger uniaxial anisotropy), a uniform grain morphology and a narrow grain size distribution are suggested.

Ni Content (%)	Mean Diameter (nm)	Standard Deviation (nm)	Log-normal Peak (nm)
77.5	6.1 ± 0.5	1.7	4.6 ± 0.5
80.0	6.0 ± 0.5	1.7	4.7 ± 0.5
82.5	5.9 ± 0.5	1.6	4.5 ± 0.5

Table 6.2: Grain size distribution analysis outputs. All samples show near identical granular distributions.

6.4 Bulk Magnetic Measurements

The influence of Nickel/Iron composition on the bulk magnetic properties of permalloy thin films can be investigated. As stated earlier, bulk magnetic measurements were undertaken by K. McNeill and M. Janjua using tools located at Seagate Technology, UK. Along with samples being deposited onto TEM membranes for TEM imaging, samples were also deposited onto larger Si wafers. This was essential to ensure there was a large enough signal when taking hysteresis measurements on a commercial B-H loop tracer (as described in Section 2.3.1.)

Figure 6.8 (a) and (b) shows the normalised easy and hard axis hysteresis loops respectively, from the B-H loop measurements. All three samples show well-defined uniaxial hysteresis loops resulting from successful heat and field annealing treatments. Key points in the hysteresis sequence are highlighted in Table 6.3. The easy axis behaviour is near identical for all 3 compositions, with a variation of as little as 0.1 Oe for coercive field measurements. The measured H_C along the easy axis has a value of $\approx$ 1.9 Oe, and an easy axis anisotropy field of 2.6 Oe.

The hard axis behaviour sees more variation between samples, as seen from Figure 6.8 (b) by the change in slope. This results in a shift of the anisotropy field H_k value. When measured there is a change of 1.5 Oe (25%) between the three samples, with the +ve magnetostrictive sample having a H_k value of 6.0 Oe, compared to that of 4.5 Oe for the -ve magnetostrictive sample. This variation in slope can be characterised as hard axis magnetic susceptibility χ, which shows an increase in slope (χ) with increasing Nickel content. Exact values are shown in Table 6.3.

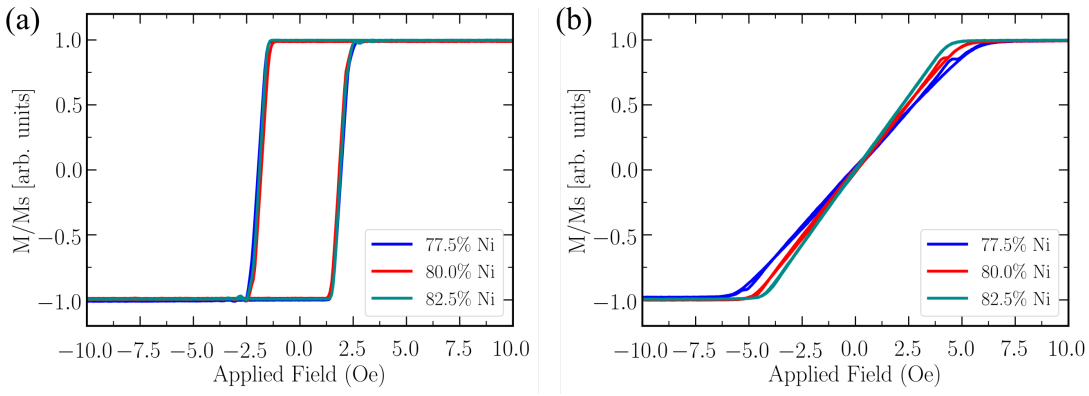

Figure 6.8: Hysteresis loops for Ni_xFe_{100-x} alloys of varying compositions, with the field applied along the (a) easy axis and (b) hard axis. Results show there is minimal variation in easy axis hysteresis loops. Hard axis results reveal a small variation in the anisotropy field H_k values, as little as 1.5 Oe.

Work presented from Queen's University Belfast showed how bulk magnetic behaviour could be manipulated through the addition of stress. [7] The changes in bulk magnetic behaviour were dependent on the magnetostrictive sign of the film and the direction of applied stress. For example, stress applied to a +ve magnetostrictive sample along the hard axis would reduce the susceptibility, meaning a larger applied field is needed to reduce magnetisation saturation i.e. an increase in H_k.

It is suggested that the applied field might cause similar modifications of hysteresis behaviour, without the need for external stresses. The hard axis did produce results with a variation of 1.5 Oe in H_k measurements between the positive and negative samples. This observation could be suggested to be consistent with magnetostriction trends, however it would be expected for there to be a variation in easy axis behaviour, that would manifest itself as a measurable effect.

There could be an argument to be made, that this effect could be due to the relation between magnetisation and volume (Equation 1.3). This equation describes magnetisation as inversely proportional to volume. If it is assumed that the magnetic moment in each atom remains unchanged, then a negative magnetostriction sample would experience a reduction in length, resulting in an increase in magnetisation. It would then be expected that there would be a change of behaviour with applied field, whereby the negative sample would reach saturation magnetisation 'quicker'

than a positive magnetostrictive sample. This effect can be easily estimated as the exact magnetostrictive constants are known for each sample. These effects can be approximated at an increase of +0.0004% of **M** for negative magnetostrictive sample, and -0.00025% for the positive sample. Obviously, these approximations are very small. However, it is worth considering as a possible trend in variation of magnetic behaviour. This might show as a small difference in the slope of a hard axis loop (susceptibility χ).

However, it is important to consider than the trends seen here could be explained by a simple variation of anisotropy with sample composition, rather than exclusively magnetostrictive effects.

Micromagnetic measurements, which will follow in Section 6.6 will provide a more detailed description on the magnetic properties of the magnetostrictive samples.

Ni Content (%)	λ_S [arb. units]	Easy Axis H_C (Oe)	Hard Axis H_K (Oe)	$\chi = \mathbf{M}/\mathbf{H}$
77.5	4×10^{-6}	1.9	6.0	0.17
80.0	1×10^{-6}	1.8	5.0	0.20
82.5	-2.5×10^{-6}	1.9	4.5	0.22

Table 6.3: Key parameters from bulk BH looper magnetic measurements, with increasing Ni% composition. All samples exhibit a well defined uniaxial anisotropy, with key parameters such as easy axis H_C and hard axis H_k showing good agreement regardless of sample composition. Susceptibility χ is determined from hard axis slope.

6.5 Micromagnetic Visualisation

Previous sections show that all 3 magnetostrictive samples have near identical physical properties, and bulk magnetic properties along the easy axis. However, hard axis bulk analysis did produce subtle variations in the measured anisotropy field H_k and hard axis slope. The aim of this section is to provide a deeper understanding into the micromagnetic behaviour, in this case magnetisation ripple, which allows for the characterisation of more subtle effects. The goal is to observe

any distinguishable differences between the three different permalloy samples, and discuss if this could be attributed to magnetostrictive effects.

The remanent field present in the microscope column allows for the application of an applied field. This involves in-situ measurements through the tilting of the sample, allowing for magnetic hysteresis measurements. The Fresnel mode of Lorentz microscopy was used for magnetic TEM imaging. The same imaging methodology was used as that described in Chapter 4 (Section 4.5).

6.5.1 Magnetisation Reversal

The hysteresis evolution along both the easy and hard axis can be acquired through Fresnel imaging of all 3 magnetostrictive samples. An external field can be applied to the specimen by tilting the sample, and using the remanent field in the microscope. The remanent field present in the microscope column at the time of image acquisition was determined to be ≈ 65 Oe. The magnetisation **M** is assumed be be proportional to cos θ, where θ is the angle between the net magnetisation direction and the applied field direction. Therefore at saturation, when the magnetisation lies at 0, or 180 degrees (as determined by FFT analysis), the magnetisation should lie at 1 and -1 (direction cosine) respectively. For example, for a sample exhibiting 'ideal' hard axis behaviour, the magnetisation will rotate with decreasing field until it lies along the easy axis at remanence. The final $\cos(\theta)$ value can be plotted against the external field **H** applied through tilting. M-H loop results are plotted in Figure 6.9 for (a) easy axis and (b) hard axis field application, with key outputs presented in Table 6.4.

The easy axis micromagnetic TEM measurements were in good agreement with bulk measurements, with the largest difference between the methods being only 0.2 Oe. The hard axis H_k behaviour was still in relatively good agreement, but with a larger method variation. It is also worth noting that the M-H hard axis behaviour appears more 'open' at lower fields, which was not seen in bulk measurements. This suggests there might have been some hysteresis present in the goniometer stage.

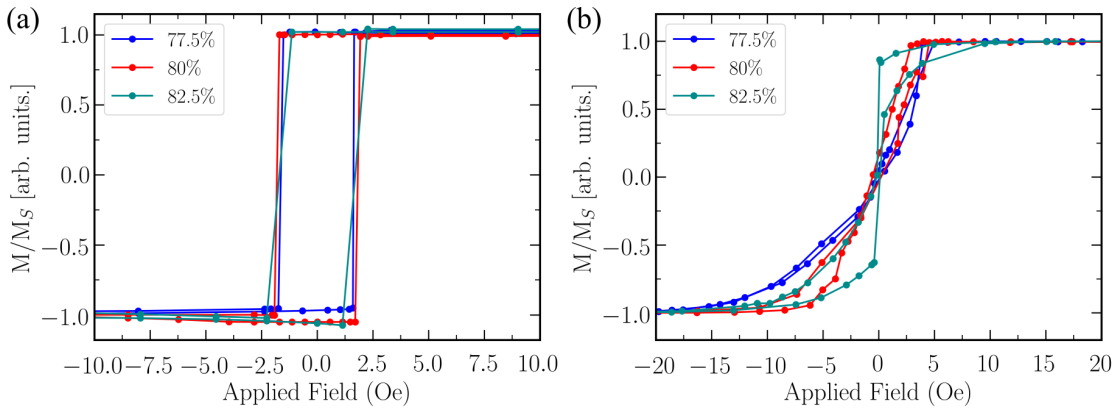

Figure 6.9: Measured M-H loops with the external field applied along the (a) easy axis and (b) hard axis for $Ni_{77.5}Fe_{22.5}$ (+λ), $Ni_{80}Fe_{20}$ (≈0 λ) and $Ni_{82.5}Fe_{17.5}$ (-λ).

Asymmetry in easy axis switching was observed for all 3 films with a value of ≈ 3 Oe. However, all samples were recalibrated to account for this.

Ni Content (%)	Bulk H_C (Oe)	TEM H_C (Oe)	Bulk H_K (Oe)	TEM H_K (Oe)
77.5	1.9	1.7	6.0	8.5
80.0	1.8	1.8	5.0	6.5
82.5	1.9	1.7	4.5	6.0

Table 6.4: Key parameters from micromagnetic measurements, with increasing Ni% composition. All samples exhibit a well defined uniaxial anisotropy, with key parameters such as easy axis H_C and hard axis H_k showing good agreement regardless of sample composition.

6.5.2 Easy Axis Reversal

For an applied field lying parallel to the easy axis of a magnetic thin film, the magnetisation reversal process normally proceeds by a single 180° domain wall sweeping across the sample. In reality, the wall was rarely/never imaged for easy axis reversal, with only a rapid event being discernible at the coercive field H_C. The applied field was increased slowly to get in close approximation to the coercive field H_C of the sample. Magnetisation ripple allows for the orientation of the magnetisation **M** to be determined as it lies perpendicular to the dominant longitudinal ripple. The easy axis reversal processes for all 3 magnetostrictive

samples will be briefly described. Example Fresnel images throughout one hysteresis sweep will be shown. These acquired images are expected to exhibit very similar micromagnetic reversal processes to the results obtained through bulk and M-H hysteresis measurements.

Figure 6.10 shows images of the reversal mechanism along the easy axis of 77.5% Ni sample, and the corresponding location on the bulk M-H hysteresis loop. On reduction of the applied field from + 8 Oe (a) to +1.5 Oe (b), there was a visible increase in ripple dispersion and wavelength. A domain wall suddenly appeared in the field of view at a switching field of approximately -1.6 Oe shown in (c), featuring cross-tie walls. Note the change in magnetisation direction (roughly approximated by blue arrow) from image (b) to (d). Any further increase of field resulted in a slight suppression of the magnetisation ripple, as seen in the comparison of Figure 6.10 (d) and (e) taken at -1.7 Oe and -8 Oe respectively.

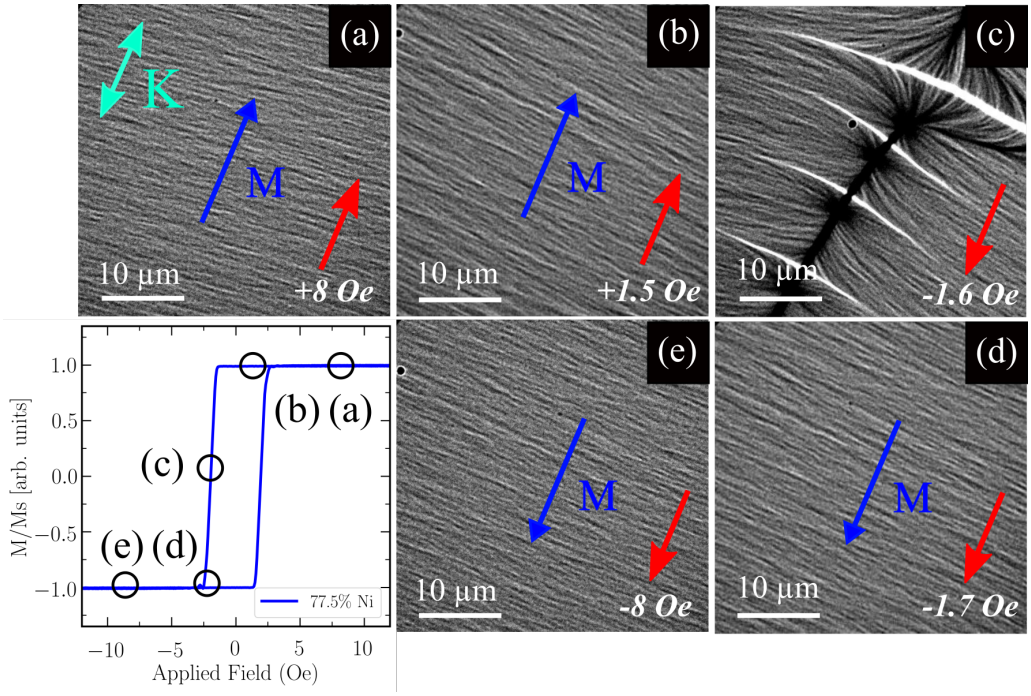

Figure 6.10: Fresnel images demonstrating the magnetisation reversal process along the easy axis of a 20 nm $Ni_{77.5}Fe_{22.5}$ thin film. The red arrows represent the direction of the applied field, H, and K is the uniaxial anisotropy direction. The corresponding location of the Fresnel image is highlighted on the bulk B-H hysteresis loop.

Similar behaviours were observed for 80% and 82.5% Ni magnetostrictive samples,

presented in Figures 6.11 and 6.12 respectively. Visually, there are subtle differences between the samples behaviours, with what appears to be increased ripple dispersion with increased Ni content, however further analysis will be needed to confirm this (Section 6.6). The characterisation methodology developed and described in Chapter 3 will be used to distinguish any subtle variation between the 3 different films.

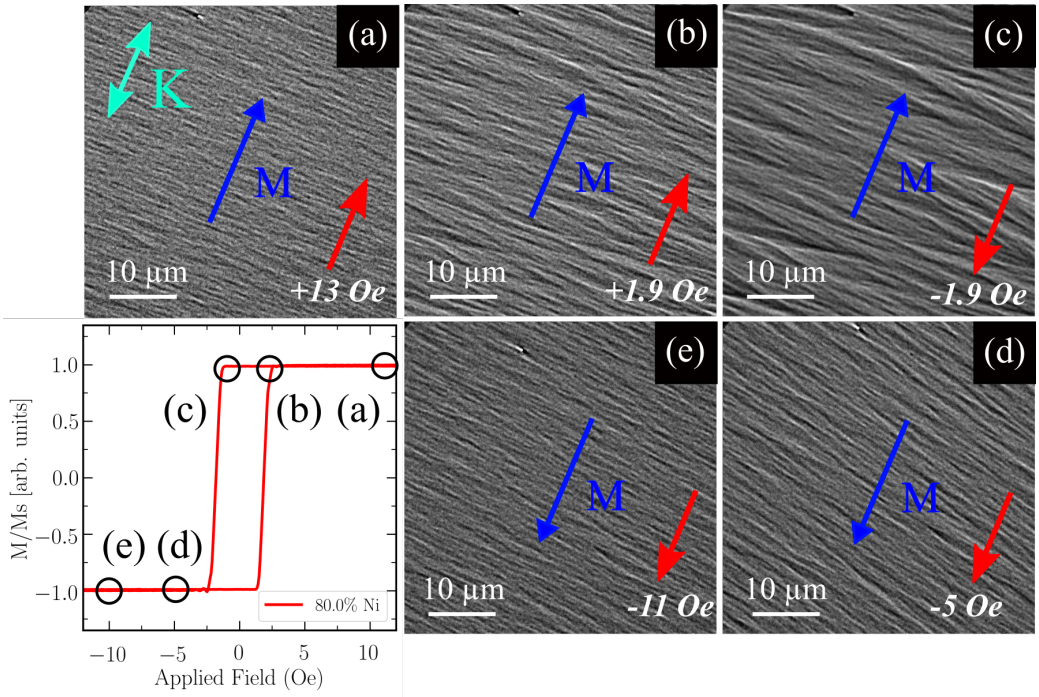

Figure 6.11: Fresnel images demonstrating the magnetisation reversal process along the easy axis of a 20 nm $Ni_{80}Fe_{20}$ thin film. The corresponding location of the Fresnel image is highlighted on the bulk B-H hysteresis loop.

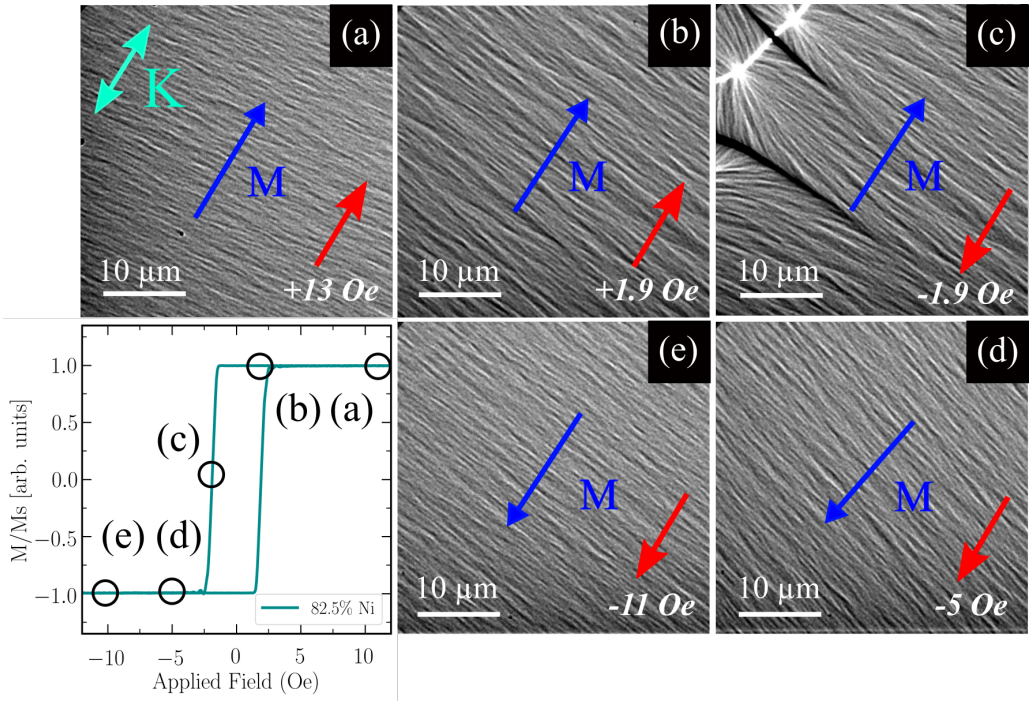

Figure 6.12: Fresnel images demonstrating the magnetisation reversal process along the easy axis of a 20 nm $Ni_{82.5}Fe_{17.5}$ thin film. The corresponding location of the Fresnel image is highlighted on the bulk B-H hysteresis loop.

6.5.3 Hard Axis Reversal

Hard axis behaviour typically involves rotation of the magnetisation and formation of domain walls with reducing applied field, assuming the field lied exactly along the hard axis. Similarly to the previous section, acquired Fresnel images at key stages in the hard axis hysteresis reversal will be shown for each magnetostrictive sample for direct comparison.

Experimental Fresnel images were acquired from the hard axis of the 77.5% Ni sample. Typical hard axis hysteresis behaviour was observed and is shown in Figure 6.13. Ripple dispersion and wavelength was increased with a reduction of the applied field (b), until the formation of low-angle domain walls (Néel-type wall), displayed in Figure 6.13(c). These domains then rotate with varying field, until the walls lie perpendicular to the hard axis (or parallel to the easy axis). An increase in field in the opposing direction will rotate the domains by 90 degrees until the magnetisation lies parallel to the field (d,e). On the reverse path, similar behaviour was observed.

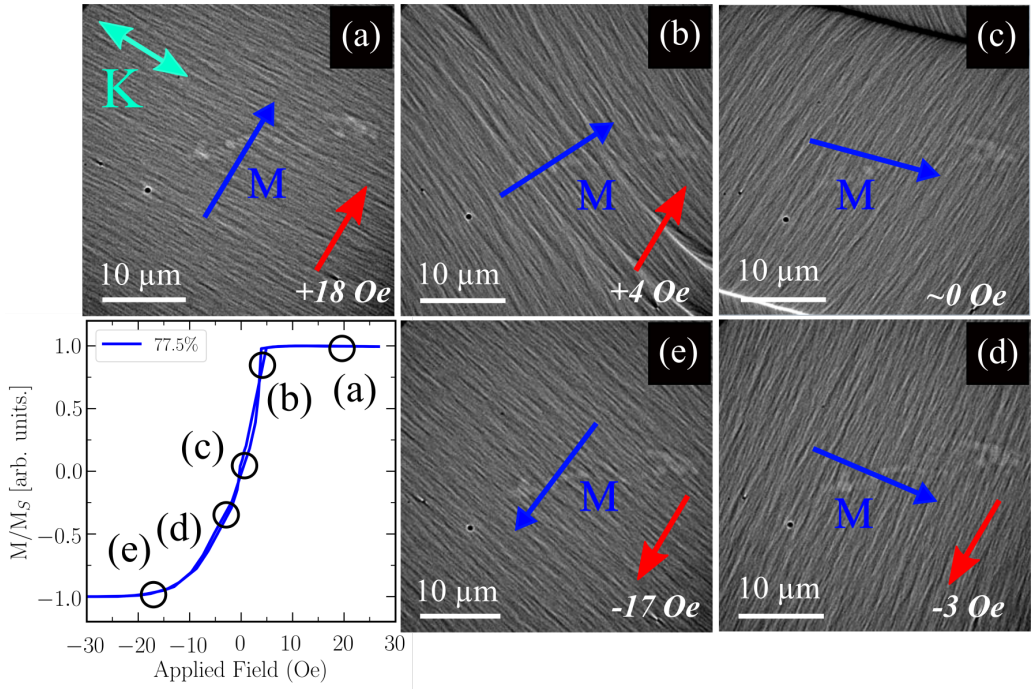

Figure 6.13: Fresnel images demonstrating the magnetisation reversal process along the hard axis of a 20 nm $Ni_{77.5}Fe_{22.5}$ thin film. The red arrows represent the direction of the applied field, H, and K is the uniaxial anisotropy direction. The corresponding location of the Fresnel image is highlighted on the bulk B-H hysteresis loop.

Figures 6.14 and 6.15 display experimental Fresnel images for the 80% and 82.5% Ni samples respectively. Both samples display typical hard axis behaviour in regards to **M** rotation and domain formation. The following section will use magnetisation ripple characterisation techniques to measure ripple properties as a function of field for both easy and hard axis behaviour.

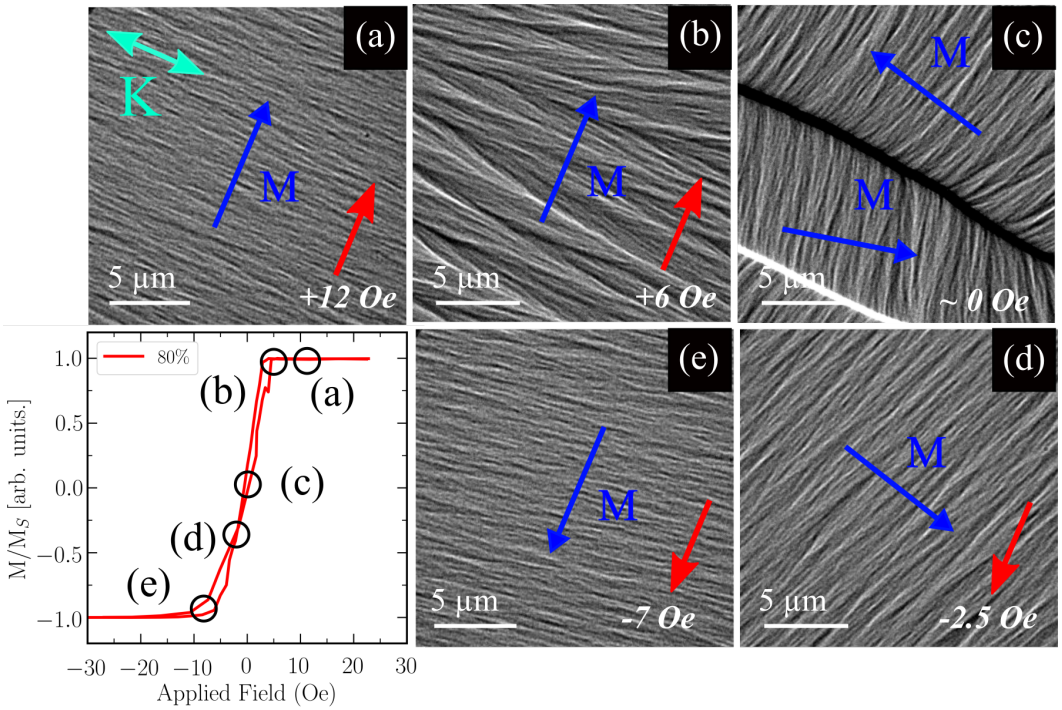

Figure 6.14: Fresnel images demonstrating the magnetisation reversal process along the hard axis of a 20 nm $Ni_{80}Fe_{20}$ thin film. The corresponding location of the Fresnel image is highlighted on the bulk B-H hysteresis loop.

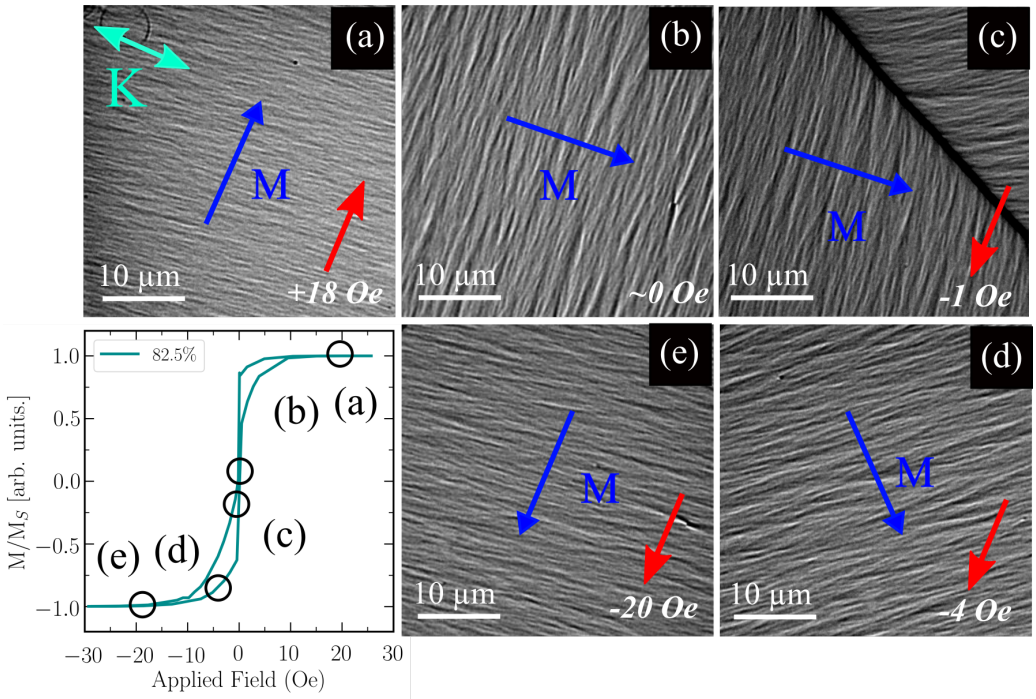

Figure 6.15: Fresnel images demonstrating the magnetisation reversal process along the hard axis of a 20 nm $Ni_{82.5}Fe_{17.5}$ thin film. The corresponding location of the Fresnel image is highlighted on the bulk B-H hysteresis loop.

6.6 Magnetisation Ripple Characterisation

Chapter 3 detailed a newly developed methodology for magnetisation ripple characterisation. It described how image processing techniques could be used to produce data in reciprocal space, which leads to more information being acquired about a specimens micromagnetic configuration during magnetisation reversal processes. This section will use the spectroid ripple wavelength $\lambda_{Spectroid}$ parameter to investigate experimental ripple wavelength (a more detailed description is provided in Section 3.8). It uses weighted averaging techniques for the full wavelength spectrum to produce a more consistent method when characterising more suppressed ripple properties for experimental Fresnel images (as shown in Chapter 4). Other wavelength determination techniques, such as dominant ripple wavelength λ_{Dom} (Section 3.7) have larger measurement errors for more suppressed ripple properties with low experimental Fresnel image contrast. All of the magnetostrictive samples were individually investigated as a function of applied field along the easy and hard axis. The hysteresis sequence is directly compared for all samples in Figures 6.16 and 6.17 for easy and hard axis hysteresis respectively. Section 6.6.1 provides further discussion and comparison between the magnetostrictive samples when considering the change in magnetisation ripple properties, specifically as the field increases towards magnetisation saturation.

Results displayed in Figure 6.16(a) show that there is a variation in ripple wavelength along the easy axis when comparing the 3 magnetostrictive samples. Generally, the 82.5% Ni (or negative magnetostrictive) sample has the largest ripple wavelength through out a full hysteresis sequence. The 80%Ni sample generally has a slightly lower ripple wavelength value, followed by 77.5% Ni exhibiting the lowest wavelength values.

Remembering the bulk magnetic measurement results presented in Section 6.4, the 77.5% (+ve magnetostrictive) sample exhibited the largest anisotropy field value and smallest hard axis slope, resulting in the strongest uniaxial anisotropy of all 3 films. Similarly to results presented in both Chapters 4 and 5, a stronger uniaxial

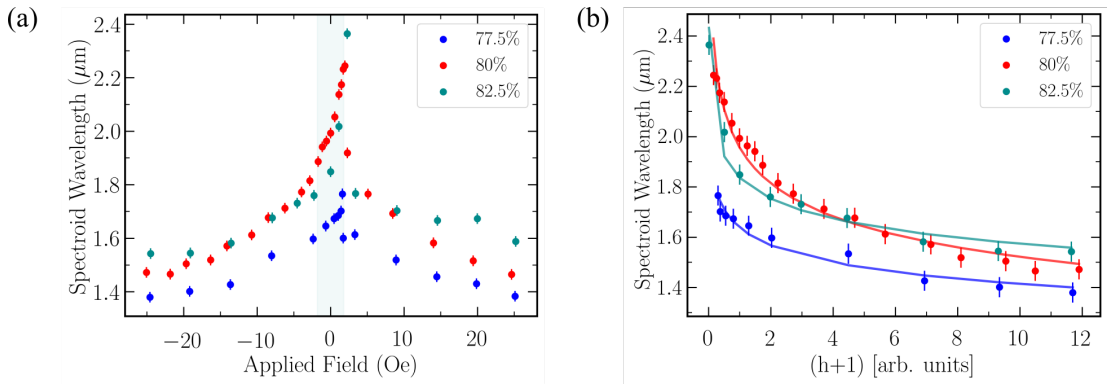

Figure 6.16: Easy axis magnetisation ripple analysis outputs for a magnetostrictive samples of varying sign. Field going from negative to positive in each case. The shaded area refers to the measured coercive field, H_C value. Outputs are plotted against field for (a) spectroid ripple wavelength $\lambda_{Spectroid}$. (b) is a specific region of (a) indicated by the box, ranging from -25 Oe to just before the switching field with best-fit power law. Note the field values have been inversely flipped for ease of analysis.

anisotropy acts to suppress magnetisation ripple wavelength and dispersion properties. Therefore, magnetisation ripple analysis presented here is also in agreement.

A line of best-fit is applied to the ripple wavelength points for all 3 sample plots (for the region outlined by the box in (a)) and is shown in Figure 6.16(b). For ease of analysis, the fields are reversed to be positive, and refer to the region of -25 Oe to just before the switching field. The wavelength is plotted against the reduced field ($h+1 = (H/H_k)+1$) for standard easy axis behaviour. This allows for the exponent of the best-fit power law to be determined, which will be discussed in the following section.

Similar trends are displayed in Figure 6.17(a) which show that there is a variation in ripple wavelength along the hard axis when comparing the 3 magnetostrictive samples. Again, the 82.5% Ni (or negative magnetostrictive) sample has the largest ripple wavelength through out a full hysteresis sequence. The 80% Ni sample generally has a slightly lower ripple wavelength value, followed by 77.5% Ni exhibiting the lowest wavelength values. The best-fit power law of the ripple wavelength points can be applied to all 3 plots using python analysis, with fields larger than the anisotropy field H_k (indicated by the box in (a)). The results are shown in Figure 6.17(b). There is a change in the ' order' of mangetostrictive samples with applied field, when compared to the 'order' seen in Figure 6.16. At -25

Oe the 80% (or near zero) magnetostrictive sample has the lowest ripple wavelength. Reasons and significance of this change of trend will be discussed in Section 6.6.1

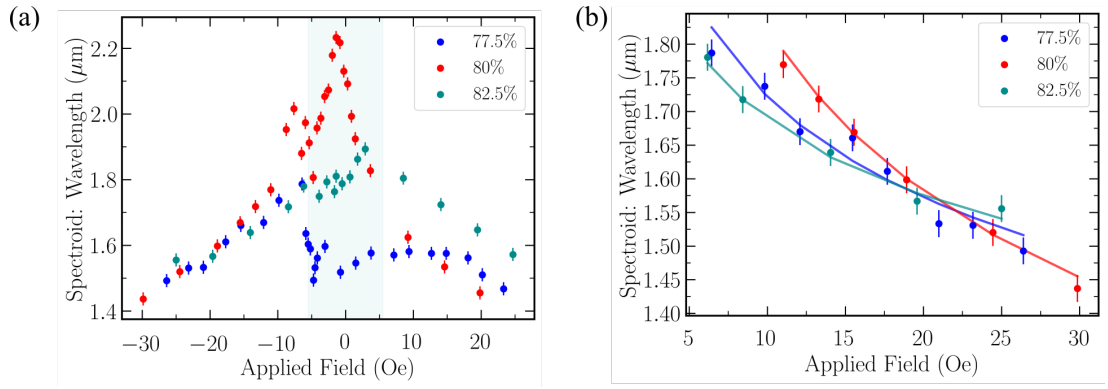

Figure 6.17: Hard axis magnetisation ripple analysis outputs for a magnetostrictive samples of varying sign. Field going from negative to positive in each case. The shaded area refers to the measured anisotropy field, H_K value. Outputs are plotted against field for (a) spectroid ripple wavelength $\lambda_{Spectroid}$. (b) is a specific region defined in (a), from a field of -25 Oe until just before the anisotropy field, with best fit power line.

6.6.1 Discussion

Magnetisation ripple analysis was completed along both the easy and hard axis reversal sequences. Ripple theory predicts that there will be a subtle suppression of ripple properties along the easy axis when compared to the hard axis with the same applied field. Experimental spectroid analysis confirms this theory for all magnetostrictive samples at a field of -25 Oe, exact values are presented in Table 6.5.

Experimental analysis was undertaken to determine if there are distinguishable differences in magnetisation ripple properties for the different magnetostrictive samples. Table 6.5 summarises key points from the spectroid curves. Note that ripple dispersion angle determination resulted in no obvious difference outside of experimental error, with all results in the order of 12 degrees at a field of -25 Oe, so will be disregarded for the rest of the discussion. The best fit power line exponents are also shown in Table 6.5. Similarly to results presented in Chapter 4, the exponents are lower than what is predicted by theory ($\lambda = H^{-0.5}$).

It is proposed that a magnetostriction effect would act to either increase or decrease ripple properties, depending on the sign. The 77.5% Ni sample, which is positive, may be expected to add a additional anisotropy factor along the applied field (easy axis), which would suppress the magnetisation ripple. A negative magnetostriction sample, 82.5% would have the opposite effect. There would be no effect on a zero magnetostrictive sample. Therefore, as proposed, there was a measurable reduction in the spectroid wavelength for the 77.5% Ni sample, when compared to both the 80 and 82.5%. The same outcome would also be expected for hard axis behaviour, with the 77.5% having the smallest wavelength, however the 80% sample measured a slightly lower wavelength (60 nm less than the 77.5% sample). Figure 6.9(b) showed the experimental M-H loops for hard axis behaviour which appeared to still retain significant magnetisation at zero field. In particular, the 80% and 82.5% loops had the largest bulk/TEM measurement difference out of the 3 samples. This should be considered when determining the validity of the increased ripple wavelength measurements for hard axis behaviour. However, one important positive to draw from the magnetisation ripple characterisation is that the 77.5% (+ve) sample consistently had a lower wavelength when compared the the 82.5% (-ve) sample, for *both* the easy and hard axis. This is expected as a larger uniaxial anisotropy (and increased H_k) acts to suppress magnetisation ripple properties.

As magnetostriction is such a small order effect (10^{-6}), the effects are expected to be subtle under current experimental and characterisation limitations. It is difficult to determine with certainty that the ripple suppression effect can be attributed to magnetostriction effects. It is much more likely that the variation between the films could be explained by changes in uniaxial anisotropy due to film composition. In reality, variation in all 3 films would be due to both compositional variations and magnetostrictive effects, where the compositional variational dominates.

As discussed, there are characterisable differences between the 3 films. In Figure 6.16, the 77.5% (+ve) Nickel samples' wavelength consistently stays smaller than the other two compositions. However, this remains the same even when there is no external field applied (at zero field), where the magnetostriction effect is expected

to be zero. It could be argued that there is a possible inherent anisotropy difference between the 3 films which is causing the magnetic variation between the films.

However, one indicator that it could be attributed to magnetostriction is that there is a larger difference between the 77.5% and 80% sample, when compared to the 80 and 82.5% sample. As stated in Table 6.1, the magnetostrictive effects are expected to be larger for the 77.5% sample when compared to the 82.5% film.

Overall, results suggest that there is a variation in both the bulk and micromagnetic properties between the 3 varying composition samples, with the 77.5% Ni having the strongest uniaxial anisotropy in the film and suppression of ripple properties. Further work would be needed to determine if this is solely due to anisotropy differences, or whether some effect can be attributed to magnetostriction. To improve the validity of the results presented here, a number of repeat experiments would be suggested to ensure consistency in the outputs.

Ni %	λ_S	EA λ_{Spec} μm	EA Fit	HA λ_{Spec} μm	HA Fit	λ Diff %
77.5	$+4 \times 10^{-6}$	1.38 ± 0.02	-0.06	1.52 ± 0.02	-0.13	+10
80	$+1 \times 10^{-6}$	1.44 ± 0.02	-0.11	1.50 ± 0.02	-0.2	+4
82.5	-2.5×10^{-6}	1.54 ± 0.02	-0.07	1.56 ± 0.02	-0.10	+1.3

Table 6.5: Easy and hard axis magnetisation ripple spectroid wavelength comparison measured at an applied field of -25 Oe. EA and HA Fit refers to the measured exponent of the best-fit power law.

6.7 Simulation of Magnetostrictive Effects

Simulations presented in this section will explore trends, with specific aims into investigating how different magnetostrictive signs may affect magnetic properties, using both simulated bulk and micromagnetic measurements (through magnetisation ripple characterisation).

Work published by QUB gave an insight into magnetostrictive behaviour on bulk measurements. [7] Using inverse magnetostrictive measurement techniques

(Section 1.5.3), stress can be applied to the film, and the change in magnetisation properties is measured. This manifests itself in a variation in anisotropy field H_k values. A positive magnetostrictive sample will experience an additional anisotropy effect in the same direction as the applied field. This acts to increase the films overall uniaxial anisotropy, thereby creating a harder loop and a larger H_k value (for hard axis measurements). A negative magnetostrictive sample will experience an opposing anisotropy effect to the applied field direction. This acts to reduce the overall uniaxial anisotropy and creates an 'easier' loop. The work presented at QUB used external stresses to produce substantial variations in magnetic behaviour that can be measured using bulk techniques. However, the work presented here focuses on characterising unstressed films, meaning the effect is expected to be much more subtle. Experimental bulk measurements (Section 6.4) showed a variation in the H_k and slope of the hard axis loops in the absence of applied stress. This was confirmed in Section 6.6 through the characterisation of magnetisation ripple which showed a reduction of magnetisation ripple wavelength when comparing the 77.5% (+ λ_S) and 82.5% (- λ_S) samples. Using experimental outputs as the basis of the simulation inputs, an investigation was undertaken with the aim of replicating positive and negative magnetostrictive effects for both bulk and micromagnetic behaviour.

6.7.1 Simulation Set-Up

The MuMax^3 simulation package can be used alongside experimental images to help further understanding micromagnetic dynamics and properties. However the MuMax^3 simulation package currently does not have the means to include a magnetostriction parameter. Therefore, other methods were devised to replicate both positive and negative magnetostrictive effects.

As described in Chapter 5, polycrystalline thin films have 2 sets of anisotropy factors. Simulations have been run using the 'Individual Anisotropy Contribution' model, developed for Chapter 5.3. Polycrystalline thin films have 2 sets of anisotropy factors. First, the random granular anisotropy K_g that is present in each grain and

can lie along any direction, and a global uniaxial anisotropy K_G that lies along a specific direction. Magnetostriction can be thought of as an additional averaged bulk anisotropy effect and will be referred to as K_M. Depending on its sign, it will act to either increase or decrease the overall uniaxial anisotropy of the film. A positive λ_S sample will have the K_M anisotropy lying parallel to the applied field. A negative λ_S sample will have the K_M lying perpendicular to the field. The resultant of all 3 anisotropies will produce a final relaxed magnetisation state. Figure 6.18 shows a simplified schematic of the anisotropy contributions used in the simulation model.

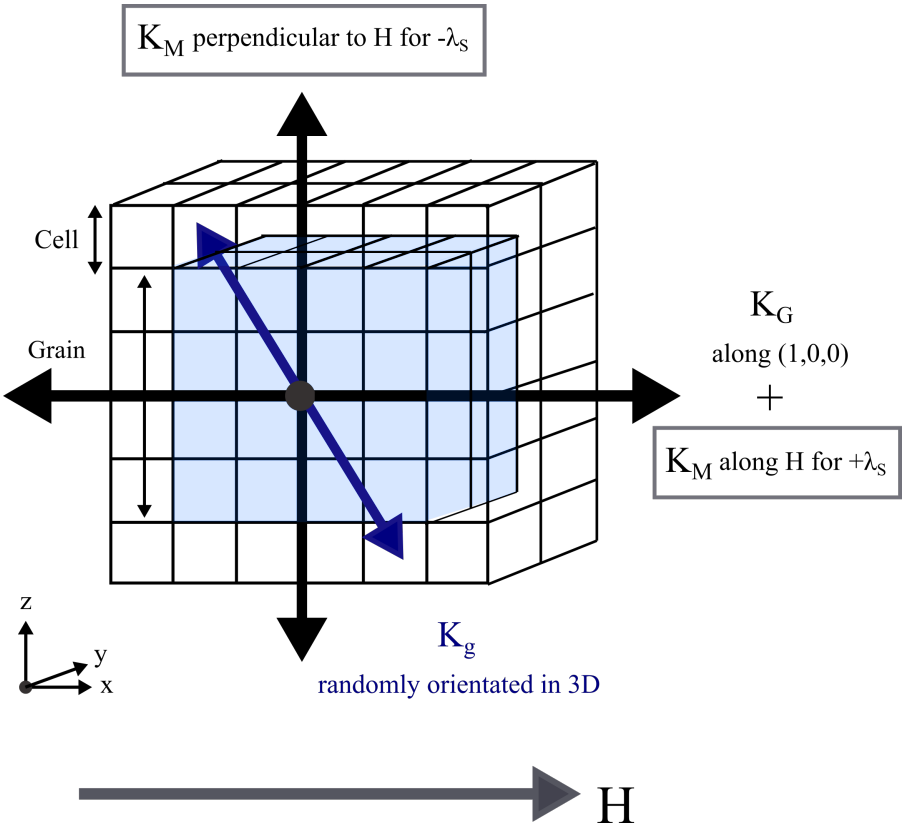

Figure 6.18: Magnetostriction MuMax^3 simulation set-up. Model allows for control of individual anisotropy components for a global uniaxial component K_G,a granular magnetocrystalline anisotropy component K_g and a magnetostriction anisotropy component K_M. The directionality of this component varies with magnetostrictive sign.

As mentioned, the simulations were performed by modifying the anisotropy model described in Chapter 5.3, for the following magnetic parameters:

- Bulk exchange constant $A = 13 \text{ x } 10^{-12}$ J/m
- Saturation magnetisation $M_s = 8.6 \text{ x } 10^5$ A/m

- Grid size = 1000 x 1000 x 1 cells
- Cell size = 5 nm x 5 nm x 20 nm
- Simulation size = 5 μm^2 x 5 μm^2 x 20 nm
- Grain size = 20 nm using Voronoi tessellation
- Periodic boundary conditions = 32 x 32 x 0 repetitions

Note that average grain size was set to 20 nm. As shown in Section 6.3.2, the grain size is significantly lower, averaging at 5 nm. However, larger cell and grain sizes were chosen to improve simulation computing time, whilst still retaining a large simulation dimensionality. As we are investigating magnetostrictive trends, this is not expected to impact results.

Table 6.6 provides a summary of the anisotropy contributions used to simulate magnetostrictive effects. Note, the K_G and K_M contributions were taken from experimental results presented in Section 6.4. The K_M values are equivalent to the variation in anisotropy field measured from the M-H loops (Figure 6.8(b)).

Composition % Ni	λ sign	Value [arb. units]	K_G J/m^3	K_g J/m^3	K_M J/m^3
77.5	+ ve	4×10^{-6}	200	100	+40
80	≈ 0	1×10^{-6}	200	100	0
82.5	- ve	-2.5×10^{-6}	200	100	-20

Table 6.6: Summary of composition of samples fabricated in this study. Magnetostrictive sign and value as a function of nickel composition in permalloy. Table includes summary of anisotropy contributions used in simulation model.

In order to obtain a hysteresis sequence for each simulation, the magnetisation of the ferromagnetic material, in this case permalloy, was initially uniformly magnetised in x-direction. A magnetic field can be applied along the same direction for an in-plane easy axis behaviour. A field can be applied perpendicular for hard-axis outputs. For all simulations a maximum field H_{max} of 50 Oe was applied from $+H_{max}$ to $-H_{max}$ for one hysteresis sweep.

6.7.2 Simulation Results

M-H Measurements

Figure 6.19 shows normalised hysteresis loops with the external field applied along (a) the easy axis and (b) hard axis. Results produced a clear variation between different magnetostrictive simulations, which follow the trends seen experimentally (Figure 6.8 for direct comparison).

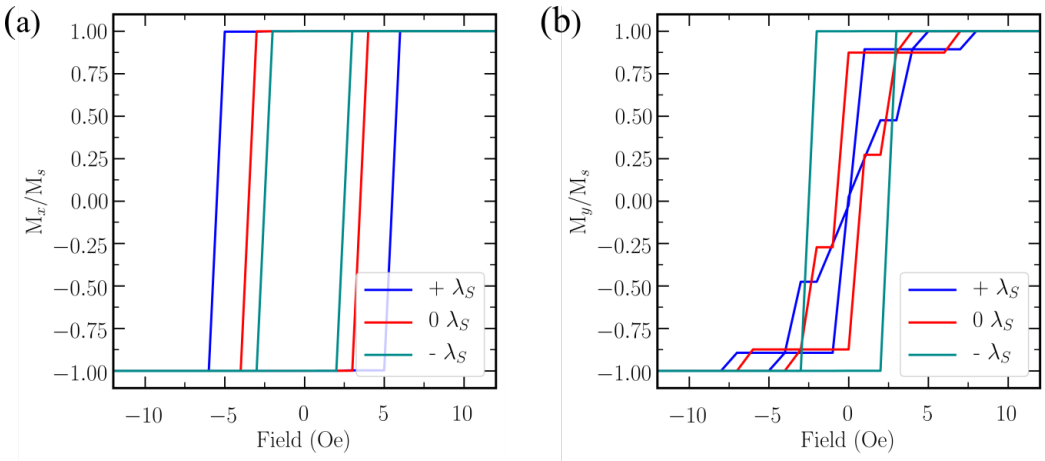

Figure 6.19: Simulated (a) easy and (b) hard axis M-H hysteresis loops for a 20 nm $Ni_{80}Fe_{20}$ thin film. Parameters of the simulation include a global anisotropy of K_G of 200 J/m^3, a granular anisotropy of K_g of 100 J/m^3 and a grain size diameter of 20 nm. The mangetostrictive anisotropy K_M was dependent on mangetostrictive sign. All inputs are highlighted in Table 6.6.

A positive magnetostrictive simulation acted to increase the films overall uniaxial anisotropy when compared to the simulation with zero magnetostrictive effects. This results in well defined unixial behaviour. Similarly, the +ve magneteostrictive simulation resulted in a 'harder' hard axis loop, through an increase in the anisotropy field H_K. The negative magnetostriction simulation produced opposite results, producing isotropic behaviour. Key points in the simulated M-H loops are highlighted in Table 6.7.

Simulated Fresnel Image Characterisation

MuMax^3 produces magnetisation components which can be used to simulate Fresnel images using Digital Micrograph. [12,13] Fresnel images are shown in Figure 6.20

Ni Content %	λ_S sign	EA H_C (Oe)	EA M_R [arb. units]	HA H_C* (Oe)	HA H_K (Oe)	HA M_R [arb. units]	K_u J/m^3
77.5	+ve	5	0.9997	-	5	0.0245	200
80	0	3	0.9997	1	4	0.8737	160
82.5	-ve	2	0.9993	2	-	0.9709	-

Table 6.7: Key parameters from simulated M-H magnetic measurements, with variation in magnetostrictive anisotropy effects K_M. Results presented for both easy axis and hard axis outputs. The effective K_u value is determined from the measured H_k where $K_u = M_S H_k/2$. *Indicates a hard axis coercive measurement, indicating more isotropic behaviour.

for a 50 Oe field applied along the easy axis. Visually, all images do exhibit similar, or possibly near identical, magnetisation ripple properties, which can then be characterised using the methodology detailed in Sections 3.7 and 3.8.

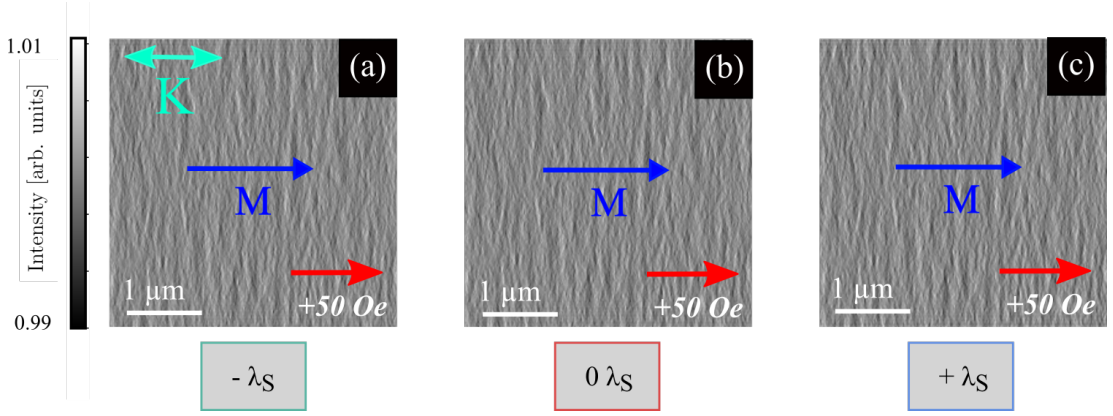

Figure 6.20: Simulated Fresnel image outputs with 500μm defocus for (a) - λ_S, (b) 0 λ_S, (c) + λ_S at a 500μm defocusing displaying magnetisation ripple properties at an applied field of +50 Oe along the easy axis.

Outputs for both spectroid and dominant ripple characterisation are shown in Figure 6.21. These represent magnetisation ripple wavelength values with a field applied along the easy axis. Analysis showed minimal variation of ripple wavelength between the 3 simulation outputs. This was again confirmed through further analysis of additional properties such as dispersion, which are highlighted in Table 6.8. Analysis did show a slight increase in ripple properties along the hard axis, when compared to easy axis outputs. This is was is predicted by theory, and also seen experimentally.

Simulation outputs for measured spectroid wavelength are significantly smaller than that seen experimentally in Section 6.6 (≈ 700 nm), by over an order of magnitude. Result presented in Chapter 5.3.3 (Figure 5.19) detailed the difference in wavelength spectrum's for both experimental and simulated magnetisation ripple. Simulated ripple consists of significantly more short wavelength contributions when compared to an experimental spectrum. Simulated dominant wavelength values are slightly larger than the spectroid wavelength, but are still much lower than experimental values. The simulated outputs presented here are not physically significant (for example, there are significant differences in grain size), however it is a useful exercise for determining trends in behaviour.

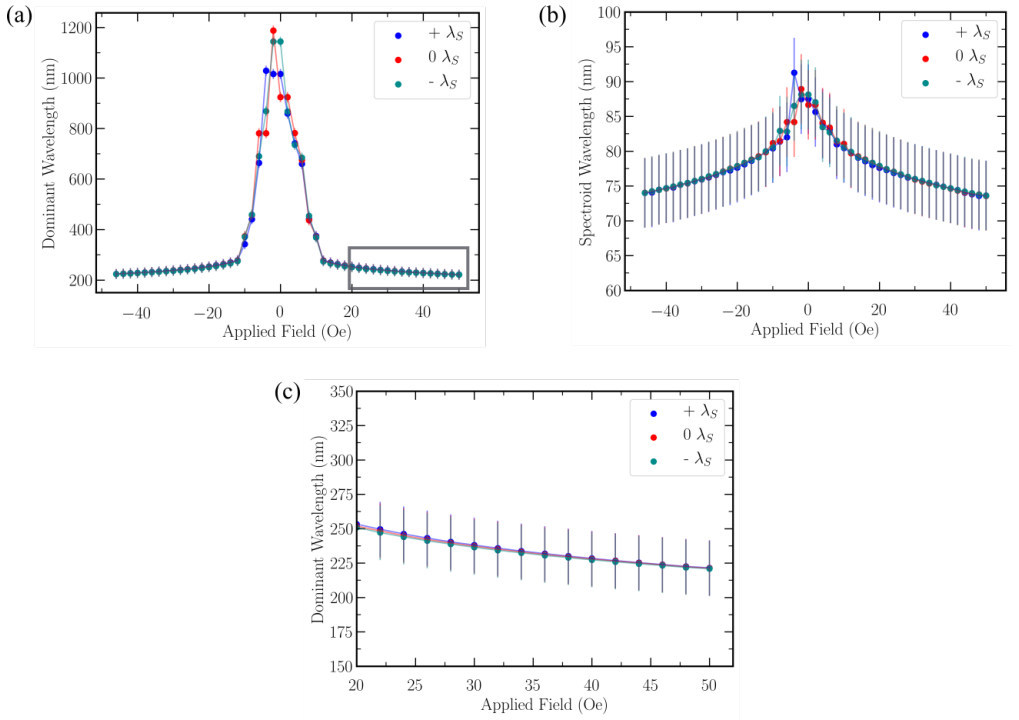

Figure 6.21: Simulated magnetisation ripple wavelength analysis for an applied field along the easy axis. (a) Dominant wavelength, (b) spectroid wavelength from +H_{max} to -H_{max} and (c) dominant wavelength over a selected range of 20 - 50 Oe, outlined by the region in (a).

Although this is a simplistic simulation model of variation in uniaxial anisotropy properties (with the aim of reproducing magnetostrictive-like effects), it has produced successful trends that replicate effects seen experimentally from bulk magnetic measurements. Although micromagnetic analysis produced negligible variation

between the simulations, it is suggested that an exaggerated magnetostrictive anisotropy contribution would produce measurable changes to investigate trends. In real systems, the magnetostriction component would be considerably smaller than that of other anisotropy contributions.

	λ sign	M/M$_s$ [arb. units]	$\lambda_{Spectroid}$ (nm)	λ_{Dom} (nm)	Dispersion θ $^\circ$	M component $^\circ$
EA	+ λ_S	0.999997	74 ± 5	220 ± 20	47 ± 1	0.12
	0 λ_S	0.999997	74 ± 5	220 ± 20	47 ± 1	0.13
	- λ_S	0.999997	74 ± 5	220 ± 20	47 ± 1	0.13
HA	+ λ_S	0.999996	74 ± 5	260 ± 20	51 ± 1	0.14
	0 λ_S	0.999996	74 ± 5	260 ± 20	51 ± 1	0.14
	- λ_S	0.999996	74 ± 5	260 ± 20	51 ± 1	0.14

Table 6.8: Key outputs from easy and hard axis ripple analysis for simulated Fresnel images at a field of +50 Oe, displaying negligible changes between samples of different magnetostrictive signs.

6.8 Heat Experiments

Facilities in The University of Glasgow allow for the option of in-situ heating experiments. An initial investigation was undertaken to determine the temperature dependence on micromagnetic properties of a 81% Ni permalloy thin film. This particular composition was chosen for a preliminary experiment as it is the current material used in data storage technology. [14-16]

In-situ heating experiments were carried out in a JEOL ARM 200cF TEM equipped with a cold-field emission gun. The microscope was operated at a standard 200 kV. The objective lens was turned off prior to sample insertion, to ensure a near field-free environment. A Gatan HC3500 sample holder was used to heat the specimen in the electron column. The maximum temperature that could be applied was 250°. Fresnel images were acquired in steps of 20 degrees, using the Gatan Orius SC1000A CCD camera. Magnetisation ripple analysis was applied to the set of acquired Fresnel images.

The spectroid wavelength outputs in plotted as a function of temperature in Figure 6.22(a). Results show there is little variation in the magnetisation ripple properties, that can be attributed outside of experimental error. It can be suggested that temperatures up to 250 degrees have negligible impact on the micromagnetic properties and the films M_S. This is confirmed again when the Fresnel image contrast was investigated as a function of temperature in Figure 6.22(b). Similarly, no significant variation was found. Ripple dispersion analysis gave the same outcome.

This reiterates what was seen in previous publications, specifically one by T. Suzuki which found that magnetisation ripple properties, such as ripple wavelength, remained nearly constant, showing only a 20% decrease of ripple wavelength before the ripple contrast disappeared at a temperature of 350°. These experiments also used permalloy alloys, of composition $Ni_{76}Fe_{24}$, with thickness's ranging from 15 to 35 nm. [17] Although direct comparison can not be made at higher temperatures due to heating limitations.

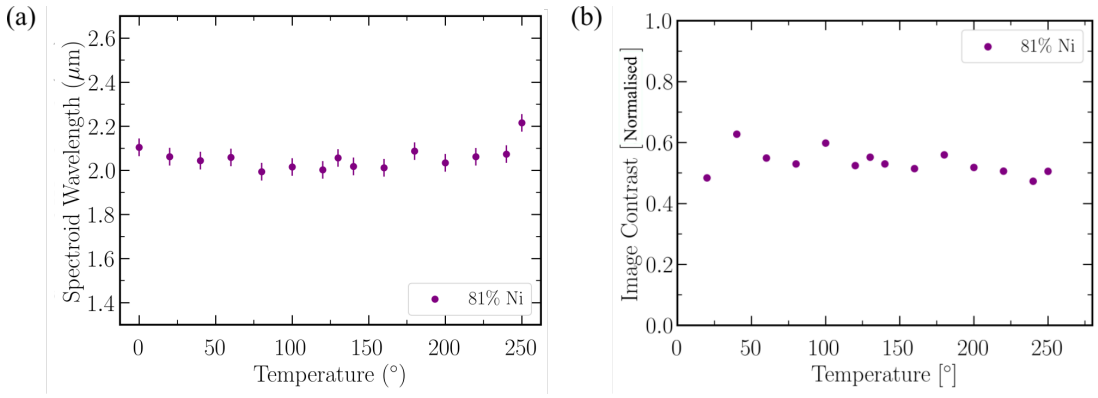

Figure 6.22: Magnetisation ripple analysis outputs for a 81% Ni magnetostrictive thin film. Outputs are plotted against temperature for (a) spectroid ripple wavelength $\lambda_{Spectroid}$ and (b) Fresnel image contrast.

6.9 Summary and Conclusions

This chapter focused on one of the most commonly used materials in data recording, permalloy with a composition varying around the 80/20 nickel to iron ratio. The reason for choosing this value is that the magnetostriction constant changes from

negative to positive around this composition as the elemental ratio changes. Thin films of different permalloy compositions were observed to be near identical from physical characterisation. Dark field TEM images showed that there was a regular distribution of the grains for each sample, and this was confirmed through log-normal analysis. Outputs for all three samples were all in agreement, with an average grain diameter of 6.0 nm. The crystal structure was also determined from SAED patterns, which confirmed all samples to be polycrystalline, with both *fcc* (NiFe) and *hcp* (Ru) layers present. There was no texture present in any sample.

Bulk magnetic measurements were taken using a B-H looper. All samples exhibited well defined uniaxial hysteresis loops. The easy axis showed near identical hysteresis loops, with negligible changes in the measured coercive field. However, the hard axis exhibited a modest variation with an increase in H_k with decreasing composition. A positive magnetostrictive material would act to increase uniaxial anisotropy in a film, so the bulk B-H results were in agreement with initial predictions.

We have demonstrated how the Fresnel mode of Lorentz microscopy can be used to provide a detailed description of the magnetisation reversal processes for the three varying composition Ni_xFe_{100-x} thin films. It allows for direct visualisation of micromagnetic processes during magnetisation reversal, allowing for a more detailed insight into micromagnetic behaviour when being compared with standard bulk BH measurements.

Permalloy polycrystalline thin films exhibit a phenomenon called magnetisation ripple. Each composition was analysed for spectroid ripple wavelength properties along both the easy and hard axis, throughout a hysteresis sequence. Results show there was a suppression of the magnetic ripple properties along the hard axis when being compared to easy axis measurements at the same applied field. This is consistent with classical ripple theory proposed by Hoffmann. Ripple analysis showed that the +ve magnetostrictive sample generally had a lower wavelength when compared to the near 0, and -ve magnetostrictive samples. The -ve magnetostrictive sample generally had the largest ripple wavelength. There are obvious differences

between the 3 samples that do follow trends that have been seen experimentally in previous publications where there is an increase in measured H_k with decreasing Ni content. [6] However, these publications used excess stress to exaggerate magnetostrictive effects. The results presented in this thesis are much more subtle and involve quantifying variations without the need for external straining.

It can be concluded that there are differences between the films, showing an increase in uniaxial anisotropy, and therefore a reduction in magnetisation ripple properties with decreasing Ni content. However, it is not possible to determine if these variations are exclusively due to differences in magnetostrictive properties. Alternatively, the anisotropy and magnetisation ripple variations between samples could be attributed to compositional variations. Further work would be needed to better determine this and will be discussed in Chapter 7.

MuMax^3 simulations were run using a modified 'Individual Anisotropy Contribution' model (developed in Section 5.3) to introduce an additional magnetostriction anisotropy term to replicate the effect of both positive and negative magnetostriction effects. Simulated bulk measurements were useful for replicating the trends seen experimentally in Section 6.4. A +ve magnetostriction effect will increase the overall uniaxial anisotropy of the film through an increase in H_k. The -ve magnetostrictive simulation resulted in the opposite effect, with a decrease in uniaxial anisotropy, so much so that the behaviour was isotropic. Magnetisation ripple analysis of simulated Fresnel images resulted in negligible variation in both ripple wavelength and dispersion. It is suggested that much larger anisotropy values would need to be used to replicate the trends seen experimentally in Section 6.6.

The final section involved a preliminary investigation into how temperature effects the magnetisation ripple wavelength of an 81% Ni thin film. This particular composition was used as it is currently used in data storage devices. It exhibits near zero magnetostriction. There was found to be no significant changes in ripple properties for up to temperatures of 250°. This agrees with other publications that show the ripple properties don't begin to degrade until a temperature of 350°.

6.10 References

[1] Osaka T. A soft magnetic CoNiFe film with high saturation magnetic flux density and low coercivity *Nature* 392, 796–798, (1998).

[2] K. Okita. 2012 Magnetostriction measurement of a giant magnetoresistance film on a practical substrate covered by a shield layer *Journal of Applied Physics.* 111 07E340–3, (2012).

[3] K. Kudo Magnetic Shield, Manufacturing Method Thereof and Thin Film Magnetic Head Employing the Same U.S. Patent No. US2008/0002308 A1, (2008).

[4] R. Grossinger, R. Turtelli and N. Mehmood. Materials with high magnetostriction. *IOP Conf. Series: Materails Science and Engineering* 60:012002, (2014).

[5] L. Yiwei. Fabrication, properties, and applications of flexible magnetic films. *Chin. Phys. B.* 22(12):127502, (2013).

[6] P. T. Squire Magnetomechanical measurements of magnetically soft amorphous materials. *Meas. Sci. Technol.* 5 67-81, (1994).

[7] C. Hill. Whole wafter magnetostriction metrology for magnetic films and multilayers. *IOP Science, Meas. Sci. Technol.*, 24:45601, (2013).

[8] R. Becker, M. Kersten. *Z. Phys.* 64,660, (1930).

[9] J. Leliaert. Fast micromagnetic simulations on GPU and recent advances made with mumax3. *Journal of Physics D: Applied Physics*. 51:12, (2018).

[10] K. Krush. Sputter parameters and magnetic properties of permalloy for thin film heads. *IEEE Transactions on Magnetics*. 22:626-628, (1986).

[11] R. Bonin. Dependence of magnetisation dynamics on magnetostriction in NiFe alloys. *Journal of Applied Physics*. 98, 123904, (2005).

[12] S. McVitie and M. Cushley. Quantitative Fresnel Lorentz microscopy and the transport of intensity equation. *Ultramicroscopy*, 106(4-5):423-431, 2006.

[13] D. R. G. Mitchell, B. Schaffer. Scripting-customised microscopy tools for DigitalMicrograph. *Ultramicroscopy*. 103:319-332, (2005).

[14] D. Weller. A HAMR media technology roadmap to an areal density of 4 Tb/in^2. *IEEE Transactions on Magnetics*. 50(1):1-8, (2014).

[15] M. Kryder. Heat assisted magnetic recording. *Proceedings of the IEEE*. 96:11, (2008).

[16] G. Ju. High density heat assisted magnetic recording media and advanced characterization – Progress and challenges. *IEEE Transactions on Magnetics* 51(11):1-1, (2015).

[17] T. Suzuki and C. H. Wilts. Quantitative study of the magnetisation ripple in ferromagnetic nife alloy. *Journal of Applied Physics*. 39(2):1151-1153, (1968).

7

Summary and Outlook

This chapter will summarise the main outcomes of the research presented in this thesis followed by suggestions for relevant future research avenues.

The work presented in this thesis centres on research into the characterisation of ferromagnetic polycrystalline thin films, with special focus on Lorentz transmission electron microscopy (LTEM). Bulk magnetic measurements, such as standard magnetometry methods, are well established techniques for characterising large magnetic wafers. However, bulk measurements don't present the full picture of a materials behaviour. Lorentz microscopy allows for in-situ visualisation of the micromagnetic structure of magnetic thin films, where the magnetic signal variation would be too low for standard bulk measurements. The nano-scale visualisation reveals a structure, commonly referred to as 'magnetisation ripple'. This is a phenomenon that occurs in polycrystalline thin films. It originates from the individual granular magnetocrystalline anisotropy of the film, that can be randomly oriented. This results in the magnetisation fluctuating around a local mean direction, rather than lying along one uniform direction.

Chapter 3 details a thorough study into previous magnetisation ripple characterisation methods. Different publications over the past 50 years have proposed

varying methods to produce a single output for magnetisation ripple properties, such as ripple wavelength and dispersion angle. Difficultly in characterisation arises as the magnetisation ripple properties consist of a spectrum of values, rather than one standard output. However, there has not been a newly developed methodology proposed since 2002. Discussions described how previous methodology's might produce inaccurate outputs and how these methods can be improved up. This chapter presents a detailed discussion into a newly developed method of characterisation for the purposes of this thesis, which allows for large sets of both experimental and simulated Fresnel images throughout a hysteresis sequence to be characterised with ease. These new proposed methods, of (a) ripple dispersion angle θ, (b) dominant ripple wavelength λ_{Dom}, (c) weighted mean of the wavelength spectrum $\lambda_{Spectroid}$ and (d) FFT image intensity I, were used for ripple analysis in all following results chapters. The benefits of an automated characterisation method include reducing human biasing effects, with the additional convenience of producing results quickly. This method creates additional information, specifically for the $\lambda_{Spectroid}$ wavelength, that has not been seen before in previous publications. This methodology has the potential to be used as a standard in future magnetisation ripple characterisations.

The rest of the results presented in this thesis includes characterisation of permalloy thin films of varying compositions, for different applications.

Chapter 4 presented the influence of ultra-thin $Ni_{79}Fe_{21}$ seed layers on thin $Ni_{45}Fe_{55}$ polycrystalline films with soft magnetic properties. $Ni_{45}Fe_{55}$ has long been a high moment alternative for the more commonly used permalloy composition of $Ni_{80}Fe_{20}$ in hard disk (HDD) read-write head design. The goal of this work was to investigate how seed layers can control both the physical and magnetic properties of the film, with the aim of creating a higher moment film, that still retained a strong uniaxial anisotropy. Grain size distribution analysis using bright-field and dark-field imaging showed that the addition of ultra-thin seed layers drastically reduced the average grain size by over 75% when compared to the unseeded sample. It also reduced the spread of the grain sizes to produce a more regular distribution. SAED analysis showed a reduction in film texture with seed layer addition. Bulk

magnetic measurements showed a vast increase in uniaxial anisotropy which was confirmed through magnetisation ripple analysis of experimental Fresnel images. Similarly to grain size reduction, there was a 75% suppression of ripple wavelength through an addition of 0.5 nm seed layer. The 0.5 nm and 1.0 nm samples had a very subtle suppression of magnetic properties, suggesting a thicker seed layer sample would not improve magnetic properties further. The dramatic effect of seed layer addition suggests the film is a good candidate for controlling properties of $Ni_{45}Fe_{55}$ thin films, whilst maintaining a high magnetic moment density. This project has been extremely successful in controlling high moment materials magnetic properties. $Co_{70}Fe_{30}$ materials could also be an interesting avenue since it has a high saturation magnetisation of 1.8 T, building on the 1.6 T seen in $Ni_{45}Fe_{55}$ materials (compared to 1.0 T seen in $Ni_{79}Fe_{21}$). Previous work has shown the coercive field is nearly 50% larger than that seen in the unseeded sample presented in Chapter 4, meaning manipulation of the magnetic properties might prove more difficult. [1-3] However, if the coercivity and anisotropy can be controlled, like seen in this project, it could be a viable option for reader applications.

Work presented in Chapter 5 features a study into development of micromagnetic models using MuMax^3 software, with the aim of producing trends in magnetisation ripple properties for permalloy polycrystalline thin film to match trends seen experimentally in Chapter 4. Two different models have been developed to simulate magnetisation ripple properties. First, a 'Granular Magnetocrystalline Anisotropy Axis Variation model', which has a directional variation about a mean direction of magnetisation, whilst a second model introduces a more sophisticated methodology consisting of two 'Independent Anisotropy Contributions' for global and granular anisotropy.

Both models were successful in producing qualitatively excellent simulated Fresnel images which visually replicated experimental magnetisation ripple properties and followed typical easy and hard axis hysteresis behaviour. The latter model was used to simulate the effect of grain size to replicate the trends presented in Chapter 4. It proved to have a significant change effect on magnetic properties, with a smaller

grain size increasing the simulated uniaxial anisotropy. All magnetisation ripple properties, such as wavelength and dispersion, increased with increasing grain size. This confirmed what was seen experimentally in Chapter 4 proving the validity of the model for predictive trends in magnetisation ripple properties. The effect of intergranular exchange coupling had a more subtle effect when compared to the grain size variation. However, it did produce an increase in ripple dispersion and a decrease in wavelength with decreasing coupling, which are in agreement with trends predicted by magnetisation ripple theory. However, the simulated ripple spectrum had a much greater high spatial frequency contribution when compared to an experimental spectrum, which provides a problem for future work. There are still many parameters within the models that could lead to additional investigations. An obvious variable would be thickness dependence of magnetisation ripple properties, as that is something that is well known experimentally whereby a thicker sample will experience a suppression of properties. [4] Similarly, the effect of heat on magnetisation ripple can be easily simulated within the models, whereby the magnetisation strength, and therefore the ripple will degrade with increasing temperature. These models will be useful for simulation studies in magnetisation ripple, as they can be easily modified for a variation of material constants, physical properties and anisotropy contributions.

Lastly, we quantitatively assessed the magnetic effect magnetostriction has on the hysteresis behaviour of magnetostrictive samples with varying signs, without the need for external straining. Previous publications detail effects of magnetostriction under external applied stress. The effect of magnetostriction under normal operating conditions is less well understood. A micromagnetic and simulation modelling investigation was undertaken. Results show that although all 3 films of varying magnetostrictive signs exhibited near identical physical properties, there was a subtle variation in micromagnetic properties. The negative magnetostrictive sample exhibited a decrease in uniaxial anisotropy, with the positive magnetostrictive sample exhibiting the opposite. This was confirmed in micromagnetic characterisation of magnetisation ripple, resulting in a small suppression of ripple wavelength

for the positive magnetostrictive sample. Variations between magnetostrictive samples in this work have been characterised without any stress effects, and are therefore much more subtle. Simulation modelling produced similar trends for bulk magnetic behaviour, however found negligible changes for simulated ripple properties. Although there are subtle variations between samples, it is difficult to exclusively attribute these changes to simple compositional variations or magnetostrictive effects.

Proposals for potential future work of magnetostrictive characterisation include several options that could be used for in-situ straining of samples within the microscope column. This would lead to much more obvious stress effects and therefore easier characterisation. There are several mechanical straining TEM sample holders that would allow for control of in-situ straining whilst using Lorentz imaging to characterise the effect on micromagnetic behaviours. [5-7] There would also be the option of local strain mapping under in-situ standard TEM. [8] Another alternative method to in-situ strain effects could be the use of heat. [9-13] The magnetic material can be directly deposited onto a heating chip, which will act as a substrate, which is known to expand when heating. Alternative imaging techniques, such as magneto-optic Kerr effect (MOKE) microscopy and magnetic force microscopy (MFM) are also viable options for imaging in-situ stress effects. [14,15] However this would not allow for the imaging of the magnetisation ripple structure, but rather the domain configurations.

7.1 References

[1] G. Scheunert. A review of high magnetic moment thin films for microscale and nanotechnology applications. *Applied Physics Reviews.* 3, 011301, (2016).

[2] T. Osaka. A High Moment CoFe Soft Magnetic Thin Film Prepared by Electrodeposition. *Electrochemical and Solid State Letters.* 6(4), (2003).

[3] B. Zong. Ultrasoft and High Magnetic Moment CoFe Films Directly Electrodeposited from a B-Reducer Contained Solution. *Research Letters in Physical Chemistry*. 342976, (2008).

[4] T. Suzuki and C. H. Wilts. Quantitative study of the magnetisation ripple in ferromagnetic NiFe alloy. *Journal of Applied Physics*. 39(2):1151-1153, (1968).

[5] M. Legros. In situ mechanical TEM: Seeing and measuring under stress with electrons. *Comptes Rendus Physique*. 15:224-240, (2014).

[6] Z. Q. Feng. In-situ TEM investigation of fracture process in an Al–Cu–Mg alloy. *Materials Science and Engineering: A*. 586:259-266, (2013).

[7] X. Q. Zhu. In situ high resolution transmission electron microscopy investigation of deformation mechanism in sub-10-nm Au crystals. *Materials at High Temperature*. 30:7, (2014).

[8] C. Cao. Local strain mapping of GO nanosheets under in situ TEM tensile testing. *Applied Materials Today*. 14:102-107, (2019).

[9] H. Saka. In Situ Heating Transmission Electron Microscopy. *MRS Bulletin*. 33(2):93-100, (2008).

[10] Y. Song. In situ heating TEM observations of a novel microstructure evolution in a low carbon martensitic stainless steel. *Materials Chemistry and Physics*. 165:103-107, (2015).

[11] T. A. Macgregor. Preparation and testing of MEMS-based samples for in situ heating and biasing in the TEM/STEM. *Microscopy and Analysis.* (2019).

[12] T. Almeida. Quantitative TEM imaging of the magnetostructural and phase transitions in FeRh thin film systems. *Nature Scientific Reports.* 7:17835, (2017).

[13] G. Macauley. Tuning magnetic order with geometry: Thermalization and defects in two-dimensional artificial spin ices. *Physical Review B.* 101,144403, (2020).

[14] W. Rave. Quantitative observation of magnetic domains with the magneto-optical kerr effect. *Journal of Magnetism and Magnetic Materials.* 65:7-14, (1987).

[15] J. McCord. Progress in magnetic domain observation by advanced magneto-optical microscopy. *Journal of Physics D: Applied Physics.* 48,333001. (2015).